RECEIVED
LAWRENCE
BERKELEY LABORATORY
APR 7 1986
LIBRARY AND
DOCUMENTS SECTION

BMI/OCRD-17 c.1
LBL-14975

Verification and Characterization of Continuum Behavior of Fractured Rock at AECL Underground Research Laboratory

Technical Report

February 1985

For Reference
Not to be taken from this room

J. C. S. Long
of
Lawrence Berkeley Laboratory
University of California

prepared for

Office of Crystalline Repository Development
Battelle Memorial Institute
505 King Avenue
Columbus, Ohio 43201-2693

OCRD
Office of Crystalline Repository Development

BATTELLE Project Management Division

LBL-14975 c.1

BIBLIOGRAPHIC DATA

Long, J.C.S., 1985. *Verification and Characterization of Continuum Behavior of Fractured Rock at AECL Underground Research Laboratory,*, BMI/OCRD-17, LBL-14975, prepared by Lawrence Berkeley Laboratory, University of California, for Office of Crystalline Repository Development, Battelle Memorial Institute, Columbus, OH.

NOTICE

This report was prepared as an account of work sponsored by an agency of the United States Government. Neither the United States Government nor any agency thereof, nor any of their employees, makes any warranty, expressed or implied, or assumes any legal liability or responsibility for the accuracy, completeness, or usefulness of any information, apparatus, product, or process disclosed, or represents that its use would not infringe privately owned rights. Reference herein to any specific commercial product, process, or service by trade name, trademark, manufacturer, or otherwise, does not necessarily constitute or imply its endorsement, recommendation, or favoring by the United States Government or any agency thereof. The views and opinions of authors expressed herein do not necessarily state or reflect those of the United States Government or any agency thereof.

Printed in the United States of America
Available from
National Technical Information Service
U.S. Department of Commerce
5285 Port Royal Road
Springfield, VA 22161

NTIS price codes
Printed copy: A12
Microfiche copy: A01

BMI/OCRD-17
LBL-14975

Verification and Characterization of Continuum Behavior of Fractured Rock at AECL Underground Research Laboratory

Technical Report

Februrary 1985

J. C. S. Long
of
Lawrence Berkeley Laboratory
University of California

prepared for

Office of Crystalline Repository Development
Battelle Memorial Institute
505 King Avenue
Columbus, Ohio 43201-2693

The content of this report was effective as of September 1982. This report was prepared by Lawrence Berkeley Laboratory, University of California, with Battelle Project Management Division, Office of Crystalline Repository Development under Contract Nos. DE-AC03-76SF00098 and DE-AC02-83CH10139 with the U.S. Department of Energy.

ACKNOWLEDGMENTS

I would like to take this opportunity to thank many of the people who have helped and guided me while this work was being done. I would like to thank Paul Witherspoon. His support, enthusiasm, and guidance are behind the achievements I have made. My success and the successes of his many students testity to Paul's unusual qualities as an advisor, and I am very proud to be his student.

Many thanks are due to Charlie Wilson. Many of the ideas in this report are the direct result of discussions with Charlie. More importantly though, Charlie has a unique ability to culture individual achievement, and I have greatly benefited from him in this regard.

Discussions I had with Tom Doe in the initial stages of this work were instrumental to my understanding of the statistics of fracture systems. Tom's geological point of view kept the real world from getting lost. Janet Remer programmed the mesh generator used in all the calculations. Janet also wrote a plotting program to plot the fracture networks. Her work was skilled and thorough. Kenzi Karasaki did a very competent job of writing the program to plot the permeability results. Oliver Wan and Peggy Maclean also provided skilled programming. Diane Heinze helped with several tasks. To these people I am very grateful.

I would also like to mention Shalomo Neuman, T. N. Narasimhan, Paul Day, Iraj Javandel, Howard Endo, and Jahandar Noorishad who have each in some way influenced me and this work. Thanks are due to Irving Fatt and Kent Udell for reviewing this document.

This work was supported by the United States Department of Energy through the Office of Nuclear Waste Isolation (ONWI) of Battelle Columbus. Individuals at ONWI responsible for obtaining this support include Jim Duguid, Mike Wigley, and Bill Ubbes. The data analyzed in Chapter 7 are from the Atomic Energy of Canada Limited. I am indebted to Cliff Davison of that organization for providing the data. This research was performed in the Earth Sciences Division (ESD) of Lawrence Berkeley Laboratory. To John Phillips and Bill Stromdahl of the ESD, I am indebted for project management.

I cannot say enough nice things about Lois Armetta, Ellen Klahn, and Marille Bailey. Lois and Ellen did a masterful job of word processing all

these pages. Marilee Bailey is responsible for the excellent drafting. I owe a great deal to their skill, patience, sympathy and humor through all the changes.

This work could not have been done without the people who took care of my children while I was working. The oft beleaguered U.C. Childcare Program provided skilled and warm care for Matt and Jenny. This work must be taken as a testament to the need for such facilities. In particular, I want to thank Janet Robinson, Jill Maeder, Amber Leonard, Duff Munson, Yvonne Rollins, Ken Nakamurra, Christy Shoemaker, Maryanne Wardell, and Linda Wooley.

To may husband, Charlie, my children, Matt and Jenny; and my parents Grace and Fernando Sisto: many, many thanks.

ABSTRACT

The purposes of this study are to determine when a fracture system behaves as a porous medium and what the corresponding permeability tensor is. A two-dimensional fracture system model is developed with density, size, orientation, and location of fractures in an impermeable matrix as random variables. Simulated flow tests through the models measure directional permeability, K_g. Polar coordinate plots of $1/\sqrt{K_g}$, which are ellipses for equivalent anistropic homogeneous porous media, are graphed and best fit ellipses are calculated. Fracture length and areal density were varied such that fracture frequency was held constant. The examples showed the permeability increased with fracture length. The modeling techniques were applied to data from the Atomic Energy of Canada Ltd.'s Underground Research Laboratory facility in Manitoba, Canada by assuming the fracture pattern at the surface persists at depth. Well test data were used to estimate the aperture distribution by both correlating and not correlating the aperture with fracture length. The permeability of models with uncorrelated length and aperture were smaller than those for correlated models. A Monte Carlo type study showed that analysis of steady state packer tests consistently underestimate the mean aperture. Finally, a three-dimensional model in which fractures are discs randomly located in space, interactions between the fractures are line segments, and the solution of the steady state flow equations is based on image theory was discussed.

TABLE OF CONTENTS

Page

NOMENCLATURE xiii

1 INTRODUCTION 1

2 LITERATURE REVIEW 3
2.1 DETERMINATION OF EQUIVALENT POROUS MEDIA PERMEABILITY FROM FRACTURE GEOMETRY 3
2.2 HOMOGENEOUS ANISOTROPIC PERMEABILITY 8
2.3 STATISTICS OF FRACTURE GEOMETRY 25
2.4 CONCLUSIONS FROM THE LITERATURE SURVEY 37

3 DESCRIPTION OF THE NUMERICAL ANALYSIS 39
3.1 INTRODUCTION 39
3.2 MESH GENERATION 39
3.3 STATISTICAL CONSIDERATIONS 42
3.4 MEASUREMENT OF CONDUCTIVITY 42
3.5 ROTATION OF THE FLOW REGION 46
3.6 FRACTURE FLOW PROGRAM 48
3.7 MATHEMATICAL DESCRIPTION OF RANDOM GENERATION 50
3.8 CALCULATION AND PLOTTING OF AVERAGE ISOPOTENTIALS 53
3.9 VERIFICATION OF THE CONDUCTIVITY MEASUREMENT 54
3.10 EXAMPLES OF RANDOM FRACTURE SYSTEMS 59

4 FRACTURE GEOMETRY STUDIES 69
4.1 EFFECT OF FRACTURE DENSITY 69
4.2 EFFECT OF APERTURE AND ORIENTATION DISTRIBUTION 72
4.3 SCALE EFFECT 74
4.4 CONCLUSIONS 77

5 REGRESSION ANALYSIS TO DETERMINE THE PERMEABILITY TENSOR 79
5.1 INTRODUCTION 79
5.2 DISTRIBUTION OF $K_g(\alpha)$ 80

TABLE OF CONTENTS
(Continued)

Page

5.3 REGRESSION TECHNIQUES 82
5.4 SOLUTION OF REGRESSION EQUATIONS 85
5.5 PRINCIPAL PERMEABILITIES AND DIRECTIONS 88
5.6 MEAN SQUARE ERROR 90

6 LENGTH-DENSITY STUDY 92
6.1 BACKGROUND 92
6.2 PARAMETERS USED IN THE LENGTH-DENSITY STUDY 93
6.3 RESULTS OF THE FIRST SERIES OF LENGTH DENSITY STUDIES 97
6.4 THE MONTE-CARLO STUDY 110
6.5 STUDY ON THE EFFECT OF FLOW REGION SIZE 115
6.6 REPRESENTATIVE ELEMENTARY VOLUME STUDY 124
6.7 CONCLUSIONS 140

7 USE OF FIELD DATA FROM UNDERGROUND RESEARCH LABORATORY 143
7.1 INTRODUCTION 143
7.2 TWO-DIMENSIONAL ANALYSIS OF A THREE-DIMENSIONAL FRACTURE SYSTEM 145
7.3 INPUT PARAMETERS USED IN THE STUDY 147
7.4 RESULTS OF THE PERMEABILITY STUDY 155
7.5 THE MONTE CARLO PACKER SPACING STUDY 166
7.6 CONCLUSIONS AND RECOMMENDATIONS 176

8 EXTENSION OF THE MODEL TO THREE DIMENSIONS 179
8.1 INTRODUCTION 179
8.2 SOLUTION OF THE FLOW EQUATION 183
8.3 REQUIRED OUTPUT FROM THE FRACTURE MESH GENERATOR 208

9 SUMMARY 210

TABLE OF CONTENTS
(Continued)

Page

10 CONCLUSIONS AND RECOMMENDATIONS 215
10.1 USE OF THIS TECHNIQUE 215
10.2 MODELING TECHNIQUES 216
10.3 PARAMETER STUDIES 218
10.4 THE THREE-DIMENSIONAL MODEL 221

11 REFERENCES 223

APPENDIX A: FIELD DATA WHICH CAN BE USED TO DETERMINE THE INPUT PARAMETERS 232

LIST OF FIGURES

		Page
Figure 2-1.	General Flow Conditions in Anisotropic Media	18
Figure 2-2.	Statistical Definition of a Representative Elementary Volume (REV)	21
Figure 3-1.	Superposition of Random Sets of Fractures	41
Figure 3-2.	Boundary Conditions Applied to Fracture Models for Permeability Measurement	44
Figure 3-3.	Distortion of Isopotentials in an Anisotropic Medium with "No Flow" Boundaries	45
Figure 3-4.	A. Generation Region; B. Flow Region	47
Figure 3-5.	Two different Flow Regions Within a Generation Region	49
Figure 3-6.	Generation Region for "Infinite", Equally Spaced Fractures 30° Apart	55
Figure 3-7.	Flow Regions Taken From the Generation Region of Figure 3-6	56
Figure 3-8.	Comparison Between the Theoretical Permeability Ellipse and the Numerical Results for "Infinite Fractures" Shown in Figures 3-6 and 3-7	57
Figure 3-9.	Generation and Flow Regions for Network 1	58
Figure 3-10.	Generation and Flow Regions for Network 2	61
Figure 3-11.	Generation and Flow Regions for Network 3	62
Figure 3-12.	Flow Regions from Network 3 Rotated from 0° to 180°	64
Figure 3-13.	Values of $1/\sqrt{K(\alpha)}$ Plotted on Polar Coordinate Paper for Network 3.	65
Figure 3-14.	Flow Regions of Increasing Size from Network 3	67
Figure 4-1.	Fracture Systems of Increasing Density	70
Figure 4-2.	Fracture Systems with Variation of Aperture or Orientation	73
Figure 4-3.	Fracture Samples of Increasing Size	75
Figure 4-4.	Permeability Plots for Fractures Samples of Increasing Size	76
Figure 5-1.	Example of a Set of Directional Permeability Measurements Plotted as $1/\sqrt{Kg}$ in Polar Coordinates	81

LIST OF FIGURES
(Continued)

Page

Figure 5-2. Example of a Set of Directional Permeability Measurements Plotted in Cartesian Coordinates 84
Figure 6-1. Example of Two Boreholes of Equal Length Where (A) Penetrates a System of Fractures Whose Mean Fracture Length is Twice That of (B) 94
Figure 6-2. Normalized Mean Fracture Length, ℓ in the Flow Region Versus Input Fracture Length, ℓ for Mesh Size, $L = 6.25\ell$ 96
Figure 6-3. Length-Density Study, $\ell = 2$, $\lambda_A = 0.144$, $L/\ell = 6.25$ 98
Figure 6-4. Length-Density Study, $\ell = 8$, $\lambda_A = 0.036$, $L/\ell = 6.25$ 99
Figure 6-5. Length-Density Study, $\ell = 10$, $\lambda_A = 0.0288$, $L/\ell = 6.25$ 100
Figure 6-6. Length-Density Study, $\ell = 12$, $\lambda_A = 0.024$, $L/\ell = 6.25$ 101
Figure 6-7. Length-Density Study, $\ell = 14$, $\lambda_A = 0.021$, $L/\ell = 6.25$ 102
Figure 6-8. Length-Density Study, $\ell = 16$, $\lambda_A = 0.018$, $L/\ell = 6.25$ 103
Figure 6-9. Length-Density Study, $\ell = 20$, $\lambda_A = 0.0144$, $L/\ell = 6.25$ 104
Figure 6-10. Length-Density Study, $\ell = 24$, $\lambda_A = 0.012$, $L/\ell = 6.25$ 105
Figure 6-11. Permeability and NMSE Versus Fracture Length for the First Series of Length-Density Studies 108
Figure 6-12. Ellipticity of the Length-Density Examples as a Function of Fracture Length for the First Series of Length-Density Studies 109
Figure 6-13. Results of the Monte Carlo Analysis of Length-Density Relationships for the Case of $\ell = 10$ 111
Figure 6-14. Results of the Monte Carlo Analysis of Length-Density Relationships for the Case of $\ell = 20$ 112
Figure 6-15. Results of the Monte Carlo Analysis of Length-Density Relationships 114
Figure 6-16. Results of Increasing the Flow Region Size for the Case of $\ell = 10$, $L/\ell = 6.25, 9.0, 12.5$ 116
Figure 6-17. Results of Increasing the Flow Region Size for the Case of $\ell = 12$, $L/\ell = 6.25, 9.0, 12.5$ 117

LIST OF FIGURES
(Continued)

Page

Figure 6-18. Results of Increasing the Flow Region Size for the case of ℓ = 14, L/ℓ = 6.25, 9.0 118
Figure 6-19. Results of Increasing the Flow Region Size for the Case of ℓ = 14, L/ℓ = 6.25, 10.9 119
Figure 6-20. Variation in NMSE with Mesh Size for Various Fracture Lengths 120
Figure 6-21. Average Permeability as a Function of Fracture Length, ℓ, for Various Ratios Between Mesh Size and Fracture Length (L/ℓ) 122
Figure 6-22. Variation in K_1 and K_2 with Mesh Size for Various Values of Fracture Length, ℓ 123
Figure 6-23. Flow Region Sizes at 0° Rotation for the REV Study for the Case of ℓ = 20 125
Figure 6-24. Results of REV Study with ℓ = 20 for Flow Region of 2 x 2 cm 126
Figure 6-25. Results of REV Study with ℓ = 20 for Flow Region of 5 x 5 cm 127
Figure 6-26. Results of REV Study with ℓ = 20 for Flow Region of 7.5 x 7.5 cm 128
Figure 6-27. Results of REV Study with ℓ = 20 for Flow Region of 10 x 10 cm 129
Figure 6-28. Results of REV Study with ℓ = 20 for Flow Region of 15 x 15 cm 130
Figure 6-29. Results of REV Study with ℓ = 20 for Flow Region of 20 x 20 cm 131
Figure 6-30. Results of REV Study with ℓ = 20 for Flow Region of 25 x 25 cm 132
Figure 6-31. Results of REV Study with ℓ = 20 for Flow Region of 30 x 30 cm 133
Figure 6-32. Results of REV Study with ℓ = 20 for Flow Region of 40 x 40 cm 134

LIST OF FIGURES
(Continued)

Page

Figure 6-33. Results of REV Study with ℓ = 20 for Flow Region of 50 x 50 cm 135
Figure 6-34. Results of REV Study with ℓ = 20 for Flow Region of 60 x 60 cm 136
Figure 6-35. Results of REV Study with ℓ = 20 for Flow Region of 75 x 75 cm 137
Figure 6-36. Results of REV Study with ℓ = 20 for Flow Region of 100 x 100 cm 138
Figure 6-37. Results of REV Study with ℓ = 20 for Flow Region of 125 x 125 cm 139
Figure 6-38. Summary of Results of REV Study with ℓ = 20 141
Figure 7-1. Underground Research Laboratory Site Map. 144
Figure 7-2. Essential Differences between Three-Dimensional and Two-Dimensional Analysis 146
Figure 7-3. Fracture Trace Map of the Underground Research Laboratory Site 148
Figure 7-4. Fracture Pattern for the Underground Research Laboratory Data 151
Figure 7-5. Length-Aperture Correlation Models Used in the Underground Research Laboratory Data Study 153
Figure 7-6. Superimposed Flow Regions for the Underground Research Laboratory Data Study 157
Figure 7-7. Reduced Flow Regions for the Underground Research Laboratory Data. 158
Figure 7-8. Permeability from Models A and B1 of the Underground Research Laboratory. 159
Figure 7-9. Permeability from Models B2 and B3 of the Underground Research Laboratory. 160
Figure 7-10. Permeability from Models C and D of the Underground Research Laboratory. 161

LIST OF FIGURES
(Continued)

Page

Figure 7-11. Permeability from Model E Underground Research Laboratory 162
Figure 7-12. Generation Region for One Realization of the Packer Spacing Study 167
Figure 7-13. An Example of One Realization: Flow Regions from 100 x 100 cm to 25,000 x 25,000 cm 168
Figure 7-14. Reduced Flow Regions from 7-13 169
Figure 7-15. Plot of Mean Aperture, $\bar{b}_1$, and $\bar{b}_A$ Versus Zone Length 171
Figure 7-16. Mean Permeability in the X-Direction as a Function of Zone Length 173
Figure 7-17. Two Fractures in Series 174
Figure 8-1. Three-Dimensional Fracture Model 181
Figure 8-2. Three-Dimensional Generation and Flow Region 182
Figure 8-3. Flow Conditions in a Fracture 184
Figure 8-4. Image System for a Point Source in a Circle 187
Figure 8-5. Construction of the Nodal Images 188
Figure 8-6. A Fracture Intersection in a Fracture Disc 191
Figure 8-7. Construction for Calculating the Distribution of Strength along an Image Arc 193
Figure 8-8. Construction for Calculation of Potential Due to Sources on the Image Arc 195
Figure 8-9. A. Radial Intersection. B. Radial Image 198
Figure 8-10. Example Three-Dimensional Fracture System 204
Figure A-1. Example Trace Length Data Plot 233
Figure A-2. Example Orientation Data Plots 236
Figure A-3. Example Length-Apparent Aperture Data Plot 238

LIST OF TABLES

		Page
Table 3-1.	Comparison of Theoretical and Numerical Results for "Infinite" Fractures	59
Table 3-2	Input Parameters for the Random Example	60
Table 3-3	Characteristics of the Flow Region	60
Table 3-4	Total Fluxes (cm^3/s) for the Three Realizations Realizations	63
Table 3-5.	Resulting Fluxes (cm^3/s for the Random Case	66
Table 3-6.	Resulting Fluxes (cm^3/s) for Flow Regions of Different Sizes	68
Table 4-1.	Fracture System Characteristics for the Density Study	69
Table 6-1.	Parameters Common to the Whole Length-Density Study	95
Table 6-2.	Input Parameters Used in First Series of Length-Density Studies	95
Table 6-3.	Input Parameters used in Second Series of Length-Density Studies	115
Table 7-1.	Underground Research Laboratory Fracture Statistics	149
Table 7-2.	Input Data	150
Table 7-3.	Aperture Data	152
Table 7-4.	Description of Length and Aperture Coordinates Used to Plot Points 1,2,3, and 4 on Figure 7-5	154
Table 7-5.	Input and Output Aperature Statistics for the Underground Research Laboratory Models	156
Table 7-6.	Permeability Results for the Underground Research Laboratory Data	163
Table 8-1.	Description of Intersections for Figure 8-10	205
Table 8-2.	Fracture List	208
Table 8-3.	Node or Intersection List	208
Table 8-4.	Fracture Geometry List	209
Table A-1.	Sample Data Form for Area Surveys	234
Table A-2.	Sample Data Form for Line Surveys	235

NOMENCLATURE

A	area	(L^2)
b	aperture of a fracture	(L)
$E(x)$	expected value of x	
$F(x)$	distribution function of x	
$f(x)$	probability density function of x	
$f(xy)$	probabilistic density of x given y	
g	gravitation constant	(L/T^2)
h	total hydraulic head (in Chapter 8 only)	(L)
J_i	potential gradient = $\partial\phi/\partial xi$ (dimensionless)	
K_{ij}, K	hydraulic conductivity	(L/T)
$K_{ij,k}$	intrinsic permeability	(L^2)
L	flow region dimension	(L)
LD	length density parameter, $LD = \lambda_A \ell$	(L^{-1})
ℓ	fracture length	(L)
$\bar{\ell}$	mean fracture length	(L)
$P(x)$	probability of x	
q	flux	(L^3/T)
v	volume	(L^3)
v_i	flux per unit area (specific discharge)	(L/T)
$Var(x)$	variance of x	
δ_{ij}	Kronecker delta, $\delta ij = \begin{cases} 1 & i = j \\ 0 & i \neq j \end{cases}$	
λ	exponential distribution parameter	$(1/L)$
$\lambda, \lambda_1, \lambda_2$	eigenvalue of the conductivity tensor	(L/T)
λ_L	linear fracture density	$(1/L)$
λ_A	area fracture density	$(1/L^2)$
λ_V	volumetric fracture density	$(1/L^3)$
μ	mean value or viscosity	(M/LT)
ρ	density	(M/L^3)
σ^2	variance	
ϕ	total hydraulic head	(L)

1 INTRODUCTION

Interest in storing nuclear waste in deep underground facilities has prompted research to analyze the regional ground-water flow systems in dense, fractured* rocks. At depth, the permeability of these dense rocks may be completely due to secondary porosity, i.e., fractures (Davis, 1969). Regional flow analysis through great volumes of fractured rock cannot be handled by describing each of these discrete flow paths deterministically because the information describing every fracture in the region is not available. Further, present computer methods cannot manage such volumes of data. Continuum or equivalent porous medium analysis could be used if equivalent porous medium parameters can be assigned to the fractured systems. This research is an attempt to determine if such appropriate equivalent porous media permeability** values exist and determine their values from statistical information on the geometry of the discrete fracture system.

Work reported here includes a literature survey, development of a numerical approach to the study of the permeability of random fracture systems, and application of this approach to several case studies. The literature survey is in three parts. The first covers previous work that has been done to relate fracture geometry to equivalent porous media values of permeability. The second part covers the theory and measurement of homogeneous, anisotropic permeability. The third part is a review of fracture geometry statistics as observed in the field. The numerical approach includes the adoption of a statistical fracture geometry model and the development of a computer program which generates random models of fracture systems and codes them for finite element analysis of fluid flow. The fluid flow analysis was used to measure

---

*For the purposes of this report, the words "fracture", "joint", and "discontinuity" are used interchangeably.

**The term "permeability" is used in a generic sense throughout this report. All calculations are actually of hydraulic conductivity (L/T) which is also called the coefficient of permeability. Hydraulic conductivity, K, is equal to $k\rho g/\mu$ where k is the intrinsic permeability with the dimensions of $[L^2]$. See nomenclature for definition of terms.

the permeability of the fracture system. First the permeability of a system of regular fractures of infinite extent was studied in order to validate the model. Then the permeability of random systems of finite fractures were studied.

Series of random fracture systems were studied to see the effect on permeability of fracture density, aperture and orientation distribution, and scale of measurement. Then a regression analysis was developed to determine the best-fit permeability tensor for the fracture system. This analysis was applied to a series of cases designed to test how well the permeability of a rock mass can be predicted from the fracture spacing in a well. A further analysis used data from the Atomic Energy of Canada Limited's Underground Research Laboratory in Pinawa, Manitoba to examine the effect of correlation between fracture length and aperture and the applicability of surface trace data to the analysis of the fracture system at depth. Also steady-state packer tests were simulated to see if they can be used to determine the aperture distribution of a fracture system. Finally the theoretical basis for extending the numerical model to three dimensions was discussed.

2 LITERATURE REVIEW

2.1 DETERMINATION OF EQUIVALENT POROUS MEDIA PERMEABILITY FROM FRACTURE GEOMETRY

Work that has been done to determine the equivalent permeability of fractured rocks from information on fracture geometry (assuming an impermeable matrix) can be classified into two categories. Most of this work falls into the first category where fractures are assumed to be of infinite extent (continuous or extensive fractures). Very little work has been done in the second category, which takes into account the finite or nonextensive nature of fracture size.

Study of the permeability of continuous fracture systems is based on the principle that the total permeability of the rock mass can be found by summing the contributions of each fracture. The principle holds for fractures which transect the entire rock mass; i.e., continuous or "infinite fractures". Also, the assumption is made that head losses in the fracture intersections are negligible. The contribution of each individual fracture is determined by study of isolated fractures under various conditions of flow and stress (Huitt, 1956; Louis, 1969; Sharp, 1970; Maini, 1971; Iwai, 1976; Rissler, 1978; Witherspoon et al, 1979; Strack, 1980; and others). However, for application to the study of fracture systems, flow in individual fractures is usually assumed to obey the cubic law for flow between parallel plates:

$$q = -\nabla\phi \; \rho g \frac{b^3}{12\mu} W \qquad (2\text{-}1)$$

where $\nabla\phi$ is the component of hydraulic gradient parallel to the fracture and W is the width of the flow system.

Simple models of fracture networks based on the cubic law have been reviewed by Wilson (1970), including work by Serafim and del Campo (1965), Crawford and Collins (1954), Crawford and Landrum (1955), and Ollos (1963). These were either physical models based on electrical or pipe-flow analogs, or mathematical models based on orthogonal fractures of equal aperture and spacing. Irmay (1955) and Childs (1957) also developed similar models.

More sophisticated mathematical studies of extensive fracture systems were made by Snow (1965, 1969). Snow developed a mathematical expression for

the permeability tensor of a single infinite fracture of arbitrary orientation and aperture relative to a fixed coordinate system. The permeability tensor for a network of fractures is therefore the tensor formed by adding the respective components of the permeability tensors for each individual fracture. Mathematically, the intrinsic permeability tensor of rock with reference to the i,j coordinates can be written:

$$k_{ij} = \frac{1}{12} \sum \frac{b^3}{S} (\delta_{ij} - n_i n_j) \qquad (2\text{-}2)$$

where the summation is taken over all the fracture sets in the volume of rock, S is the spacing, and n_i is the unit vector normal to each fracture. If fractures are all randomly oriented, S becomes equal to the dimension of the sample perpendicular to the individual fracture. If fractures in a set are parallel and equally spaced, then S is constant and equal to the spacing for that set.

With this model, Snow was able to examine the effect of random variations in orientation and aperture of extensive fractures on the permeability of the rock mass. In the statistical study, the aperture of each fracture in a set was chosen as the absolute value of a normally distributed parameter. The orientation of each fracture was chosen with a Fisher distribution. As each fracture was randomly generated, the total permeability tensor was progressively cumulated. Thus the effect of sample size on total permeability can be seen. Snow found that an increase in sample size increases the geometric mean permeability. The explanation for this is that as sample size increases the probability of adding a rare large-aperture fracture increases. Since the permeability contribution of a fraction is proportional to b^3, a single large-aperture fracture tends to have a very large effect on the total permeability.

For the aperture distributions studied by Snow, most model systems had stable permeabilities at sample sizes of about 200 fractures. A few continued to increase in permeability for sample sizes larger than 200. The change in permeability from small sample sizes (with 20 to 30 fractures) to large samples was from 5 to 25 percent of the results for an infinite number of fractures. This implies that a representative sample of the continuously fractured rocks studied by Snow usually contains about 200 fractures. The volume of rock con-

taining these 200 fractures depends on the density or spacing of the conductors. Throughout the remainder of this report, a volume of rock containing a representative sample of fractures will be called a representative elementary volume, or REV.

For the purpose of comparison, it is useful to examine the size of an REV in fractured rock as estimated by other authors. Rats and Chernyashov (1965) made a rough approximation based on a statistical analysis that a homogeneous porous medium analysis can be used if the dimensions of the rock being studied are at least ten times larger than the order of magnitude of the rock mass heterogeneity, i.e., fracture spacing. Maini's (1971) analysis, based on injection test data, claims continuum or homogeneous conditions can be assumed for rock containing nine or more fractures. Further estimates have been reviewed by Roegiers et al (1978). The reliability of such methods of estimation has not been demonstrated.

The method of determining the equivalent porous medium permeability (EPMP) proposed by Snow has several limitations, some major and some minor. The method does not account for fracture roughness and infilling. This deficiency may be overcome by using an equivalent flow aperture (Iwai, 1976) or a correction factor as described by Rissler (1978).

A much more important theoretical limitation is that this model assumes all the fractures transect the entire volume of rock. It can be seen in the field that fractures are clearly of finite dimensions. For example, Marine (1980) performed tracer tests on a permeable fractured zone in metamorphic rock. The tracer tests demonstrated that the permeability was due to interlacing fractures, not a system of continuous conductors. The fact that fractures are finite means that each fracture can contribute to the permeability of the rock only insofar as it intersects other conducting fractures. Such interconnected fractures comprise the effective secondary porosity. In the extreme, an isolated fracture which does not intersect any other fracture effectively contributes nothing to the permeability of the total rock mass. Another limitation of Snow's (1965) approach is that it is difficult to obtain data on effective or hydraulic aperture distributions. Further discussion of aperture statistics can be found in Section 2.3.

Three approaches have been taken to overcome the theoretical difficulties with Snow's method. Parsons (1966) and Caldwell (1971, 1972) used analog

models to study finite fractures. Parson's analysis utilized the approach of Fatt (1956) who had analyzed the capillary properties of a network of random-diameter tubes, and Warren and Price (1961) who had studied random three-dimensional arrays of porous blocks. Rocha and Franciss (1977) proposed a field method for finding a correction factor to Snow's analysis. Sagar and Runchal (1982) proposed an analytic extension of Snow's method.

Parsons studied two-dimensional regular networks of fractures with random apertures. Both square patterns and triple hexagonal patterns similar to those of Fatt (1956) were studied. Values from a given distribution of conductances were randomly assigned in the pattern. In many of the conductance distributions used, the probability of having a zero conductance element was finite, which means not all fractures were continuous across the model. After assigning these conductances, boundary conditions were imposed on the model to simulate quasi-linear flow in either the x, y, or 45 degrees from the x and y directions. The pressure distribution and flow in each element was calculated with a relaxation technique. Total flow was found by summing the flow across a plane perpendicular to the overall gradient through the system. Overall permeability per unit height of model was calculated as the ratio of total flux to gradient. Anisotropy was studied by doubling the random values of conductance oriented in one direction. From 1 to 23 random models were generated for each of the studied statistical distributions for aperture. The mean and standard deviation of the resulting directional permeability were calculated.

Parsons did not study the effect of the size of the network on the value of the calculated permeability. Nor did he find the complete permeability tensor. He did not find any correlation between the overall permeability and the element conductance distribution. Parsons did conclude that the larger the standard deviation of the conductance distribution was, the larger would be the standard deviation of the overall permeabilities calculated with the models. Also, he found that the geometric mean of the conductance distribution is a fair approximation to the permeability of the square network.

A significant result of Parson's (1966) work was that doubling the permeability of all fracture elements in the x-direction increased the permeability in the y-direction. This effect would not be seen in continuous fractures,

but with discontinuous fractures the net flow in the y-direction must proceed through some fractures oriented in the x-direction. Also, for a similar reason, permeability in the x-direction is less than doubled. This is an important effect in fracture networks that must be kept in mind.

Caldwell (1971) modeled flow in discontinuous fractures. His method consisted of cutting joint sets from conducting paper and measuring the potential distribution in the model. He determined a "best fit" permeability tensor by comparing the measured potential distributions with theoretical solutions for different values of the permeability tensor. The accuracy of this trial-and-error method is questionable. The author was aware that the "best fit" tensor is not a unique solution.

Caldwell also studied models with two orthogonal joint sets. One set consisted of continuous, regularly spaced fractures. The second set had joint lengths that were randomly selected from an exponential distribution and spacing equal to one-fourth of the spacing of the continuous set. Three such models were studied where the mean length of the discontinuous fractures were one, two, and four times the spacing of the orthogonal joint set. In this limited analysis, Caldwell found that where the mean joint length was equal to the joint spacing, less than half the joints were hydraulically active. Where the mean joint length was at least twice the spacing, Caldwell indicated that the permeability of the joint model was equal to the permeability of a model with two continuous joint sets. Caldwell (1971) also extended these results to nonorthogonal joints.

Rocha and Franciss (1977) proposed a well test to determine a correction factor to the theoretical tensor obtained using Snow's method. From the calculated tensor, the equivalent isotropic permeability is calculated as the cube root of the product of the three principal permeabilities, $\sqrt[3]{K_1K_2K_3}$. This permeability is used to calculate a steady state flow rate under a given pressure. Then a well test is performed. The ratio of the flow measured in the field to the flow calculated from the theoretical tensor gives the correction factor, ρ, to be applied to the permeability tensor:

$$K_{ij} = \begin{bmatrix} \rho K_1 & 0 & 0 \\ 0 & \rho K_2 & 0 \\ 0 & 0 & \rho K_3 \end{bmatrix}. \qquad (2\text{-}3)$$

This single correction factor does not allow for any rotation of the principal axes. The authors also propose a trial-and-error solution for applying a different correction factor to each of two fracture sets separately. This method would permit rotation but there is no evidence that such tensors are correct for flow systems other than the radial flow system from which they were derived.

Sagar and Runchal (1982) attempted to extend Snow's (1965, 1969) theory for permeability of fractured systems to account for finite fracture size. Some of the assumptions made in their work are physically incorrect. The authors assumed that flow in any fracture is independent of flow in the other fractures if disturbances at the fracture intersections are negligible and flow is laminar. Thus each fracture was assumed to experience a component of the field gradient which depends only on the orientation of the fracture. From this the authors concluded that "any fracture which does not appear on the boundary of the rock element considered is of no interest in the calculation of the equivalent permeability" (Sagar and Runchal, 1982). These assumptions are correct for the extensive fracture systems analyzed by Snow. However, these assumptions are not reasonable for nonextensive fractures (see Section 7-6).

In summary, very little work has been done to quantify the effect of finite fracture length in combination with other geometric factors such as aperture distribution, fracture spacing, and orientation.

2.2 HOMOGENEOUS ANISOTROPIC PERMEABILITY

2.2.1 Anisotropy

One of the purposes of this research is to determine when a fractured medium behaves as a homogeneous anisotropic porous medium. The theory and measurement of homogeneity and anisotropy are reviewed here.

If the permeability of a medium is not the same in all directions, the medium is said to be anisotropic. Darcy's law was originally postulated for one-dimensional flow. Since directional properties have no impact on one-dimensional flow, permeability was represented as a single scalar quantity. In order to extend Darcy's law to two or three dimensions in the most general

case of an anisotropic medium, Ferrandon (1948) and others proposed that permeability be represented by a tensor quantity. This proposal is generally supported by either heuristic reasoning or associated laboratory experiments.

Collins (1961) gives heuristic arguments for extending Darcy's law to three dimensions. In order to show what fracture systems will be compared to, it is important at this point to review the arguments presented by Collins. Darcy's law is extended in such a way that the flux remains linearly dependent on the gradient. In one dimension,

$$v_x = -k \frac{\rho g}{\mu} \frac{d\phi}{dx} . \tag{2-4}$$

In three dimensions for an isotropic medium,

$$v_i = -k \frac{\rho g}{\mu} \frac{\partial \phi}{\partial x_i} , \qquad i = 1, 2, 3. \tag{2-5}$$

For three dimensions and an anisotropic medium, in general,

$$v_i = - \frac{\rho g}{\mu} \left[k_{i1} \frac{\partial \phi}{\partial x_1} + k_{i2} \frac{\partial \phi}{\partial x_2} + k_{i3} \frac{\partial \phi}{\partial x_3} \right] \quad i = 1, 2, 3, \tag{2-6}$$

or, using the summation convention

$$v_i = - \frac{\rho g}{\mu} k_{ij} \frac{\partial \phi}{\partial x_j} \qquad \begin{array}{l} i = 1, 2, 3 \\ j = 1, 2, 3 \end{array} \tag{2-7}$$

The nine quantities k_{11}, k_{12}, k_{13}, k_{21}, k_{22}, k_{23}, k_{31}, k_{32}, k_{33}, form a tensor. The matrix equation for Darcy's law is

$$\begin{bmatrix} v_1 \\ v_2 \\ v_3 \end{bmatrix} = - \frac{\rho g}{\mu} \begin{bmatrix} k_{11} & k_{12} & k_{13} \\ k_{21} & k_{22} & k_{23} \\ k_{31} & k_{32} & k_{33} \end{bmatrix} \begin{bmatrix} \frac{\partial \phi}{\partial x_1} \\ \frac{\partial \phi}{\partial x_2} \\ \frac{\partial \phi}{\partial x_3} \end{bmatrix} . \tag{2-8}$$

The most general form of the permeability matrix is assumed to be symmetric. If k_{ij} is symmetric, the matrix can be transformed to a diagonal form by a physical or mathematial model and rotation of coordinate axes:

$$k_{ij} = \begin{bmatrix} k_1 & 0 & 0 \\ 0 & k_2 & 0 \\ 0 & 0 & k_3 \end{bmatrix} . \tag{2-9}$$

The coordinate system which diagonalizes this matrix form the principal axes and the values k_1, k_2, k_3, are called the principal permeabilities. In this coordinate system, for $i \neq j$, $k_{ij} = 0$. Therefore, Darcy's law becomes

$$v_i = -\frac{\rho g}{\mu} k_i \left[\frac{\partial \phi}{\partial x_{(i)}} \right], \tag{2-10}$$

where (i) here is exempt from summation. Thus in this form flux is proportional to gradient in the principal directions and this is the basis for the extension of the original Darcy's law. For any medium having orthogonal principal axes, k_{ij} will be symmetric and the above form of Darcy's law will be correct. A medium with orthogonal principal axes has the following properties: (1) a reversal of gradient results in equal but opposite flux, and (2) for arbitrary orthogonal axes x, y, z, flow in the x-direction due to a unit gradient in the y-direction is equal to flow in the y-direction due to a unit gradient in the x-direction, etc. That is, $k_{ij} = k_{ji}$.

Experimental evidence supports this theory. Anisotropic materials which were tested did in fact have orthogonal principal axes. However, as Collins (1961) points out, there is no guarantee that every porous material has a symmetric permeability tensor. In fact it is likely that there are materials which do not have symmetric permeability tensors.

Darcy's law can be derived for idealized cases. For example, a porous medium can be assumed to consist of an assemblage of elementary flow tubes or fissures. A good review of these methods is given in Bear (1972). As Bear points out, the problem with physical models such as flow tube models is that they attempt to represent an inherently disordered medium by an inherently ordered medium. This drawback also means that these models are of less interest to this research on the permeability of fractured rock. Assumptions made to produce an ordered physical model cannot easily be compared to the assumptions made to produce a random model.

The number and variation of models studied (Ferrandon, 1948; Childs, 1957; Scheidegger, 1960; Kozeny, 1927; Carman, 1937; Fatt, 1956) does, however, lend support to the concept of anisotropic permeability as a symmetric tensor for many media. Elementary flow tube models all presume flow in the tubes follows Poiseuille's law. Poiseuille's law states that flux q in a tube is linearly proportional to the hydraulic gradient along the tube, $d\phi/dx$. The constant

of proportionality is a function of the diameter of the tube, d, density ρ, viscosity μ, and the gravitational constant g:

$$q = -\frac{\pi d^4}{128}\frac{\rho g}{\mu}\frac{d\phi}{\partial x} . \tag{2-11}$$

Any number of tubes of arbitrary direction and diameter can be added together. The resulting flow law is always of the form

$$v_i = -k_{ij}\frac{\partial\phi}{\partial x_j} \tag{2-12}$$

where k_{ij} is the permeability tensor and V_i is the specific discharge (Ferrandon, 1948 and Childs, 1957). Each specific model will produce a different relationship between k_{ij} and the geometric properties of the model. Scheidegger (1960) used the pore size distribution to arrive at the tube diameter distribution. Kozeny (1927) and Carman (1937) derived an expression for flow in noncircular, nonlinear tubes. Fatt (1956) modeled networks of tubes in a similar manner.

The fissure models discussed previously are similar to the tube models. However, flow in the fissures is governed by the cubic law, which is the solution to the Navier-Stokes equation for flow between parallel plates. Further models based on the resistance to flow provided by the soil grains are reviewed by Bear (1972) and are not discussed here. The net result for all these models is expressed in Equation 2-12 where total flux is linearly proportional to the gradient.

Another type of derivation of Darcy's law is based on statistical averaging. The geometric properties of the medium are allowed to be random and assumptions are made about the average or macroscopic behavior of flow. Some of the work which leads to a tensor form for permeability will be discussed here. More extensive reviews of this subject can be found in Scheidegger (1960) and Bear (1972).

Day (1974) gives a derivation which leads to Darcy's law for anisotropic homogeneous media. The derivation is based on work by Hall (1956) and Hubbert (1940, 1956). Day extends Hall and Hubbert's work from isotropic to anisotropic media.

Day, Hall, Hubbert, and also Irmay (1968) and Gray and O'Neill (1976) all used the same basic plan to derive Darcy's law. These authors start with the Navier-Stokes equations as applied to the details of flow. Then some form of averaging is applied under a set of assumptions about the nature of the flow regimes. The result is an expression relating the average gradient to the average flux, i.e., Darcy's law.

For saturated flow, Day starts with the following assumptions: (1) nonturbulent flow, (2) negligible inertial forces, (3) rigid solid phase, (4) incompressible liquid, (5) viscosity unaffected by the proximity of the solid phase, and (6) velocity is zero at the solid-liquid interface.

Starting with the Navier-Stokes equation for creeping incompressible flow which assumes $\partial v_i/\partial t$ is negligible

$$\frac{\partial \phi'}{\partial x_i} = \frac{\mu}{\rho g} \frac{\partial^2 v_i'}{\partial x_j^2} , \tag{2-13}$$

where v'_i is local velocity, ϕ' is local potential, μ is viscosity, and ρ is density. Differentiating we have:

$$\frac{\partial^2 \phi'}{\partial x_i^2} = \frac{\mu}{\rho g} \frac{\partial^3 v_i'}{\partial x_i \partial x_j^2} . \tag{2-14}$$

Continuity for an incompressible liquid is given by

$$\frac{\partial v_i'}{\partial x_i} = 0, \tag{2-15}$$

so we have the Laplace equation

$$\frac{\partial^2 \phi'}{\partial x_i^2} = 0. \tag{2-16}$$

We seek a solution to the Laplace equation which will satisfy the boundary conditions of the detailed porous medium. Note that if ϕ is a

solution, then $c\phi$ is also a solution if c is a constant. Also if $c\phi$ is the solution, the velocity will be cv_i since from Equation 2-13

$$\frac{\mu}{\rho}\frac{\partial^2}{\partial x_j^2}(cv_i') = c\frac{\mu}{\rho g}\frac{\partial^2 v_i'}{\partial x_j^2} = c\frac{\partial\phi'}{\partial x_i} = \frac{\partial}{\partial x_i}(c\phi'). \tag{2-17}$$

Day next defines macroscopic potential as a volume average of the microscopic or local potential

$$\phi = \frac{1}{V}\int_V b\phi'\, dV, \tag{2-18}$$

where V is bulk volume, ϕ'_i is the local potential, and b = 1 in the liquid phase and b = 0 in the solid phase. Thus the average gradient is

$$\frac{\partial\phi}{\partial x_i} = \frac{1}{V}\int_V b\frac{\partial\phi'}{\partial x_i}\, dV. \tag{2-19}$$

The major assumption in the analysis is that the local and average velocities are connected by a relationship of the form

$$v_i' = c_{ij}v_j\ , \tag{2-20}$$

where c_{ij} are functions of position and independent of the local velocity, v_i'. Differentiating this equation twice, we have

$$\frac{\partial^2 v_i'}{\partial x_k^2} = v_j\frac{\partial^2 c_{ij}}{\partial x_k^2}\ . \tag{2-21}$$

Substituting this in the Navier-Stokes Equation (2-13) gives

$$\frac{\partial\phi'}{\partial x_i} = \frac{\mu}{\rho g}\frac{\partial^2 v_i'}{\partial x_k^2} = \frac{\mu}{\rho g}v_j\frac{\partial^2 c_{ij}}{\partial x_k^2}\ . \tag{2-22}$$

Using the definition of macroscopic potential, Equation (2-22) becomes

$$\frac{\partial\phi}{\partial x_i} = \frac{1}{V}\int_V b\frac{\partial\phi'}{\partial x_i}\, dV = \frac{1}{V}\int_V b\frac{\mu}{\rho g}v_j\frac{\partial^2 c_{ij}}{\partial x_k^2}\, dV, \tag{2-23}$$

$$\frac{\partial\phi}{\partial x_i} = v_j \frac{1}{V} \int_V b \frac{\mu}{\rho g} \frac{\partial^2 c_j}{\partial x_k^2} dV. \tag{2-24}$$

Letting

$$A_{ij} \equiv -\frac{1}{V} \int_V b \frac{\mu}{\rho g} \frac{\partial^2 c_{ij}}{\partial x_k^2} dV, \tag{2-25}$$

gives

$$\frac{\partial\phi}{\partial x_i} = -v_j A_{ij}, \tag{2-26}$$

or

$$v_j = -(A_{ij})^{-1} \frac{\partial\phi}{\partial x_i}, \tag{2-27}$$

and

$$K_{ij} = (A_{ij})^{-1}. \tag{2-28}$$

There are several weak points in this derivation. A major weakness has been pointed out by Narasimhan (1980). Narasimhan points out that volume (or ensemble) averages only make physical sense for extensive quantities, such as mass and energy. However, intensive quantities such as temperature or potential cannot be simply averaged. This is because potential or temperature of two disconnected subdomains cannot be added to find the total potential or temperature. Quantities such as potential and temperature must be modified by capacity functions in order to be averaged. Thus a correct definition of average potential would be

$$\phi = \frac{1}{Vm_c} \int_V b m_c' \phi' \, dV, \tag{2-29}$$

where m_c is the average specific fluid mass capacity of the medium and m_c' is the local value. The average specific mass capacity may also be difficult to

evaluate because in heterogeneous systems, m_c' is not additive. Only for steady state problems where the potential distribution is independent of the capacity terms can we have

$$\phi = \frac{1}{V} \int_V b\phi' \, dV. \tag{2-30}$$

Day's use of the above form of volume average for ϕ without m_c implies the result is applicable only to steady flow. Day implicitly assumed nearly steady flow from the beginning by neglecting $\partial v_i/\partial t$ in the Navier-Stokes equation.

Philip's (1957) approach to this problem was to accept the fact that Darcy's law really applies only to steady flow. He then examined the transition from rest to steady flow for incompressible fluids using the Navier-Stokes equation including the acceleration term:

$$\frac{\partial v_i}{\partial t} = -\frac{\partial \phi}{\partial x_i} + \frac{\mu}{\rho} \frac{\partial^2 v_i}{\partial x_j^2} . \tag{2-31}$$

Philip found that steady flow was established very quickly, within seconds or a fraction of a second for most media. Thus Day's assumption that the acceleration terms of the Navier-Stokes equation are negligible may not be too bad. In other words, as long as the boundary conditions are changing slowly, the velocity field can be related to the potential field with the form of the Navier-Stokes equation used by Day. So, at least for homogeneous media, the simplified form of the volume average may also be approximately correct.

A further problem in this analysis is the Equation 2-20:

$$v' = c_{ij} v_i .$$

If c_{ij}, and therefore permeability, is to be unique, the local velocity distribution must be constant or at least a constant multiple of the velocity distribution for which the components of c_{ij} were derived. The components of c_{ij} will change when the soil particles move (e.g., in compaction) or when there are any changes in the distribution or amount of water in the medium (nonsteady flow). In fact the c_{ij} will be unique only for a given type of boundary conditions

and steady (or incompressible) flow. That is, the c_{ij} will be invariant only for kinematically similar, steady flows.

Day has shown that permeability is a tensor for any given kinematic state of steady or incompressible flow if $v_i' = c_{ij}v_i$. He has not shown that a unique permeability tensor can be found for a given medium which controls any laminar steady or unsteady flow state. The permeability tensor will be unique if

$$A_{ij} = -\frac{1}{V}\int_V b\,\frac{\mu}{\rho}\,\frac{\partial c_{ij}^2}{\partial x_k}\,dV \tag{2-32}$$

is invariant for any laminar flow conditions. This can only be proven for specific cases as discussed above when the full details of the flow system are known. Only in these cases are the components of c_{ij} known throughout the flow field under any flow conditions.

Darcy's law cannot be proven for the general case. The only way to show that a given random medium has a symmetric permeability tensor is to actually measure the directional permeability. The theory of directional permeability measurement is given below.

2.2.2 Measurement of Directional Permeability

Directional permeability can be measured under steady flow conditions. If the correct form of Darcy's law is

$$q = k_{ij}\frac{\partial\phi}{\partial x_j} = K_{ij}J_j\ , \tag{2-33}$$

then this expression can be used to examine the theory of directional permeability measurement. Fundamental to directional permeability measurement is the fact that flow and gradient are not necessarily in the same direction. Only when flow and gradient coincide with one of the principal axes of permeability will flow and gradient be in the same direction. This can be seen from inspection of the above Darcy equation.

Scheidegger (1954) and Maasland (1957) both give analyses of directional permeability. Neither stated that there is a difference between measurements made in the direction of flow and measurements made in the direction of

gradient. Marcus and Evenson (1961), Marcus (1962), and Bear (1972) all give the expressions for both permeability in the direction of flow and permeability in the direction of gradient. They show how the results of directional permeability measurement can be plotted as ellipsoids. A summary of these analyses is presented here in simplified form.

If a steady flow system is set up where the direction of flux is known, then permeability in the direction of flux, K_f, can be defined as

$$q = - K_f J_i m_i \ , \tag{2-34}$$

where J_i is the gradient vector, m_i is a unit vector in the direction of the flux, and q is the flux per unit area. Therefore, $J_i m_i$ is the component of the gradient in the direction of the flux (Figure 2-1).
We have

$$\frac{1}{K_f} = - \frac{J_i m_i}{v} \tag{2-35}$$

J_i can be found from Darcy's law:

$$v_j = - K_{ij} J_i \tag{2-36}$$

$$J_i = - v_j (K_{ij})^{-1} = -m_j (K_{ij})^{-1} v. \tag{2-37}$$

Substituting Equation 2-37 into 2-35 gives

$$\frac{1}{K_f} = m_i m_j (K_{ij})^{-1}, \tag{2-38}$$

or

$$1 = (\sqrt{K_f}\ m_i)(\sqrt{K_f} m_j)(K_{ij})^{-1}. \tag{2-39}$$

Substituting

$$m_i = \frac{x_i}{\sqrt{K_f}} \tag{2-40}$$

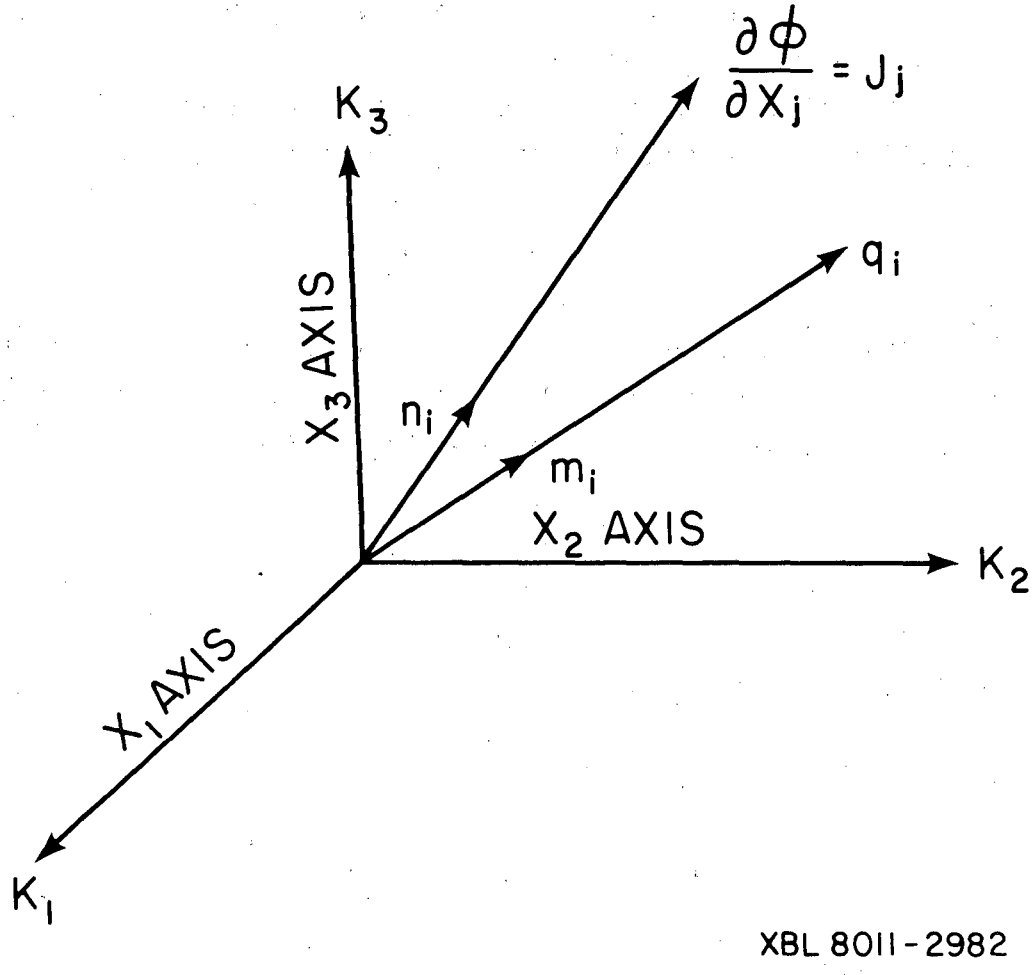

Figure 2-1. General Flow Conditions in Anisotropic Media

into 2-39 implies the components of x_i give the coordinates of a ray of length $\sqrt{K_f}$ plotted (as measured) in the direction of flux, m_i. Substituting 2-40 into Equation 2-39 we have:

$$1 = x_i \, x_j \, (K_{ij})^{-1}, \tag{2-41}$$

which is the equation of an ellipsoid with semiaxes of length $\sqrt{K_1}$, $\sqrt{K_2}$, $\sqrt{K_3}$, where K_1, K_2, and K_3 are the principal permeabilities.

Permeability in the direction of the gradient K_g is defined by

$$q_i n_i = - K_g J \tag{2-42}$$

$$K_g = - \frac{q_i n_i}{J} \tag{2-43}$$

where q_i is the flux per unit area, n_i is a unit vector in the direction of the gradient, $v_i m_i$ is the component of flux in the direction of the gradient and J is the magnitude of the gradient. Substituting Darcy's law:

$$q_i = - K_{ij} J_j \, , \tag{2-44}$$

into Equation 2-43 gives,

$$K_g = \frac{K_{ij} J_j}{J} n_i \tag{2-45}$$

$$K_g = K_{ij} n_j n_i \tag{2-46}$$

or

$$1 = K_{ij} (\sqrt{K_g} \, n_j)(\sqrt{K_g} \, n_i) \tag{2-47}$$

Substituting

$$n_1 = \frac{x_i}{\sqrt{K_g}} \tag{2-48}$$

Equation 2-47 implies that the components of x_i give the coordinates of a ray of length $1/\sqrt{K_g}$ plotted (as measured) in the direction of gradient. This gives:

$$1 = K_{ij} x_i x_j \tag{2-49}$$

which is the equation of an ellipsoid with semiaxes of lengths $1/\sqrt{K_1}$, $1/\sqrt{K_2}$, and $1/\sqrt{K_3}$. Recall in Equation 2-41 for permeability measured in the direction of flow the semiaxes are $\sqrt{K_1}$, $\sqrt{K_2}$, $\sqrt{K_3}$. For permeability measured in the direction of flux the major axis of the ellipsoid is in the direction of maximum permeability. For permeability measured in the direction of the gradient the major axis of the ellipsoid is in the direction of minimum permeability.

Scheidegger (1954) reanalyzed directional permeability measurements made in the direction of the gradient by Johnson and Hughes (1948). Scheidegger plotted $1/\sqrt{K(\alpha)}$ as a function of α on polar coordinate paper for each set of data. A best-fit ellipse was calculated. The standard deviation of the laboratory values as compared to the best-fit ellipse was about 10 percent. This deviation can easily be accounted for by heterogeneities in the samples. Greenkorn et al (1964) and Morita and Gray (1980) used a method of measuring conductivity in the direction of flow with a whole core type permeameter. Results in both cases plotted as an ellipse. This type of laboratory analysis tends to confirm that the behavior of many porous media can be predicted by a symmetric permeability tensor.

2.2.3 Homogeneity

Homogeneity has been discussed by Hubbert (1956), Fara and Scheidegger (1961), Toth (1967), Bear (1972), and Freeze (1975). Freeze pointed out that there is really no such thing as a truly homogeneous medium in geology. However, in order to have a tractable analysis of flow, a scale of measurement (the macroscopic scale) must be found for which the porous medium is seen as continuous (Hubbert, 1956). On this scale the medium is said to behave as if it were homogeneous. The scale at which such analysis is possible is commonly illustrated with a diagram such as Figure 2-2. The volume at which the parameter of interest (permeability in the case of Figure 2-2) ceases to vary was defined earlier as the representative elementary volume (REV). With respect to permeability, the REV of a medium can be sought by measuring the average permeability of increasing volumes of rock until the value does not change significantly with the addition or subtraction of a small volume of rock. An alternative to this theory was proposed by Fara and Scheidegger (1961) and Moran (1962). These authors suggested the use of an autocorrelation function

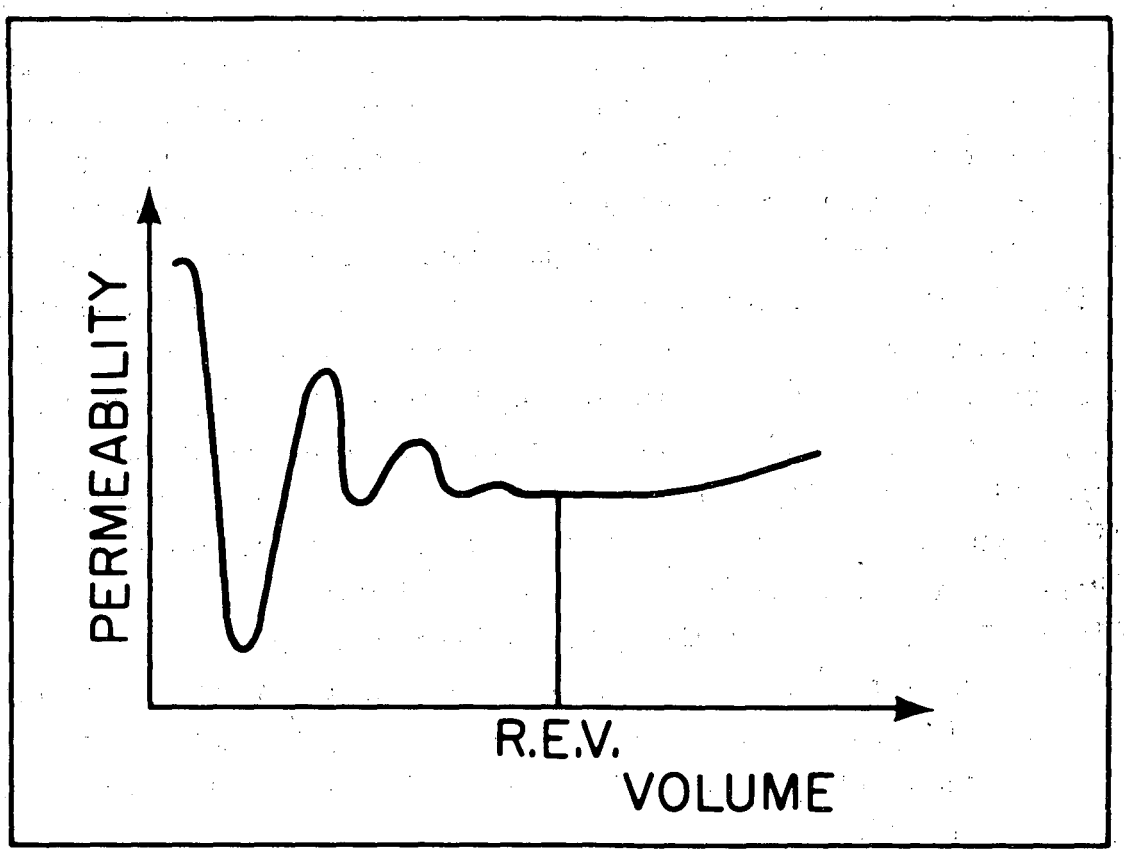

XBL 813-2735

Figure 2-2. Statistical Definition of a Representative Elementary Volume (REV)

which could be evaluated along random lines through a given porous medium. If the medium is homogeneous and isotropic, the autocorrelation function should be equal for any line, provided the sample is as large as the REV.

There is no guarantee that such an REV exists for every permeable system. Indeed, Snow's (1969) theoretical and experimental work shows the permeability of fractured rock may continue to increase with the volume tested. This implies that within the practical limits of the geologic strata the statistical sample continues to change with the size of the sample. A further problem has been studied by Freeze (1975), Smith and Freeze (1979a and b), and Smith (1978). They have concluded that for some problems it may not always be possible to define equivalent homogeneous properties for inherently heterogeneous systems. Using numerical simulation, Smith and Freeze studied arbitrary flow systems in one- and two-dimensional heterogeneous porous media. Elements of the model were assigned permeability in a random manner. Hydraulic equivalence between the heterogeneous systems and an equivalent homogeneous system was based on two criteria (Smith and Freeze, 1979b):

1. The mean value of the hydraulic head at any point, as determined from a stochastic solution that recognizes the spatial heterogeneities, must equal the head value at that point, as determined from a single deterministic solution using the effective conductivity of the medium.
2. The mean value of any integrated flow measurement determined from the stochastic solution must equal the single value provided by the deterministic run.

Smith and Freeze concluded that in two dimensions these conditions were met only when very restricted conditions were placed on the nature of heterogeneity and the flow system operating within the domain. However, this conclusion was based on two somewhat limiting assumptions. First, the geometric mean permeability was always used as the equivalent permeability. Although the geometric mean is a good approximation for some flow systems, there is no guarantee that it is always the best estimate of equivalent permeability. Second, the equivalent permeability was only allowed to be isotropic. An anisotropic value may have met the above criteria. For any given set of boundary conditions, Smith and Freeze might have been able to find an

equivalent anisotropic permeability which produced the same average flux as the heterogeneous system. The difficulty in identifying this equivalent permeability is that the equivalent permeability tensor that works for one set of boundary conditions will not necessarily predict the correct flux for another set of boundary conditions. The difficulty arises because, in general, different boundary conditions induce different gradients in different parts of the flow field. The permeability in one part of the field which has a higher gradient will have more effect on the total flux than the permeability in another part of the field which has a lower gradient. When the boundary conditions change, the emphasis changes. Therefore, a given equivalent permeability tensor will only apply to kinematically similar flow systems. Recall that this is the same difficulty identified in the derivation of Darcy's law by Day (1974).

Maini (1971) points out that the same medium can be considered homogeneous or heterogeneous, depending on the size of the flow system operating in it. A small flow system in a given medium can be classed as a heterogeneous problem while a large flow system in the same medium would behave as if it were in a homogeneous medium. The physical implications of Maini's remark are important: the size of the appropriate REV depends on the flow system of interest. The REV must be large enough to contain a representative statistical sample as discussed by Hubbert and others and as shown in Figure 2-2. However, for a particular application, the unit volume that can be used in an analysis must be small enough relative to the flow system being studied so that the gradient throughout the volume is approximately constant in magnitude and direction. This concept is familiar to ground-water flow modelers: the smaller the mesh size is, the more accurate the results are because the head distribution within each element is more nearly linear.

If the average flow lines through an internally heterogeneous volume remain linear, it may be possible to define a unique equivalent permeability tensor which will be correct for flow in any direction. However, if the isopotentials and flow lines are curved relative to the dimensions of the statistically determined REV, then the value of the equivalent permeability of the REV will depend on the particular kinematics of the flow system. In this case, no unique permeability tensor can be defined. Further, a prediction of the behavior of the flow system as a whole would depend on the knowledge of

the equivalent permeability which itself would depend on the flow system. So a unique solution to a flow problem would be very difficult to achieve.

If, on the other hand, the average gradient is constant within the statistically determined REV, then there may exist a single permeability tensor which can be used to correctly predict flow in any direction. However, even under these constraints there is no guarantee that a unique, symmetric permeability tensor will exist for every medium on a given scale.

Given a flow system similar to that studied by Freeze and Smith (1979a and b), for example, flow under a dam, the appropriate volume for an element must be small enough to experience a constant average gradient. To satisfy the definition of a homogeneous continuum, however, it must also be at least large enough to contain a representative sample of the heterogeneities. In some cases, a statistically defined REV may be too large to have constant average gradient. In this case, either a smaller REV must be found as the basis for analysis or a classical continuum analysis will not apply.

Freeze and Smith did not consider the size of the REV relative to the size of their problems when they looked for an equivalent porous medium permeability. It may be that a larger, statistically defined REV exists on the same or larger scale as that of the flow problems they studied. However, the boundary conditions imposed on their flow systems systems produced a nonconstant gradient field. Thus the largest appropriate REV they could have found had to be small compared to the variation in the magnitude and direction of the gradient. In fact, the REV in their problems was, a priori, the size of the individual blocks that were initially assigned a homogeneous single permeability. Constant gradients must be imposed on models such as those developed by Freeze and Smith in order to determine if and when a homogeneous equivalent system exists on a scale larger than that of the individual blocks.

The above review leads to several conclusions central to this investigation. First, it only makes sense to look for equivalent porous medium behavior in fractured rock systems using flow systems which would produce linear isopotentials and flow lines in a truly homogeneous, anisotropic medium. Boundary conditions that will result in such a flow system will be described in Section 3.4. Second, the following criteria must be met in order to replace a heterogeneous system of given dimensions with an equivalent homogeneous system for the purposes of analysis:

1. There is an insignificant change in the value of the equivalent permeability with a small addition or subtraction to the flow volume
2. A single equivalent symmetric permeability tensor exists which predicts the correct flux when the direction of gradient in an REV is changed.

Criterion (1) implies that the size of the sample under consideration is a good statistical sample of the heterogeneities. Criterion (2) is based on the assumption that boundary conditions are applied to the sample which would produce a constant gradient throughout a truly homogeneous, anisotropic sample. The actual gradient within the heterogeneous sample does not have to be exactly constant for (2) to be satisfied. The average isopotentials of the heterogeneous system will probably be the same as the isopotentials in the equivalent homogeneous system, if (1) and (2) above are met. However, it is not necessary to have a constant actual gradient in order to have a tractable porous medium analysis. For example, if a block of material the size of the REV is removed from a flow system and replaced with a block of equivalent homogeneous material, the overall characteristics of the flow system will not change significantly if criteria (1) and (2) are met. Each block will have experienced the same boundary conditions and produced the same average fluxes across the boundaries. Further, each block will contain a relatively linear flow field. The shape of the isopotentials within the two blocks may be different in detail, but this by itself will have no import on the overall description of the flow system.

2.3 STATISTICS OF FRACTURE GEOMETRY

2.3.1 Introduction

Under a given set of boundary conditions, the hydraulic behavior of a fractured rock mass with an impermeable matrix is determined entirely by the geometry of the fracture system. Real fractures have complex surfaces and variable apertures, but for the purposes of this study and most other studies of fracture systems, the geometric description is simplified. The assumption is made that individual fractures lie in a single plane and have a constant hydraulic aperture.

Characterization of a fracture system is considered complete when each fracture is described in terms of (1) its hydraulic or effective aperture, (2) its orientation, (3) its location, (4) its size and, for a three-dimensional description, (5) its shape. In two dimensions, size means length. This survey is organized into three sections corresponding to these geometric properties. Size and location are discussed together.

2.3.2 Apertures

The hydraulic behavior of fractures has been shown to be a function of their aperture, b. Witherspoon et al (1979) has reviewed the data on laminar flow in fractures and concluded that flow in fractures obeys the cubic law:

$$\frac{q}{\nabla\phi} = Cb^3, \qquad (2\text{-}50)$$

where q is flux, $\nabla\phi$ is the gradient, C is a constant, and b is the hydraulic aperture. Characterization of the permeability of a fracture requires determining the hydraulic aperture.

Iwai (1976) was able to define a hydraulic or effective aperture for non-ideal sample fractures in the laboratory. Iwai studied flow through rough tension fractures in granite, basalt, and marble, under various conditions of normal loading and opening. First he showed that for a fixed aperture, flux was proportional to gradient, i.e., Darcy's law was obeyed. He then tried to create a zero-aperture fracture by applying 20 MPa across the fractures. Fractures in this condition continued to conduct water. The effective parallel-plate aperture, b_o, which would account for this residual flow, was calculated. As load was released, the fractures opened by Δb. The effective aperture which accounted for the flow was found to be $b_o + \Delta b$.

Significantly, the effective apertures could not have been measured directly for two reasons. First, the fracture that was subject to maximum stress and appeared to be completely closed could still conduct water. Second, the fractures were rough and the sides had some contact with each other. The net effect of roughness and contact area could be measured only hydraulically. Thus the effective aperture must be measured by performing hydraulic tests.

Unfortunately, it is very difficult to perform hydraulic tests on isolated fractures in the field. Such attempts may be hampered by inability to isolate single fractures in the borehole, the effect of intersecting fractures, and low flow rates required for nonturbulent flow near the wellbore. Limited attempts have been made to test individual fractures. For example, Gale (1975) isolated a limited number of horizontal fractures with packers and performed injection tests to determine their apertures. His data also show that hydraulic and measured (apparent) apertures are not the same. The apertures measured from a borehole periscope log were at least one order of magnitude higher than the corresponding hydraulic apertures calculated from injection flow rates. Gale's data, however, are not extensive enough to make significant analysis of the relationship between hydraulic and apparent apertures.

Because of the difficulty involved in hydraulically isolating a single fracture underground, the knowledge of fracture aperture distributions is limited to apparent apertures that have been observed directly in cores or well logs. Methods for direct measurement of fracture aperture have been refined by Rocha and Franciss (1977) and Bianchi and Snow (1968). Rocha and Franciss proposed a technique called integral sampling. This method consists of drilling a small pilot hole and injecting a grout. Then an overcore is taken and the grout filled fractures are measured. Bianchi and Snow used a fluorescent dye process to reveal the fractures on the surface of a rock sample. Apertures are then measured with a caliper. The distribution of apertures measured by Bianchi and Snow was found to be very close to lognormal.

It may be reasonable to expect the distribution of true hydraulic apertures to also be distributed lognormally, Snow (1969) assumed this and was able to estimate the mean and standard deviation of aperture distribution from normalized pressure test data. He also assumed a Poisson distribution of fracture spacing. Individual injection test results were normalized to the same length of test zone. Snow then used the frequency of zero discharge zones to estimate the mean fracture density, λ. He then concluded that the mean discharge of individual fractures is equal to the mean discharge of all samples of fractures encountered by the uniform test lengths divided by λ. From the mean discharge, Snow calculated the mean aperture. This analysis does not differentiate the aperture distributions for individual sets; all the fractures are assumed to be perpendicular to the hole.

A further consideration in understanding the aperture distribution of fractures is that fractures of greater extent may be likely to have larger apertures. Thus fracture length and apertures are possibly correlated. This important topic has not yet been studied. Support for such a correlation comes from the literature on fracture formation where the width of a crack can be calculated as a function of its length for various stress states (Sun, 1969; Secor and Pollard, 1975; Pollard, 1978; Pollard, 1976; Pollard and Muller, 1976; Simonson et al, 1978). Also studies of roughness show that the scale of roughness is linearly related to fracture length (Sayles and Thomas, 1978). The possibility of the size of the asperities partially determining the aperture is further evidence for a relationship between length and aperture. The exact nature of the relationship between length and hydraulic aperture is not yet fully understood.

In conclusion, the best estimate currently available is that apertures are distributed lognormally. However, confirmation of this estimate and the relationship of fracture aperture to lateral extent awaits extensive hydraulic field testing and mapping of isolated individual fractures.

2.3.3 Orientation

The statistics of fracture orientation are perhaps the best understood of all the geometric properties of fractures. There are three reasons for this. First, it is relatively easy to obtain a measure of the orientation of a large number of fractures. Orientation can be measured in cores or in outcrops with simple tools. Second, information on fracture orientation has been developed in the pursuit of several different types of engineering projects, notably those concerning structural stability of rock masses. These analyses are useful for hydrologic purposes. In contrast, effective fracture apertures are harder to measure. Apertures are only of direct interest to hydrologic problems and are therefore not studied by other disciplines. Third, the mathematics of orientation analysis has been of interest to many fields. Statistical analysis of such data is well developed. Pincus (1953) gives an extensive table of references from the earth science field alone.

Fracture orientation distributions are usually studied by plotting the poles of each fracture plane on either a stereo net or a Lambert equal-area

net. Terzaghi (1965) gives a description of these projections. Data from a single or several related sites plotted in this manner usually form clusters or sets. Each set can be identified and analyzed separately. In general, a parametric analysis of this type of data consists of determining (1) the form of the distribution, (2) a parameter representing the central tendency or mean direction, (3) a measure of the dispersion around this mean, and (4) a measure of the goodness of fit of the data to the theoretical distribution.

For example, Fisher (1953) gave a simple method for estimating the mean direction of a collection of poles. The mean direction is simply the direction of the vector sum of all the unit vector poles. This vector sum is called the resultant. Fisher assumed the probability density is proportional to $e^{k\cos\theta}$ where θ is the angular displacement from the mean and $k>0$ is a measure of dispersion. If all N measurements are in the exact same direction, the resultant R would be of length N. Therefore k is a function of N and R. Fisher found

$$k = \frac{N - 1}{N - R}, \tag{2-51}$$

is a good estimate when $N - R < 2$. It should be noted that Fisher's distribution is symmetrical about the mean direction. Snow (1965) applied Fisher's distribution to the Monte Carlo calculation of the permeability of sets of randomly distributed infinite fractures.

Pincus (1953) gives a thoughtful discourse on the methodology of statistical analysis of orientation data. He discusses requirements for sample size and suggests the method of sequential sampling. In this method successive increments of data are collected "until the total picture changes with the addition of the last increment by an amount less than that required by the precision of the investigation." If a model distribution is hypothesized, Pincus suggests use of the chi-square (χ^2) test for model validity. Pincus also suggests methods for applying linear, circular, and spherical normal distribution theory to two- and three-dimensional problems.

Before statistical theory can be applied to orientation data, sample bias must be removed. Terzaghi (1965) explains the geometric causes of sample bias. Orientations are usually measured either in core or on an outcrop. Fractures which are more nearly parallel with the core or outcrop have a lower proba-

bility of being sampled. The number of fractures, N_{90}, which would be intersected by a hole (or an outcrop) perpendicular to the joints is given by

$$N_{90} = \frac{N_\alpha}{\sin\alpha} \tag{2-52}$$

where N_α is the number of fractures intersected by the same hole (or outcrop) which makes an angle α with the fractures. This formula can be used to correct orientation data. However, the reliability of such corrected data decreases as α becomes small. When α is zero no correction can be made. This problem can be overcome by sampling several outcrops or core holes in a variety of orientations.

Mahtab et al (1972) developed a computerized method for analyzing clusters of orientation data. This program divides the sphere on which the poles are plotted into 100 patches of equal area and obtains the density of poles in each patch. Clusters are defined as "collections of all points in adjacent patches where each patch possesses a density that exceeds the threshold value". Mahtab compares the density against a Poisson distribution to identify threshold values. Once clusters have been identified they are compared to Arnold's hemispherical normal distribution with probability density $\nu(\psi, k)$ given by

$$\nu(\psi, k) = \left(\frac{k}{4\pi(e^k - 1)}\right) e^{k\cos\psi} \tag{2-53}$$

where ψ is the random variable which assumes values ψ_i, the angle between the ith observation and the mean vector, and k is a measure of dispersion. This distribution is similar to the univariate normal distribution. Mahtab gives the estimate of k for $k > 6$ as

$$k = \frac{N}{N - R} \, . \tag{2-54}$$

Also, the probability P of an observation being within ψ of the mean is given by

$$\cos\psi = 1 + \frac{1}{k} \log_e(1 - P). \tag{2-55}$$

Once the estimate of k is found, the χ^2 goodness-of-fit test is applied. Mahtab et al applied this method to porphyry copper fracture data. The cluster analysis showed a major orthogonal joint system. One of the clusters passed the χ^2 test for Arnold's hemispherical normal distribution; the other two did not. Other distributions, for example Fisher's, could have been examined for these two sets.

2.3.4 Location and Dimension

The mathematical descriptions of fracture locations and fracture dimensions are interrelated. Therefore, these two topics will be discussed together. Fracture traces can be observed in outcrops or in excavations. The location of fractures intersecting a borehole can also be determined. Using trace length and borehole data, we wish to determine the location of fractures in space and their shape and dimensions.

Robertson (1970) studied fractures exposed in the tunnels of the de Beers mine. Trace lengths of fractures were recorded using a category system with four intervals. The distributions obtained were compared to exponential distributions. In most cases, the fit was considered good. Robertson experienced difficulty in the placing of joints in the correct class intervals. Where traces continued into the walls, roof or floor, the correct trace length could not be measured. Statistical methods which correct for this censoring were not invoked. Robertson also made an effort to estimate fracture shape. The author made "bivariate plots of dip trace length against strike trace length". The authors then assumed that fractures were circular, and concluded that joint sizes are underestimated by trace lengths according to the relationship

$$A = \frac{16}{\pi^2} A' , \tag{2-56}$$

where A' is the joint area calculated from the visible trace lengths. Taking A to be the average area, then the average fracture radius, r, would be

$$E(r) = \sqrt{\frac{A}{\pi}} = \sqrt{\frac{16A'}{\pi^3}} = \frac{4}{\pi}\sqrt{\frac{A'}{\pi}} = \frac{4}{\pi} E\left(\frac{L}{2}\right), \tag{2-57}$$

where E(L/2) is one-half the expected value of the trace length.

Robertson (1970) estimates the volumetric density of jointing, λ_V, given the number of joints, n, intersecting a simple line of length L as

$$\lambda_V = \frac{n}{L\ a(\cos\delta)(\cos\theta)}, \tag{2-58}$$

where a is the average area of the joints and θ and δ are the horizontal and vertical angles between the sample line and the joint set pole. This estimate is based on the assumption that parallel joints are randomly distributed in space. The probability of intersecting n joints was assumed to follow the binomial law.

Some further information on fracture shape has come from research on fracture formation. An example of such work is given by Pollard (1978). Pollard suggests that the form of sheet intrusions in sedimentary rock should be similar to the form of hydraulic fractures since the mechanics of formation are similar. He finds that vertical dikes tend to be greater in length than height and horizontal sills tend to be equidimensional. Inclined intrusions are rare. Thickness-to-length ratios ranged from about 1/100 to 1/1000. Some intrusions were stacked up in groups with small spacings and some were arranged in echelon patterns. Fractures formed in echelon would have decreased conductivity at the "steps" in the echelon pattern. An elliptical model for fracture shape may be applicable, at least to the extent that fractures in a rock mass were created by hydraulic fracturing. However this model may not apply to fracture networks produced by tectonic movements.

Priest and Hudson (1976) and Hudson and Priest (1979) examined the distribution of fracture spacing along a scan line and concluded that spacing values can be approximated with a negative exponential distribution

$$f(x) = \lambda e^{-\lambda x}, \tag{2-59}$$

where f(x) is the frequency of discontinuity spacing, x, and λ is the average number of fractures per meter. An evenly spaced distribution of fractures, such as in columnar basalt, would result in a normal distribution. Clustered distributions could occur near lithological boundaries or due to stress effects. Random spacing, which could occur in homogeneous rock, leads to a negative

exponential distribution. Geologically complex rock is likely to have a combination of evenly spaced, clustered, and random distributions. Superposition of these fractures tends to result in a distribution similar to the negative exponential because superposition tends to preserve the smaller spacings and break up the larger ones. Hudson and Priest (1979) used numerical simulation to demonstrate the evolution of a negative exponential distribution from superposition.

Hudson and Priest also analyzed scanline measurements from several tunnels. A negative exponential distribution for spacing was found to be a good approximation. It is interesting to note that at least 200 measurement values were required to clearly define a negative exponential histogram. The mean and standard deviation of the theoretical negative exponential are equal. Priest and Hudson's measurements of the mean and standard deviation were within 20 percent of each other.

Baecher et al (1977) reviewed the literature on spacing and length distribution. Both spacing and length have been reported to vary both exponentially and lognormally. The authors proceeded to analyze joint data from sedimentary and complex metamorphic rocks. Trace length distributions were compared to exponential, normal, gamma, and lognormal distributions. Lognormal provided the best fit to the data. Spacing distributions were measured by extending joints found in outcrops to infinite planes. Distributions of spacing were measured for lines of various orientations on an exposed rock surface. Spacings were fit to exponential, negative binomial and lognormal distributions. Exponential distributions provided the best fit regardless of the orientation of the sample line.

Baecher et al (1977) developed a conceptual joint geometry model. Joint trace lengths are assumed to be lognormally distributed and spacings are assumed to be exponentially distributed. The authors infer that joints are discs randomly distributed in space. Joint radii are shown to be lognormally distributed. Using this model, the authors estimated the expected joint radii from the expected trace length much as Robertson (1970) did. However, unlike Robertson, Baecher et al lower this estimate to account for the sampling bias of larger joints appearing disproportionately in the sample. They give the expected value of r as

$$E(r) \cong [2.2E^{-1}(L) + 6.96\ \mathrm{Var}(L)\ E^{-3}(L)]^{-1}, \tag{2-60}$$

where L is the trace length, E(L) is the expected value of L, and Var(L) is the variance. From the spacing distribution data the density of jointing for a set of parallel joints was estimated as

$$\lambda = \frac{N/L}{\pi(\cos\theta)E(r^2)}, \tag{2-61}$$

where N is the number of joints intersected on a line of length L which makes an angle θ with the joint poles. This estimate is similar to Robertson's (1970) result. However, as explained above, Baecher's estimate of joint size includes a correction for sampling bias.

Baecher and Lanney (1978) further examined bias in trace length sampling. They identify three types of bias: size bias, truncation bias, and censoring bias. Size bias occurs because larger joints have a larger probability of being sampled. Truncation bias occurs because joints smaller than a certain size are eliminated from the survey. Censoring bias occurs because the full trace length of some joints is not observable.

Size bias can be accounted for if assumptions are made about the shape and distribution of joints in space. Baecher assumed joints are circular discs randomly located in space. Then the probability of a joint being intersected by an outcrop is proportional to its radius. Baecher shows that the distribution of trace lengths, L, is given by

$$f(L|\theta) = \int_{L/2}^{\infty} Cr \frac{L}{2r\sqrt{4r^2 - L^2}} f(r|\theta)\, dr, \tag{2-62}$$

where C is a constant and θ is a vector of parameters (not explicitly defined by the authors). For exponential or lognormal forms for f(r), Baecher and Lanney show that the expected value of trace length, E(L), is greater than twice the expected value of the unconditional average. Also, f(L) has lognormal form whether f(r) is lognormal or exponential.

Truncation also leads to systematic overestimation of average joint size since smaller joints are systematically removed from the sample. This error is greater for exponential distributions than for normal or lognormal

distributions. For an exponential distribution of true trace length, Baecher finds the estimated mean trace length is up to three times larger than the true mean, depending on the truncation limit. Censoring tends to cause an underestimation of mean trace length. This bias cannot be easily corrected, but Baecher and Lanney present some approximate corrections.

Barton (1978) studied an unusual outcrop where all the joints belonged to a single set perpendicular to the outcrop. The size of the outcrop was such that there was no apparent censoring, and truncation at the lower limit was at a well-defined 30 mm. Barton established a numerical model of the joints which placed parallel circular discs randomly in space. Various distributions of radius were assigned to the discs. The numerical model was used to calculate trace length distributions for a plane intersecting the model perpendicular to the fractures. Barton found that chords from circles with lognormally distributed diameters were distributed in a similar manner to the trace lengths of the field site. Further, the analysis showed that the standard deviation of the trace length distribution is always higher than the standard deviation of the diameter population. This can be understood by considering the case where the discs are all the same size but the traces are not. The model also showed that size bias becomes more important as the size range of the population sample increases.

Slightly different models of fracture systems were presented by Veneziano (1979) and Conrad and Jacquin (1973) for application to rock mechanics. Conrad and Jacquin's two-dimensional model separates fractures into two superimposed networks. First there is a network of large fractures called major fractures, which are infinite straight lines. These lines form convex polygons in the plane. The second is a network of small segments called minor fractures. These straight line segments extend at most to the perimeter of the polygons defined by the major fractures. The network of major fractures is formed by Poisson major fractures. The network of major fractures is formed by Poisson lines of variable density according to direction. The network of minor fractures consists of line segments of random location, length, and orientation.

The Poisson lines are constructed as follows: a base line is drawn perpendicular to the direction of each set of major fractures. A certain number of Poisson points are generated on this base line. Poisson lines are drawn through these points perpendicular to the base line. This is similar to the

method employed by Lippmann (1973) in his study of heterogeneous porous media. The Boolean diagram of minor fractures is constructed such that the center, orientation, and length of the fractures are random. Then the fractures are truncated where they intersect a major fracture. Using statistics obtained from an observed network of fractures, Conrad and Jacquin simulated a random network. The model was used to calculate geometric parameters of the blocks such as area perimeter and height. Most of these geometric comparisons between the observed network and simulated model were favorable. The authors suggest the model could be improved by truncating the major fractures and extending the model to three dimensions.

Veneziano's (1979) model is similar to that of Conrad and Jacquin (1973). However, Veneziano defines only one type of network. The fracture network is constructed using two processes. The primary process includes a random network of anisotropic Poisson lines in two dimensions or planes in three dimensions. The secondary process partitions each line or plane into two random sets: one set for intact rock and the other for open fractures. In two dimensions, each line is partitioned into segments by a Poisson point process. In three dimensions, the plane is partitioned with a random polygonal tesselation induced by a homogeneous Poisson network of lines in the plane. The probability that each line segment or polygon is an open fracture is allowed to vary with the orientation of the line or plane. A homogeneous, anisotropic network of joints results. By taking limiting cases of the parameters, this model becomes essentially the same as the model proposed by Baecher et al (1977) except that Baecher used circular fractures, and Veneziano's are polygonal. Veneziano's model has the advantage of easily simulating systems with more than one fracture in a given plane or generating fractures with variable apertures. Veneziano used this model to predict rock failure in slope stability problems.

In summary, the best current estimates based on field data for the geometry of fracture location and length result in elliptical fractures located randomly in space. This is essentially the model of Baecher et al (1977). (Note that circles are subsets of ellipses.) Thus the spacing between fractures is likely to be distributed in a negative exponential manner. Fracture radii, if fractures are taken as circular, are distributed either lognormally or in a negative exponential manner. Correlations between fracture length and hydraulic aperture are not available. Correlations of length and density with

orientation are available since fractures are commonly divided into sets for analysis. For certain rocks, however, some variation of the more complex models of Conrad and Jacquin (1973) and Veneziano (1979) may be more applicable than Baecher's model. So far, the above models of fracture geometry have been used to analyze slope stability but not to predict hydraulic behavior of a rock mass.

2.4 CONCLUSIONS FROM THE LITERATURE SURVEY

The permeability of fractured rocks where the fractures transect the entire rock mass is well understood (Snow, 1965). The permeability of systems of nonextensive fractures is not well understood. There can be no generalized analytic formulation which can account for the random interconnections between nonextensive fractures. Some modeling work on nonextensive fracture systems has been done but this work has not yet examined the circumstances under which it is reasonable to represent fractured systems with an equivalent porous medium permeability.

In order to examine this problem, it is necessary to understand the nature of porous medium permeability. In general, porous media are anisotropic. Although the anisotropic permeability tensor is usually assumed to be symmetric, this assumption may not always be valid. The only way to find out if a given medium has a symmetric permeability tensor is to measure the directional permeability. For a symmetric tensor, permeability measured in the direction of the gradient or the flux can be plotted such that it forms an ellipse. In the case of the permeability measured in the direction of the gradient, $1/\sqrt{K_g(\alpha)}$ plotted in polar coordinates versus α, the direction of measurement, is an ellipse. The values of the components of K_{ij} can then be determined from the plot of the ellipse.

If a volume of fractured rock can be represented by an equivalent volume of homogeneous anisotropic material, then the calculation of regional groundwater flow will be tractable. Also, in order to perform the analysis, an appropriate REV must be found. An appropriate REV is the volume that is (1) large enough to contain a representative sample of the heterogeneities and (2) small enough relative to the flow problem of interest to experience a constant average gradient. Thus it is possible that the appropriate REV may either be very small or nonexistent for a particular flow system in a particular medium.

A block of fractured rock can be tested to see if it behaves as an equivalent homogeneous porous medium. Boundary conditions which would induce a constant gradient throughout an anisotropic homogeneous medium are imposed on the rock. Flux is measured and permeability calculated. This process is repeated in many directions and the results plotted on polar coordinate paper as described above. If an ellipse is obtained, the permeability of the rock is a symmetric tensor. Then the rock must be tested to see if the addition or subtraction of a small volume to the sample of rock significantly changes the value of the tensor. If a volume of rock tested as described above has a symmetric permeability tensor which is constant with small volume changes, then that volume may be replaced by an equivalent porous medium in the analysis of flow problems which are large compared to the volume tested.

The literature on fracture geometry was reviewed to find realistic fracture systems to test for porous medium behavior. Based on the information available, a realistic two-dimensional fracture system model has the fracture centers randomly located in the plane. Fractures are generally elliptical in three dimensions, so they are line segments in two dimensions. Their orientations by sets are distributed normally, trace lengths are distributed either exponentially or lognormally, and apertures are distributed lognormally.

3 DESCRIPTION OF THE NUMERICAL ANALYSIS

3.1 INTRODUCTION

In order to determine when a fracture network can be treated like a porous medium, a numerical approach has been taken in this work. A numerical program was developed to generate sample fracture systems and measure their directional permeability. The program was then used to study examples of extensive and nonextensive fracture systems and determine how well their behavior approximates that of a porous medium.

A two-dimensional mesh generator produces random realizations of a population of fractures. Input to the generator includes specification of the distributions that describe the fracture population. The mesh generator can randomly choose fractures for the sample according to these distributions. A finite-element analysis can then be used to calculate Q_g, the component of flow through the pattern in the direction of the gradient. Using Darcy's law, the hydraulic conductivity in the direction of the gradient, K_g, of the sample fracture pattern is calculated by

$$K_g = \frac{Q_g}{\nabla\phi A} \tag{3-1}$$

where A is the gross area perpendicular to flow. This program can be used to study the effect of sample size on conductivity measurement. First a large fracture pattern is generated. A small piece of this sample can be numerically removed and subjected to the numerical conductivity test described above (Equation 3-1). Succeedingly larger pieces can be tested and the results compared.

The program can also be used to study the variation in conductivity between different realizations of a statistically described fracture system. This Monte Carlo type of analysis can also be used to analyze statistical data collected in the field. An expected value and standard deviation of equivalent porous media conductivity are obtained in this way.

3.2 MESH GENERATION

Fracture patterns are produced according to the best currently available description of real fracture systems. Sets of fractures are assumed to be

independent and individual fractures are randomly located in space. Length distributions are assumed to be lognormal or exponential. Apertures are assumed to be lognormally distributed. Orientation is normally distributed.

The permeability test that is applied to the fracture model is independent of the way the fracture pattern is generated. A fracture model, such as that proposed by Veneziano (1979), could also have been used and the remaining analysis of permeability would still have been valid.

A particular sample fracture pattern is randomly generated in a rectangular or square area (generation region) of a specified dimension. A general description of this process follows. Each set of fractures is generated independently. Then the individual sets are superimposed (Figure 3-1). The location of each fracture in a set is found by assuming the center of the fractures are randomly distributed (Poisson distribution) within the generation region (Figure 3-1a). For each set, a density (number of fractures per unit area) must be supplied to determine the total number of fracture centers to be generated.

The orientation of each fracture in a set is determined next (Figure 3-1a). Orientation of fractures in a set has been assumed to be normally distributed. Therefore the mean and variance for orientation must be supplied for each set. At this point, the equation of the line on which the fracture lies is identified.

The length of each fracture is chosen next (Figure 3-1c). Fracture length within a set is assumed to be distributed lognormally or exponentially. If the length is distributed lognormally the mean and variance must be supplied. In the case of the exponential distribution, the parameter λ, is equal to $1/\bar{\ell}$ where $\bar{\ell}$ is the expected value of the fracture length. The value of $\bar{\ell}$ must be supplied for each set. Fracture centers have been constrained to lie within the generation region. However, when lengths are assigned, part of the fracture may be outside the boundaries. These fractures are truncated at the boundaries of the generation region.

Finally, apertures are assigned to each fracture (Figure 3-1d). This can be done in two ways. The simplest way is to assume that apertures are lognormally distributed within a set. For this approach a mean and variance for aperture must be supplied for each set. A second way is to assume that apertures are correlated with fracture length according to some model. A

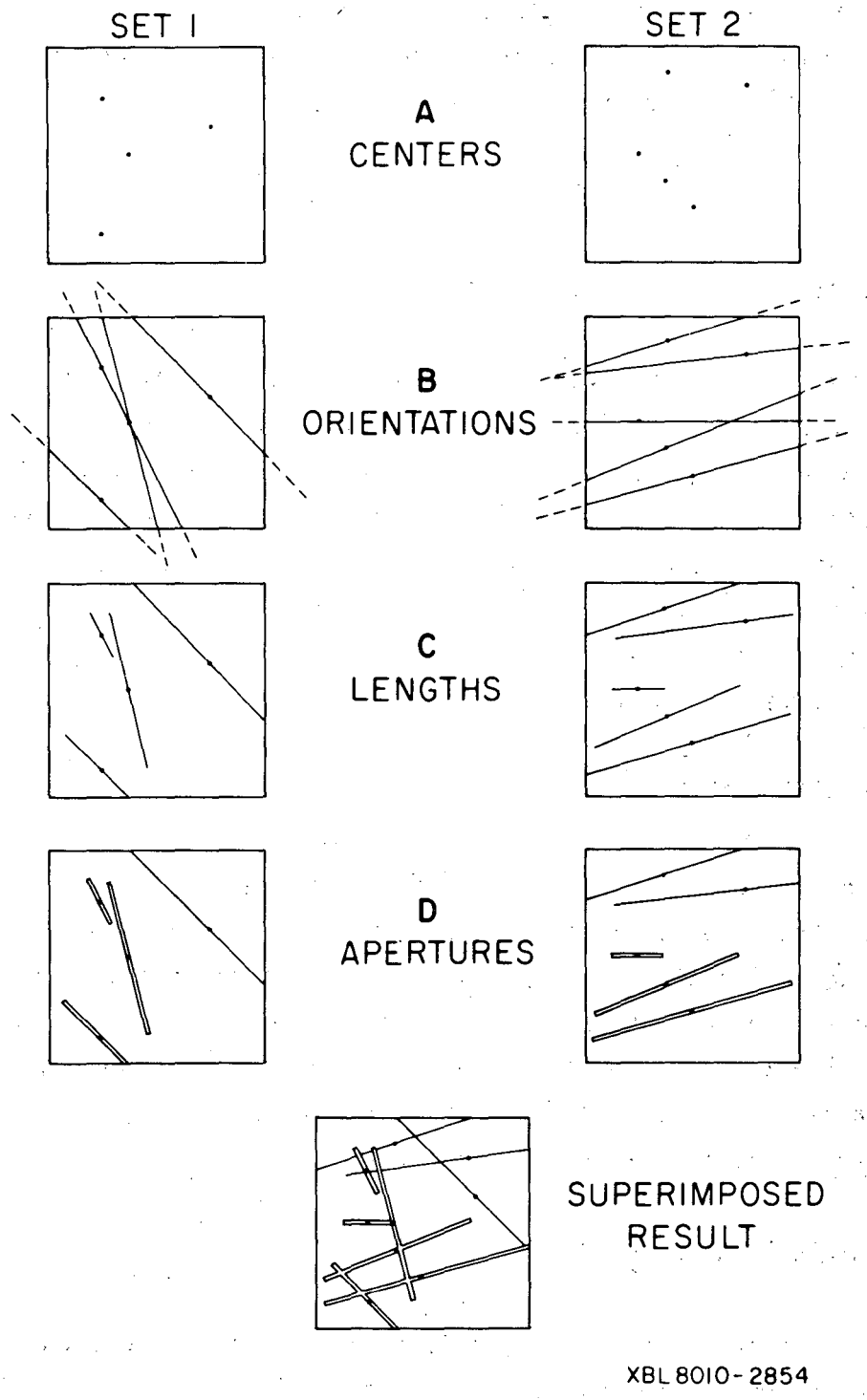

Figure 3-1. Superposition of Random Sets of Fractures

simple model has been incorporated into this mesh generation procedure. This model assumes that the mean fracture aperture associated with a particular fracture length is proportional to the log of fracture length to some power:

$$\bar{b}(\ell) = \log CP^{1/n}. \tag{3-2}$$

The actual value of b assigned to a particular fracture is found by allowing $\bar{b}(\ell)$ to be the mean value of a normal distribution. To use this method, two parameters to describe the relationship between $\bar{b}(\ell)$ and ℓ and a third parameter, the standard deviation of the normal distribution of b around $\bar{b}(\ell)$, must be supplied. Use of this option and definition of the input parameters is described in Chapter 7 and Appendix A.

When all the sets have been generated, a flow region is selected. The fractures which lie in the flow region are identified and the coordinates of each intersection are calculated. A more detailed explanation of the mathematics is given in Section 3-7.

3.3 STATISTICAL CONSIDERATIONS

This model is designed to study variation in conductivity for fracture systems that are homogeneous in a statistical sense. That is, the geometric characteristics of aperture, length, orientation, and location of the fractures in the system are assumed to be distributed in the same manner throughout the rock. Fractures in the field may or may not be homogeneous within discernible boundaries. Conclusions drawn from this study will apply only to regions of rock which are statistically homogeneous.

3.4 MEASUREMENT OF CONDUCTIVITY

As previously discussed, conductivity of a homogeneous medium can be defined either in the direction of flow or in the direction of the gradient. In a heterogeneous medium such as fractured rock, conductivity must be measured in the direction of the gradient. The average gradient can be constant in magnitude and direction throughout a heterogeneous region in steady flow if the region behaves like a homogeneous porous medium. The direction of flow,

however, is controlled by the direction of the fractures. Since the direction of the gradient can be controlled, measuring permeability in the direction of the gradient is much easier than measuring in the direction of flow.

The boundary conditions necessary to produce a constant gradient in a rectangular anisotropic flow region are illustrated in Figure 3-2. They consist of two constant-head boundaries (ϕ_2 and ϕ_4) and two boundaries with the same linear variation in head from $\phi_2 = 1.0$ to $\phi_4 = 0$. Conductivity is measured in the direction perpendicular to Sides 2 and 4.

The linearly varying boundary conditions in Sides 1 and 3 are necessary because, in general, the medium in the flow region is anisotropic. Without these boundaries, the lines of constant head would be distorted near Sides 2 and 4 as shown in Figure 3-3. When the isopotentials are distorted, only part of the flow region can experience a constant gradient. In an arbitrary heterogeneous system of unknown anisotropy. it is impossible to determine what part of the system is experiencing a constant gradient and what part is not. Therefore when no flow boundaries are used, it is not always possible to measure only that part of the flux which is due to a known constant gradient.

The boundary conditions used in Figure 3-2 insure that the whole fracture system is equally stressed by the hydraulic gradient. Under these boundary conditions, whether or not a constant gradient actually exists in the flow region depends only on how well the fracture system is interconnected. If the system is well connected, it will behave like a porous medium and have a constant gradient. See Chapter 10 for a discussion of the limitations associated with the use of these boundary conditions.

Applying Darcy's law to an LxL flow region under the boundary conditions of Figure 3-2 we have

$$\frac{Q_x}{L} = K_{xx}\frac{\partial\phi}{\partial x} + K_{xy}\frac{\partial\phi}{\partial y},$$

$$\frac{Q_y}{L} = K_{yx}\frac{\partial\phi}{\partial x} + K_{yy}\frac{\partial\phi}{\partial y}, \qquad (3\text{-}3)$$

where Q_x and Q_y are the total fluxes per unit thickness in the x and y directions, respectively, and L is the dimension of the square flow region.

For the boundary conditions shown in Figure 3-2, $\partial\phi/\partial y$ is zero. K_{xx} can be calculated:

$$K_{xx} = \frac{Q_x}{\frac{(\phi_2 - \phi_4)L}{L}} = \frac{Q_x}{\phi_2 - \phi_4}. \qquad (3\text{-}4)$$

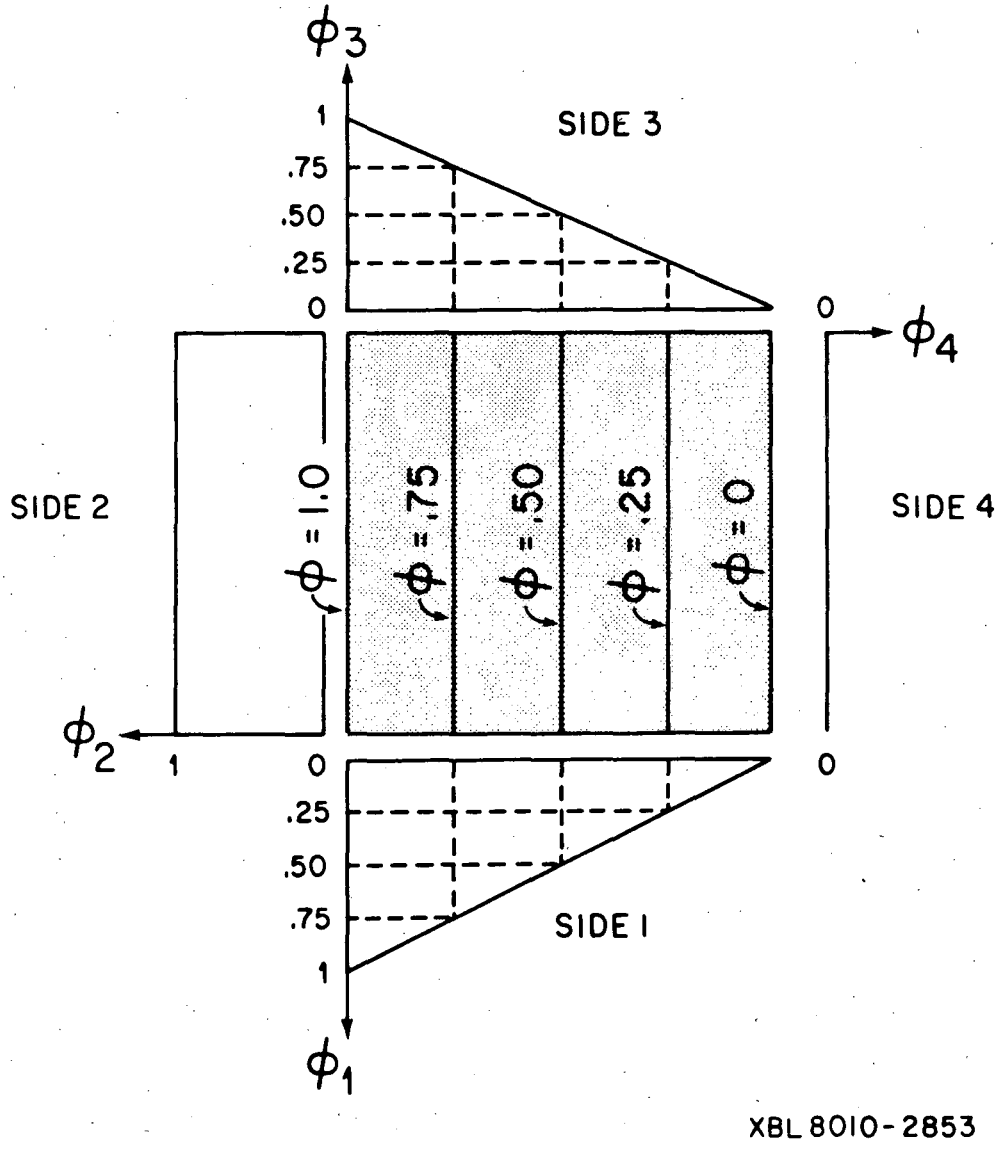

Figure 3-2. Boundary Conditions Applied to Fracture Models for Permeability Measurement

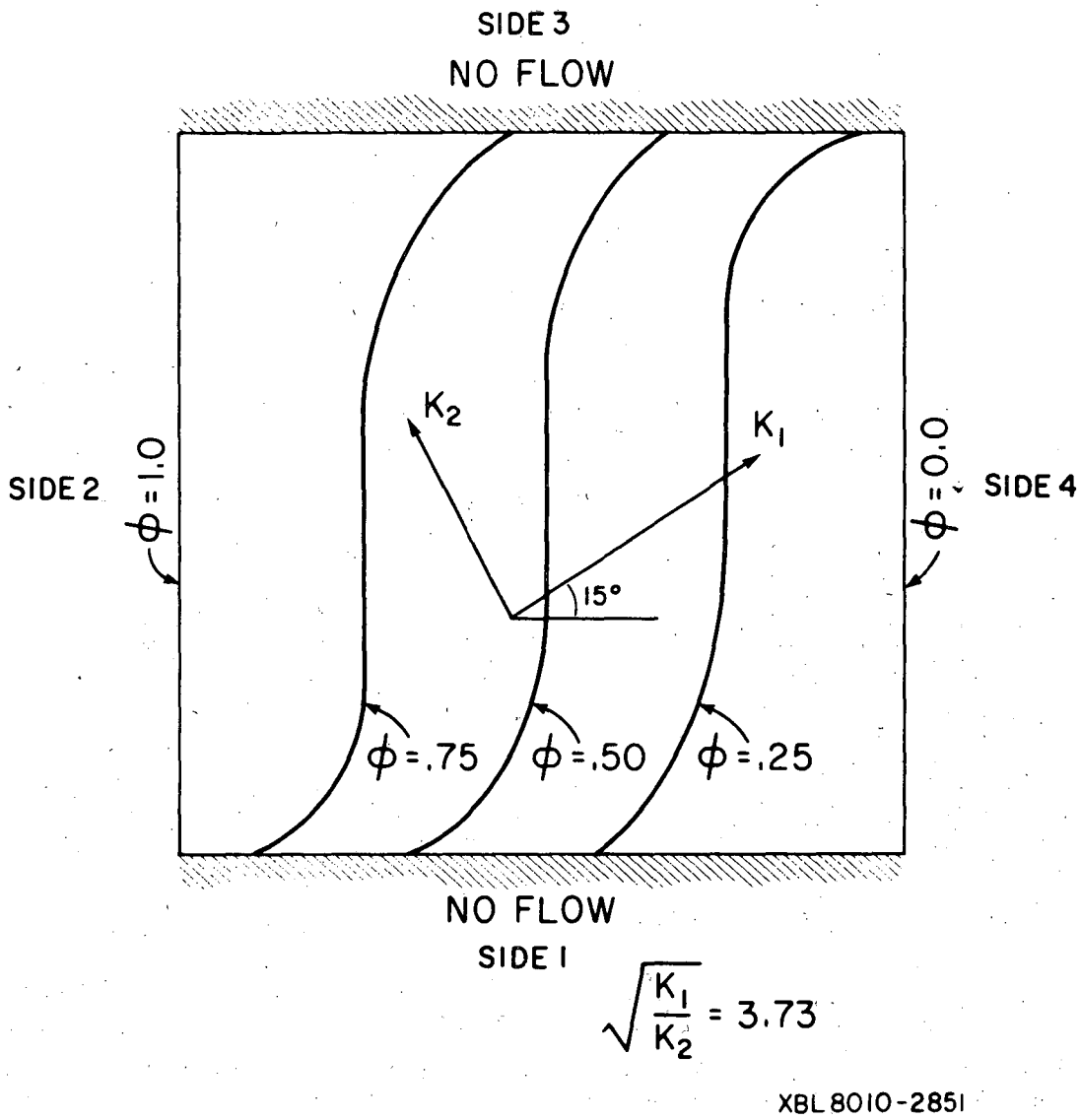

Figure 3-3. Distortion of Isopotentials in an Anisotropic Medium with "No Flow" Boundaries

For $\phi_2 = 1$ and $\phi_4 = 0$, and consistent units, K_{xx} is numerically equal to Q_x. Since Q_y is also known, K_{xy} can be calculated:

$$K_{xy} = \frac{Q_y}{\frac{(\phi_2 - \phi_4)L}{L}} = \frac{Q_y}{\phi_2 - \phi_4} . \tag{3-5}$$

For $\phi_2 = 1$ and $\phi_4 = 0$, as above, $K_{xy} = Q_y$.

3.5 ROTATION OF THE FLOW REGION

Conductivity in a fracture pattern can be measured in any direction chosen. Figure 3-4a shows a sample fracture pattern called a generation region. An arbitrarily oriented rectangular section of the region (called a flow region) can be chosen for analysis as shown in Figure 3-4b. Boundary conditions are applied to the boundaries of this flow region and conductivity is measured in the direction of the orientation of the flow region. This direction is specified by α, the angle between Side 1 and the x-axis.

In general, the fracture pattern forms an anisotropic medium. For homogeneous anisotropic media the directional conductivity, $1/\sqrt{K_{xx}(\alpha)}$ where α is the angle of rotation, is an ellipse when plotted in polar coordinates. However, for heterogeneous fractured media, $1/\sqrt{K_{xx}(\alpha)}$ may not plot as a smooth ellipse. In fact, the shape of a polar plot of measured values of $1/\sqrt{K_{xx}(\alpha)}$ for a given area of rock may be quite erratic. This plot can establish whether or not the given area can be approximated as a homogeneous porous medium. If $1/\sqrt{K_{xx}(\alpha)}$ does not plot at least approximately as an ellipse, then no single symmetric conductivity tensor can be written to describe the behavior of the medium on the scale of measurement. If there is no conductivity tensor, then flow through the medium cannot be analyzed by existing continuum techniques.

If $1/\sqrt{K_{xx}(\alpha)}$ does not plot approximately as an ellipse, behavior of the block of rock in situ cannot be predicted by application of the boundary conditions of Figure 3-2. This is because these boundary conditions are unlikely to apply in situ if $1/\sqrt{K_{xx}(\alpha)}$ does not plot as an ellipse. A technique for predicting the behavior of such systems is discussed in Chapter 10.

If the flow region is to be rotated, it cannot be as large as the generation region. If the generation region is a L x L square, the largest

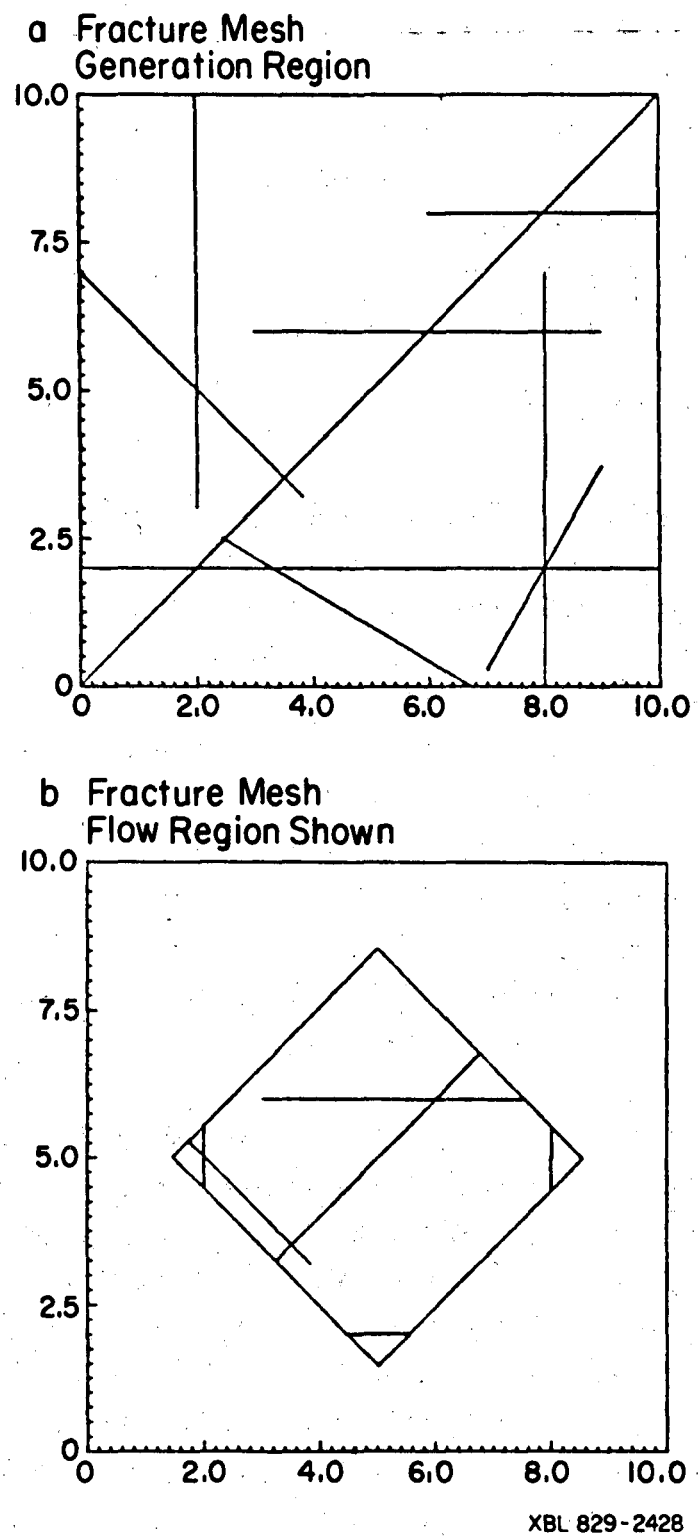

Figure 3-4. A. Generation Region; B. Flow Region

square flow region which can be rotated within the generation region is $L/\sqrt{2} \times L/\sqrt{2}$. Each flow region of a different orientation will contain different parts of the fracture pattern. In Figure 3-5, for example, the corners of flow region B are not included in A. Likewise, the corners of A are not included in B. A and B are, therefore, not exactly the same sample. This limitation of geometry is assumed to be negligible if the fracture geometry statistics of each flow region are nearly equal.

3.6 FRACTURE FLOW PROGRAM

Flow through the fracture system is calculated using LINEL, a finite-element program developed by Wilson (1970) for fracture flow. Fractures are represented as line elements with flux related to aperture by the cubic law. The rock matrix is assumed to be impermeable. Only the steady state flow rate is calculated.

This line element program solves a series of equations, one equation for each fracture intersection or endpoint (i.e., node). The equation for each node is simply a mass balance equation, flow into the node equals flow out of the node. For N nodes, there are N equations and N unknowns. The N unknowns are either the head or the flux at each node. If these N equations are written in matrix form, the matrix of coefficients is symmetric and banded. The original version of LINEL does not exploit this symmetry in its solution technique.

The size of fracture problem that can be studied using the original version of LINEL is limited by the size of the coefficient matrix. This size limitation has been the major obstacle to studying statistically representative systems. To reduce this problem the solution scheme of LINEL was replaced by a solution scheme which requires storage of only one half of the band width of the symmetric coefficient matrix.

The results of this effort were somewhat disappointing. The increase in the allowable problem size has been less than an order of magnitude. However the program was then rewritten to run on the VAX-11 machine. Very large problems requiring millions of bytes of storage can easily be run.

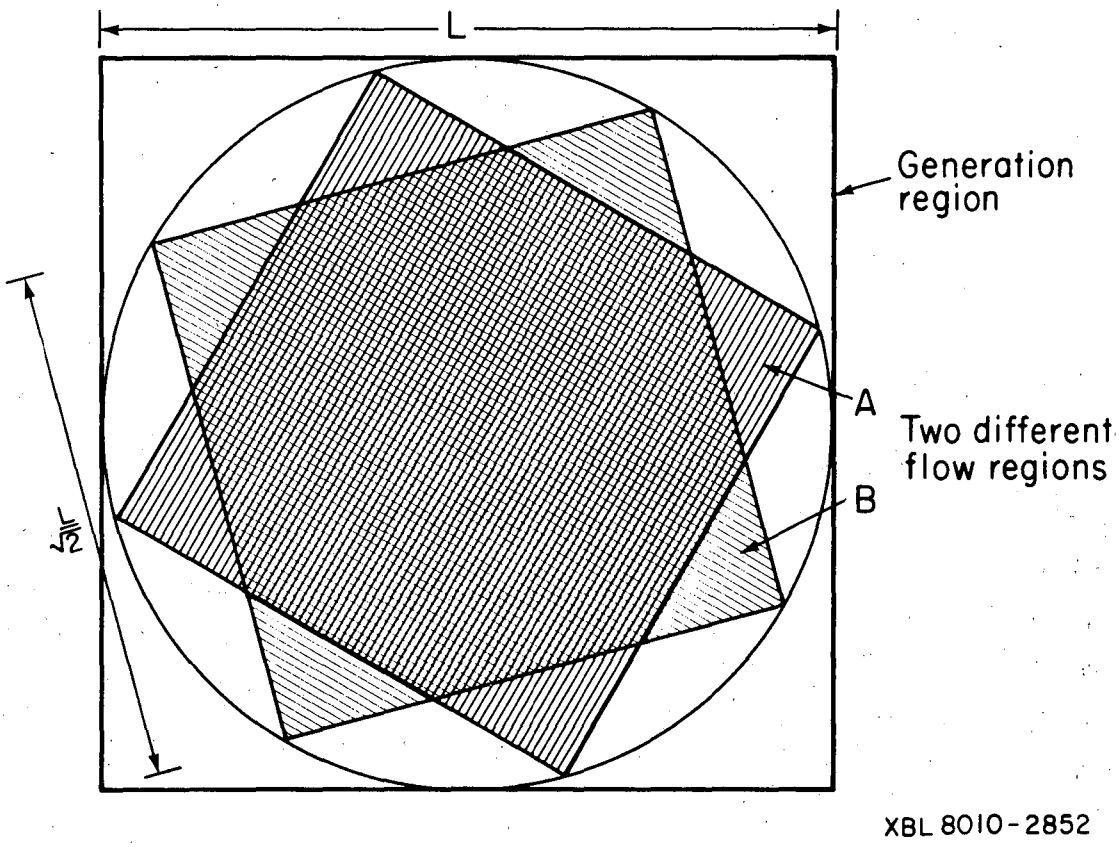

Figure 3-5. Two Different Flow Regions Within a Generation Region

3.7 MATHEMATICAL DESCRIPTION OF RANDOM GENERATION

The following describes the mathematics of generating a random network of fractures.

3.7.1 Poisson Distribution

Fracture centers for a given set are assumed to be randomly distributed in space by a Poisson distribution. A random sample of fracture centers for a given generation region is obtained by simply taking pairs of random numbers between zero and one. The number of significant figures in these random numbers is set by the user. These pairs become the coordinates of the center points when multiplied by the length and width of the generation region, respectively. One only needs to know the density of points or alternatively how many points to generate in the given area. The original generation region has the density specified by the user. The smaller flow region, however, may have a slightly different density. Also, as the flow region is rotated, the density of the different flow region samples may not be exactly the same.

3.7.2 Normal Distribution

In two dimensions, the orientation of fractures in a given set is specified by the angle the fracture makes with the x axis. For a given set, these angles are assumed to be distributed normally. Because the angle θ is effectively the same as the angle $\theta + 2n\pi$, $n = 1, 2, 3, \ldots$, the distribution resulting from the simulation is not exactly the same as the model distribution. This difference is ignored at this point.

A normally distributed variable x, with mean μ and variance $\sigma 2$ can be simulated as follows. By the Central Limit Theorem, sums of random numbers are approximately normally distributed. Hammersly and Hanscomb (1964) show that the sum of 25 random numbers is a good approximation of a normally distributed variate. Let

$$S_n = \sum_{n=1}^{N} R_n \,, \tag{3-6}$$

where R_n is a uniformly distributed random number between 0 and 1, $E(R_n) = 1/2$, and $Var(R_n) = 1/12$. Now the expected value of S_n is

$$E(S_n) = N[E(R_n)] = \frac{N}{2}, \tag{3-7}$$

and its variance is

$$Var(S_n) = E[S_n - E(S_n)]^2 = \frac{N}{12}. \tag{3-8}$$

Let

$$S_n^* = \frac{S_n - E(S_n)}{\sqrt{Var\ S_n}}. \tag{3-9}$$

Now S_n^* is normally distributed with $E(S_n^*) = 0$ and $Var(S_n^*) = 1$. Substituting Equations 3-7 and 3-8 into 3-9 gives

$$S_n^* = \frac{S_n - \frac{N}{2}}{\sqrt{\frac{N}{12}}}. \tag{3-10}$$

For N = 25, Equation 3-9 becomes

$$S_n^* = \frac{\left(\sum_{n=1}^{25} R_n\right) - 12.5}{\sqrt{\frac{25}{12}}}. \tag{3-11}$$

If $x = \sigma S_n^* + \mu$, then x is normally distributed with $E(x) = \mu$ and $n\ Var(x) = \sigma^2$. So we have

$$x = \sigma \left\{ \frac{\left(\sum_{n=1}^{25} R_n\right) - 12.5}{\sqrt{\frac{25}{12}}} \right\} + \mu. \tag{3-12}$$

3.7.3 Lognormal

Apertures and fracture lengths within a set can be distributed lognormally. We have shown how to generate normally distributed values of x with mean μ and variance of σ^2. The probability density of x is

$$f(x) = \frac{1}{\sigma(2\pi)} \exp\left[\frac{-(x - \mu)^2}{2\sigma^2}\right]. \tag{3-13}$$

Let $x = \ln y$. Now $f(y)$ is lognormally distributed with probability density given by Benjamin and Cornell (1970) as follows:

$$f(y) = \frac{1}{y\sigma\sqrt{2\pi}} \exp\left\{-\frac{1}{2}\left(\frac{\ln y - \mu}{\sigma}\right)^2\right\}, \quad y > 0, \tag{3-14}$$

Let $E(y) = \alpha$ and $Var(y) = \beta^2$. Then by integration,

$$E(y) = \alpha = e^{\mu}e^{\sigma^2/2}, \tag{3-15}$$

$$Var(y) = \beta^2 = (e^{\sigma^2} - 1)e^{(\sigma^2+2\mu)}. \tag{3-16}$$

Solving for μ and σ^2, we have

$$\mu = \ln\alpha - \frac{1}{2}\ln\frac{\beta^2}{\alpha^2} + 1, \tag{3-17}$$

$$\sigma^2 = \ln\left[\left(\frac{\beta}{\alpha}\right)^2 + 1\right]. \tag{3-18}$$

Given values of α and β^2, we calculate μ and σ^2. Then μ and σ^2 are used to find normally distributed values of x as previously described. Values of y are found as $y = \exp x$.

3.7.4 Exponential

Fracture length is sometimes assumed to be distributed exponentially within a set. The exponential density and distribution functions are given, respectively, as

$$f(x) = \begin{cases} \lambda e^{-\lambda x} & x > 0 \\ 0 & x \leq 0 \end{cases} \tag{3-19}$$

$$F(x) = \begin{cases} 1 - e^{-\lambda x} & x > 0 \\ 0 & x \leq 0 \end{cases} \tag{3-20}$$

where $E(x) = 1/\lambda$. So λ is equal to the inverse of the mean length.

Simulation of $f(x)$ can be accomplished as follows. Let y be distributed uniformly on (0, 1). Then the probability density $g(y)$ and distribution function $G(y)$ are

$$g(y) = \begin{cases} 1 & 0 < x < 1 \\ 0 & \text{elsewhere,} \end{cases} \tag{3-21}$$

and

$$G(y) = \begin{cases} 0 & x < 0 \\ x & 0 \leq x \leq 1 \\ 1 & x > 1. \end{cases} \tag{3-22}$$

Let $x = -(1/\lambda)[\ln(1 - y)]$. Then the probability density of x for $\lambda>0$ can be shown to be exponential (Hoel et al, 1971), since

$$\begin{aligned} F(x) = P(X \leq x) &= P(-\lambda^{-1} \ln(1 - Y) \leq y) \\ &= P(Y \leq 1 - e^{-\lambda x}) \\ &= 1 - e^{-\lambda x} \end{aligned} \tag{3-23}$$

$$F'(x) = f(y) = \begin{cases} \lambda e^{-xy} & \text{for } y > 0 \\ 0 & \text{for } y \leq 0. \end{cases} \tag{3-24}$$

Since 1 - y is distributed the same way as y, exponentially distributed values of x may be obtained simply by letting $x = (1/\lambda)(\ln y)$ where y is a random number between 0 and 1.

3.8 CALCULATION AND PLOTTING OF AVERAGE ISOPOTENTIALS

The constant head boundaries shown in Figure 3-2 should in fact produce a constant average gradient in a fractured sample which behaves like an equivalent porous medium. The program, PCTOUR has been developed to locate and plot these average isopotentials.

The program LINEL calculates the head at each fracture intersection or endpoint (i.e. at each node). Given the value of the isopotential of interest, PCTOUR checks the endpoints of each fracture segment (element) to see if the head at one endpoint is below the isopotential value and the other is above the value. If this is the case, PCTOUR does a linear interpolation to find the point on the fracture where the isopotential crosses the fracture segment. For each isopotential all the points where the particular value of head is found are plotted. The x- and y-axes are defined such that the x-axis is in the direction of the gradient and the y-axis is perpendicular to the gradient. PCTOUR goes on to calculate the average x-coordinate of the points found as described above and plots a line parallel to the y-axis through this point. The standard deviation of the points from the line is also calculated. For the usual head difference of 1.0 cm across the flow region, the 0.75 cm,

0.5 cm, and the 0.25 cm average isopotentials are usually plotted. For a homogeneous anisotropic medium, these isopotentials should be equally spaced. The more nearly homogeneous the system is, the smaller the standard deviation should be, but this is not a necessary condition for a medium to have an equivalent porous medium permeability.

3.9 VERIFICATION OF THE CONDUCTIVITY MEASUREMENT

Fracture systems of known theoretical conductivity were tested to verify the numerical method of permeability measurement. The conductivity of fracture systems with infinitely long fractures is known from the theory developed by Snow (1965) and others. Because of the physical basis of this fracture model, we could only examine finite pieces of such fracture systems. The infinite fractures are seen in a finite model as fractures which transect the entire model. Fracture systems with two sets of parallel, evenly spaced, equal aperture fractures were tested to avoid problems of representativeness as much as possible. Effort was concentrated on fracture sets of equal apertures 30° apart in order to study an anisotropic case. The results of these tests are presented here.

Figure 3-6 is the generation region used to obtain all the subsequent flow regions given in Figure 3-7 and discussed below. The spacing of the fractures in these meshes is 10 cm. The apertures are all 0.1 cm. Arrows on the figure show the direction of the gradient and the direction of the conductivity measurement. Due to the symmetry of this example conductivity measurements were only made for angles of rotation every 15° from $\alpha = 0°$ to $\alpha = 105°$. Values of $1/\sqrt{K_{xx}(\alpha)}$ were plotted on polar coordinate paper and compared with the theoretical ellipse (Figure 3-8).

In all, agreement between theoretical and numerical results is good. The differences in values can be attributed to the finite nature of the numerical model. Conductivity in the model is calculated with the equation

$$K_{xx}(\alpha) = \frac{q_x(\alpha)}{\nabla\phi L}, \tag{3-25}$$

where the dimensions of the flow region are LxL. To be exactly equal to the theoretical results, L would have to be an even multiple of the component of

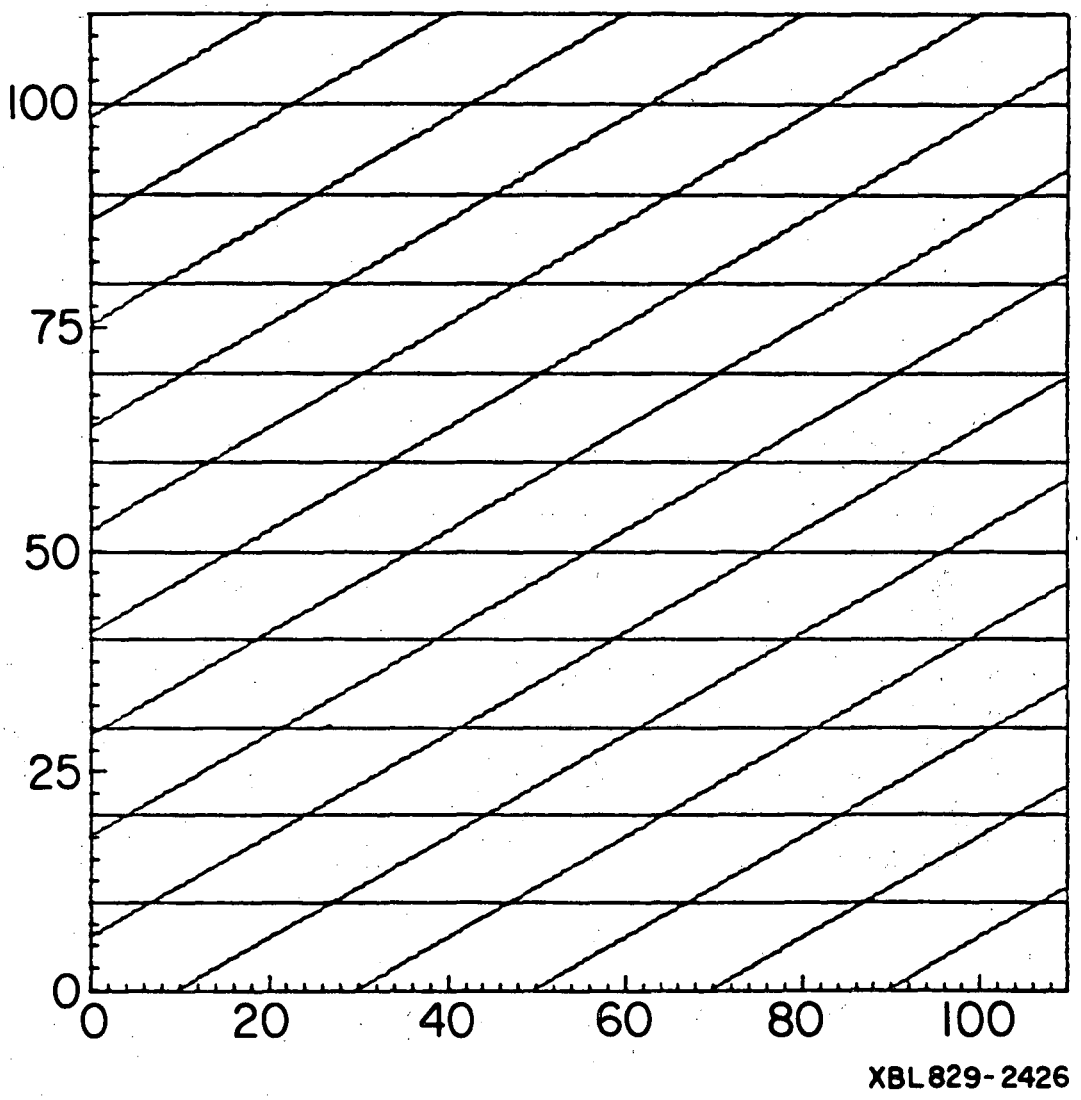

Figure 3-6. Generation Region for "Infinite", Equally Spaced Fractures 30° Apart

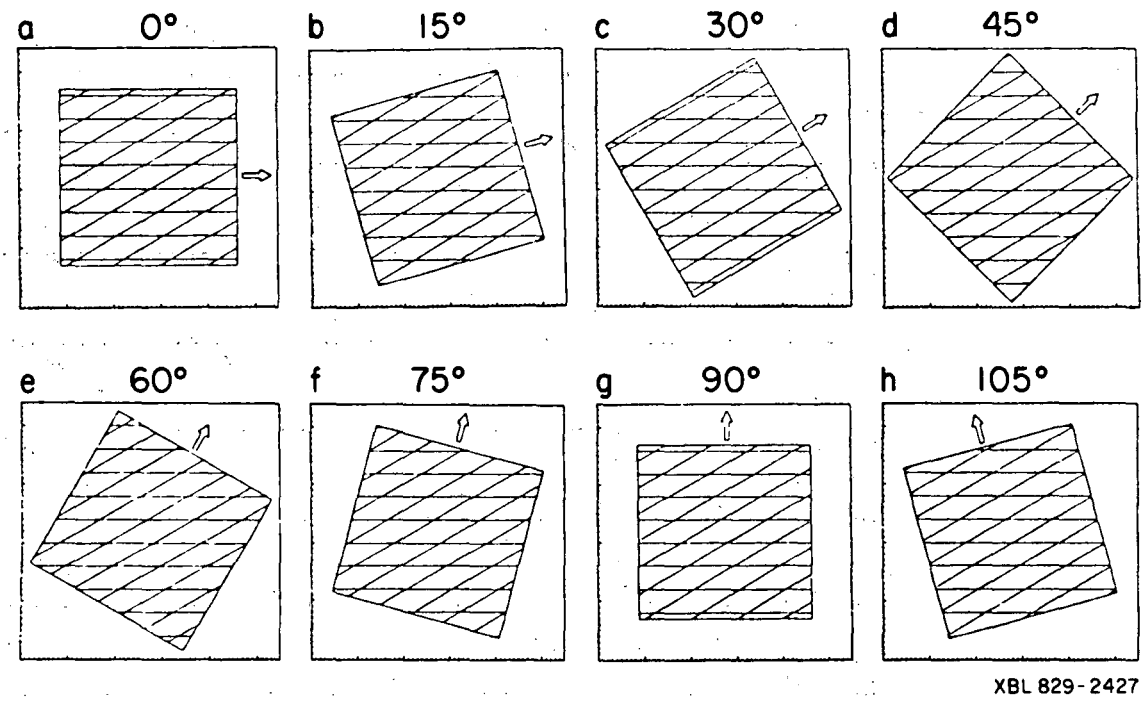

Figure 3-7. Flow Regions Taken from the Generation Region of Figure 3-6

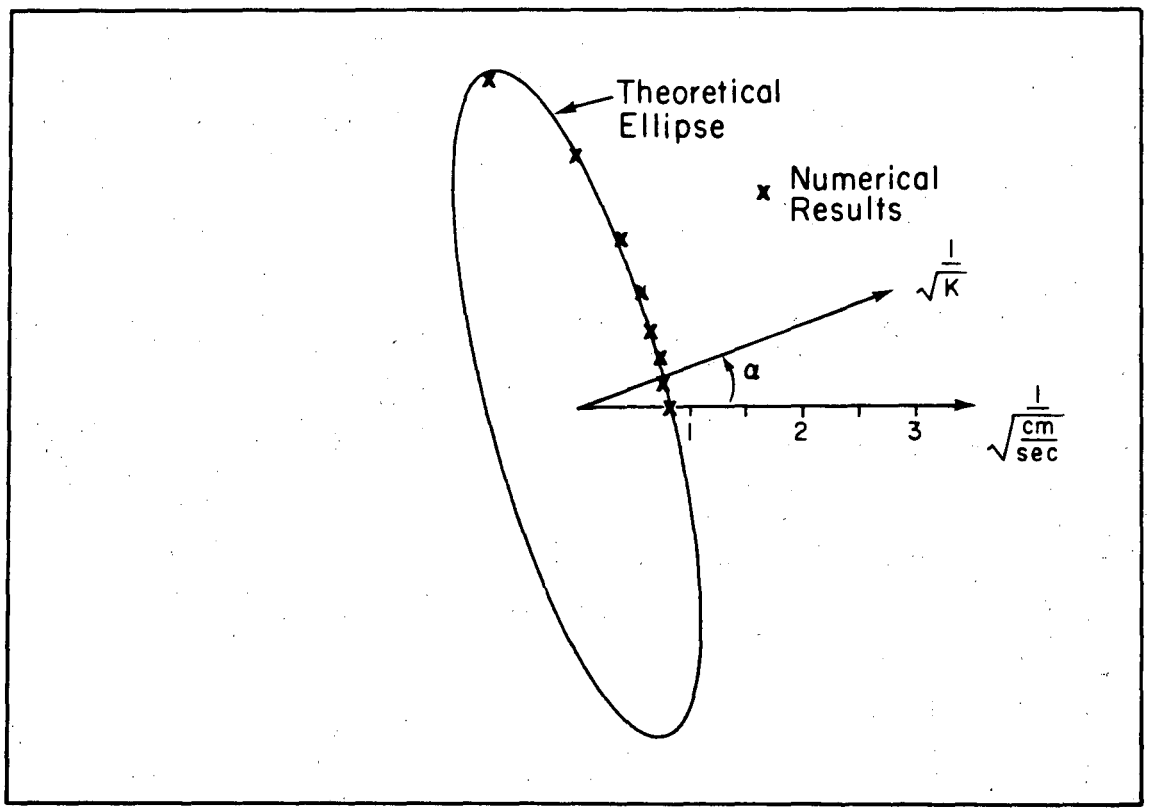

XBL 8010-2850A

Figure 3-8. Comparison Between the Theoretical Permeability Ellipse and the Numerical Results for "Infinite Fractures" Shown in Figures 3-6 and 3-7

spacing of the fractures perpendicular to the gradient for every direction of measurement. This can only occur for all sets and all rotations in the limit as L approaches infinity. Since L is arbitrary, the larger the sample or the closer the spacing, the smaller the deviation should be. In order to check this trend, fractures with different spacing were tested. Results are presented in Table 3-1. Note that the conductivity of a set of fractures with spacing of 5 is twice that of spacing of 10. In order to compare results, K/2 has been given for spacing of 5. Results for a spacing of 5 are on the average slightly better than for a spacing of 10 as expected.

Table 3-1. Comparison of Theoretical and Numerical Results for "Infinite" Fractures (Hydraulic Conductivities in cm/s)

Angle of Rotation	Spacing = 10 cm				Spacing = 5 cm	
	Theoretical		Numerical		Numerical	
α	K_{11}	K_{12}	K_{11}	K_{12}	$K_{11}/2$	$K_{12}/2$
0	1.4301	0.3539	1.43788	0.377431	1.4306	0.377463
15	1.5250	0.0	1.68397	~0	1.57875	~0
30	1.4301	0.3539	1.43788	0.377433	1.4306	0.377461
45	1.170	0.6129	1.22724	0.595736	1.21316	0.59576
60	0.817	0.7077	0.784133	0.704374	0.83137	0.73165
75	0.46335	0.6129	0.441600	0.610839	0.480139	0.59676
90	0.204	0.3539	0.217907	0.326920	0.217951	0.354179
105	0.109	0.0	0.112750	~0	0.112774	~0

3.10 EXAMPLES OF RANDOM FRACTURE SYSTEMS

In order to check the various functions of the numerical model, a random example was chosen for conductivity testing. Table 3-2 gives the statistics used to generate the fractures. The generation region was 110 x 110 cm.

Three different random realizations were generated (Figures 3-9a, 3-10a, 3-11a). Flow regions 75 x 75 m at rotation angle 0° were examined in each of these realizations (Figures 3-9b, 3-10b, 3-11b). The three flow regions had characteristics given in Table 3-3. In comparing the flow regions with their respective generation regions, note that fractures in the generation region which do not intersect any other fractures have been eliminated from the flow region.

Table 3-2. Input Parameters for the Random Example

	Parameters	Set 1	Set 2
Density	(Number of Fractures)	49	100
Orientation	Normal distribution μ, σ^2 (deg)	30, 5	60, 10
Length	Lognormal distribution μ, σ^2 (cm)	40, 10	30, 7.5
Aperture	Lognormal distribution μ, σ^2 (cm)	0.001, 0.005	0.005, 0.0001

Table 3-3. Characteristics of the Flow Regions

Network	Number of Fractures	Number of Fracture Intersections	Number of Nodes	Number of Elements
1	81	123	285	327
2	86	110	282	306
3	90	139	319	368

Boundary conditions were applied to these three flow regions such that conductivity in the x-direction was measured. That is, Sides 1 and 3 were given a linearly varying head distribution, Side 2 had a constant head of 1, and Side 4 had a constant head of 0 (see Figure 3-2). Table 3-4 gives the total fluxes through each side for each flow region. A positive sign indicates flow into the region and a negative sign indicates flow out of the region.

Examination of Table 3-4 leads to several observations. First, there is a great deal of variation between the three realizations of the same statistical fracture population. As shown in Table 3-3, the number of fractures in each flow region varies. Thus some of the variation in flow rate is due to nonergotic sampling. Recall that under the boundary conditions used, for an ideal porous medium the flux in the x-direction (Side 2 to Side 4) is

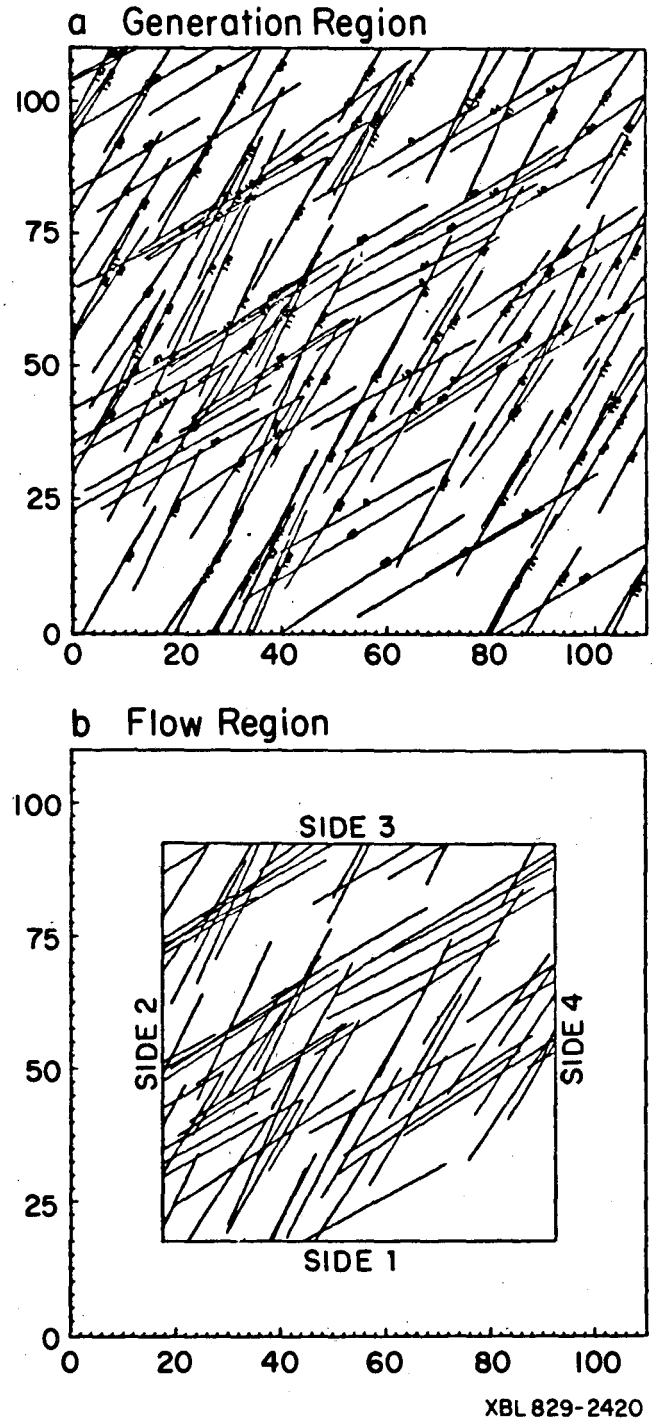

Figure 3-9. Generation and Flow Regions for Network 1

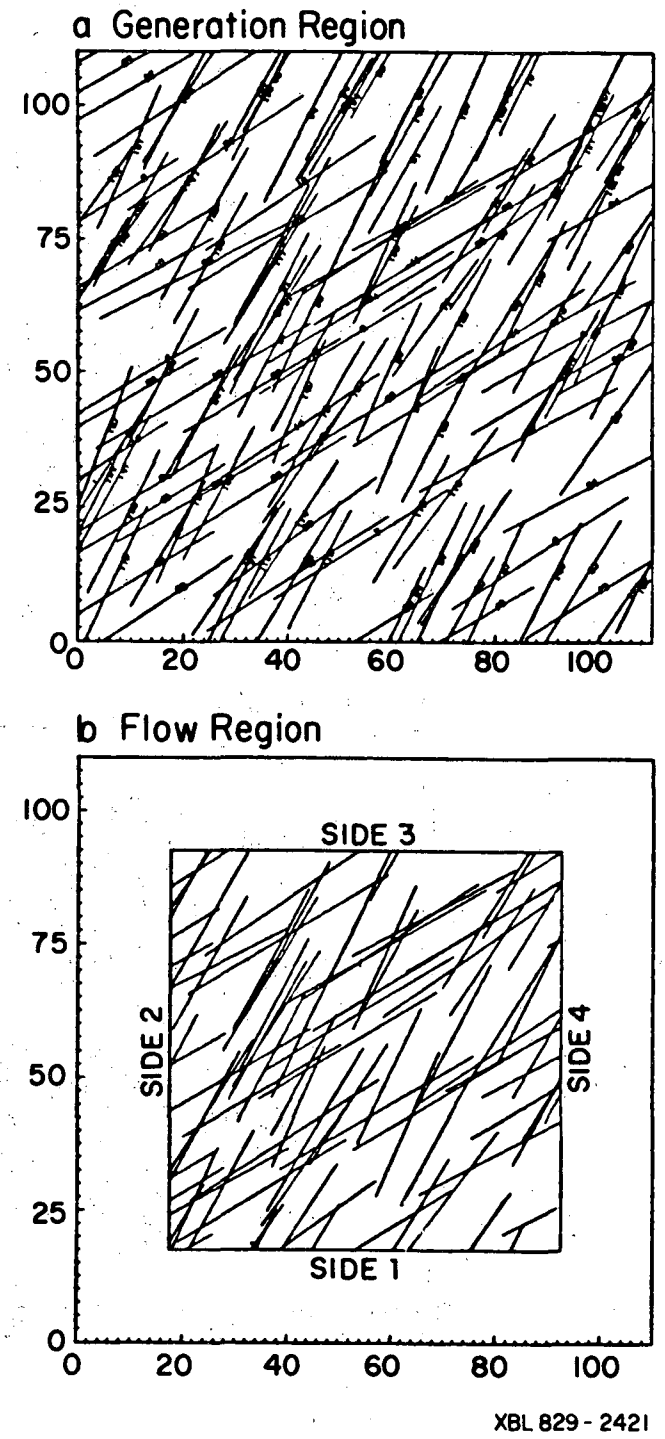

Figure 3-10. Generation and Flow Regions for Network 2

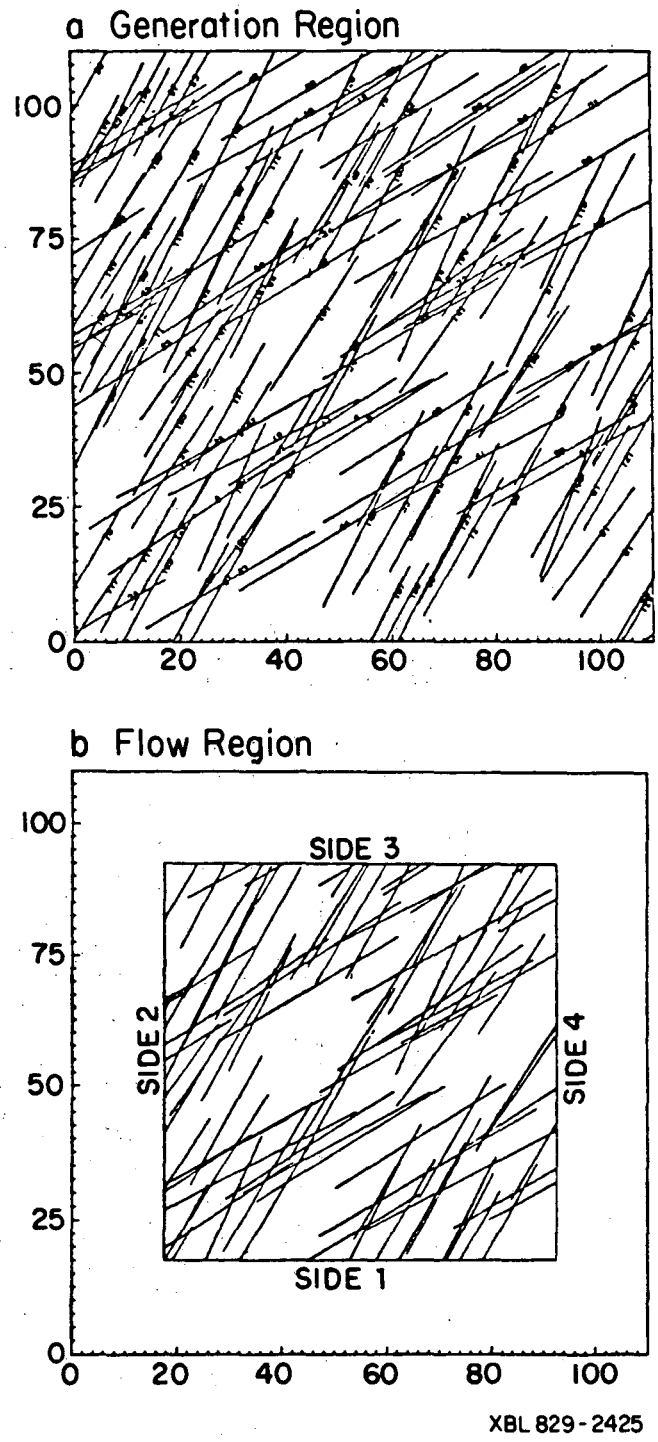

Figure 3-11. Generation and Flow Regions for Network 3

numerically equal to the conductivity. Table 3-4 shows that the flux into Side 2 does not equal the flux out of Side 4. The sum of the fluxes through all sides, however, is zero as expected. These samples are clearly not behaving like porous media, since in anisotropic porous media under the chosen boundary conditions the flux on opposite sides would be equal.

Table 3-4. Total Fluxes (cm^3/s) for the Three Random Realizations

Network	Σ Fluxes Side 1	Σ Fluxes Side 2	Σ Fluxes Side 3	Σ Fluxes Side 4
1	3.13402E-19	4.41796E-7	-4.41384E-7	-4.11388E-10
2	-3.3926 E-10	2.00821E-5	-2.00809E-5	-8.67380E-10
3	5.42390E-10	1.01927E-4	-1.01927E-4	-8.97845E-11

These sample fracture systems do not act like porous media. A more nearly continuum-type result could possibly be achieved in two ways. The relative density of the same fractures could be increased or a larger sample with the same statistics could be examined.

In order to check the functions of the numerical model, Network 3 (Figure 3-11) was chosen for further analysis of directional conductivity and the effect of sample size on permeability measurement. Flow regions 75 x 75 m at rotation angles, α, every 15° from 0° to 180° were tested (Figure 3-12). The results are given in Table 3-5.

The fact that inflow does not equal outflow on opposite sides leads to a problem in defining conductivity. If conductivity is arbitrarily defined as numerically equal to the inflow into Side 2, no information lost. Side 4 for α = 0° becomes Side 2 for α = 180°, etc. Using this convention, symmetry in the permeability plot implies that inflow does equal outflow on opposite sides.

Figure 3-13 shows the values of $1/\sqrt{K(\alpha)}$ for Network 3 plotted on polar coordinate paper where $K(\alpha)$ is defined in terms of flux across Side 2. The results clearly do not plot as an ellipse; nor are they symmetric. For certain angles of rotation (e.g., 75°, 90°) the value of $1/\sqrt{K(\alpha)}$ becomes very large and goes off the scale of the graph. For these angles $K(\alpha)$ is very

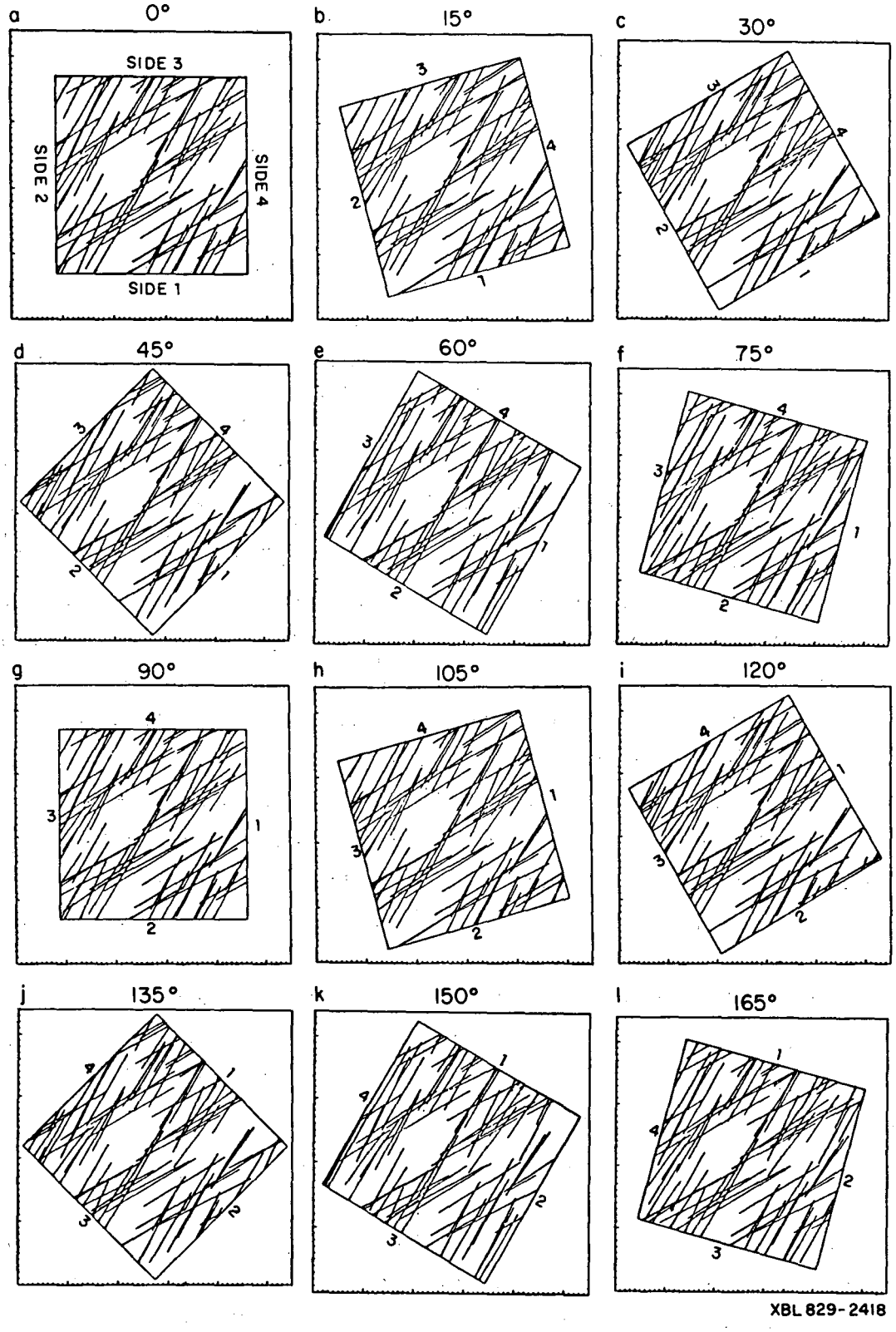

Figure 3-12. Flow Regions from Network 3 Rotated from 0° to 180°

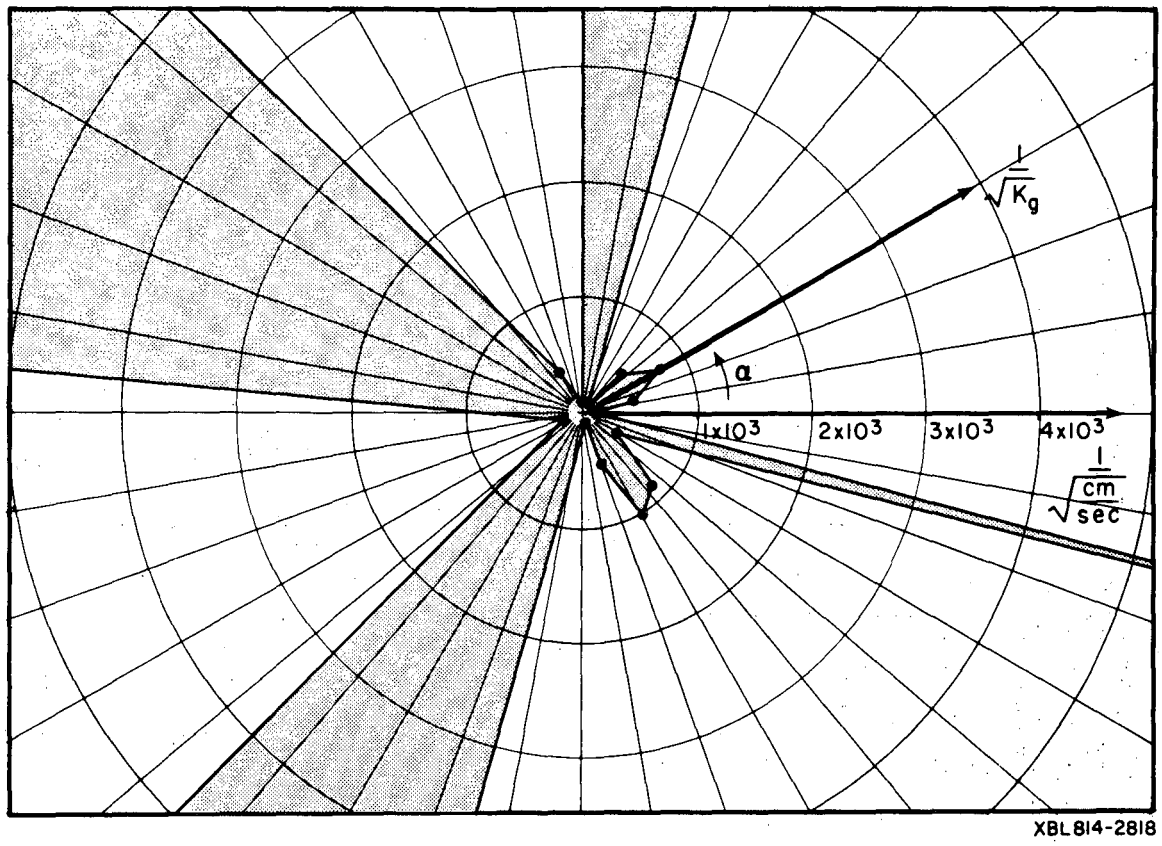

Figure 3-13. Values of $1/\sqrt{K(\alpha)}$ Plotted on Polar Coordinate Paper for Network 3

Table 3-5. Resulting Fluxes (cm^3/s) for the Random Case

Angle of Rotation	Σ Fluxes Side 1	Σ Fluxes Side 2	Σ Fluxes Side 3	Σ Fluxes Side 4
0	5.42390E-10	1.0927 E-10	-1.01927E-04	-8.97845E-11
15	1.22374E-04	4.74181E-06	-4.74124E-06	-1.22375E-04
30	1.02261E-05	1.59838E-05	-1.59731E-06	-1.02271E-05
45	-1.15375E-12	4.39136E-06	-4.38238E-06	-8.97228E-09
60	-7.40427E-11	1.56620E-04	-1.56612E-04	-8.02968E-09
75	-1.08876E-10	6.93567E-10	7.46410E-09	-8.04880E-09
90	-9.88001E-11	6.83398E-10	1.71904E-04	-1.71905E-04
105	-1.17851E-04	1.17851E-04	4.17830E-06	-4.17789E-06
120	-5.76379E-06	5.76347E-06	9.17211E-07	-9.16885E-07
135	7.36028E-09	4.25565E-13	1.39285E-06	-1.40021E-06
150	1.39114E-09	2.65264E-11	8.45053E-06	-8.45195E-06
165	2.29966E-09	6.02192E-11	-3.04834E-10	-2.05505E-04
180	1.01927E-04	8.97845E-11	-5.42392E-10	-1.01927E-04

small because there is essentially no hydraulic connection between Sides 2 and any other side. This cannot be completely confirmed visually from the plots of these flow regions because aperture has not been included in the figures. Although isopotentials have not been plotted for these samples, it is fairly certain they will not be linear.

If we define K_{yx} as numerically equal to the flow into or out of Side 3, then K_{xy} is the flow into or out of Side 1 when the flow mesh is rotated 90°. K_{xy} should equal K_{yx} if K_{ij} is symmetric. Examination of Table 3-5 confirms again that no symmetry is present.

The tests described above show clearly that the sample chosen did not have an equivalent porous medium symmetric conductivity tensor. As further proof of the nonhomogeneous nature of the sample, flow regions of different sizes were extracted and tested. All the flow regions were at 0° rotation. Flow regions from 25 cm x 25 cm to 75 cm x 75 cm were tested (Figure 3-14). Results are given in Table 3-6. Conductivity varies by orders of magnitude from sample to sample, again indicating marked departure from continuum behavior.

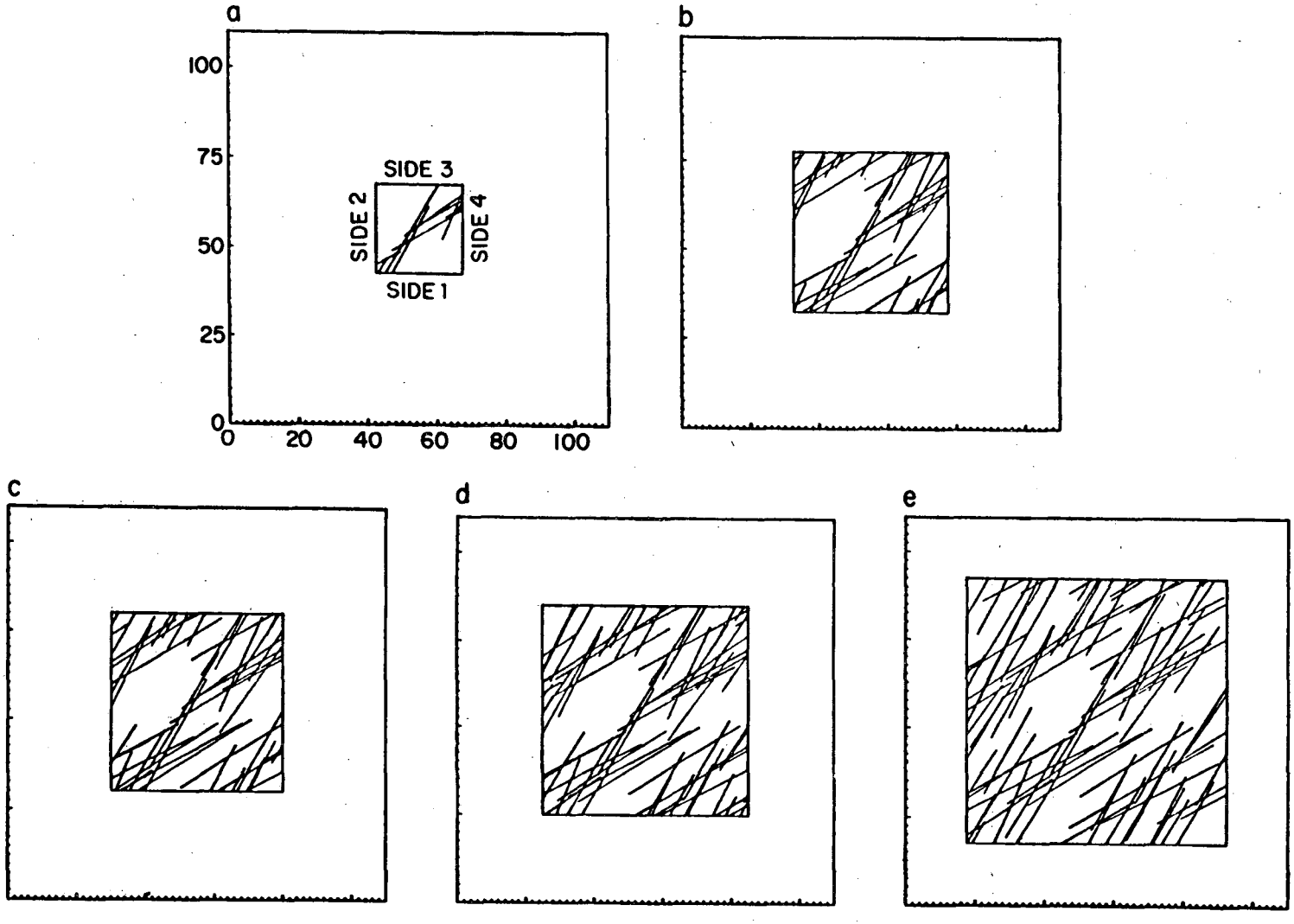

XBL829-2445

Figure 3-14. Flow Regions of Increasing Size from Network 3

Table 3-6. Resulting Fluxes (cm^3/s) for Flow Regions of Different Sizes

Size of Flow Region (cm)	Σ Fluxes Side 1	Σ Fluxes Side 2	Σ Fluxes Side 3	Σ Fluxes Side 4
25 x 25	2.23427E-05	4.84085E-17	-2.23421E-05	-5.74141E-10
45 x 45	6.10129E-04	3.10717E-06	-3.10003E-06	-6.10136E-04
50 x 50	-3.04850E-09	2.18729E-06	-2.18409E-06	-1.53793E-10
60 x 60	4.58843E-04	2.70645E-08	-2.29660E-08	-4.58841E-04
75 x 75	5.42390E-10	1.01927E-04	-1.01927E-04	-8.97845E-11

4 FRACTURE GEOMETRY STUDIES

A series of preliminary numerical experiments were run to illustrate some of the key effects of fracture geometry on fracture system permeability. These experiments show trends in behavior. They mainly serve the purpose of confirming behavior that is intuitively expected. Increase in fracture density increases permeability. Permeability decreases with increase in the spread of the aperture distribution or decrease in the spread of the orientation distribution. The behavior of the fracture system is different depending on the scale of measurement. These experiments are detailed below.

4.1 EFFECT OF FRACTURE DENSITY

In order to see how the density of fractures affects the hydraulic behavior, the following three examples were analyzed. All three examples consist of two fractures sets with the uniform characteristics given in Table 4-1. Fracture centers were randomly located.

Table 4-1. Fracture System Characteristics for the Density Study

	Uniform Orientation	Uniform Length (cm)	Uniform Aperture (cm)	Number of Fractures
SET 1	30°	10	0.001	60
SET 2	60°	20	0.002	40

Figures 4-1, A, B and C show the three fracture meshes studied. The difference between A, B and C is that the same fractures have been squeezed into succesively smaller areas with successively greater fracture densities. Figure 4-1A is 40 x 40 cm, 4-1B is 30 x 30 cm and 4-1C is 25 x 25 cm. Thus the number of fracture intersections and, therefore, the number of hydraulically active fractures increases as the fracture density increases. Figures 4-1D, E and F show the corresponding permeability "ellipses" for fracture systems 4-1A, B and C, respectively. The rotated flow regions used to measure permeability in each case were as large as possible.

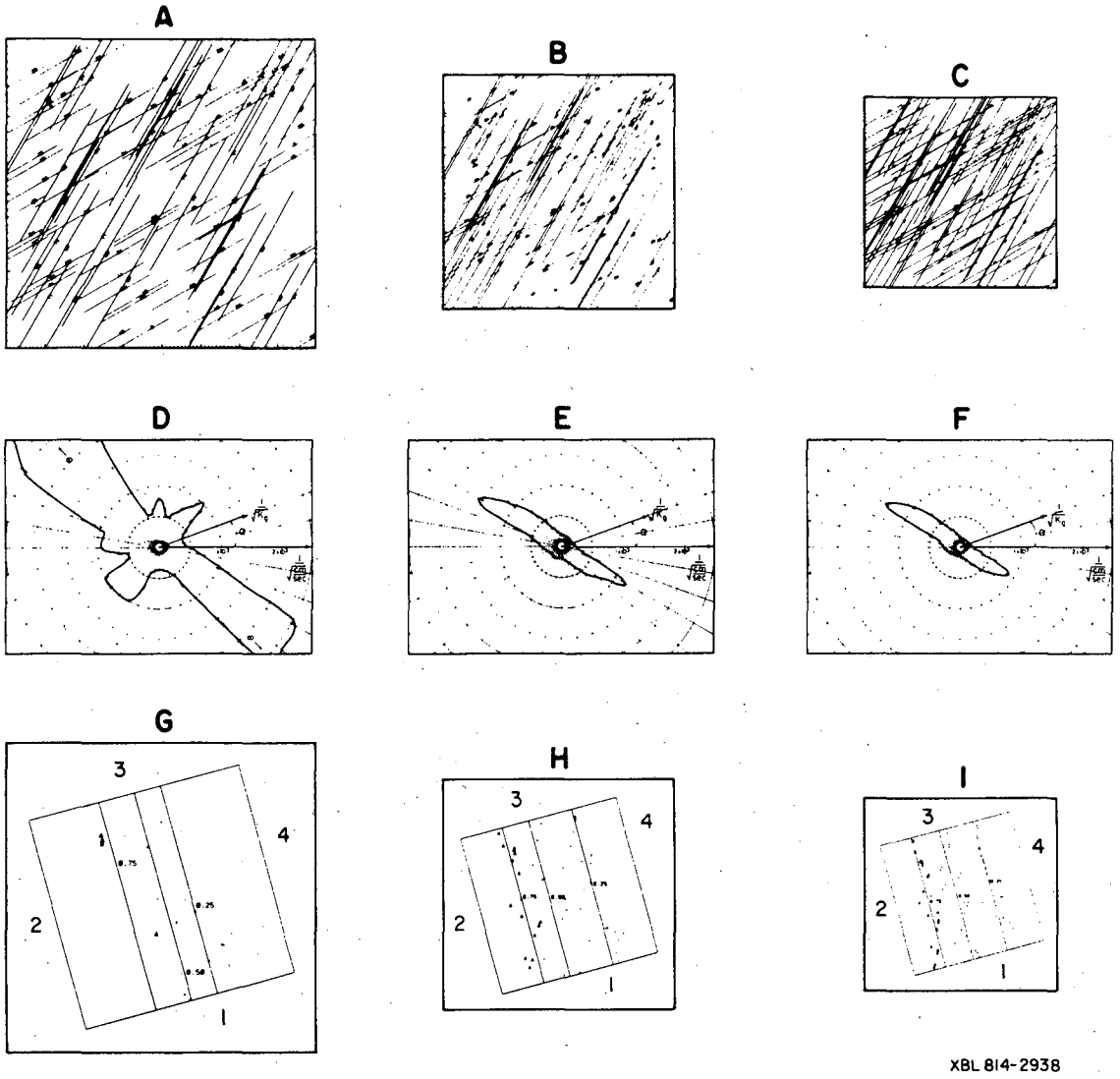

Figure 4-1. Fracture Systems of Increasing Density

Comparing the plots from left to right in order of increasing density, a significant improvement in the ellipticity of the plots is evident. The illustration shown in Figure 4-1D is irregular and nonsymmetric. The value of $1/\sqrt{K}$ goes to infinity for several directions of measurement. Where the plot goes to infinity the permeability in that direction is zero. This happens for a given direction of measurement when no conducting fractures intersect Side 2 since the flow into Side 2 is always used to define permeability. For Figure 4-1D this occurred when Side 2 was roughly parallel to fracture set 2. It should be noted that the choice of a slightly larger or smaller flow region may have eliminated this condition. For Figure 4-1E, the fracture density increased to the point where Side 2 always intersects some conducting fractures. Thus no zero permeability directions were found. The ellipse is fairly regular but not symmetric, especially in the direction of minimum principal permeability. Figure 4-1F is slightly improved in this regard. The size of the ellipses decreases from left to right as expected, since denser fracture systems are more permeable. The direction of minimum and maximum permeability is roughly the same in all three plots.

Figures 4-1G, H and I show average isopotentials for flow regions at 15° of rotation. For other rotations, the plots are similar. The locations on the fractures where heads are 0.75, 0.50 and 0.25 are plotted. For a continuum, the isopotentials should be equally spaced and all the points should lie on the lines. For Figure 4-1G, very few points are plotted because few fractures actually conducted water. The spacing of the average isopotentials improves from G to I. The scatter of the plotted points also decreases in this direction.

In summary, the hydraulic behavior of the fracture systems becomes more like that of a homogeneous, anisotropic material as fracture density increases. This is an expected result. However the trend in hydraulic behavior was augmented by the design of the experiment. The same fractures were squeezed into increasingly smaller areas to increase the density. As a result, in the more dense examples many more fractures transect the flow region. More conductivity is achieved for this reason alone. In later examples, the size of the flow region is scaled to a constant multiple of the fracture length to eliminate this effect.

4.2 EFFECT OF APERTURE AND ORIENTATION DISTRIBUTION

The effect of distributing aperture or orientation is illustrated in Figure 4-2. The fractures shown in Figure 4-2 are exactly the same as the fractures in Figure 4-1B. Consequently, 4-2E and H are the same as 4-1E and H, respectively. Figure 4-2A is the same as 4-2B except that aperture has been distributed lognormally. Figure 4-2A looks exactly like Figure 4-2B because aperture is not shown on the plot. Figure 4-2C is the same as 4-2B except that orientation has been distributed normally. All other parameters are uniform. The permeability plot is the most skewed for the case where aperture was allowed to vary (Figure 4-2D). In this case not all the conductors are of equal strength. For some directions of measurement, notably at $\alpha = 135°$, the hydraulic connections to Side 2 were evidently through fractures with lower than average aperture. At $\alpha = 30°$, higher than average aperture fractures were intersected by Side 2. The flux through a fracture is proportional to b^3. Therefore, the measured flux through Side 2, which is used to define the permeability, is greatly affected by the size of the fractures intersected by Side 2. Fracture meshes 4-2A and 4-2B have the same number of fracture intersections, but because there is a great variation in the conductivity of the individual fractures of 4-2A the results shown in Figure 4-2D are more irregular than the results in Figure 4-2E.

Varying the orientation of the fractures improves the hydraulic behavior. In this case, the number of fracture intersections increases because fractures of the same set are no longer parallel and now can intersect. The degree of fracture interconnection is thus increased and the permeability plot becomes more symmetric and regular.

The isopotential plots in Figures 4-2G, H and I show slightly improved spacing and decrease in scatter from left to right. In general, fracture systems with distributed orientations behave more like homogeneous porous media than do systems with uniform orientations. Fracture systems with distributed apertures behave less like homogeneous media than uniform aperture systems.

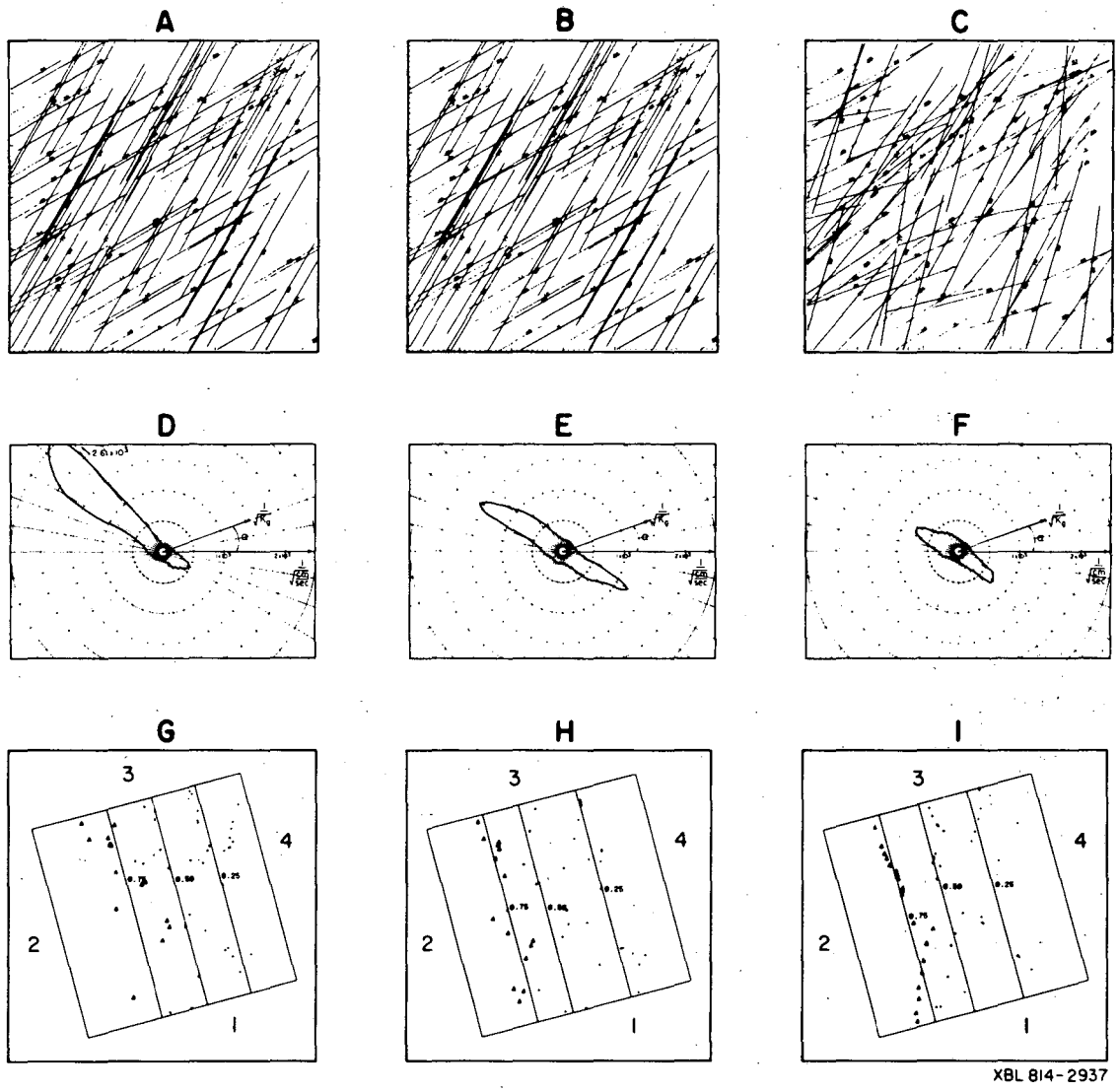

Figure 4-2. Fracture Systems with Variation of Aperture or Orientation

4.3 SCALE EFFECT

The effect of fracture length on the permeability of a fracture system is very sensitive to the scale of measurement. At a scale of measurement smaller than the length of the fractures, the system may act like a system of infinite fractures relative to the chosen boundaries. At this small scale, the hydraulic behavior may become like that of a homogeneous, anisotropic medium. However, as the scale of measurement increases, the fractures no longer transect the entire measurement volume. The hydraulic behavior of the system may become less regular. In this case, only one criterion for equivalent porous medium behavior is met by the small scale volume; the permeability plots as an ellipse, but the results are still sensitive to volume change.

In order to illustrate the scale effect, a system of fractures was chosen which consisted of two perpendicular sets of fractures all with the same aperture and length. The orientation distribution about the mean for each set was the same. The fracture system generated is shown in Figures 4-3A and 4-4A. Theoretically, two orthogonal sets with equal characteristics should have a circular permeability plot. Random variations from the circle can only be due to insufficient density of fractures or insufficient sample size.

Figures 4-3B - L show flow regions of increasing size for which permeability measurements were made. The flow regions at 0° rotation are shown for illustration. Flow regions at every 15° rotation were used for analysis. Figures 4-4B through 4-4L show the corresponding permeability ellipses for the corresponding flow regions in Figure 4-3.

For Figures 4-4B, C and D, the results are erratic. Only a few fractures are included in each sample. In 4-4B, only the vertical set is represented and in C and D there is only one fracture from the horizontal set. The type of fractures included in the sample is a random function of the location of the flow region. If the flow region had been taken in the upper right-hand corner, the result might have been the opposite with a greater preponderance of horizontal fractures. Although in these three figures most of the fractures transect the flow region, for certain values of the rotation angle, no fractures intersect Side 2. The permeability in this direction, therefore, is zero and $1/\sqrt{K_g}$ is infinite.

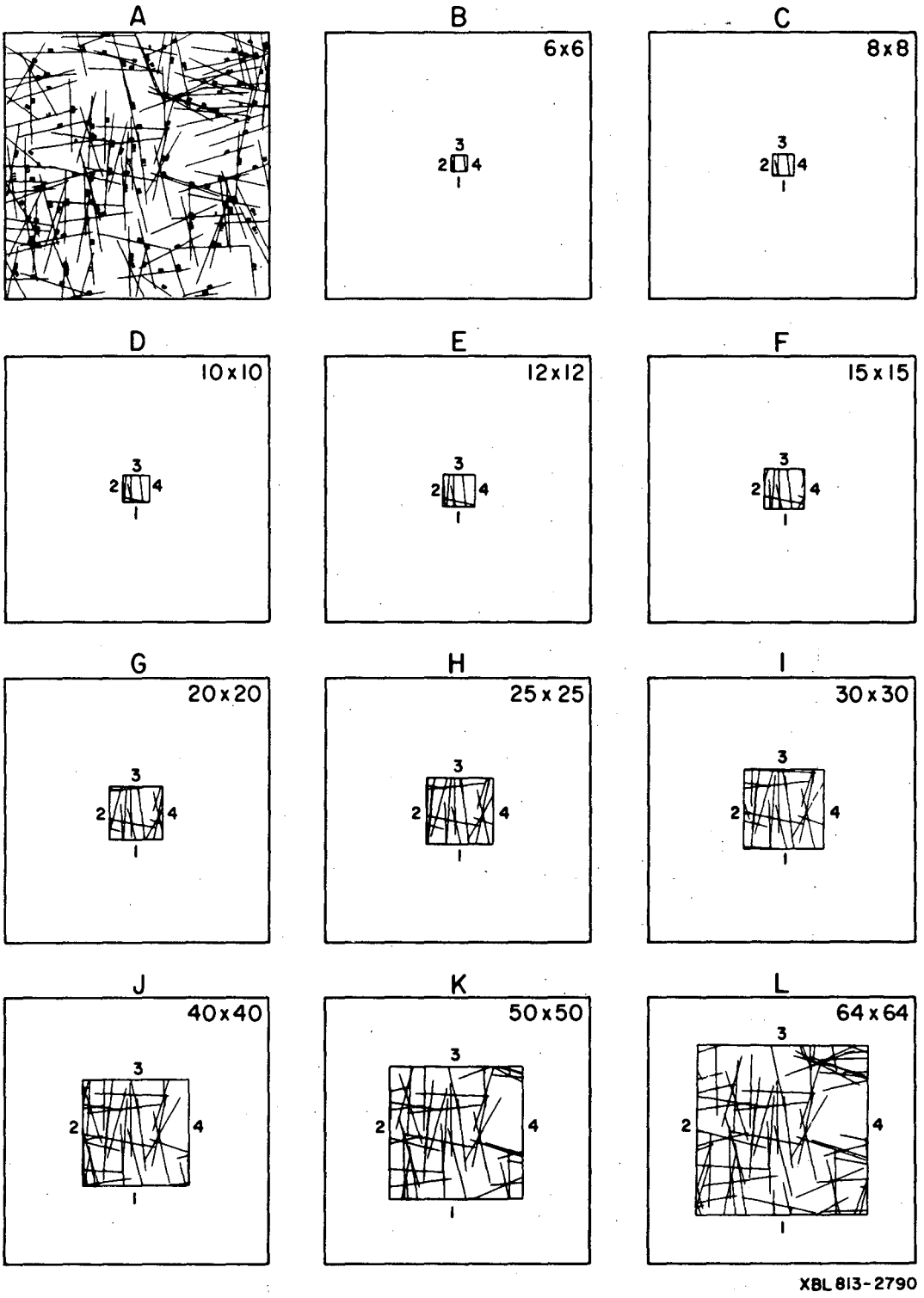

Figure 4-3. Fracture Samples of Increasing Size

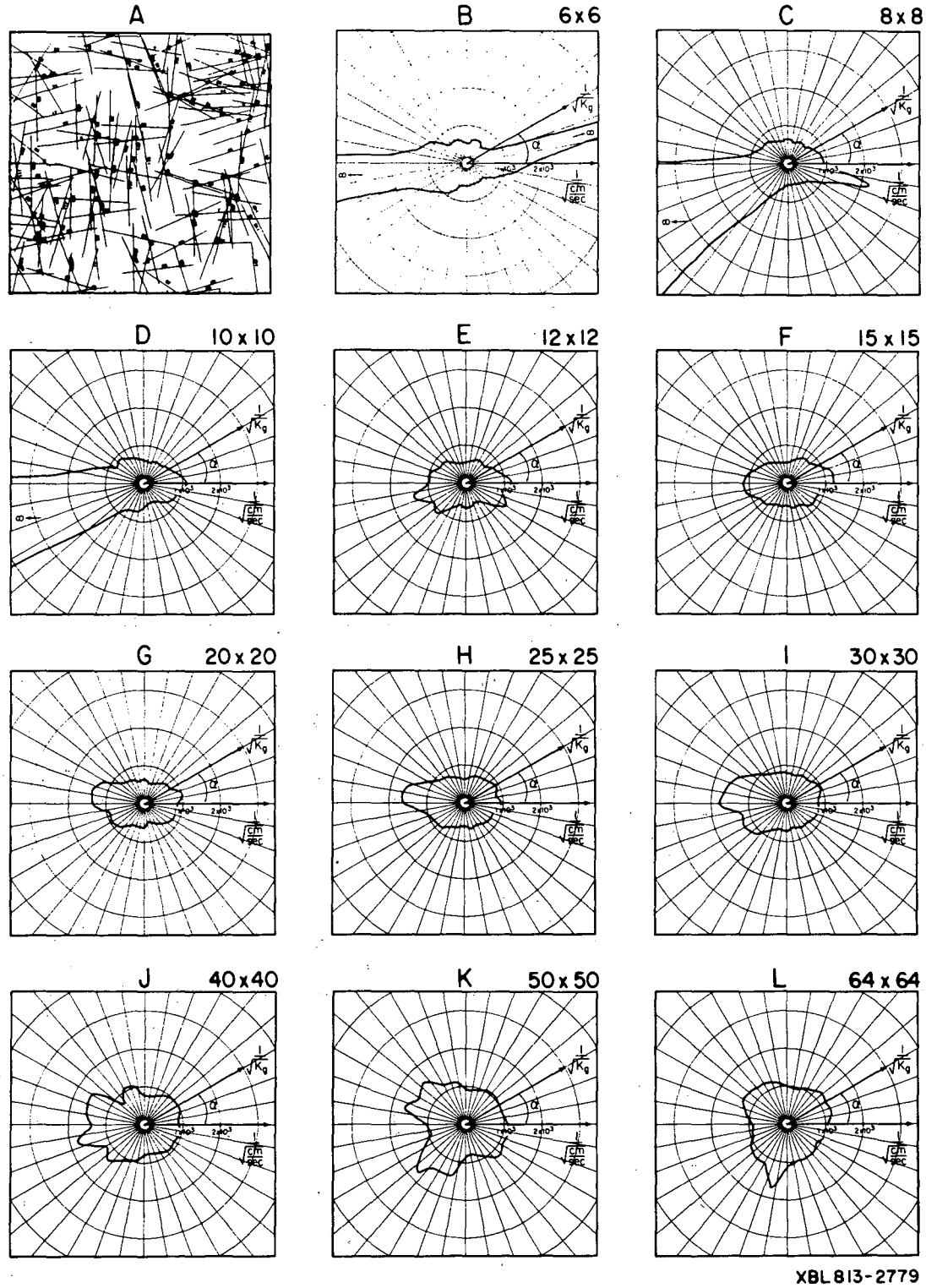

Figure 4-4. Permeability Plots for Fracture Samples of Increasing Size

In Figures 4-3E and 4-4E, enough fractures have been included to provide flow through Side 2 for any rotation. In 4-4F, the larger 15 x 15 cm mesh has produced a fairly regular symmetric ellipse. Figure 4-3F shows that for this flow region size many of the fractures transect the entire flow region. However the ellipse in Figure 4-3F is not circular, as expected. Figures 4-4G through 4-4L show how the form of the permeability ellipse is changed as the flow region is further increased in size. As more fractures are gradually added to the sample, the effect of each fracture is to deform the ellipse in some way.

Although Figure 4-4F shows a seemingly regular ellipse, this is misleading because Figure 4-3F does not include a representative sample of the fracture population. Figure 4-3L is the largest sample size which could be studied by these programs on the CDC 7600. It is a better sample and Figure 4-4L does have a more circular shape. However, Figure 4-4L still shows some perturbations in hydraulic behavior. The permeability plots may improve somewhat with a further increase in sample size. This can be seen by noticing that there is still a large proportion of truncated fractures in the 64 x 64 cm mesh of Figure 4-4L. To obtain a good statistical sample of fracture length in the flow region, the flow region should be large compared to the fracture length. In this way a relatively small number of fractures are truncated. Samples larger than 64 x 64 cm would be necessary for determining if the perturbations in the permeability plot are a function of the sample size or inherent in the fracture population.

4.4 CONCLUSIONS

This chapter presents some simple examples which illustrate how various fracture geometry parameters affect bulk permeability. All of the results conform to intuition. Increasing the standard deviation of aperture creates a more heterogeneous medium which behaves less like a homogeneous porous medium. Increasing the standard deviation of orientation creates more connections between fractures and thus increases the permeability and makes the behavior more like that of a porous medium. The results of permeability measurements are determined by the extent of the fractures relative to the scale of measurement. Measurements made on scales very small relative to the fracture extent

are very erratic. Porous media behavior is unlikely on such a small scale. When the scale of measurement approaches the same scale as the fracture extent, porous media behavior may be observed, but it may be an artifact of the measurement technique. This is because the boundaries of the model truncate many of the fractures at both ends. All of these fractures therefore become conductors. In situ all these fractures would not be as well connected to the boundaries. Thus measurements on a scale which is the same as or smaller than fracture extent may be misleading.

The understanding of fracture system behavior illustrated in this chapter was used to design the experiments presented in Chapters 6 and 7. For these studies the programs FMG and LINEL were revised to run on the VAX/11. As such much larger problems could be handled.

5 REGRESSION ANALYSIS TO DETERMINE THE PERMEABILITY TENSOR

5.1 INTRODUCTION

In the previous chapter, directional permeability measurements were simply plotted and the resemblance of these plots to ellipses was noted in a qualitative way. Appropriate quantification of the best-fit ellipse and a measure of the goodness of fit of the data to the best-fit ellipse would be very useful for comparing the behavior of different fracture systems. This chapter gives a regression technique for calculating the components of the best-fit permeability tensor and the error associated with using the best-fit tensor as opposed to the actual measured values of directional permeability.

Directional permeability measurements of random fracture systems are made as previously described. From the measured values of directional permeability, $K_g(\alpha)$, we wish to determine the three components of the permeability tensor, K_{ij}, which best fit these measurements. We also wish to determine the principal values (eigenvalues) and principal axes (eigenvectors) of the permeability tensor. Further, we wish to find a quantitative measure of the difference between the measured values, $K_g(\alpha)$, and the best-fit values.

Recall that for an ideal anisotropic homogeneous porous medium directional permeability, K_g, measured in the direction of the gradient α, is defined by the following equation:

$$q_i n_i = K_g J, \tag{5-1}$$

where n_i is a unit vector in the direction of the gradient, J is the magnitude of the gradient, and q_i is the specific flux. Solving Darcy's law for q_i and substituting this into Equation 5-1 gives

$$K_{ij} J_j n_i = K_g J, \tag{5-2}$$

and since $J_j/J = n_j$ we have

$$K_g = K_{ij} n_i n_j, \tag{5-3}$$

or

$$K_g = K_{11}\cos^2\alpha + 2K_{12}\cos\alpha\sin\alpha + K_{22}\sin^2\alpha, \tag{5-4}$$

where n_1 and n_2 are direction cosines and $n_1 = \cos\alpha$, $n_2 = \sin\alpha$.

If $1/\sqrt{K_g}$ is plotted in the direction α (the direction of the gradient), then $n_1 = \cos\alpha = x\sqrt{K_g}$ and $n_2 = \sin\alpha = y\sqrt{K_g}$. Equation 5-4 becomes

$$K_g = K_{11}x^2K_g + 2\,K_{12}xyK_g + K_{22}y^2K_g\ , \tag{5-5}$$

$$1 = K_{11}x^2 + 2K_{12}xy + K_{22}y^2, \tag{5-6}$$

$$1 = K_{ij}x_ix_j \qquad \text{where } x_i = \begin{Bmatrix} x \\ y \end{Bmatrix}. \tag{5-7}$$

Equation 5-7 is the quadratic form of the permeability ellipse equation.

If each measurement of $K_g(\alpha)$ can be considered an independent measurement of the value of K_{ij}, then methods of statistics can be used to estimate the parameters K_{11}, K_{12} and K_{22}. The statistical technique can be used on measurements of $K_g(\alpha)$ from different, equally incremented directions on one fracture pattern or the combined measurements from any number of fracture pattern realizations.

5.2 DISTRIBUTION OF $K_g(\alpha)$

In a random fracture pattern, the measured values of $K_g(\alpha)$ will not all plot on a single, unique ellipse (Figures 5-1). In order to use all of the individual measurements to derive a single, most representative set of parameters for the permeability tensor, we must assume that each measurement is independent and similarly distributed. Figure 5-1 shows an example of a set of measurements, $K_g(\alpha)$, and a possible ellipse with parameters K_{11}, K_{12} and K_{22}. Each measurement can be assumed to be distributed about a different mean which is a point on the ellipse determined by α. Therefore, the value of the mean for each measurement depends on α. Thus, each $K_g(\alpha)$ is considered to be distributed with the same form but each has a different or shifted mean. The variance of each $K_g(\alpha)$ is assumed to be identical. In this way, all the measurements are considered as one population.

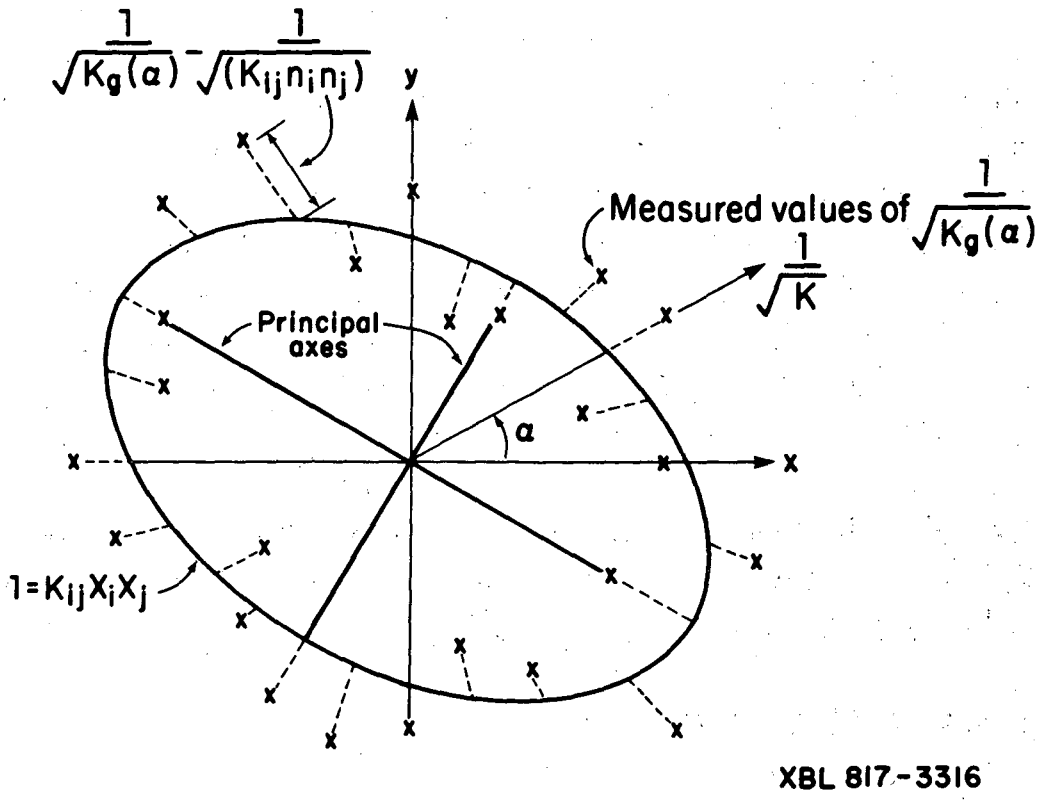

Figure 5-1. Example of a Set of Directional Permeability Measurements Plotted as $1/\sqrt{K_g}$ in Polar-Coordinates

It would be very useful to be able to define a likely distribution function for $K_g(\alpha)$, but this is not easily done. The normal distribution does not match the data because $K_g(\alpha)$ can never be less than zero. A lognormal is not proper because the probability of $K_g(\alpha) = 0$ is finite, not zero. Exponential, Gamma and Beta distributions also are not suitable. A normal distribution truncated at $K_g(\alpha) = 0$ is a likely choice. Unfortunately, assumption of this distribution leads to a contradiction with the basic assumption that all the measurements are members of the same distribution. At each angle α, the mean value of the distribution is different. However, since all the distributions are truncated at zero, the difference between the mean value and the truncation limit is different for each value of α. This means that each measurement must be a member of a different, truncated normal distribution and not just a shifted one as required in the original assumptions. Since a simple, likely, distribution form for $K_g(\alpha)$ which conforms to the basic assumptions cannot be identified, a least squares regression technique must be used to derive estimates of the parameters K_{11}, K_{12} and K_{22}.

5.3 REGRESSION TECHNIQUES

Two regression techniques are discussed here. They are based on a technique, discussed by Scheidegger (1954), which will also be briefly described. The most direct approach to finding the best-fit ellipse is to find the ellipse which minimizes the sum R_I, where

$$R_I = \sum_{n=1}^{N} \left(\frac{1}{\sqrt{K_g(\alpha_n)}} - \frac{1}{\sqrt{K_{ij} n_i n_i}} \right)^2 , \tag{5-8}$$

$$R_I = \sum_{n=1}^{N} \left(\frac{1}{\sqrt{K_g(\alpha_n)}} - \frac{1}{\sqrt{K_{11}\cos^2\alpha_n + 2K_{12}\cos\alpha_n \sin\alpha_n + K_{22}\sin^2\alpha_n}} \right)^2 , \tag{5-9}$$

where N is the number of measurements made, either on one fracture pattern or all measurements on all realizations of the fracture pattern. The difference between $1/(\sqrt{k_g(\alpha_n)})$ and $1/(\sqrt{K_{ij} n_i n_j})$ in each case is the actual distance on the permeability ellipse plot between the plotted measurement and the ellipse (Figures 5-1). Note that this distance is not the perpendicular distance, but

rather the distance along the ray inclined at the angle $\alpha°$. To minimize R we solve for K_{11}, K_{12} and K_{22} in the following equations:

$$\frac{\partial R_I}{\partial K_{11}} = \sum_{n=1}^{N} 2\left[(K_g(\alpha_n))^{-1/2} - (K_{ij}n_in_j)^{-1/2}\right](K_{ij}n_in_j)^{-3/2}\cos^2\alpha_n = 0, \qquad (5\text{-}10)$$

$$\frac{\partial R_I}{\partial K_{12}} = \sum_{n=1}^{N} 4\left[(K_g(\alpha_n))^{-1/2} - (K_{ij}n_in_j)^{-1/2}\right](K_{ij}n_in_j)^{-3/2}\cos\alpha_n\sin\alpha_n = 0, \qquad (5\text{-}11)$$

$$\frac{\partial R_I}{\partial K_{22}} = \sum_{n=1}^{N} 2\left[(K_g(\alpha_n))^{-1/2} - (K_{ij}n_in_j)^{-1/2}\right](K_{ij}n_in_j)^{-3/2}\sin^2\alpha_n = 0. \qquad (5\text{-}12)$$

These nonlinear equations are difficult to solve. An iterative method would have to be employed.

The second regression technique is to minimize the function R_{II}:

$$R_{II} = \sum_{n=1}^{N} \left[K_g(\alpha_n) - (K_{ij}n_in_i)\right]^2. \qquad (5\text{-}13)$$

In this case we are not directly regressing to the best-fit ellipse. We are finding the parameters K_{11}, K_{12}, and K_{22} which best fit the data expressed by $K_g(\alpha_n)$ in Equation 5-5. Figure 5-2 illustrates the type of three parameter curve which is fitted to the data. This curve is less easily visualized than the ellipse is but it is much simpler mathematically. There is no reason to expect the two techniques to give the same answer, but there is also no obvious physical reason to expect one technique to give a better answer than the other. As such, the second technique is pursued here.

A similar technique was used by Scheiddeger (1954). Scheiddeger minimized the function

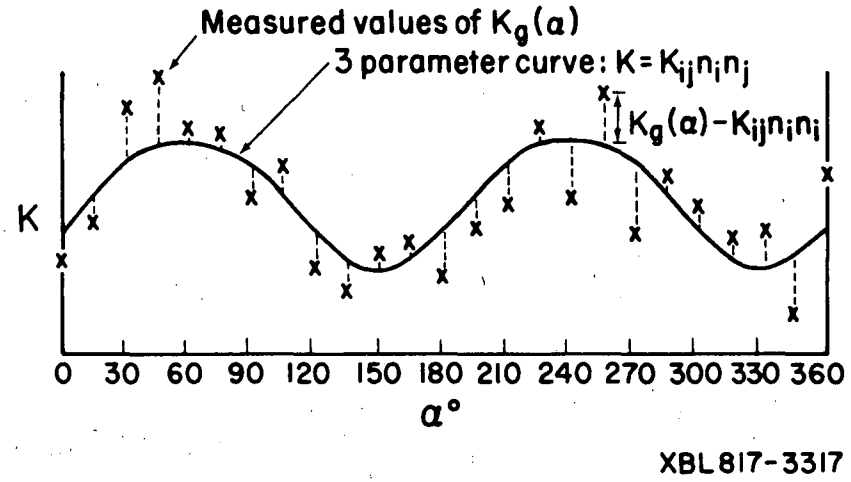

Figure 5-2. Example of a Set of Directional Permeability Measurements Plotted in Cartesian Coordinates

$$R = \sum_{m=1}^{N} \left[(K_f^1(\alpha_m))^{-1} - (K_{ij})^{-1} m_i m_j \right]^2. \tag{5-14}$$

Although not stated by Scheiddeger, this regression techniques applies to measurements of permeability $K_f(\alpha)$ made in the direction of flow. Thus, m_i is a unit vector in the direction of flow. To see this recall that permeability in the direction of flow is defined by

$$\frac{1}{K_f} = \frac{J_i m_i}{q}, \tag{5-15}$$

where q is the specific flux and J_i is the gradient.

Substituting Darcy's law we have

$$\frac{1}{K_f} = q_i (K_{ij})^{-1} \frac{m_i q_j}{q}, \tag{5-16}$$

$$\frac{1}{K_f} = (K_{ij})^{-1} m_j m_i. \tag{5-17}$$

So Equation 5-14 is effectively the same as Equation 5-13, except that in Equation 5-14, K_{ij} becomes the inverse of the permeability tensor.

5.4 SOLUTION OF THE REGRESSION EQUATIONS

The solution of the regression equations is exactly the same as the solution given by Scheidegger (1954) and is repeated here only for completeness. The equations are

$$\frac{\partial R_{II}}{\partial K_{11}} = 0 = \sum_{n=1}^{N} -2\left[K_g(\alpha_n) - K_{ij} n_i n_i\right] \cos^2\alpha_n, \tag{5-18}$$

$$\frac{\partial R_{II}}{\partial K_{12}} = 0 = \sum_{n=1}^{N} -4\left[K_g(\alpha_n) - K_{ij} n_i n_i\right] \cos\alpha_n \sin\alpha_n, \tag{5-19}$$

$$\frac{\partial R_{II}}{\partial K_{22}} = 0 = \sum_{n=1}^{N} -2\left[K_g(\alpha_n) - K_{ij} n_i n_i\right] \sin^2\alpha_n. \tag{5-20}$$

Rearranging, expanding $K_{ijn_in_j}$, and putting in matrix form we have

$$\begin{bmatrix} \sum_{n=1}^{N} \cos^4\alpha_n & \sum_{n=1}^{N} 2\cos^3\alpha_n \sin\alpha_n & \sum_{n=1}^{N} \sin^2\alpha_n \cos^2\alpha_n \\ \sum_{n=1}^{N} \cos^3\alpha_n \sin\alpha_n & \sum_{n=1}^{N} 2\sin^2\alpha_n \cos^2\alpha_n & \sum_{n=1}^{N} \sin^3\alpha_n \cos\alpha_n \\ \sum_{n=1}^{N} \cos^2\alpha_n \sin^2\alpha_n & \sum_{n=1}^{N} 2\sin^3\alpha_n \cos\alpha_n & \sum_{n=1}^{N} \sin^4\alpha_n \end{bmatrix} \begin{bmatrix} K_{11} \\ K_{12} \\ K_{22} \end{bmatrix} = \tag{5-21}$$

$$\begin{bmatrix} \sum_{n=1}^{N} K_g(\alpha_n)\cos^2\alpha_n \\ \sum_{n=1}^{N} K_g(\alpha_n)\cos\alpha_n \sin\alpha_n \\ \sum_{n=1}^{N} K_g(\alpha_n)\sin^2\alpha_n \end{bmatrix}$$

Now, if for each fracture mesh, measurements are made at equal angle intervals from 0 to 2π, all sums with only odd powers of sine and cosine drop out and the equation becomes:

$$\begin{bmatrix} \sum_{n=1}^{N} \cos^4\alpha_n & 0 & \sum_{n=1}^{N} \sin^2\alpha_n\cos^2\alpha_n \\ 0 & \sum_{n=1}^{N} 2\sin^2\alpha_n\cos^2\alpha_n & 0 \\ \sum_{n=1}^{N} \cos^2\alpha_n\sin^2\alpha_n & 0 & \sum_{n=1}^{N} \sin^4\alpha_n \end{bmatrix} \begin{bmatrix} K_{11} \\ K_{12} \\ K_{22} \end{bmatrix} =$$

$$\begin{bmatrix} \sum_{n=1}^{N} K_g(\alpha_n)\cos^2\alpha_n \\ \sum_{n=1}^{N} K_g(\alpha_n)\cos\alpha_n\sin\alpha_n \\ \sum_{n=1}^{N} K_g(\alpha_n)\sin^2\alpha_n \end{bmatrix} \tag{5-22}$$

Solving for K_{11}, K_{12}, and K_{22} gives

$$K_{11} = \frac{\left(\sum_{n=1}^{N} K_g(\alpha_n)\sin^2\alpha_n\right)\left(\sum_{n=1}^{N}\cos^2\alpha_n\sin^2\alpha_n\right) - \left(\sum_{n=1}^{N} K_g(\alpha_n)\cos^2\alpha_n\right)\left(\sum_{n=1}^{N}\sin^4\alpha_n\right)}{\left(\sum_{n=1}^{N}\sin^2\alpha_n\cos^2\alpha_n\right)^2 + \left(\sum_{n=1}^{N}\cos^4\alpha_n\right)\left(\sum_{n=1}^{N}\sin^4\alpha_n\right)}, \tag{5-23}$$

$$K_{12} = \sum_{n=1}^{N} K_g(\alpha_n) \cos \alpha_n \sin \alpha_n \Big/ \sum_{n=1}^{N} 2\sin^2\alpha_n \cos^2\alpha_n \ , \tag{5-24}$$

$$K_{22} = \frac{\sum_{n=1}^{N} K_g(\alpha_n)\cos^2\alpha_n}{\sum_{n=1}^{N} \sin^2\alpha_n \cos^2\alpha_n} - \left\{ \left(\frac{\left(\sum_{n=1}^{N} K_g(\alpha_n)\sin^2\alpha_n\right)\left(\sum_{n=1}^{N} \cos^2\alpha_n \sin^2\alpha_n\right) - \left(\sum_{n=1}^{N} K_g(\alpha_n)\cos^2\alpha_n\right)\left(\sum_{n=1}^{N} \sin^4\alpha_n\right)}{\left(\sum_{n=1}^{N} \sin^2\alpha_n \cos^2\alpha_n\right)^2 + \left(\sum_{n=1}^{N} \cos^4\alpha_n\right)\left(\sum_{n=1}^{N} \sin^4\alpha_n\right)} \right) \cdot \left(\frac{\sum_{n=1}^{N} \cos^4\alpha_n}{\sum_{n=1}^{N} \sin^2\alpha_n \cos^2\alpha_n} \right) \right\} . \tag{5-25}$$

5.5 PRINCIPAL PERMEABILITIES AND DIRECTIONS

Knowing the values of K_{11}, K_{12}, and K_{22} the values and directions of the principal permeabilities K_1 and K_2 can be calculated with standard techniques of linear algebra. The techniques are given here only for completeness. The informed reader may wish to skip to Section 5-6. In Edelen and Kydoniefs (1972)

$$K_{ij}E_j = \lambda E_i \ , \tag{5-26}$$

where E_i is a unit vector in a principal direction, or eigenvector, for K_{ij}. The transformation $K_{ij}E_j$ gives a vector in the same direction as E_j, but of magnitude λ where δ_{ij} is the Kronecker delta. Thus,

$$(K_{ij} - \lambda\delta_{ij})E_j = 0. \tag{5-27}$$

Here the components of E_j and λ are unknowns. This equation can have a solution only if

$$\begin{vmatrix} K_{11} - \lambda & K_{12} \\ K_{12} & K_{22} - \lambda \end{vmatrix} = 0, \tag{5-28}$$

or

$$\lambda^2 - (K_{11} + K_{22})\lambda + K_{11}K_{22} - K_{12}^2 = 0. \tag{5-29}$$

So the principal permeabilities are

$$K_1 = \lambda_1 = \frac{K_{11} + K_{22}}{2} + \frac{\sqrt{(K_{11} + K_{22})^2 - 4(K_{11}K_{22} - K_{12}^2)}}{2}; \tag{5-30}$$

$$K_2 = \lambda_2 = \frac{K_{11} + K_{22}}{2} - \frac{\sqrt{(K_{11} + K_{22})^2 - 4(K_{11}K_{22} - K_{12}^2)}}{2}. \tag{5-31}$$

The principal directions, $E1_j$ and $E2_j$, are found by solving the equations

$$(K_{ij} - \lambda_1\delta_{ij})E1_j = 0, \tag{5-32}$$

and

$$(K_{ij} - \lambda_2\delta_{ij})E2_j = 0, \tag{5-33}$$

for the components of the $E1_j$ and $E2_j$.

Let $E_j = \begin{bmatrix} x \\ y \end{bmatrix}$. Now for each λ we have

$$\begin{bmatrix} K_{11} - \lambda_i & K_{12} \\ K_{12} & K_{22} - \lambda_i \end{bmatrix} \begin{bmatrix} x \\ y \end{bmatrix} = 0. \tag{5-34}$$

Using row reduction we obtain

$$\begin{bmatrix} 1 & \dfrac{K_{12}}{K_{11} - \lambda_i} \\ 0 & (K_{22} - \lambda_i) - \dfrac{K_{12}^2}{K_{11} - \lambda_i} \end{bmatrix} = \begin{bmatrix} 1 & \dfrac{K_{12}}{K_{11} - \lambda_i} \\ 0 & 0 \end{bmatrix} \tag{5-35}$$

because $(K_{11}-\lambda_i)(K_{22}-\lambda_i) - K_{12}^2 = 0$ due to the choice of λ (Equation 5-29). So we can choose $x = 1$,

$$y = \frac{\lambda_i - K_{11}}{K_{12}} = \frac{K_{12}}{\lambda_i - K_{22}} . \tag{5-36}$$

The E_i can be expressed as the unit vectors

$$E1_i = \frac{1}{\sqrt{1 + \left(\frac{\lambda_1 - \lambda_{11}}{K_{12}}\right)^2}} , \frac{(\lambda_1 - K_{11})/K_{12}}{\sqrt{1 + \left(\frac{\lambda_1 - K_{11}}{K_{12}}\right)^2}} , \tag{5-37}$$

$$E2_i = \frac{1}{\sqrt{1 + \left(\frac{\lambda_2 - \lambda_{11}}{K_{12}}\right)^2}} , \frac{(\lambda_2 - K_{11})/K_{12}}{\sqrt{1 + \left(\frac{\lambda_2 - K_{11}}{K_{12}}\right)^2}} . \tag{5-38}$$

If $\lambda_1 = \lambda_2$, the ellipse is circular and any two perpendicular vectors can be eigenvectors. In this case we can choose

$$E1_j = (0,1) \qquad E2_j = (1,0). \tag{5-39}$$

5.6 MEAN SQUARE ERROR

The mean square error, MSE, is simply given by

$$\begin{aligned} MSE &= \frac{R_{II}}{N} \\ &= \frac{1}{N} \sum_{n=1}^{N} \left[K_g(\alpha_n) - \left(K_{11}\cos^2\alpha_n + 2K_{12}\cos\alpha_n \sin\alpha_n + K_{22}\sin^2\alpha_n \right) \right]^2 \end{aligned} \tag{5-40}$$

In order to use the MSE to compare the data from different fracture samples the MSE must be normalized as follows.

$$\mathrm{NMSE} = \frac{\mathrm{MSE}}{K_1 K_2} \tag{5-41}$$

$$= \frac{1}{N\,K_1 K_2} \sum_{n=1}^{N} \left[K_g(\alpha) - \left(K_{11}\cos^2\alpha_n + 2K_{12}\cos\alpha_n \sin\alpha_n + K_{22}\sin^2\alpha_n \right) \right]^2 .$$

As NMSE approaches zero, the fracture systems behave more like anisotropic homogeneous porous media.

6 LENGTH-DENSITY STUDY

6.1 BACKGROUND

With the exception of the rare underground test facility, most of what is known about fracture geometry in the underground is derived from boreholes. It is relatively easy and straightforward to determine the number of open fractures which intersect a borehole and estimate their orientation. On the other hand it is relatively difficult to get a good estimate of volumetric fracture density, fracture lengths and fracture apertures from hydraulic tests. The aim of this study was to see the effect on permeability of these fracture geometry parameters that cannot easily be determined from boreholes. In particular this study looks at the effect of varying fracture length and density. The effect of varying aperture has been discussed in Chapter 5 and is discussed in greater detail in Chapter 7.

It is not necessary to look at all possible combinations of fracture length and density. As discussed in Chapter 2, the probabalistic relationship between the number of fractures per unit length of sample line, λ_L, the areal density, λ_A (or volumetric density λ_V in three dimensions), and the mean length, $\bar{\ell}$ or mean area in three dimensions), of the fractures is

$$\lambda_L = \lambda_A \bar{\ell} \cos\theta. \tag{6-1}$$

for each set of fractures, where Θ is angle between the borehole and the mean fracture pole (Robertson, 1970; Baecher et al, 1977). This equation states the probability of a fracture intersecting a unit length of borehole increases as the volumetric density increases and also as the fractures become longer.

From examination of core or TV log, the mean length or the volumetric density of the fractures cannot be determined absolutely. However, λ_L and Θ can be readily determined. Rearranging Equation 6-1 with knowns on one side and unknowns on the other, we have

$$\lambda_L/\cos\Theta = \lambda_A \bar{\ell} = LD. \tag{6-2}$$

This means that for each set of fractures we may not be able to determine λ_A and ℓ directly, but we can determine the product of λ_A and ℓ. The product of $\bar{\ell}$ and λ_A will be called LD, or the length-density parameter.

Figure 6-1 illustrates this principle. In both 6-1A and 6-1B, a borehole of length L penetrates a system of fractures. The fractures in A are twice as long as those in B, but there are half as many fractures per unit area in A as there are in B. Both boreholes intersect approximately 12 fractures. From the borehole wall, we see no difference in the two systems, but as will be shown below, there is a great deal of difference in the hydrologic behavior of the two systems.

6.2 PARAMETERS USED IN THE LENGTH-DENSITY STUDY

The parameters common to the whole length density study are given in Table 6-1. Table 6-2 gives the parameters used in the first series which was designed to study the effect of increasing length while keeping the product of length and density constant. The units used in all these studies are length in centimeters and hydraulic conductivity in cm/s.

In all of the length-density studies presented in Chapter 6, the length-density parameter LD, is 0.288/cm. This means a borehole through such a rock would intersect roughly 288 fractures in 10 m. However, these model results could easily be scaled to represent a fractured rock having an LD of say 0.288/m or about 3 fractures every 10 meters of borehole. The relative magnitude of the results is important in this study, not the absolute magnitude. Also, larger values of LD will produce systems of higher permeability; lower values will produce lower permeability. Since LD can be measured, different values of LD were not tried in these simulations.

Orthogonal fracture sets were used because if the sample size is sufficiently large, the theoretical shape of the permeability ellipse for orthogonal fractures of constant length and aperture is a circle. Thus the degree of anisotropy was not an unknown. Apertures were held constant and orientations were varied with a 20° standard deviation. This arrangement provided the best opportunity of finding porous medium behavior in fracture meshes that were small enough to be solved within the size limitation of the computer. Fracture lengths were kept constant only for the sake of simplicity.

$$\lambda_A \bar{\ell} = \frac{\lambda_L}{\cos\theta} = \text{a measurable borehole parameter}$$

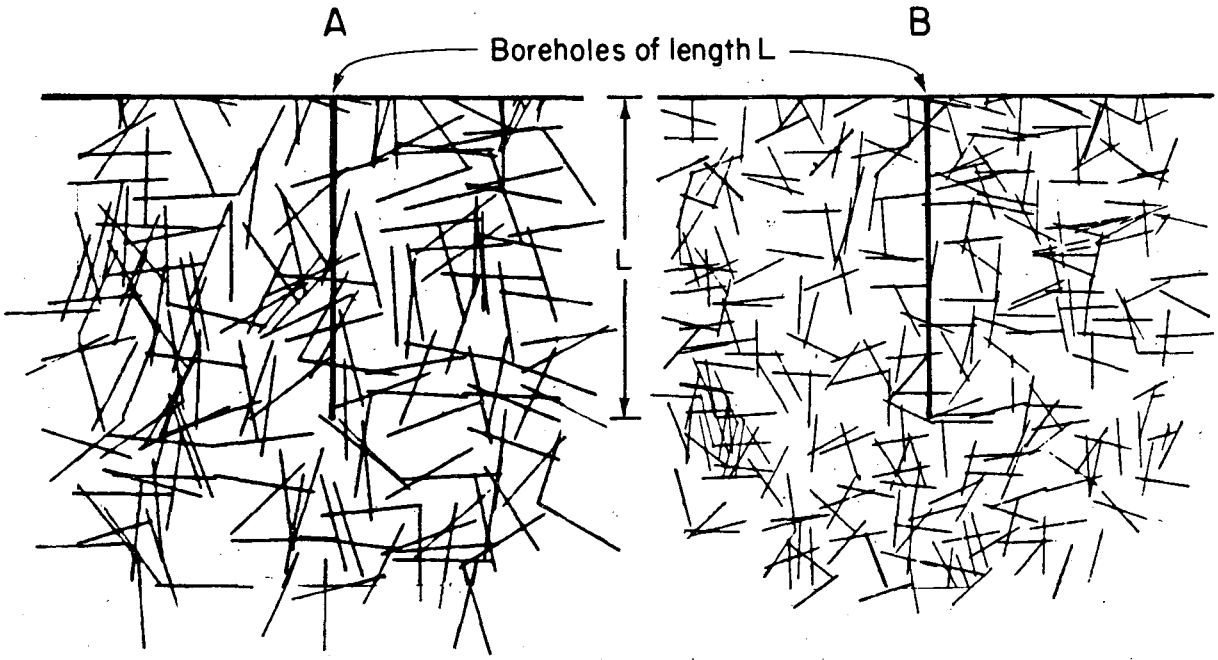

	A	B
N Number of intersecting fractures	12	12
L Borehole length	42	42
$\lambda_L = N/L$	.29	.29
$\bar{\ell}$ Mean fracture length	16	8
$\lambda_A = \frac{\text{number of fractures}}{\text{unit area}}$	.018	.036
$\lambda_A \bar{\ell} \cos\theta \ (\theta = 0)$	.29	.29

XBL 829-2419

Figure 6-1. Example of Two Boreholes of Equal Length Where (A) Penetrates a System of Fractures Whose Mean Fracture Length is Twice that of (B)

Table 6-1. Parameters Common to the Whole Length-Density Study

	Orientation		LD (cm^{-1})	Aperture (cm)	
	Mean	Standard Deviation		Mean	Standard Deviation
Set 1	04	204	0.288	0.001	0
Set 2	904	204	0.288	0.001	0

Table 6-2. Input Parameters Used in the First Series of Length-Density Studies

Name	Fracture Length ℓ (Set 1 and Set 2) (cm)	Flow Region Dimensions L x L (cm)	L/ℓ	Number of Fractures Per Set Per Unit Area λ_A (cm^{-2})
LD2	2	12.5 x 12.5	6.25	0.1440
LD8	8	50 x 50	6.25	0.0360
LD10	10	62.5 x 62.5	6.25	0.0288
LD12	12	75 x 75	6.25	0.0240
LD14	14	87.5 x 87.5	6.25	0.0206
LD16	16	100 x 100	6.25	0.0180
LD20	20	125 x 125	6.25	0.1440
LD24	24	150 x 150	6.25	0.0120

In the first series, three parameters were varied in a systematic manner. These were the flow region size, the fracture length, and the fracture density, λ_A. The length and width of the flow region, L, was kept equal to 6.25 times the fracture length to insure that an equal proportion of fractures would be truncated in the flow mesh of each case. Also, from previous experience the factor of 6.25 was expected to yield flow regions where the mean fracture length was reasonably close to the value used in input. That is, only a small proportion of the fractures were truncated by the flow region. Figure 6-2 shows mean fracture length for each rotation of all the flow regions divided by input length plotted as a function of input length. The mean fracture length was always about 85 percent of the input value. Thus each of the fracture systems was an approximately equally good statistical sample.

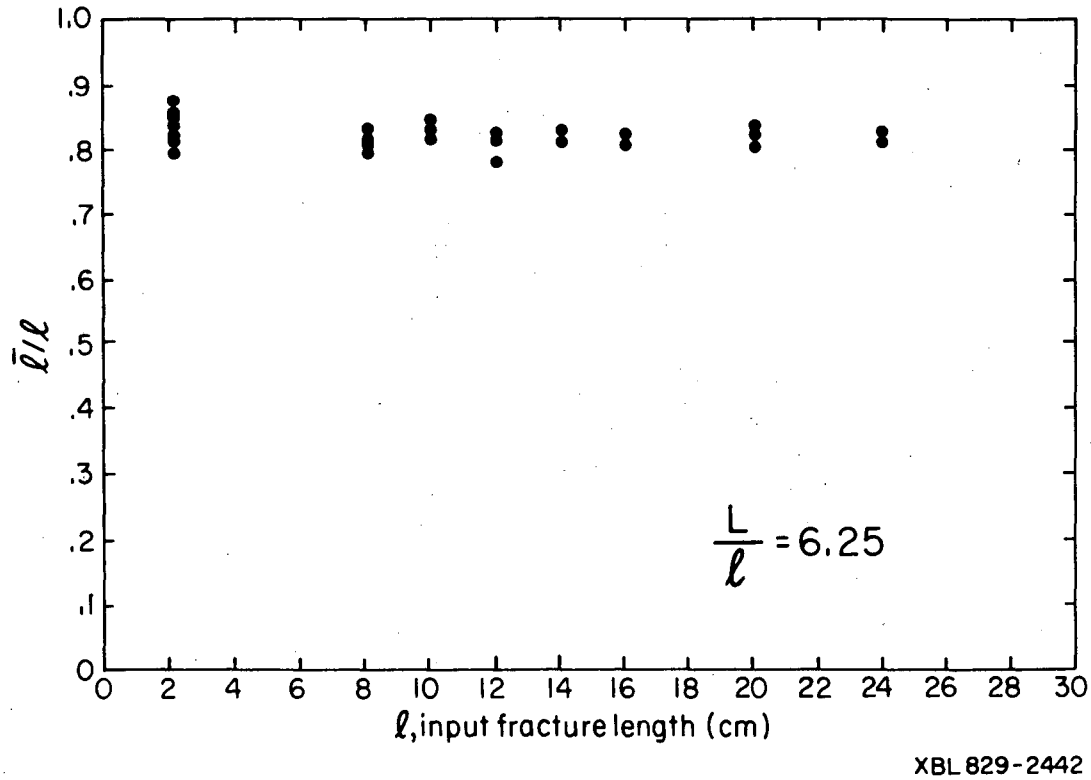

Figure 6-2. Normalized Mean Fracture Length, $\bar{\ell}$ in the Flow Region Versus Input Fracture Length, ℓ for Mesh Size, $L = 6.25\ell$

The fracture density and input length were calculated using the equation:

$$LD = \ell\lambda_A = 0.288. \tag{6-2}$$

So as ℓ became larger, L became larger and λ_A became smaller.

6.3 RESULTS OF THE FIRST SERIES OF LENGTH DENSITY STUDIES

The flow regions and permeability plots are shown in Figures 6-3 through 6-10. In each figure, the top left shows the 0° rotation flow region with all the fractures as they were generated. The top right shows the reduced version of the fracture system for the 0° rotation. The reduced version was used to calculate permeability. In the reduced version, all the dead ends on the fractures and all single isolated fractures are eliminated. Isolated patches of fractures persist because there is no simple algorithm for removing them. The flux through the reduced version is the same as the flux through the unreduced version, but the reduced version is smaller and less expensive to solve. It is easy to see flow paths and degree of connection between fractures on the plot of the reduced fracture system.

In each figure, only the 0° rotation is shown as an example, but for each model, a total of six differently oriented flow regions were defined. For each flow region, each of the four sides were sequentially used as the inflow side. Thus permeability was measured every 15° for 24 rotations in all.

When the flow regions are reduced for analysis, a fracture which connects two sides in one flow region may be isolated and nonconducting in a differently orientated flow region. In Figure 6-3 for instance, the 0° rotation had no conducting fractures. However, it can be seen from the permeability plots that conducting fractures intersecting the inflow side of the mesh for rotations of α = 15°, 30°, 75°, 105°, 120°, 225°, 315° and 345°. These conductive fractures cannot be observed in the reduced flow mesh at 0° rotation shown in the figure, but could be seen if all six rotations of the flow region were shown.

The bottom left of Figures 6-3 through 6-10 shows the permeability ellipse. The dashed lines connect the values of $1/\sqrt{K_g}$ calculated by the model. The area enclosed by the dashed lines is shaded. The solid-line

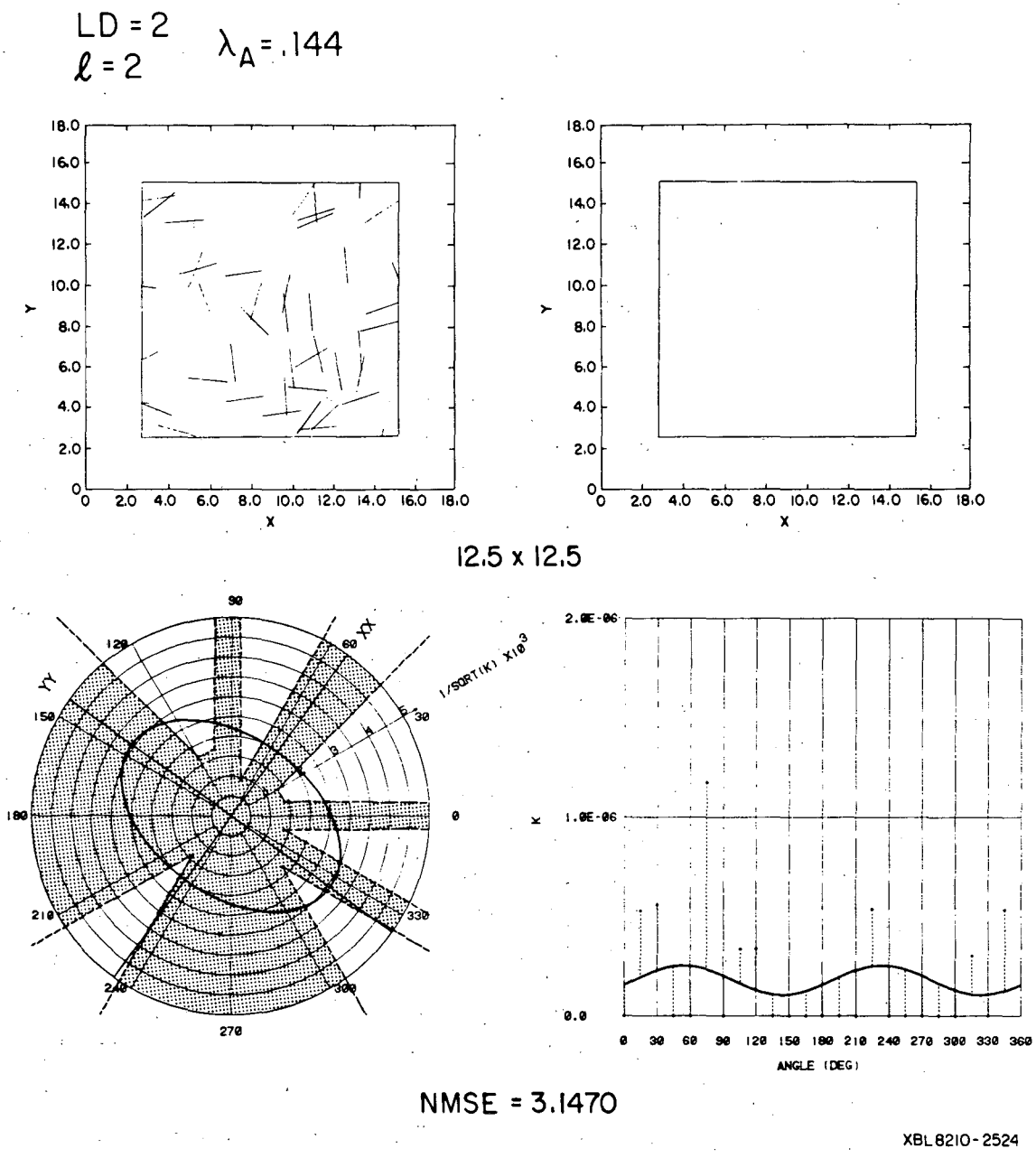

Figure 6-3. Length-Density Study, $\ell = 2$, $\lambda_A = 0.144$, $L/\ell = 6.25$

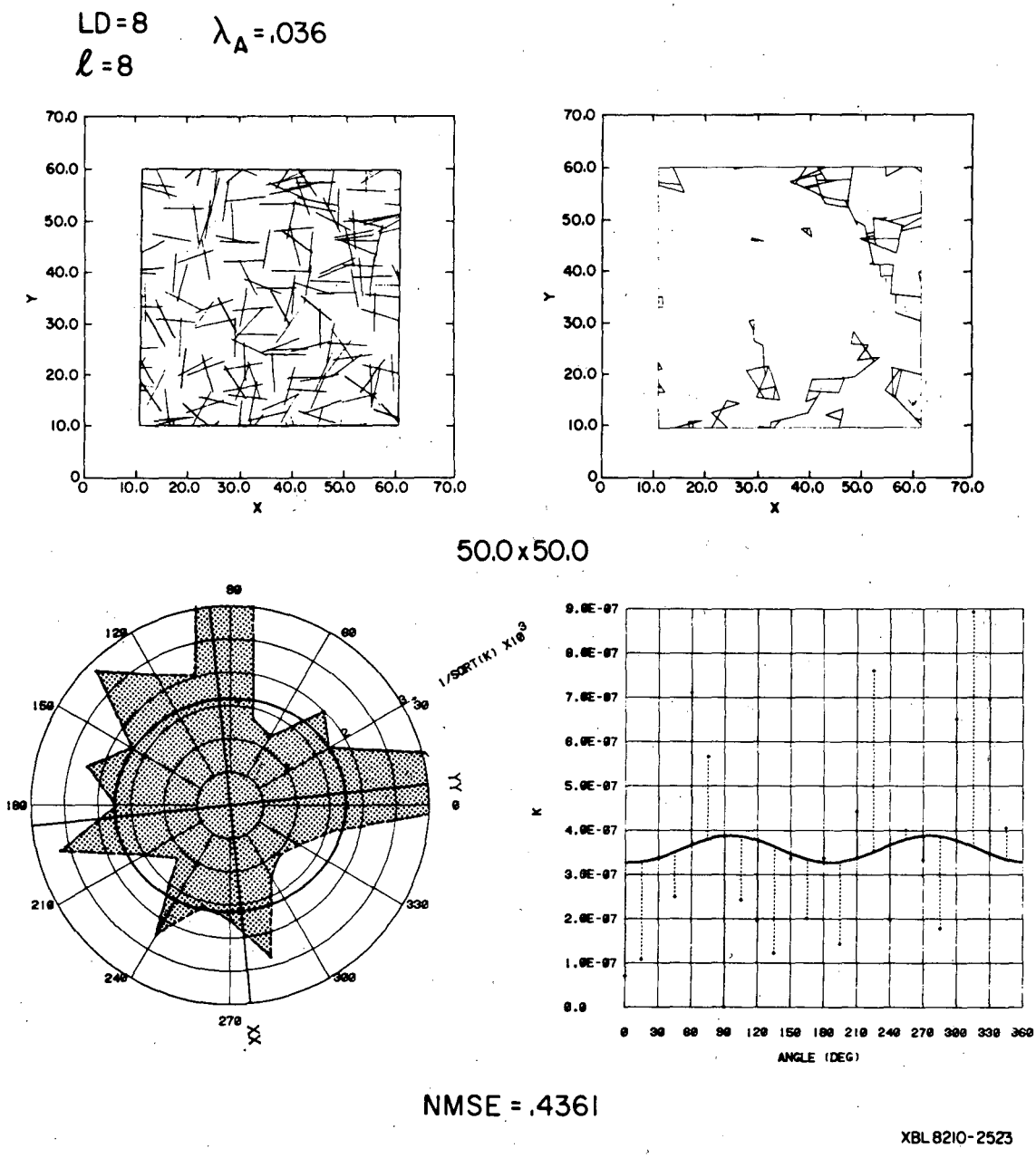

Figure 6-4. Length-Density Study, ℓ = 8, λ_A = 0.036, L/ℓ = 6.25

LD=10 λ_A =.0288
ℓ=10

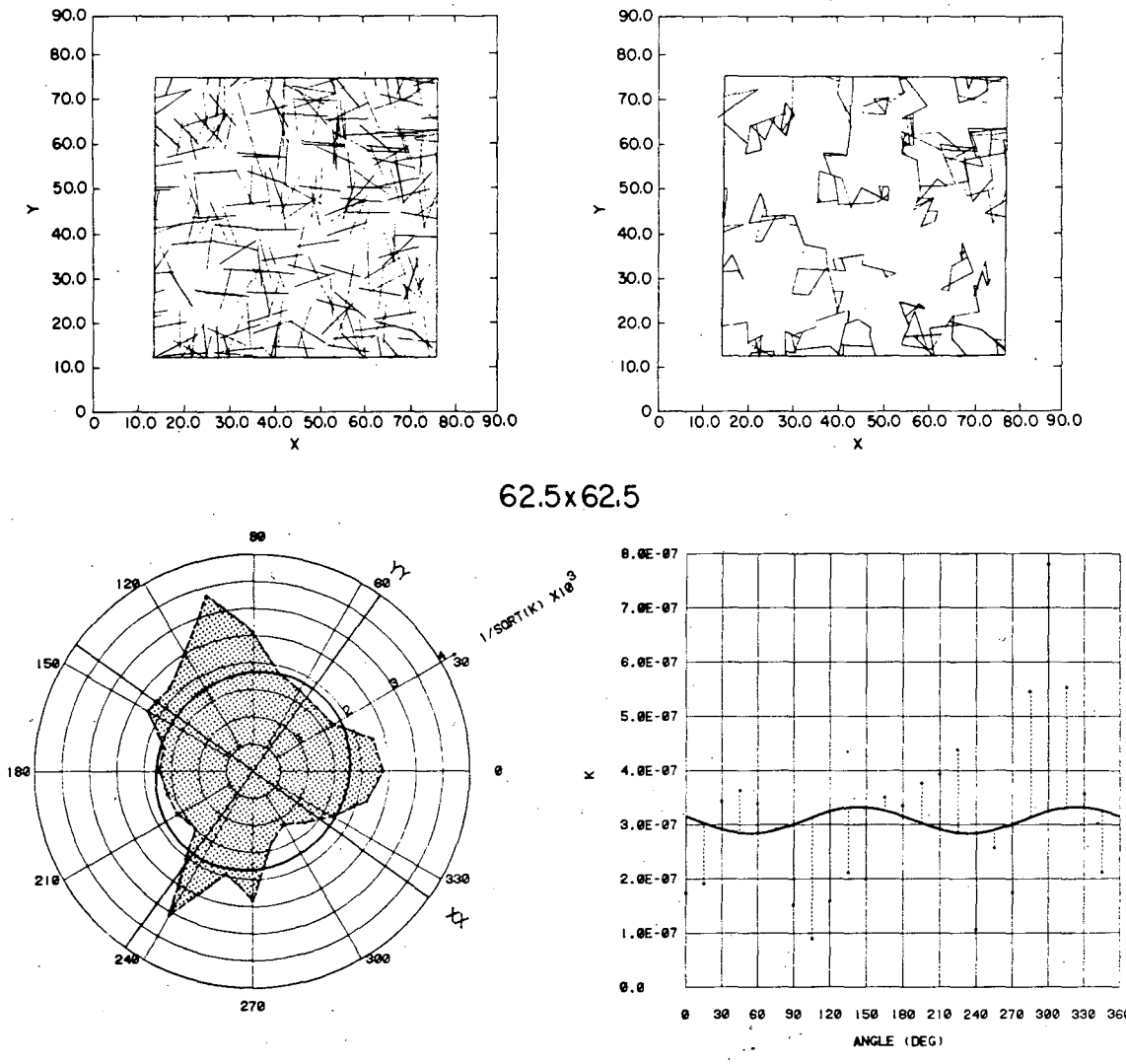

NMSE = .2603

XBL8210-2522

Figure 6-5. Length-Density Study, ℓ = 10, λ_A = 0.0288, L/ℓ = 6.25

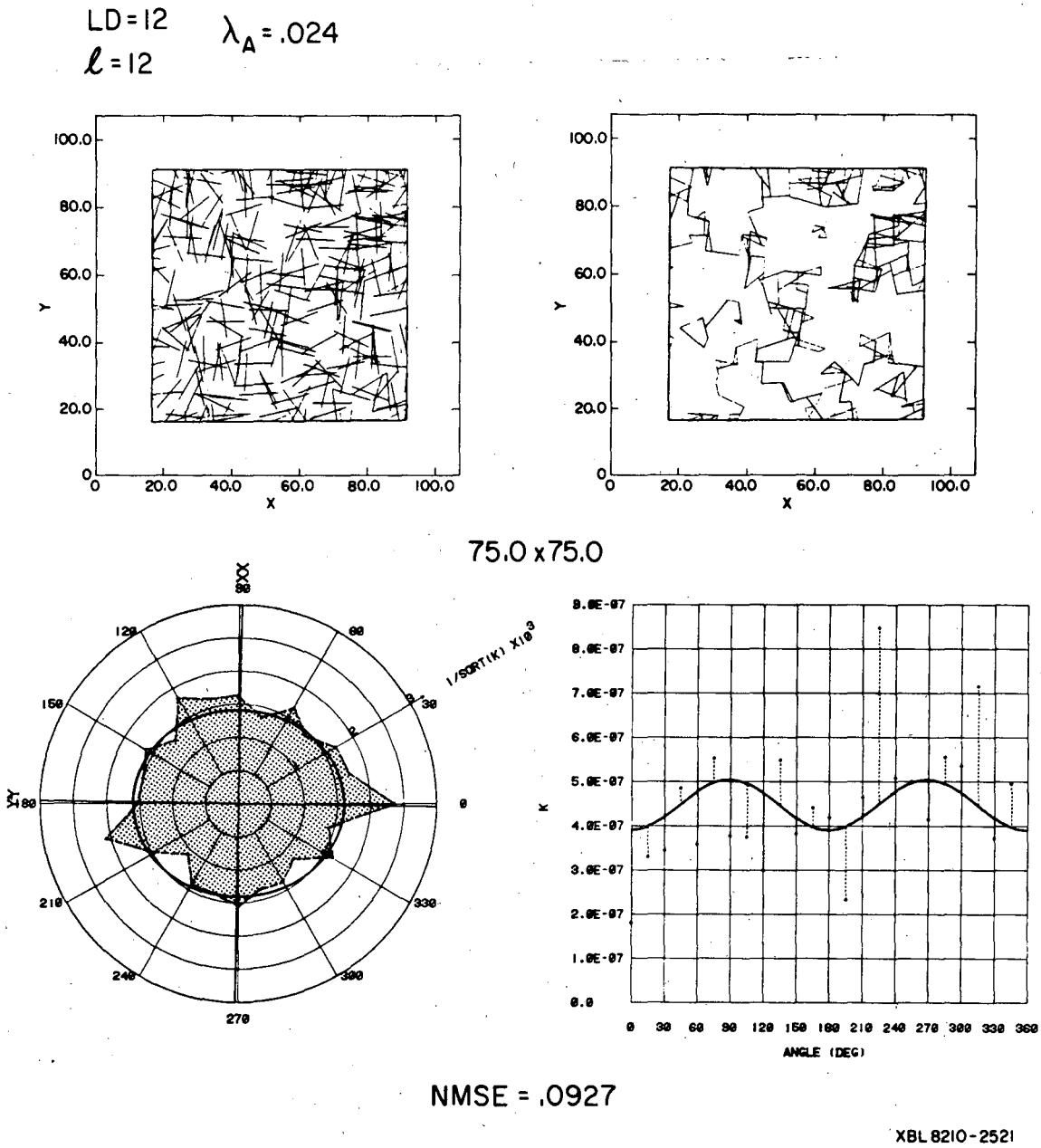

Figure 6-6. Length-Density Study, ℓ = 12, λ_A = 0.024, L/ℓ = 6.25

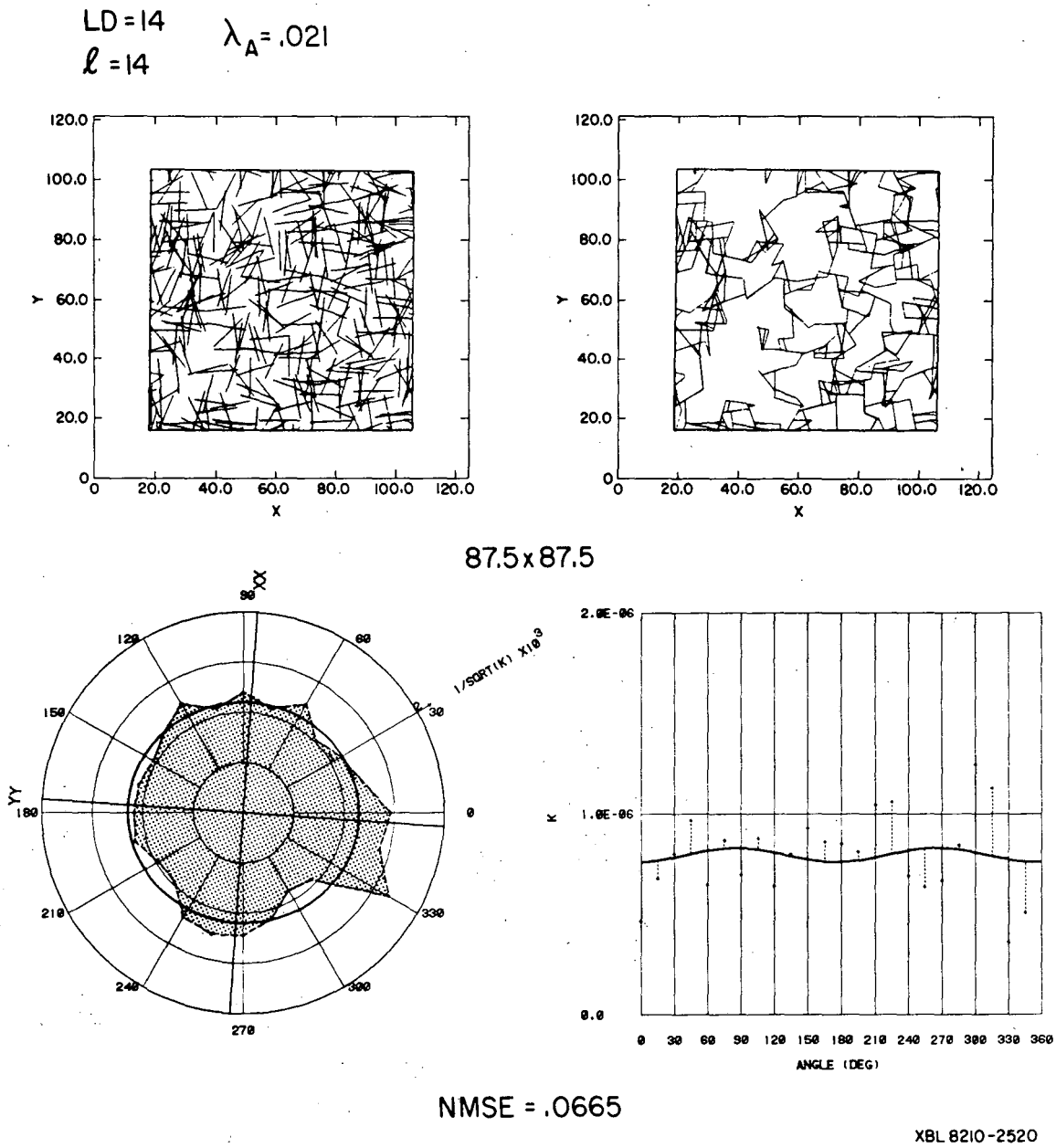

Figure 6-7. Length-Density Study, ℓ = 14, λ_A = 0.021, L/ℓ = 6.25

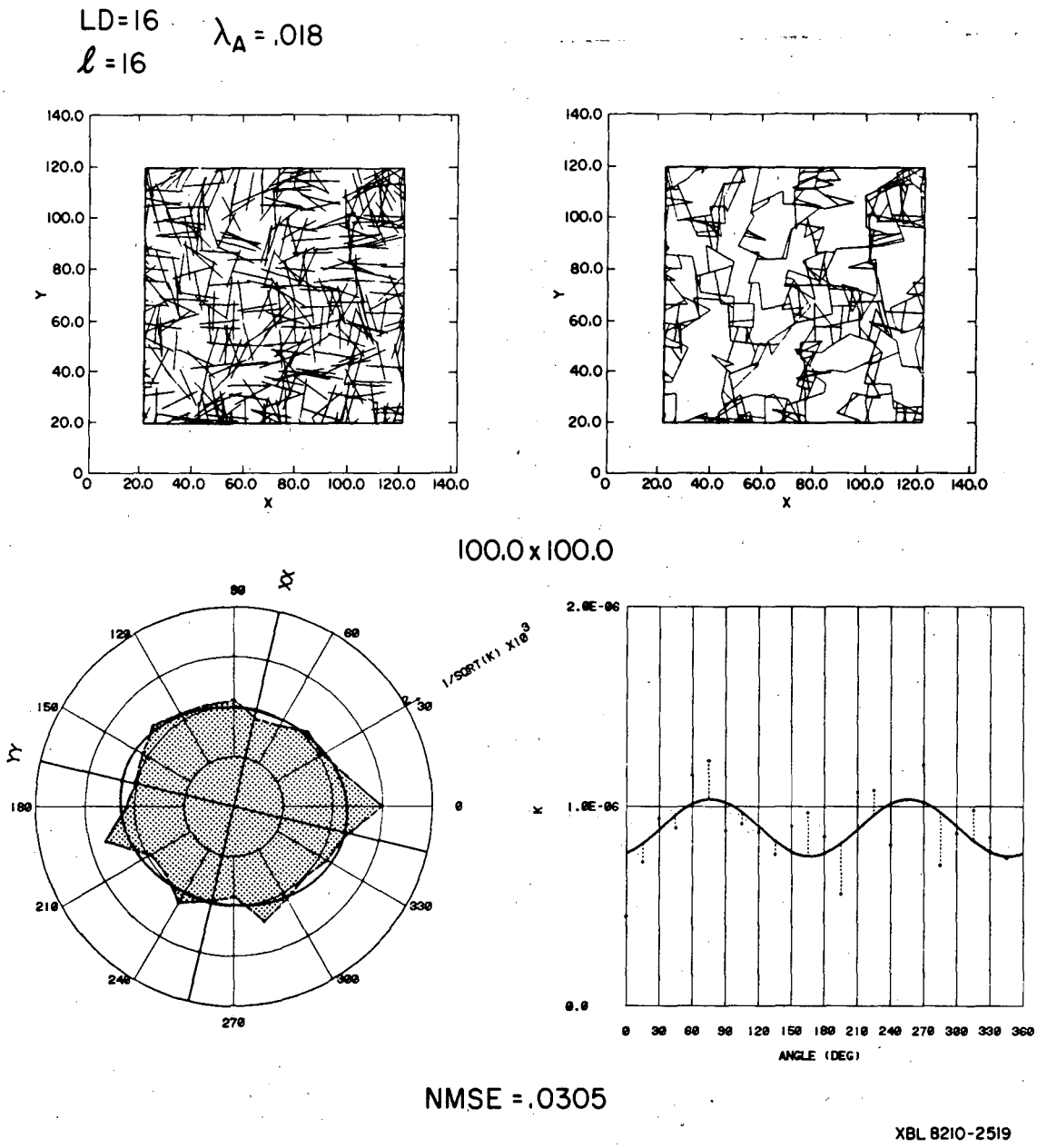

Figure 6-8. Length-Density Study, ℓ = 16, λ_A = 0.018, L/ℓ = 6.25

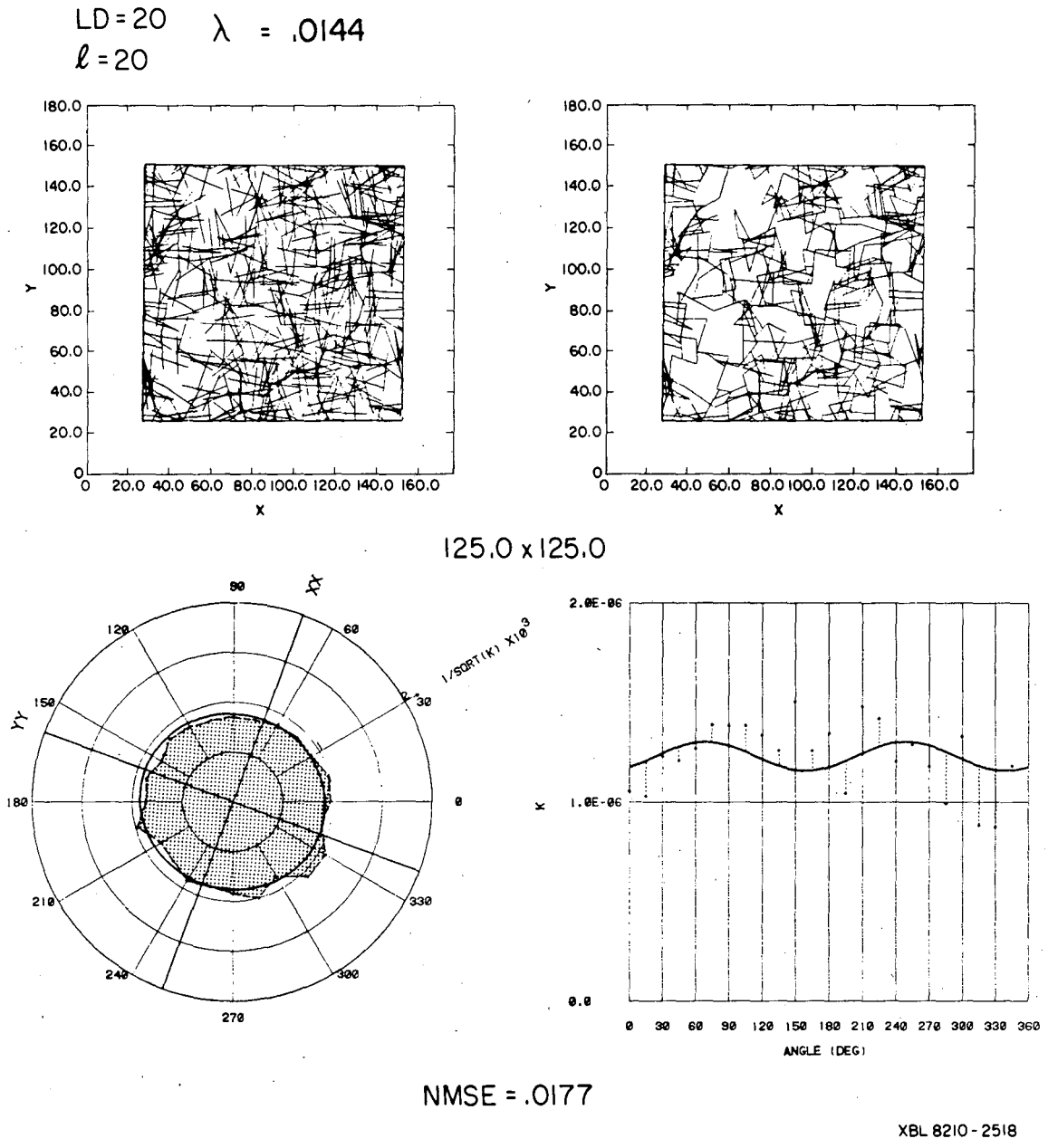

Figure 6-9. Length-Density Study, ℓ = 20, λ_A = 0.0144, L/ℓ = 6.25

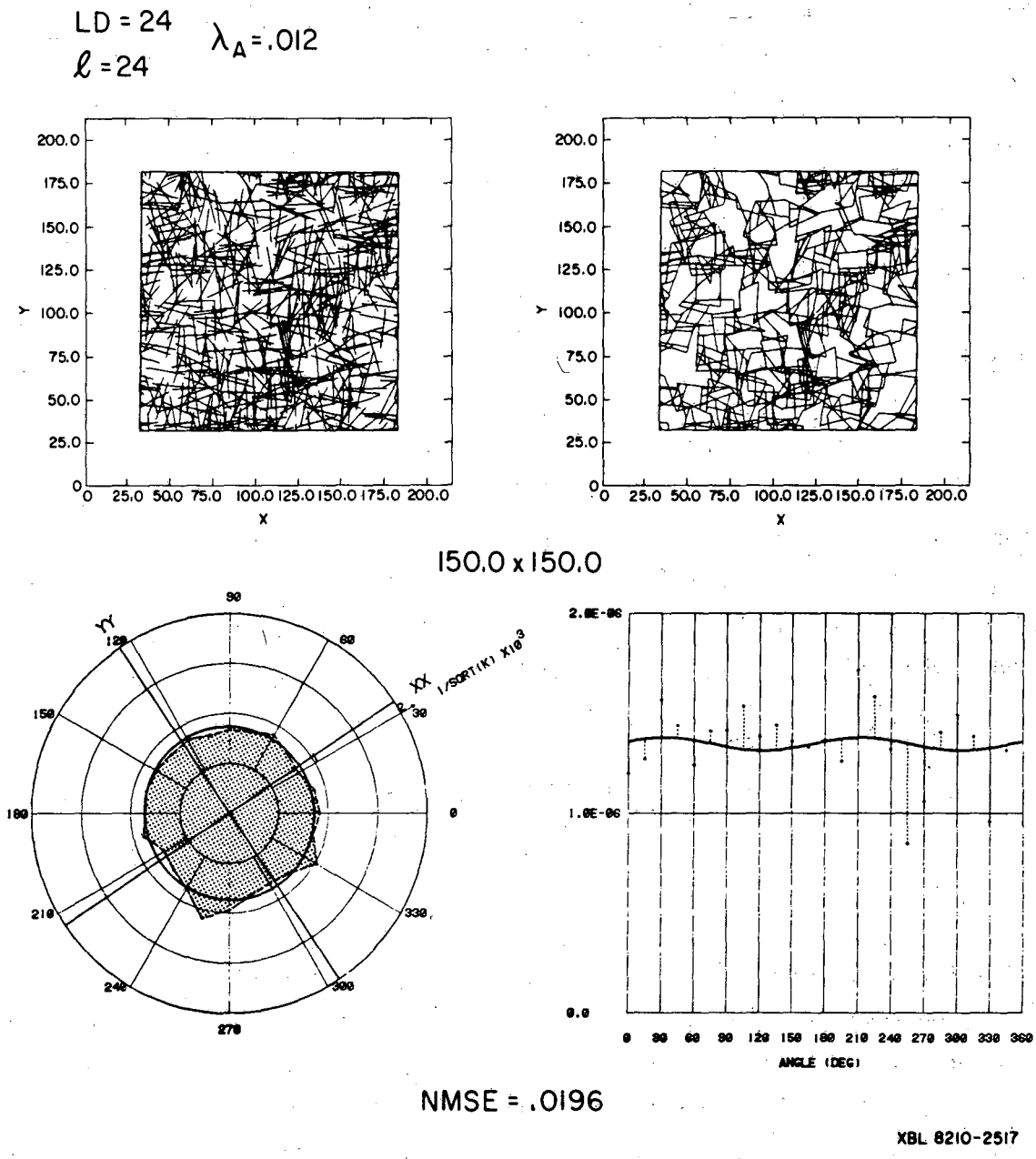

Figure 6-10. Length-Density Study, $\ell = 24$, $\lambda_A = 0.012$, $L/\ell = 6.25$

ellipse is the ellipse which best fits the data as calculated by the methods explained in Chapter 5. The XX and YY axes are the 1st and 2nd principal permeability axes, respectively. The bottom right of each figure shows a Cartesian plot of K_g versus α. The best fit values of K_g are shown by a solid curving line. The ellipse plot provides a simple visualization of how well the permeability can be represented by a symmetric tensor. The closer the shaded area is to the ellipse the better the representation. Since the Cartesian plot is linear in K_g, it is better for easy visualization of the magnitude of the permeability and the scatter of the measurements.

The fracture meshes are not plotted to the same scale. The scale is varied such that each plot is the same size on the paper. The flow region size, L, is a constant multiple of 6.25 times the fracture length, ℓ. Thus, the fractures in all the plots also appear to be the same length. Moving from Figure 6-3 to 6-10 the actual fracture length, ℓ, and the region size, L, are increasing and the areal density, λ_A, is decreasing. The net result is that the number of fractures in each mesh is increasing as ℓ increases. Thus there is an apparent increase in density which is proportional to ℓ:

$$\begin{aligned} \text{Number of fractures in the flow region} &= \lambda_A L^2 \\ &= \frac{0.288}{\ell}(6.25\ell)^2 \\ &= 11.25\ell. \end{aligned} \tag{6-4}$$

If all the meshes in Figures 6-3 through 6-10 were drawn to the same scale, it could be seen that there are actually more fractures per unit area in 6-3 than 6-4, etc., and that the fractures in 6-3 are shorter than those in 6-4, etc.

Drawing all the meshes to the same size is useful because the "apparent density" has a strong influence on the hydrologic behavior of the fracture system. The longer the fracture, the higher the "apparent density", the higher the permeability, and the lower the NMSE. Figure 6-11 is a plot of the values of K_1, K_2 and NMSE versus fracture length. For the values of ℓ studied, permeability increases and NMSE declines with increase in fracture length.

It appears that the plot of K versus ℓ levels off at the higher values of ℓ. This should occur because as ℓ becomes larger the density becomes smaller. The effect of increasing length may be partially canceled by decreasing density. In this series the limit as ℓ goes to zero can be examined but the limit as ℓ

goes to infinity is difficult to examine. This is because the number of fractures per set in each mesh is equal to 11.25ℓ. Thus the number of nodes and elements increases rapidly with the fracture length, ℓ. Therefore systems with even moderately large values of ℓ cannot be processed in the computer. In fact, the case where ℓ = 24 was the largest problem which could be run. The apparent leveling off in the K versus ℓ curve could not be confirmed.

Figure 6-12 is a plot of ellipticity, K_2/K_1 versus fracture length. Ellipticity for a good statistical sample of orthogonal fracture sets is theoretically unity. For all cases studied the value is less than unity. Perhaps the statistical sample is too small. With a larger sample, one would expect ellipticity closer to 1.0. However, since the sample is statistically isotropic, the low ellipticity values are caused in some degree by the flip-flop of the K_1 and K_2 axes, which have no preferred direction. Since K_1 is always taken as the larger value, random fluctuations are not averaged out.

Figures 6-3 through 6-10 and Figure 6-11 could be used to separate fracture systems which behave like porous media from those that do not. The closer NMSE is to zero, the more the fracture system is like a porous medium. From a perusal of the figures one might conclude that a value of NMSE greater than 1.0 means the medium would be very poorly represented by a porous medium. Permeability plots for such systems are irregular, nonsymmetric, and not necessarily even closed figures. A fairly smooth permeability ellipse seems to be produced for these systems when the NMSE is less than about 0.05 (Figures 6-8, 6-9, 6-10). Above 0.05 there is a gradual transition from a relatively smooth symmetric figure to completely irregular and nonsymmetric figure. Another transition occurs at values of NMSE above 0.3. Above this point, for some directions, K_g is zero and the permeability plots are not closed figures. Below this transition the plots are closed figures. For these systems, a cutoff point for use of a porous medium analysis could easily be put anywhere in the NMSE range of 0.05 to 0.3 depending on the degree of acceptable error in the solution.

Dashed lines are drawn on Figure 6-11 from NMSE values of 0.05 and 0.3 on the vertical axis to the NMSE curve and then down to the corresponding values of ℓ which are approximately ℓ = 15 and ℓ = 9.5, respectively. Thus for LD = 0.288, orthogonal fracture sets with 20° of standard deviation in orientation,

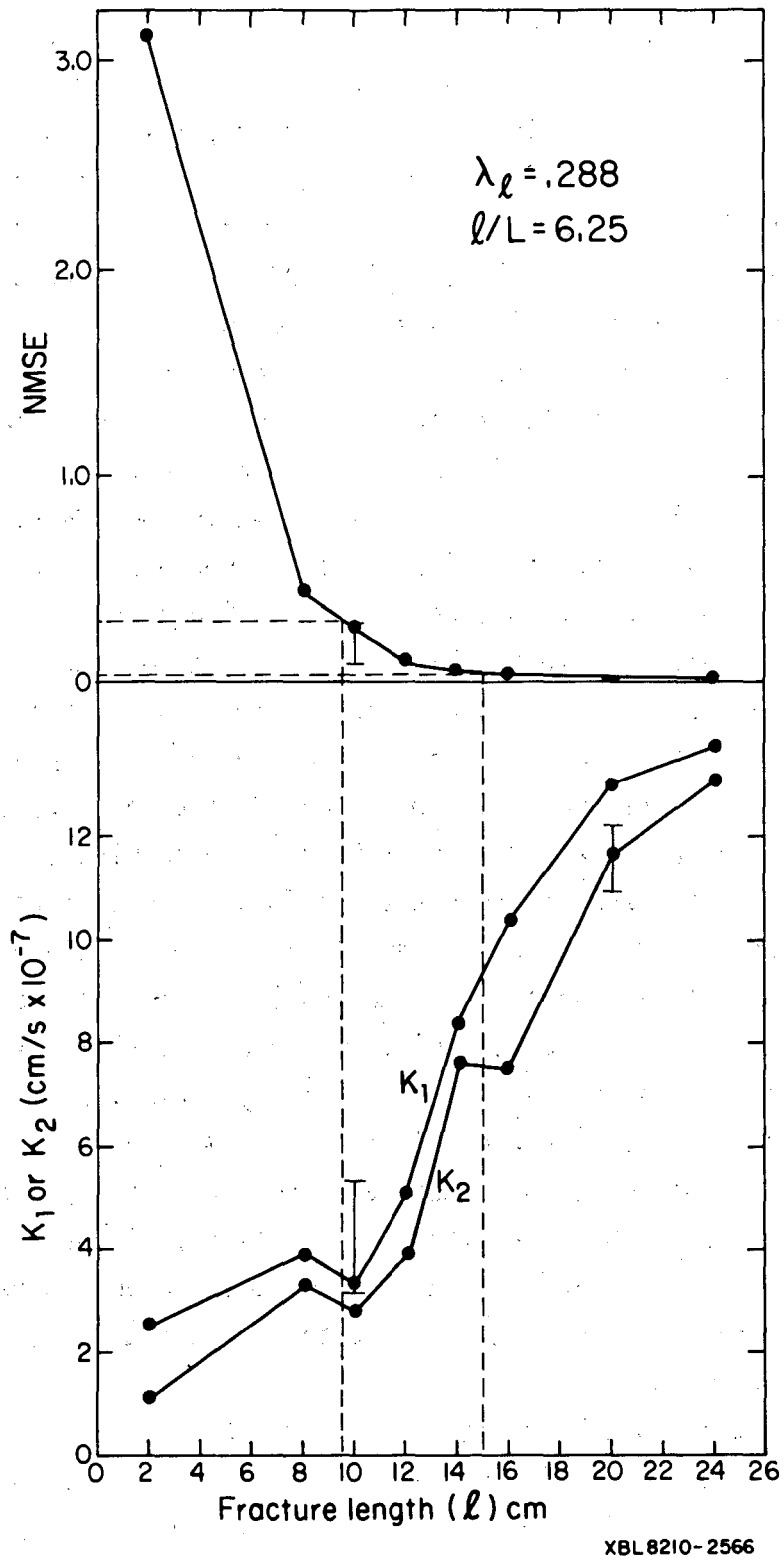

Figure 6-11. Permeability and NMSE Versus Fracture Length for the First Series of Length-Density Studies

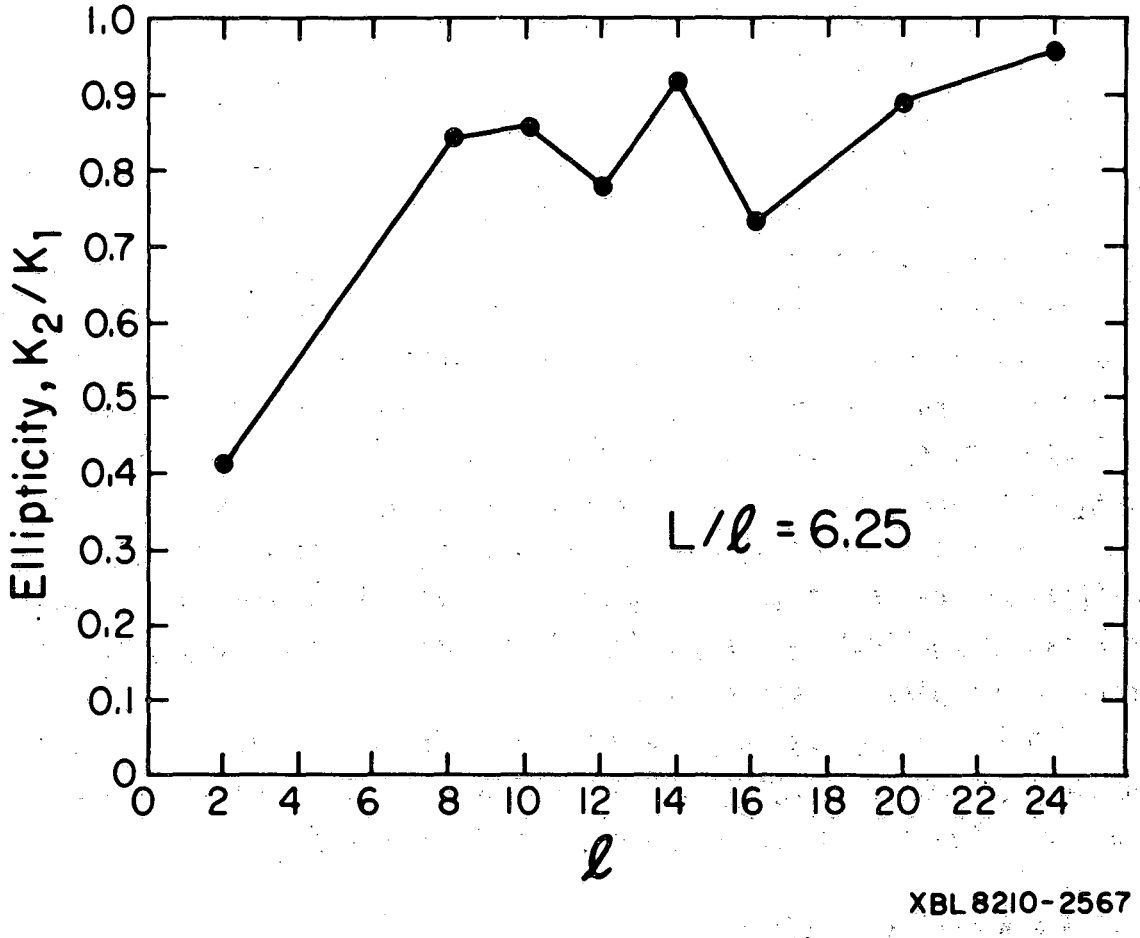

Figure 6-12. Ellipticity of the Length-Density Examples as a Function of Fracture Length for the First Series of Length-Density Studies

constant apertures, and lengths, the fracture systems can be categorized in terms of their lengths. Fracture systems with lengths greater than 15 can be well represented by a porous medium. Those with lengths less than about 9.5 cannot be well represented by a porous medium. Between 9.5 and 15 is a transition area where acceptability of the porous medium approach will depend on the accuracy required in the solution.

Caution should be used in setting up such a categorization. The NMSE calculated in this way is a measure of how well the permeability of a given fracture system is represented by a symmetric tensor. It is not directly a measure of the error involved in using a tensor for such a fracture system. This is because the more unlike a porous medium the fracture system is the more unrealistic the linear boundary conditions are. A modification of the method for measuring NMSE which makes the boundary conditions more realistic will be discussed in Chapter 10. Unless this modified method is used, categories like those determined above will be somewhat arbitrary.

Another point of caution is that these categories are based on a single realization for each fracture system. The validity of making conclusions based on a single realization was examined in a limited Monte Carlo type analysis which is explained in Section 6.4.

Finally, it may be that the value of NMSE will be smaller for flow regions larger than those tested, especially for cases where fracture length is less than 15. This possibility is examined in Section 6.5.

6.4 THE MONTE CARLO STUDY

A Monte Carlo type analysis was used to test the soundness of the observations made in Section 6.3, which were based on single realizations of each fracture system. The models for fracture lengths of 10 and 20 were chosen because 10 has a poor fit to an ellipse and 20 has a good fit. Only these two cases were run because the cost of doing this type of analysis is quite high.

In each case, the same statistical input was used to generate a series of random realizations of the fracture system. After each run the results were concatenated with the previous runs and a current best fit permeability tensor and NMSE were calculated. When the current values of K_1, K_2, and NMSE ceased to change noticeably, the study was terminated. Figures 6-13 and 6-14 show

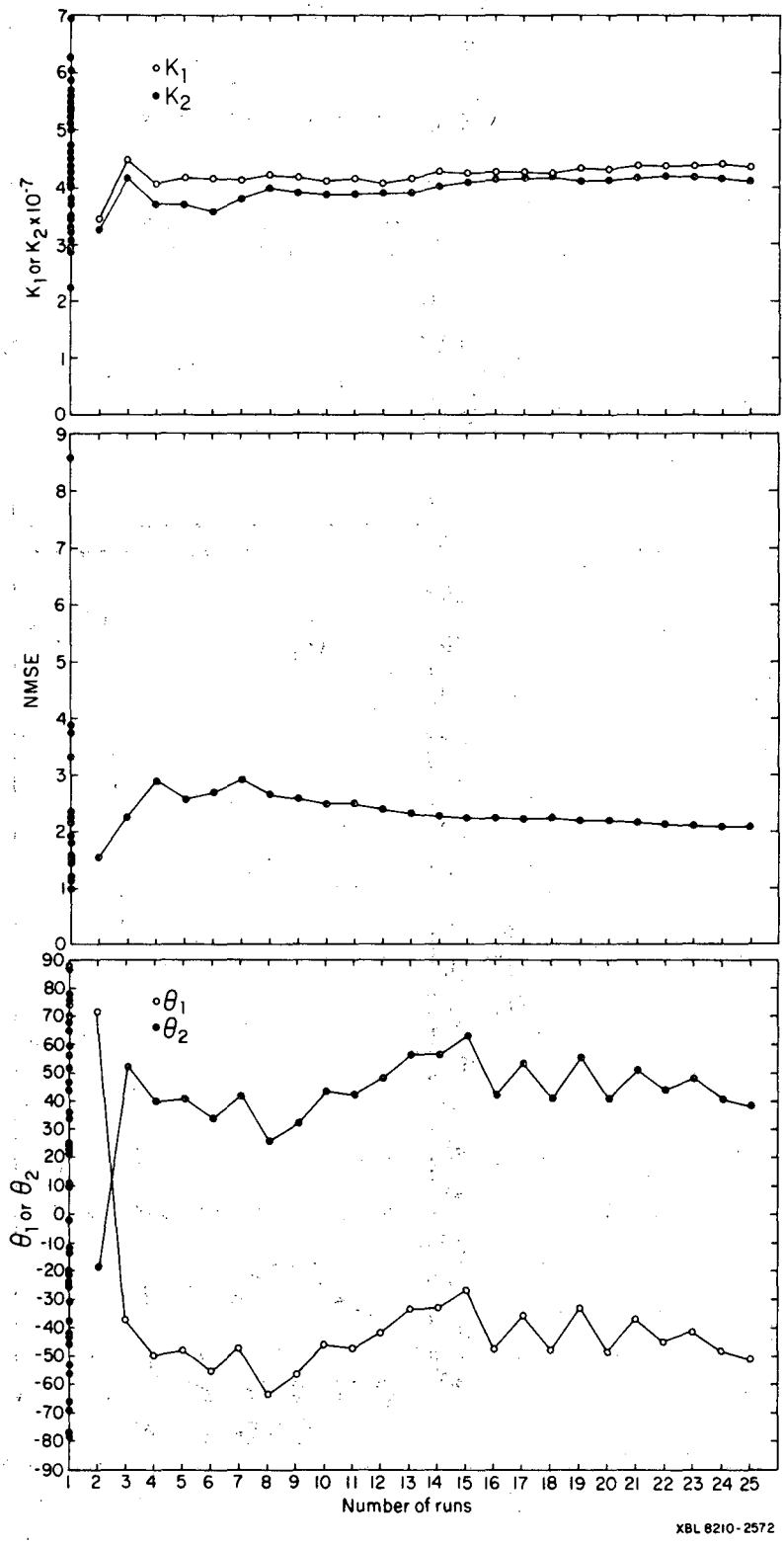

Figure 6-13. Results of the Monte Carlo Analysis of Length-Density Relationships for the Case of ℓ = 10

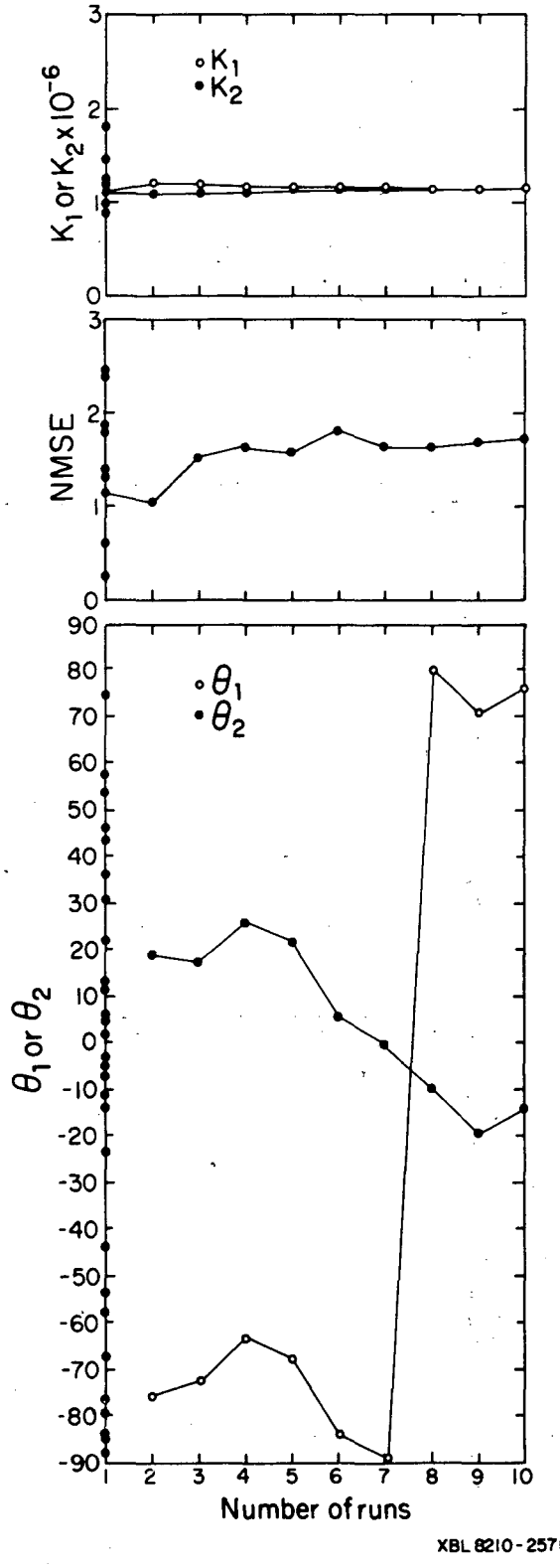

Figure 6-14. Results of the Monte Carlo Analysis of Length-Density Relationships for the Case of ℓ = 20

plots of the NMSE, K_1, K_2, and the principal directions, Θ_1 and Θ_2, versus the number of runs averaged in for $\ell = 10$ and $\ell = 20$, respectively. For $\ell = 10$, a total of 25 realizations were generated; for $\ell = 20$, 10 realizations were generated. Results of each individual run are plotted on the ordinate to illustrate the range of the data.

In the case of $\ell = 10$, the values of K_1 and K_2 never completely converge to the same value. This fact goes hand in hand with the fact that the NMSE is fairly high and the direction of the principal axes is completely random. The high value of NMSE means the connections between fractures are infrequently located. Therefore, in each run, there is usually some difference between K_1 and K_2. Since there is no preferred orientation for the principal axes, the direction of K_1 and K_2 (i.e., Θ_1 and Θ_2) changes randomly in each run. Since K_1 is always chosen to be the higher of the two principal permeabilities, the difference between K_1 and K_2 does not get averaged out as it would in a sample exhibiting strong anisotropy. With strong anisotropy, K_1 and K_2 would always be roughly in the same direction. Sometimes K_1 would be a little higher than the average, sometimes it would be lower, but eventually the differences would average out. In the isotropic case, K_1 is determined by which value of principal permeability is higher, not by orientation. So the differences between K_1 and K_2 are preserved.

Figure 6-15 shows the permeability plots for the final concatenation of all the realizations for both the $\ell = 10$ and the $\ell = 20$ cases. In both cases, the ellipses are nearly circles as expected. The $\ell = 20$ results are closer to a circle than the $\ell = 10$ results. The scatter of points is greater in the $\ell = 10$ case and the permeability is higher in the $\ell = 20$ case.

The mean plus or minus one standard deviation of all permeability measurements and NMSE from this Monte Carlo study are plotted as bars on Figure 6-11. The standard deviation is larger for $\ell = 10$ than for $\ell = 20$ for both permeability and NMSE. The standard deviation for NMSE for $\ell = 20$ is so small it shows up only as a line on Figure 6-11. These bars reinforce the general observations made in Section 6.3.

The Monte Carlo results provide the opportunity to make further observations. For a series of realizations of a fracture system, when the NMSE is higher, the standard deviation of permeability will also be higher. This trend has implications for regional stochastic modeling. The higher the

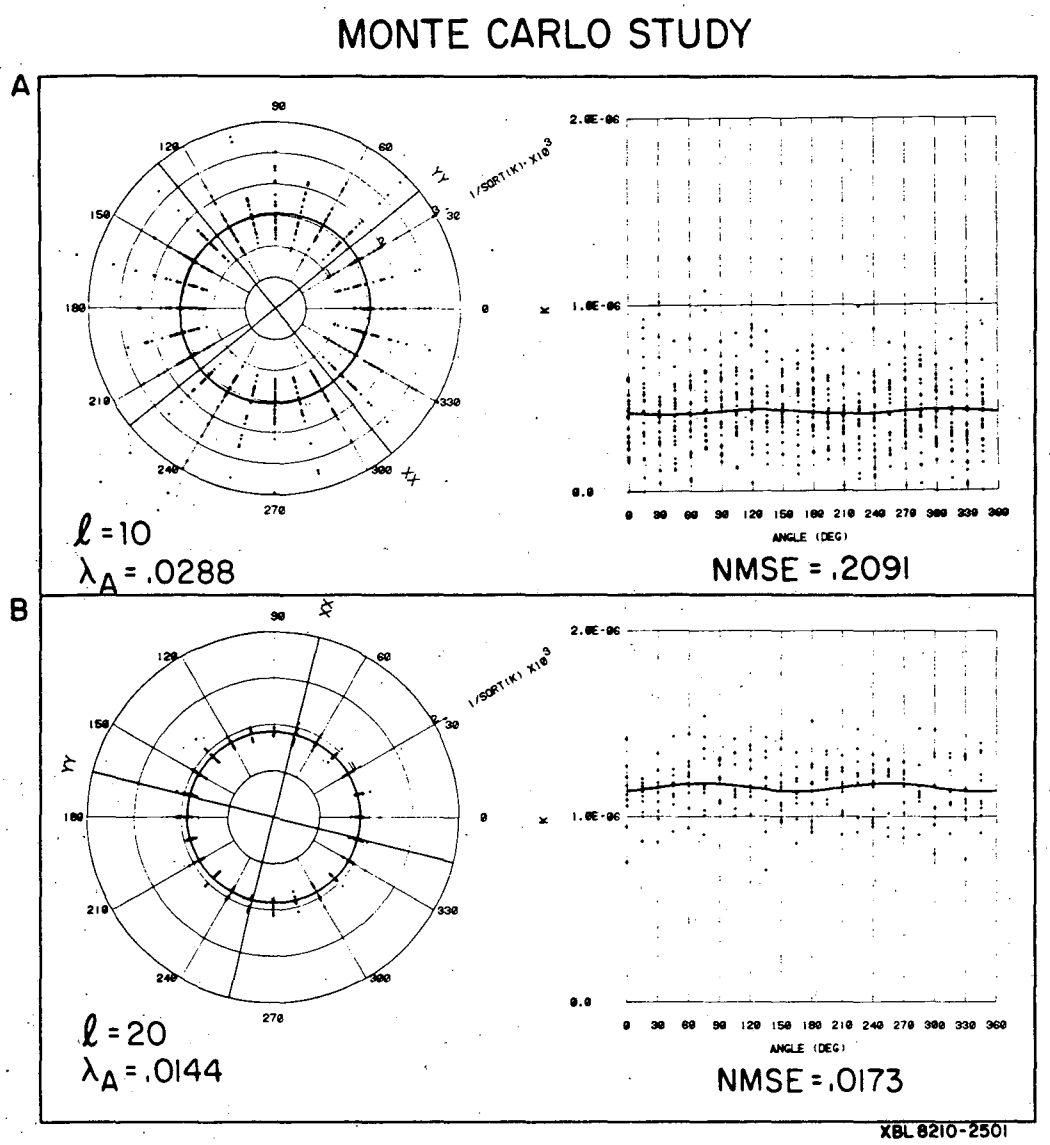

Figure 6-15. Results of the Monte Carlo Analysis of Length-Density Relationships

NMSE of the blocks chosen as REV's in the model, the greater the standard deviation that must be used to assign permeability to the blocks. This in turn will increase the standard deviation of the outcomes (Freeze 1975). Thus, the higher the NMSE, the lower the reliability of the model results.

6.5 STUDY ON THE EFFECT OF FLOW REGION SIZE

In a second series of cases, the meshs for fracture lengths 10, 12, 14 and 16 were increased in order to see if the NMSE would decrease and if the permeability would change. The input parameters for this study are given in Table 6-3. In each case, the A flow mesh is the same as presented in Sections 6.2 and 6.3 for cases where $L/\ell = 6.25$. The B mesh is larger than the A mesh, and the C mesh is larger than the B mesh.

Table 6-3. Input Parameters Used in Second Series of Length-Density Studies

Flow Mesh Name	Fracture Length ℓ (Set 1 and Set 2) (cm)	Flow Region Dimensions L x L (cm x cm)	L/ℓ	Number of Fractures Per Unit Area λA (cm^{-2})
LD10 A	10	62.5 x 62.5	6.25	0.288
B	10	90 x 90	9.00	0.288
C	10	125 x 125	12.50	0.288
LD12 A	12	75 x 75	6.25	0.024
B	12	108 x 108	9.00	0.024
C	12	150 x 150	12.50	0.024
LD14 A	14	87.5 x 87.5	6.25	0.0206
B	14	126 x 126	9.00	0.0206
LD16 A	16	100 x 100	6.25	0.0180
B	16	175 x 175	10.90	0.0180

Figures 6-16 through 6-19 show the permeability plots for fracture lengths of 10, 12, 14 and 16, respectively. On each plot the mesh size, L, is the smallest for the results shown in the top frame and is larger for each succeeding frame. Figure 6-20 is a plot of NMSE versus mesh size for each fracture length studied.

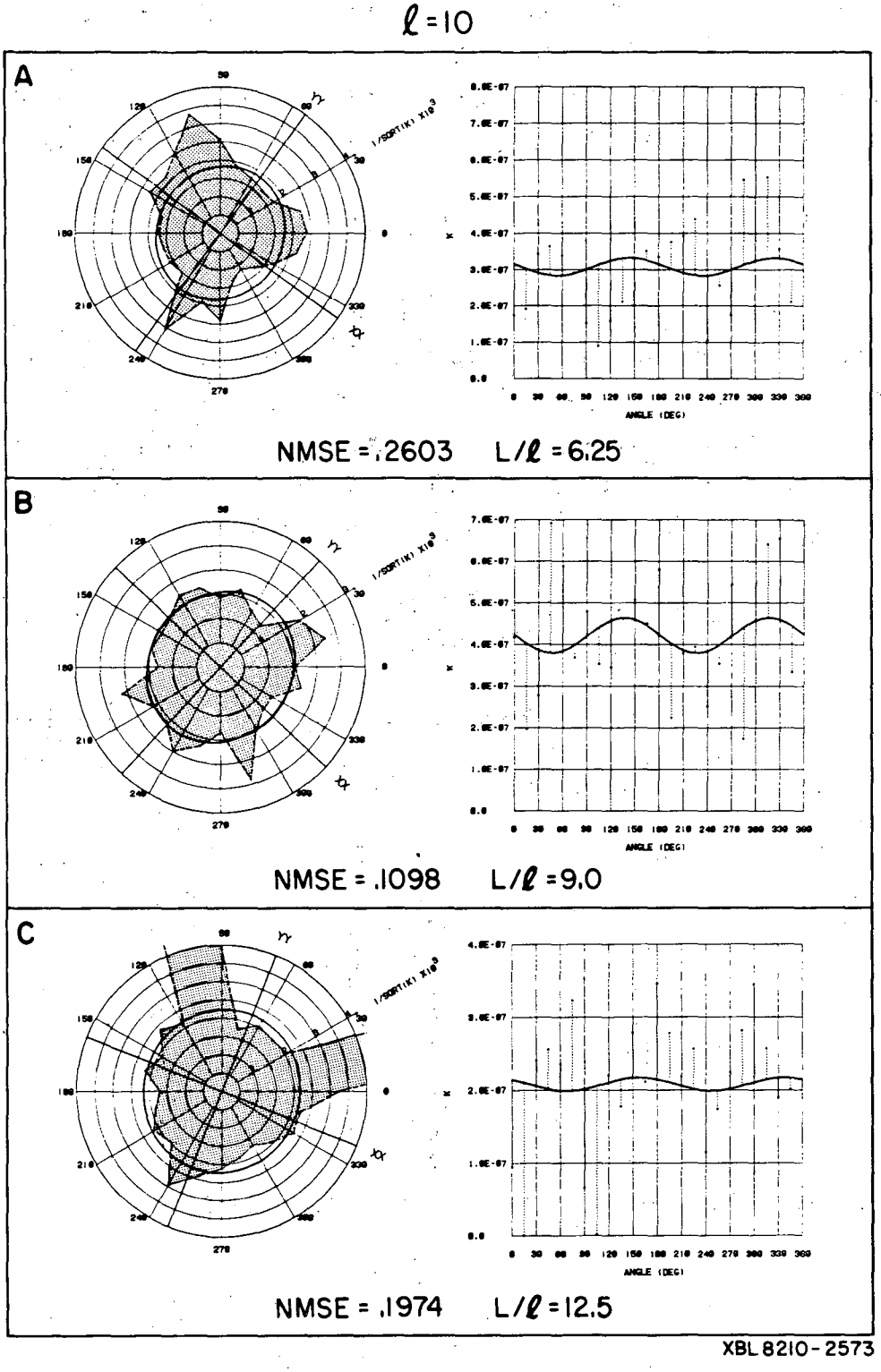

Figure 6-16. Results of Increasing the Flow Region Size for the Case of ℓ = 10, L/ℓ = 6.25, 9.0, 12.5

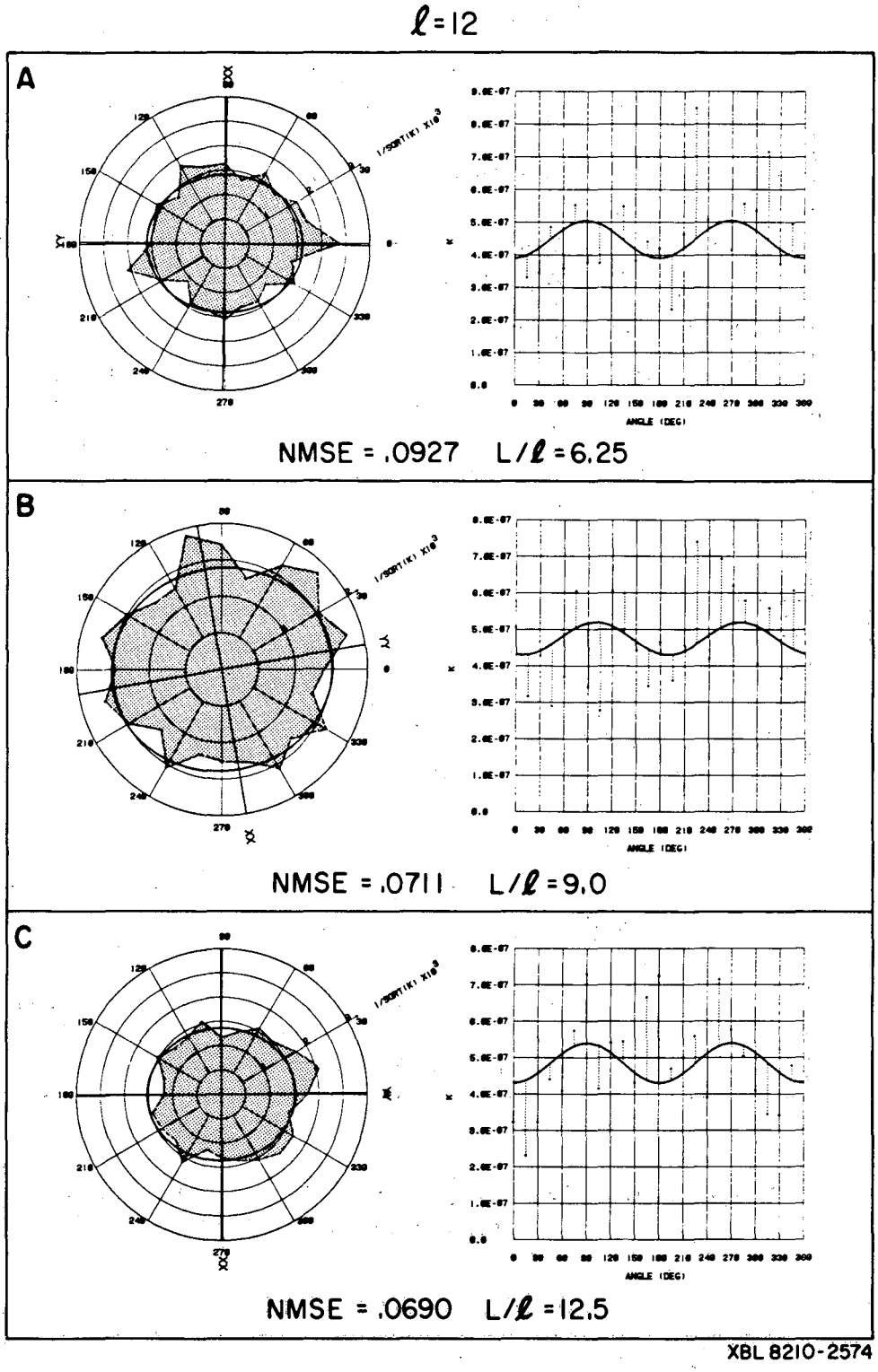

Figure 6-17. Results of Increasing the Flow Region Size for the Case of ℓ = 12, L/ℓ = 6.25, 9.0, 12.5

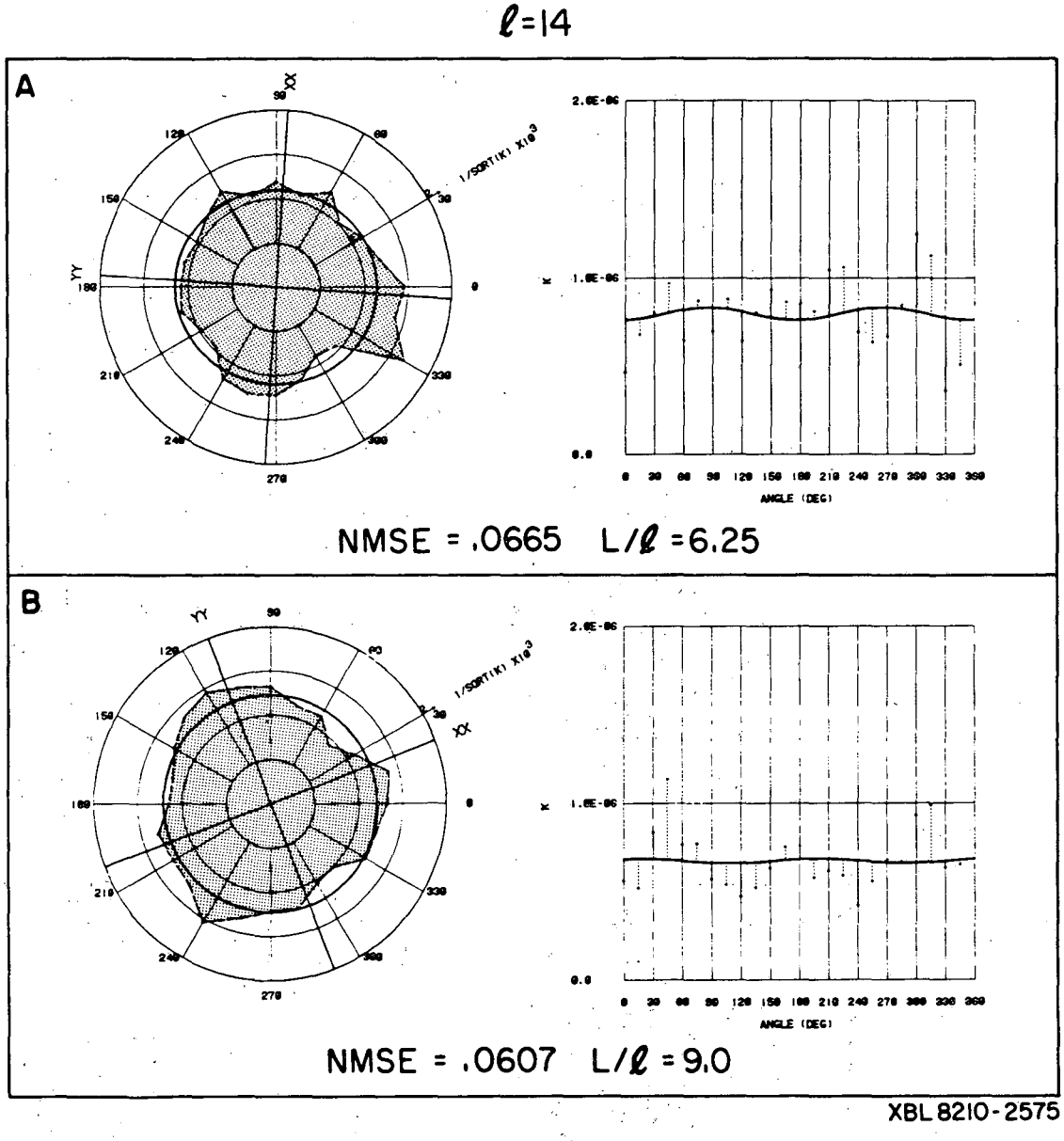

Figure 6-18. Results of Increasing the Flow Region Size for the Case of ℓ = 14, L/ℓ = 6.25, 9.0

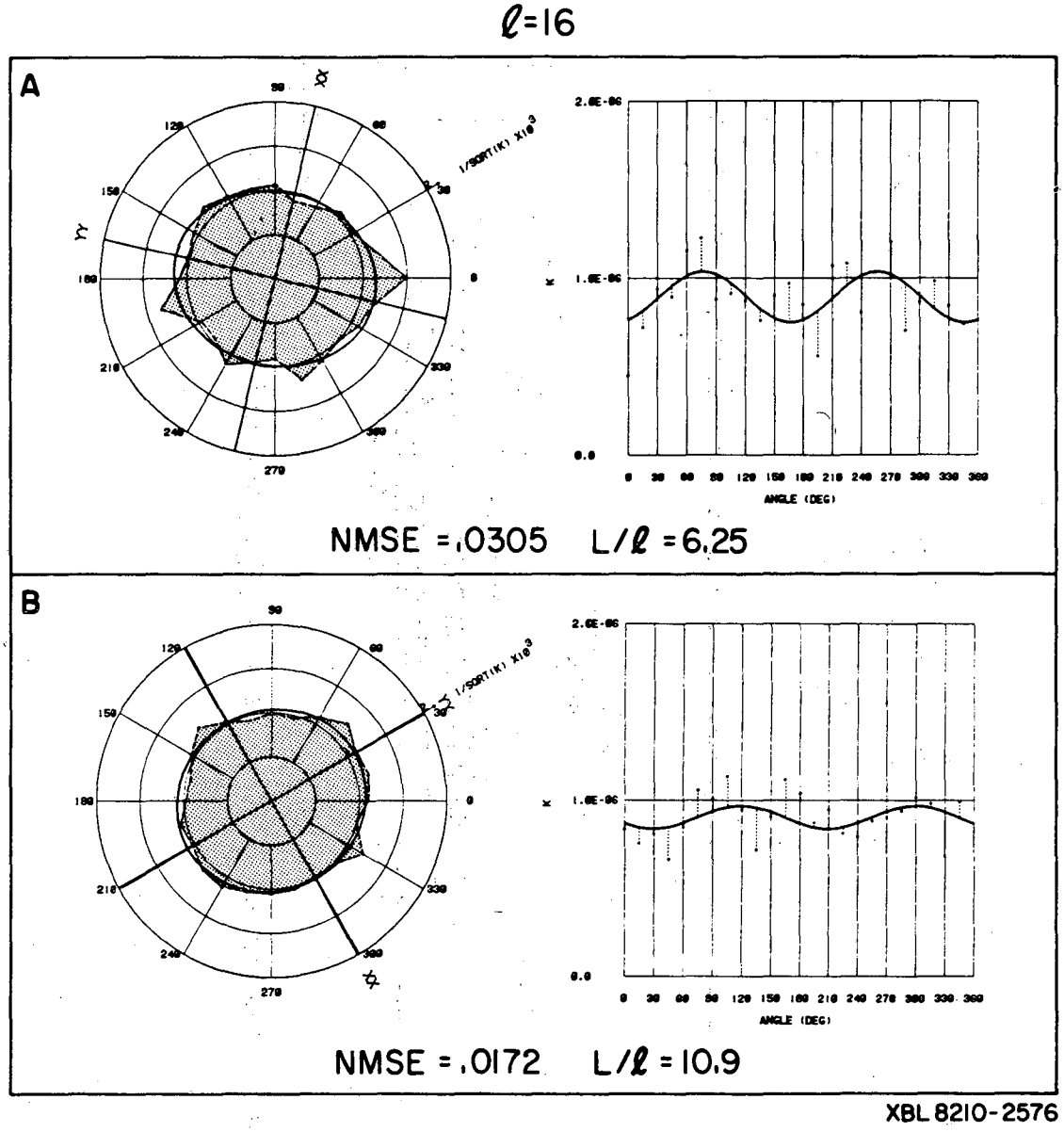

Figure 6-19. Results of Increasing the Flow Region Size for the Case of ℓ = 16, L/ℓ = 6.25, 10.9

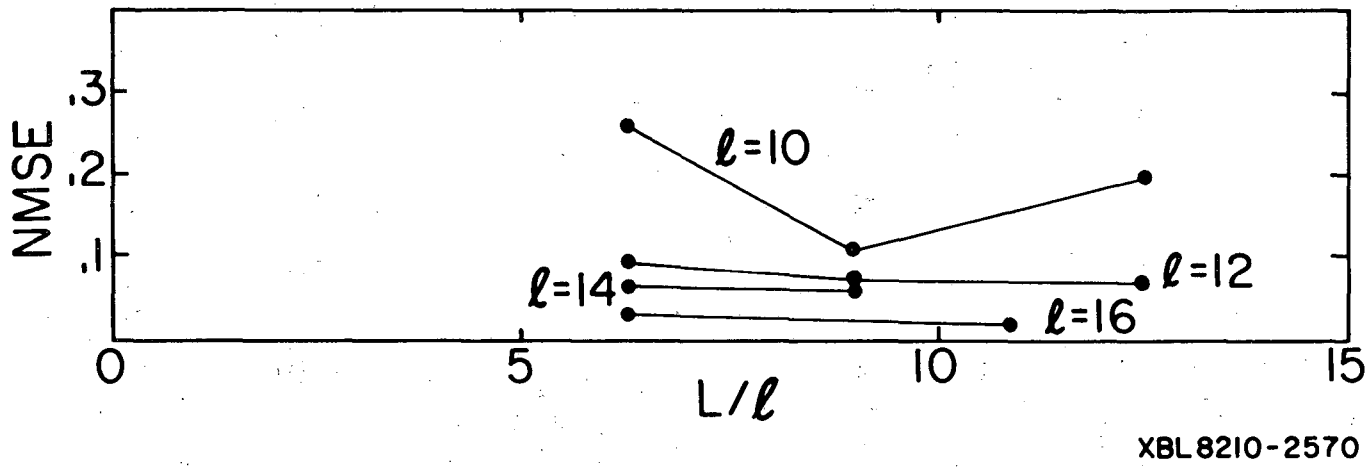

Figure 6-20. Variation in NMSE with Mesh Size for Various Fracture Lengths

In the case of ℓ = 10, increasing the flow mesh size does not consistently decrease the NMSE. Figure 6-16 shows that for L/ℓ = 9.0 the ellipse is more regular than for L/ℓ = 6.25. However for L/ℓ = 12.5, the ellipse is the least regular of the three. In fact, the values of NMSE produced by all three of these runs are within the mean plus or minus one standard deviation of NMSE found in the Monte Carlo analysis of the ℓ = 10 case in Section 6.4. Thus, for the case of ℓ = 10, increasing the mesh size may have little effect on the NMSE. For ℓ = 12, ℓ = 14, and ℓ = 16 (Figures 6-17, 18, and 19, respectively), there is a slight decrease in NMSE with increase in mesh size. The most significant decrease is for ℓ = 16 which had the lowest NMSE to begin with.

In the case of LD10B and LD16B, mesh sizes were increased such that the number of fractures in the flow region was the same as in the LD20 case described in Secton 6.3. By increasing the mesh size in this way the NMSE of LD16B became approximately equal to the NMSE of that of LD20. The NMSE of LD10B was less than that of LD10A but still greater than LD20. Furthermore, as discussed above, the NMSE increased again in LD10C, so LD10C had a value of NMSE greater than the value of NMSE for LD10A, LD10B, and LD20. Increasing the mesh size of LD10 such that it included the same or a larger number of fractures as were in LD20 did not result in lowering the NMSE to the same level as LD20.

The question of whether or not large enough samples were examined can also be addressed by looking at the change in permeability with scale of measurement. If permeability is relatively constant with scale increase, then the mesh may already be a good statistical sample and further increase in sample size will not change the conclusions.

The average of K_1 and K_2 for the first and second series versus fracture length ℓ are shown on Figure 6-21. Figure 6-22 shows all the principal permeabilities for both series versus mesh size, L. The bars on Figure 6-22 are the results of the Monte Carlo study discussed in Section 6.4. There is no substantial change in observations from Figure 6-21 versus Figure 6-11. On Figure 6-22, for all fracture lengths except ℓ = 12, K_1 and K_2 are converging to the same value with increase in mesh size. Some permeabilities increase with mesh size, some decrease. In general, increase in mesh size seems to produce random fluctuations in behavior which do not qualitatively change the observations made in Section 6.3.

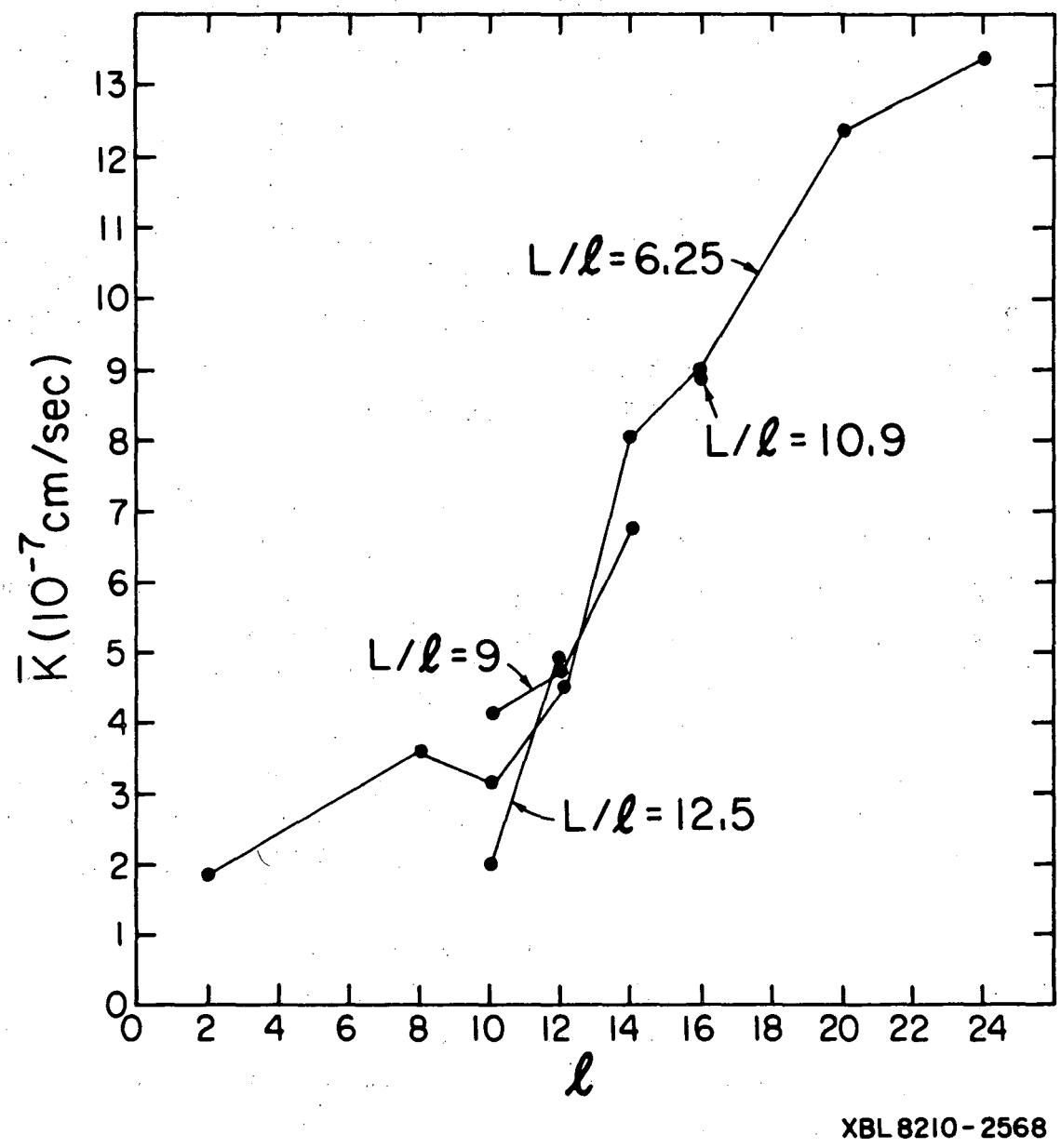

Figure 6-21. Average Permeability as a Function of Fracture Length, ℓ, for Various Ratios Between Mesh Size and Fracture Length (L/ℓ)

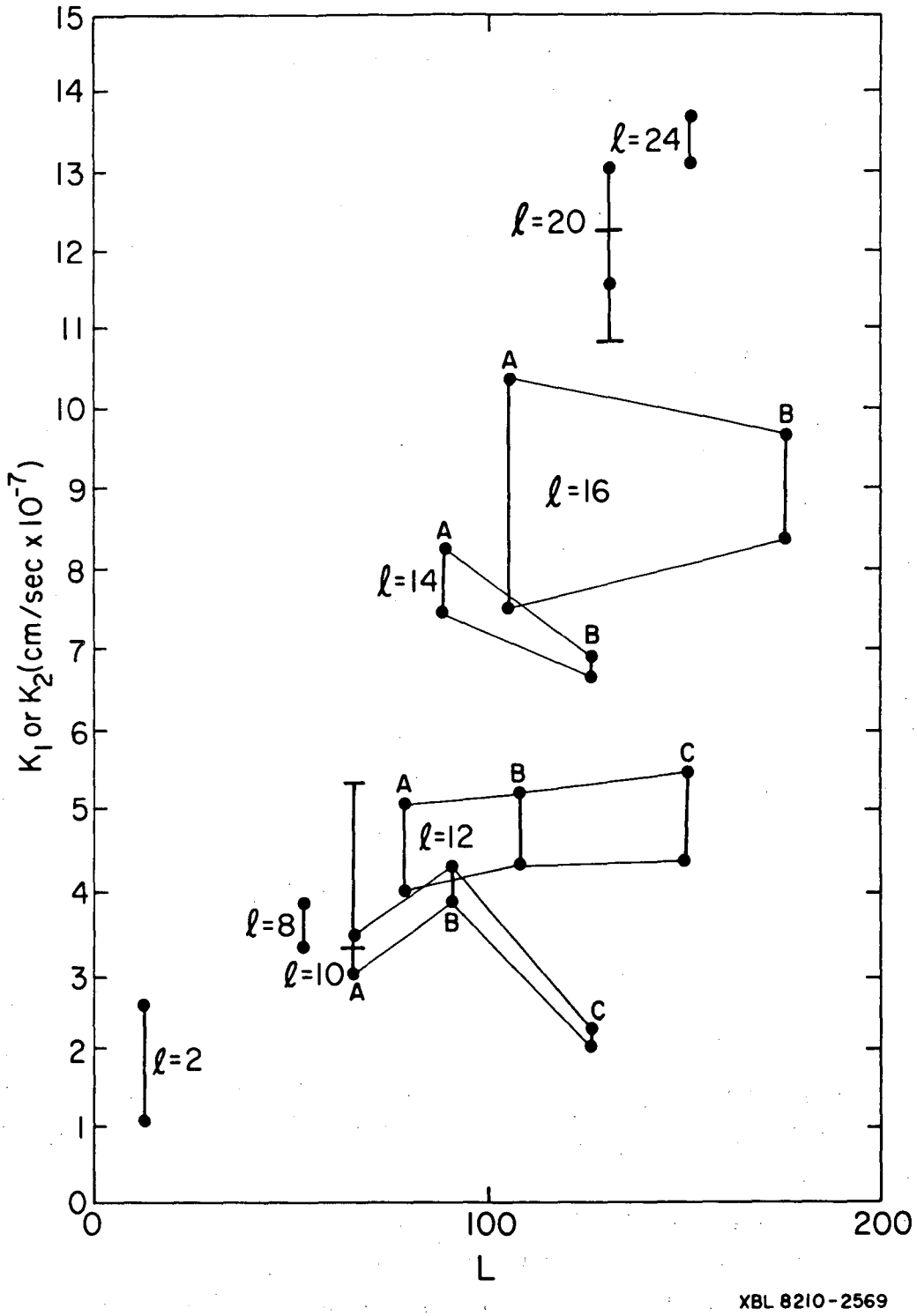

Figure 6-22. Variation in K_1 and K_2 with Mesh Size for Various Values of Fracture Length, ℓ

For the case of ℓ = 10, the Monte Carlo analysis demonstrated that the statistics used to generate this system yield permeabilities with a stable mean but a high standard deviation compared to those for the case of ℓ = 20. This section demonstrated that for ℓ = 10, the observed values of NMSE were not decreased by enlarging the scale of measurement. But, the values of K measured on larger scales are not within 2 standard deviations of the values measured on a smaller scale in the Monte Carlo analysis of LD10. Short of doing another expensive Monte Carlo analysis on a larger scale, there is no way to ensure that a larger scale of measurement would not give a different mean value of K than that previously measured. The only evidence available that LD10 was a large enough statistical sample is that the change in magnitude of K with increase in mesh size is not a clear trend: the permeability of LD10B was greater than the permeability of LD10A and the permeability of LD10C was less than LD10A (Figure 6-22).

If further increases in the scale of measurement for LD10 will not eventually decrease the NMSE, then this fracture system apparently has an inherent range in NMSE that cannot necessarily be decreased by looking at larger samples. Certainly NMSE cannot be decreased for LD2 (Figure 6-3) by considering a larger sample. In LD2 the fractures are poorly connected no matter what the scale. This concept contradicts the common assumption that all fracture systems behave as a porous medium on some scale. Some fracture systems apparently do not behave in situ like a porous medium on any scale.

6.6 REPRESENTATIVE ELEMENTARY VOLUME STUDY

The case of LD20 is a sample that does behave like a porous medium. In order to see how this behavior develops with increase in scale, the representative elementary volume (REV) study was performed. In this study, 14 different flow region sizes within the generation region were each rotated every 15° to give 24 different measurements of directional permeability. The flow regions at 0° rotation are all shown superimposed on Figure 6-23. Figures 6-24 through 6-37 show the flow region and the reduced flow region at 0° rotation, the ellipse, and the permeability plots for each of the flow mesh sizes.

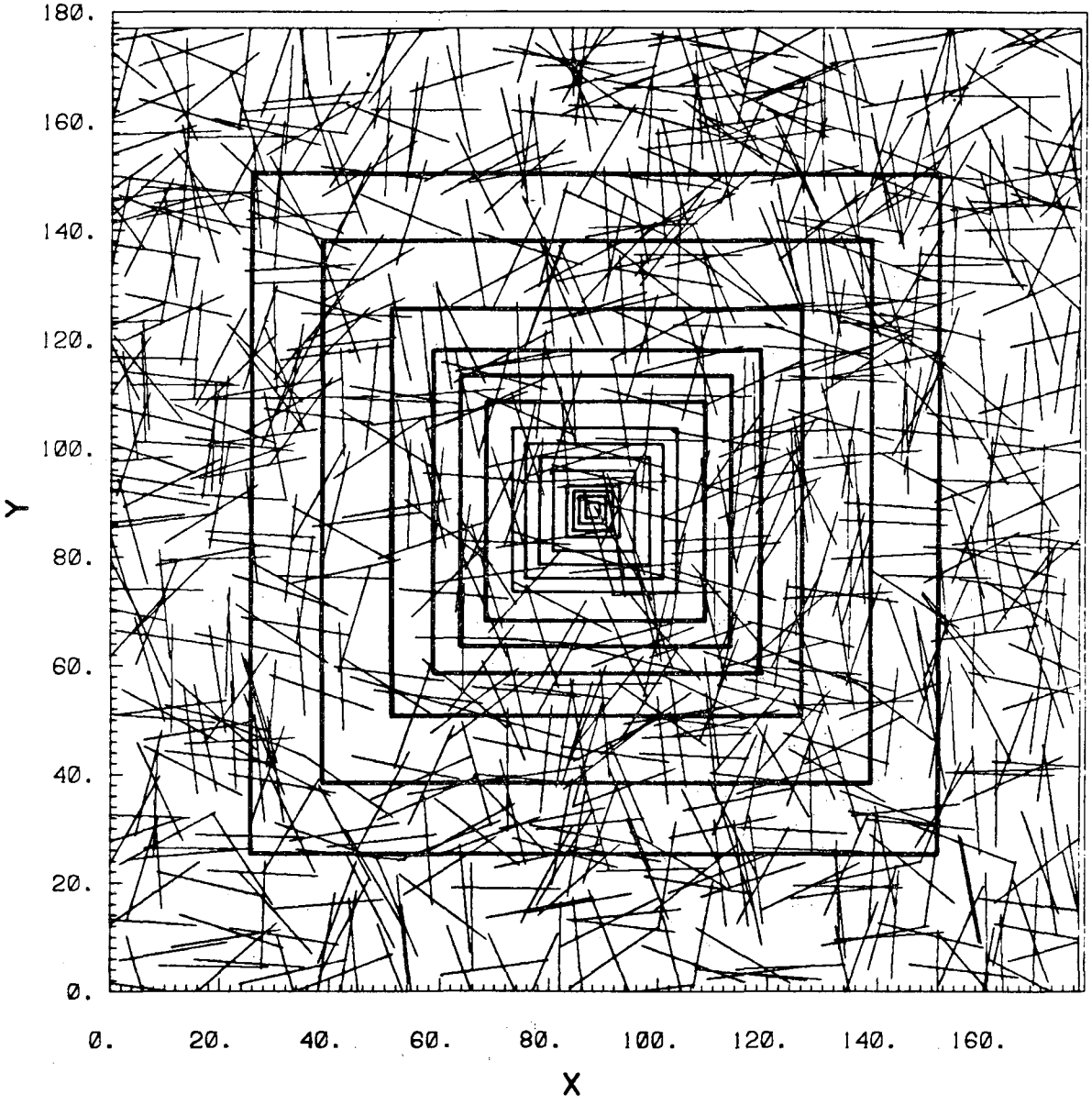

XBL 8210-2525

Figure 6-23. Flow Region Sizes at 0° Rotation for the REV Study for the Case of ℓ = 20

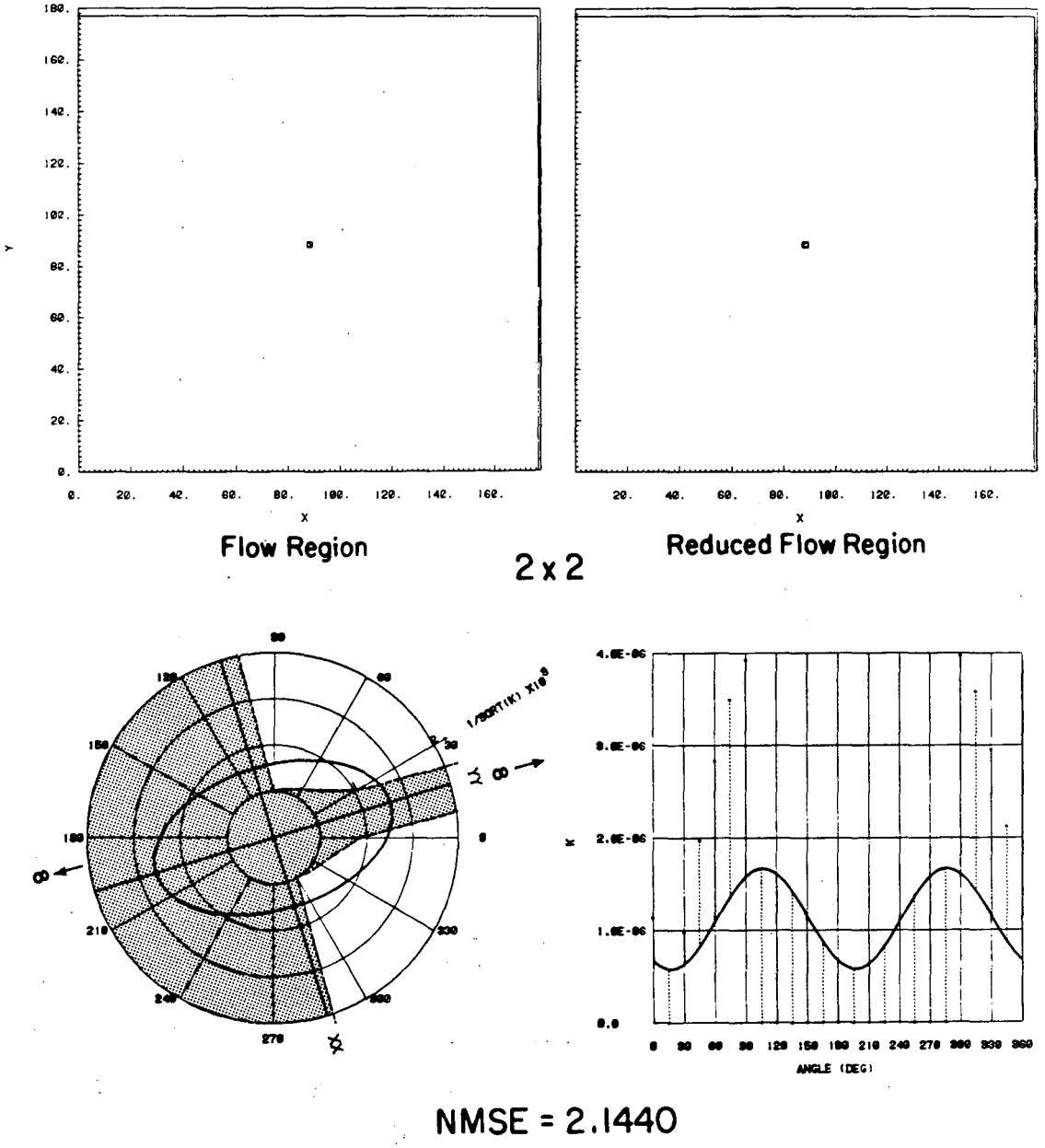

Figure 6-24. Results of REV Study with ℓ = 20 for Flow Region of 2 x 2 cm

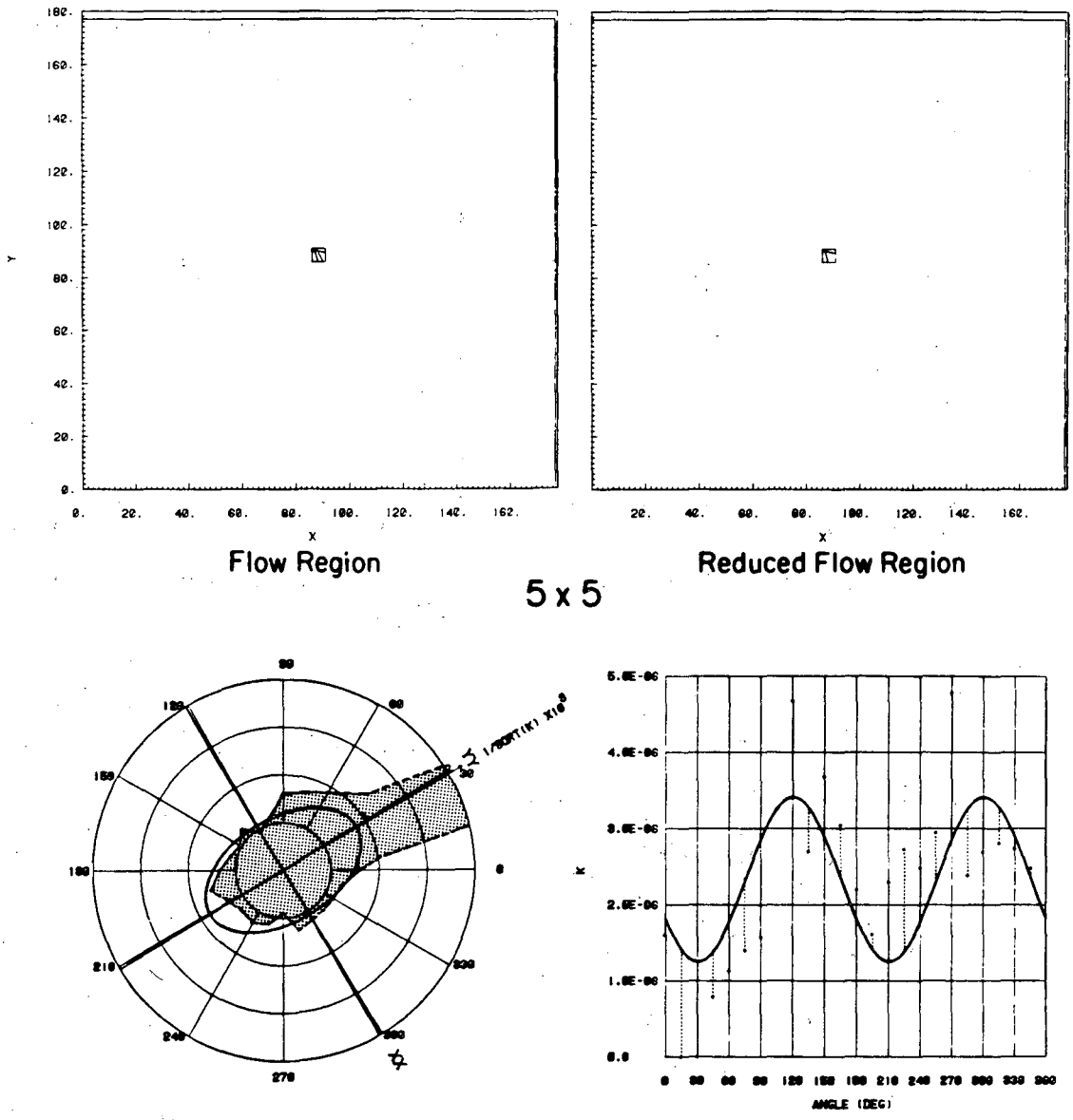

Figure 6-25. Results of REV Study with ℓ = 20 for Flow Region of 5 x 5 cm

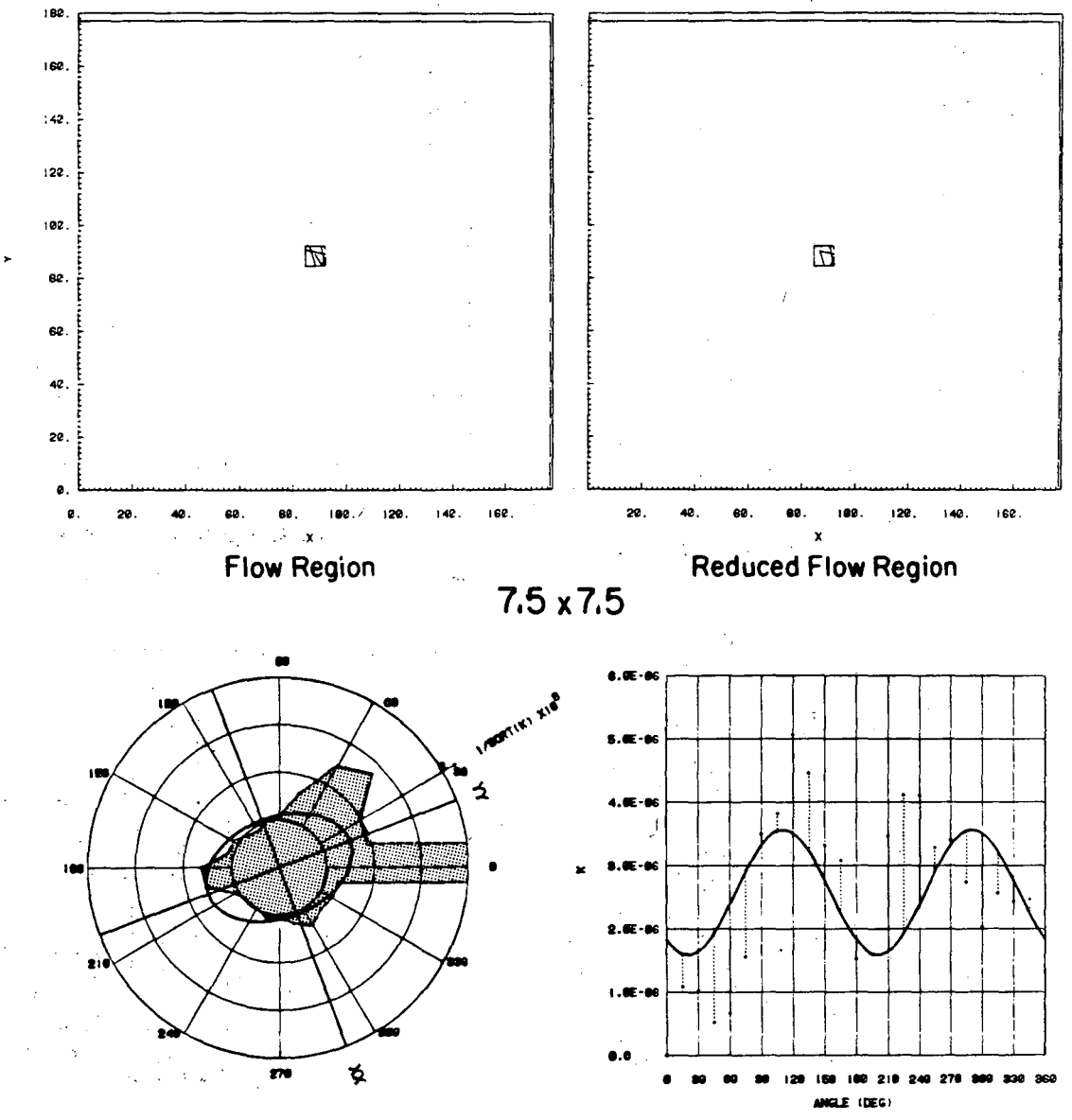

Figure 6-26. Results of REV Study with ℓ = 20 for Flow Region of 7.5 x 7.5 cm

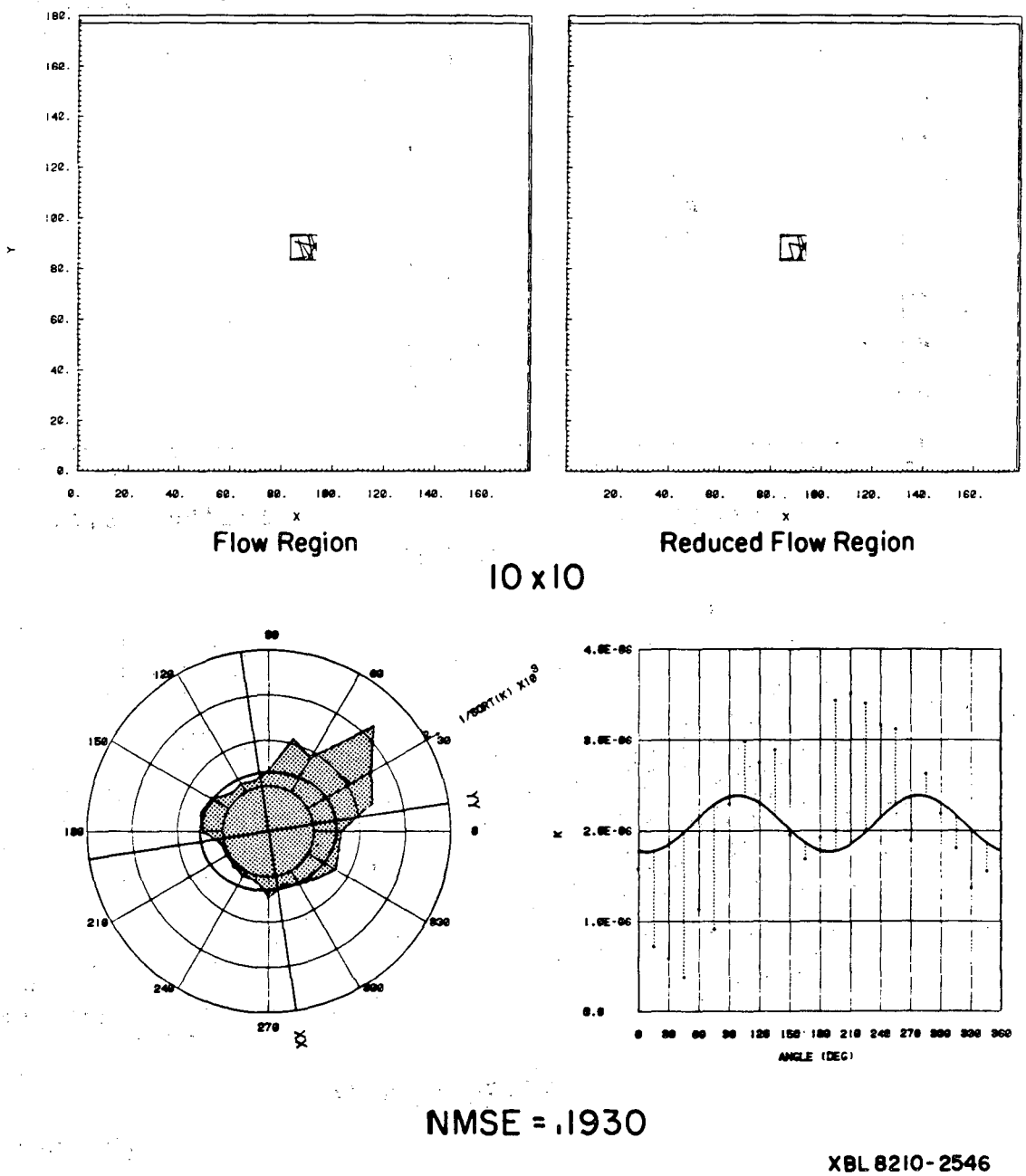

Figure 6-27. Results of REV Study with ℓ = 20 for Flow Region of 10 x 10 cm

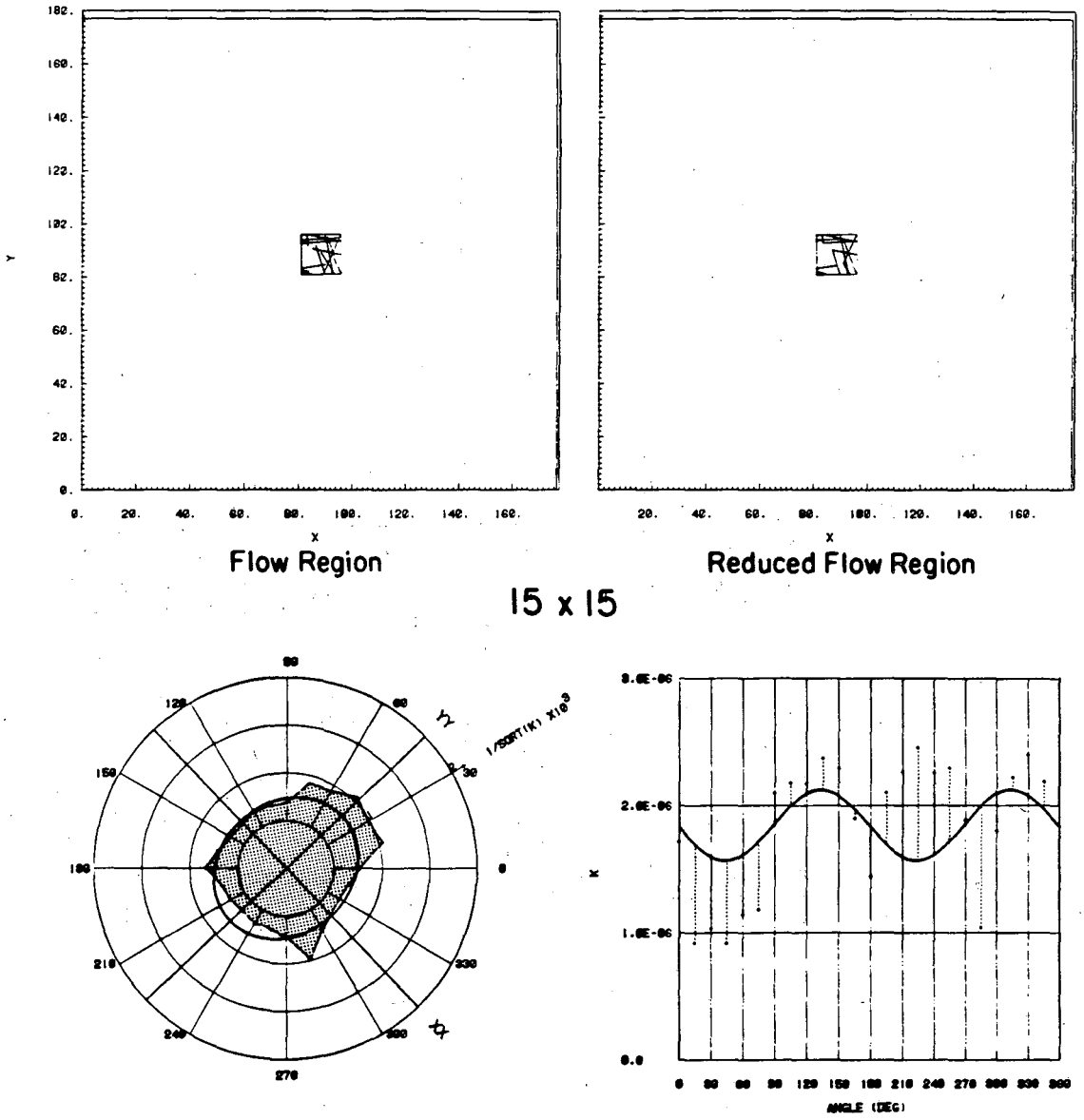

Figure 6-28. Results of REV Study with ℓ = 20 for Flow Region of 15 x 15 cm

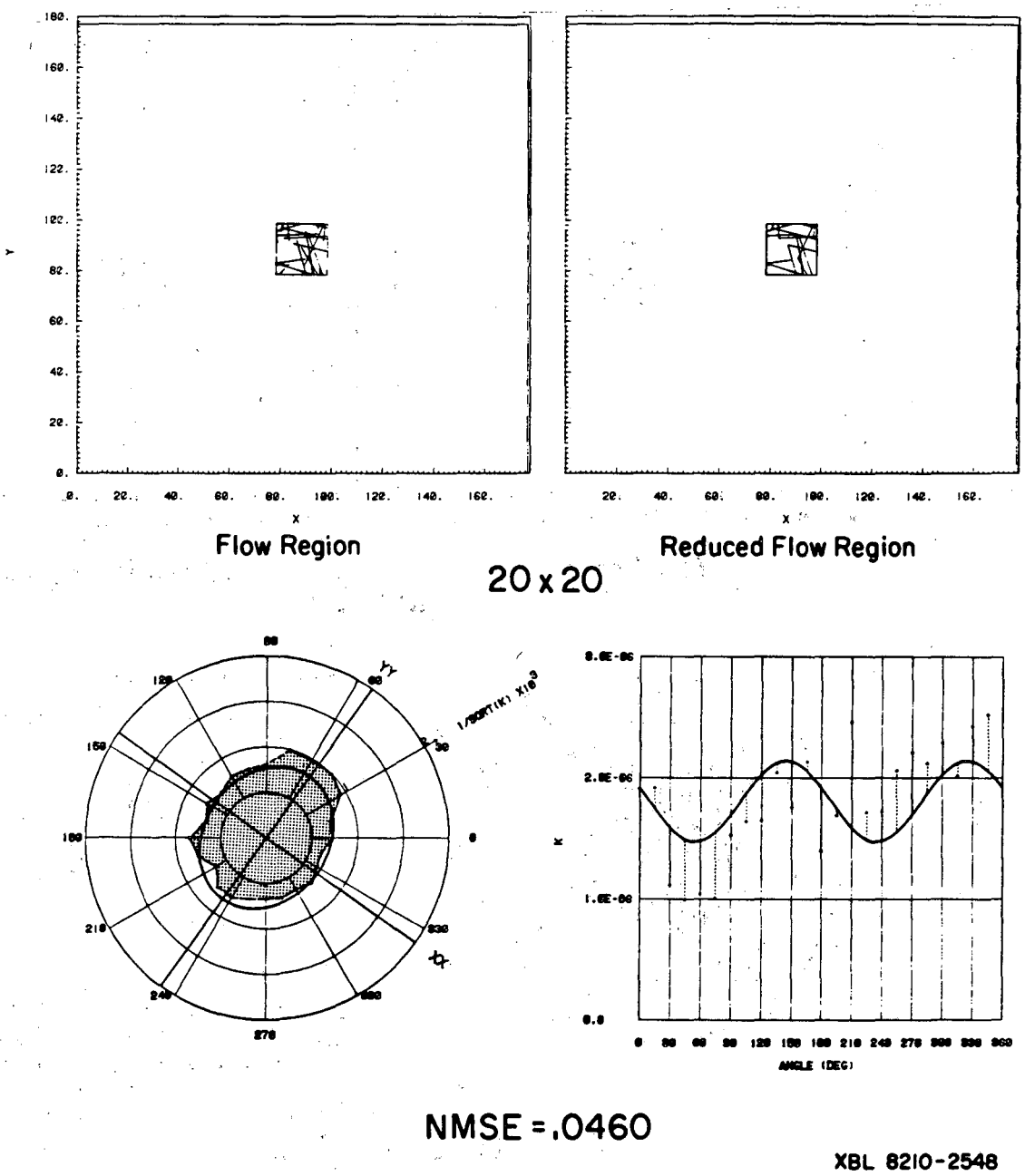

Figure 6-29. Results of REV Study with ℓ = 20 for Flow Region of 20 x 20 cm

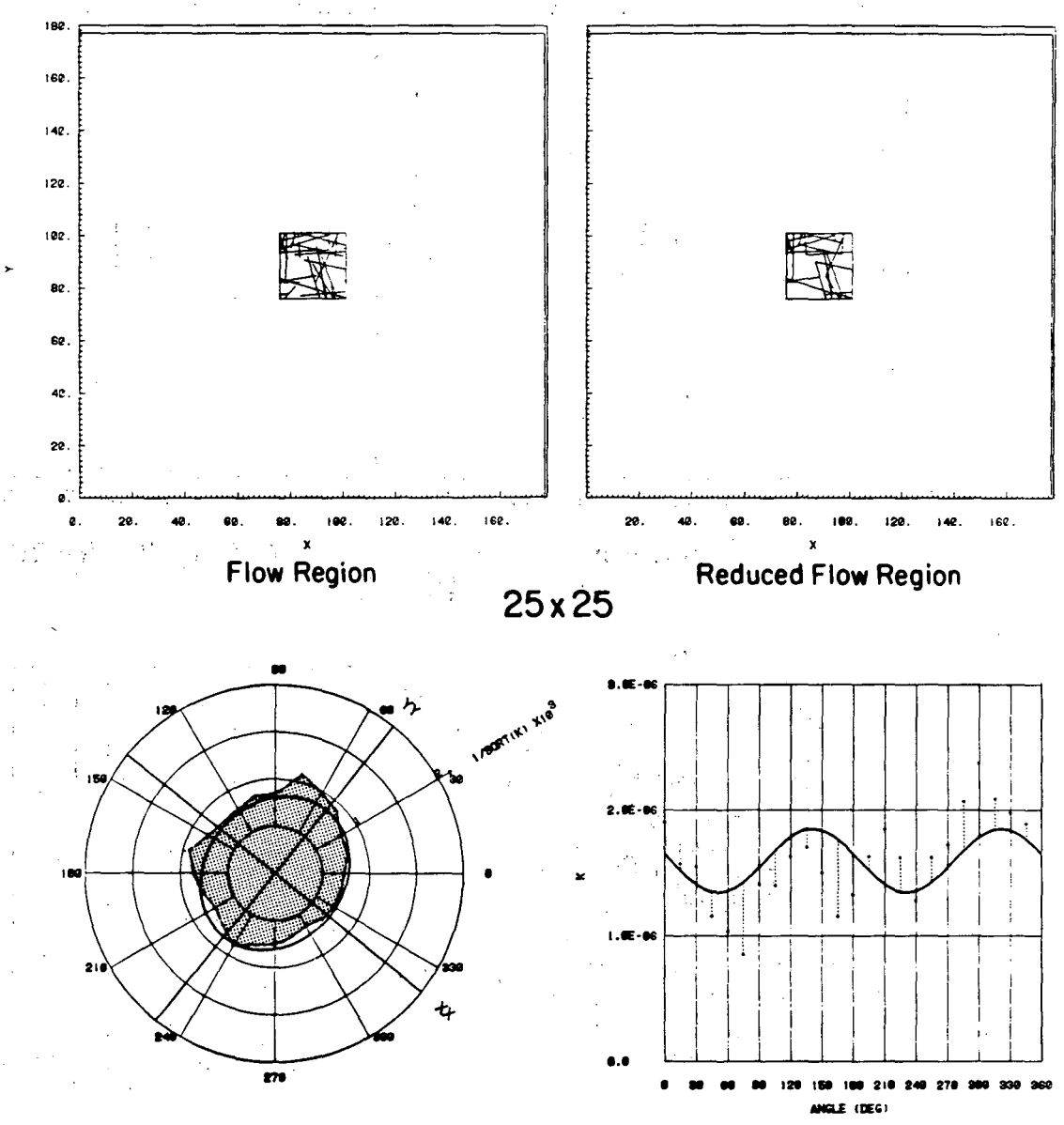

Figure 6-30. Results of REV Study with ℓ = 20 for Flow Region of 25 x 25 cm

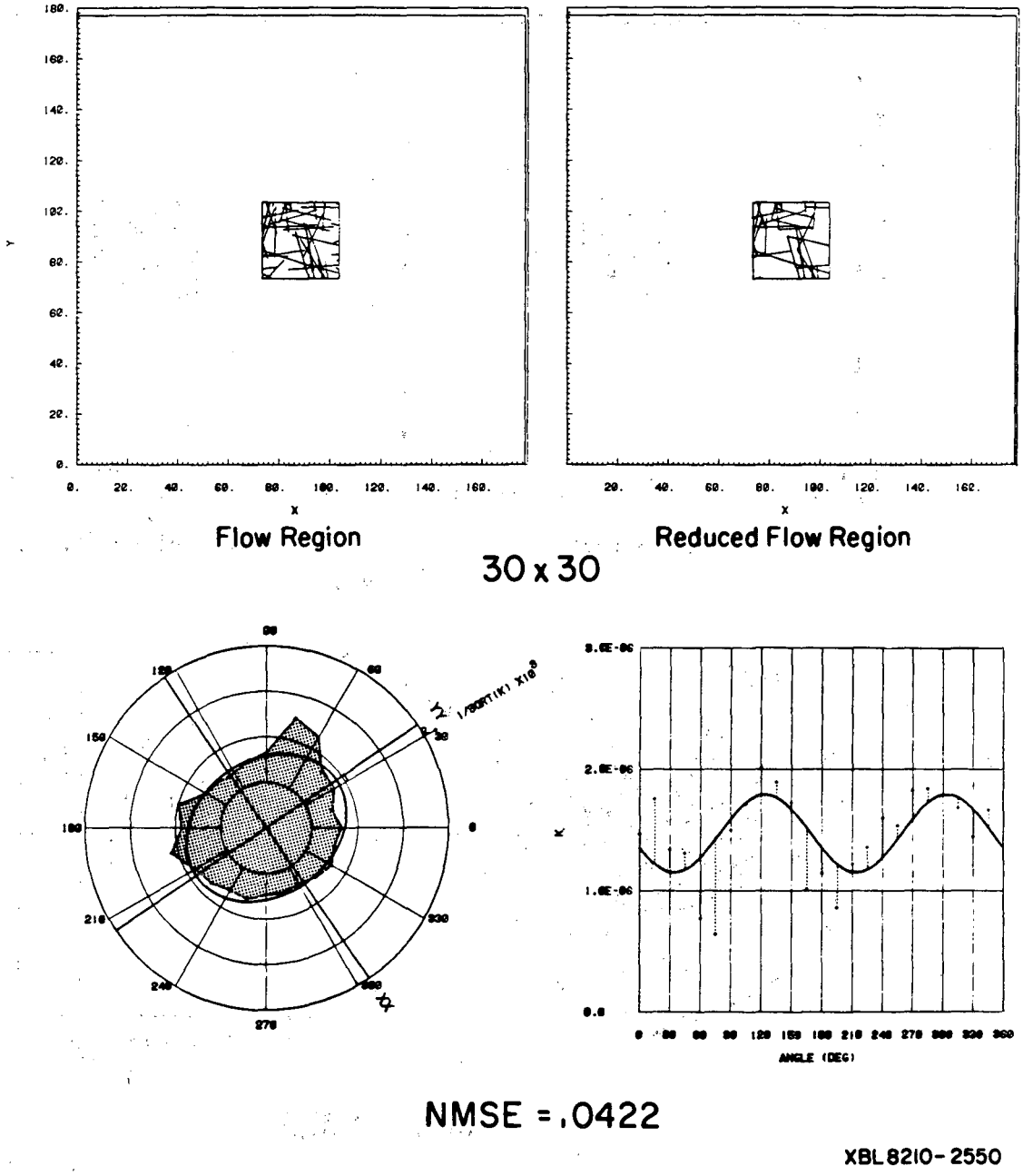

Figure 6-31. Results of REV Study with ℓ = 20 for Flow Region of 30 x 30 cm

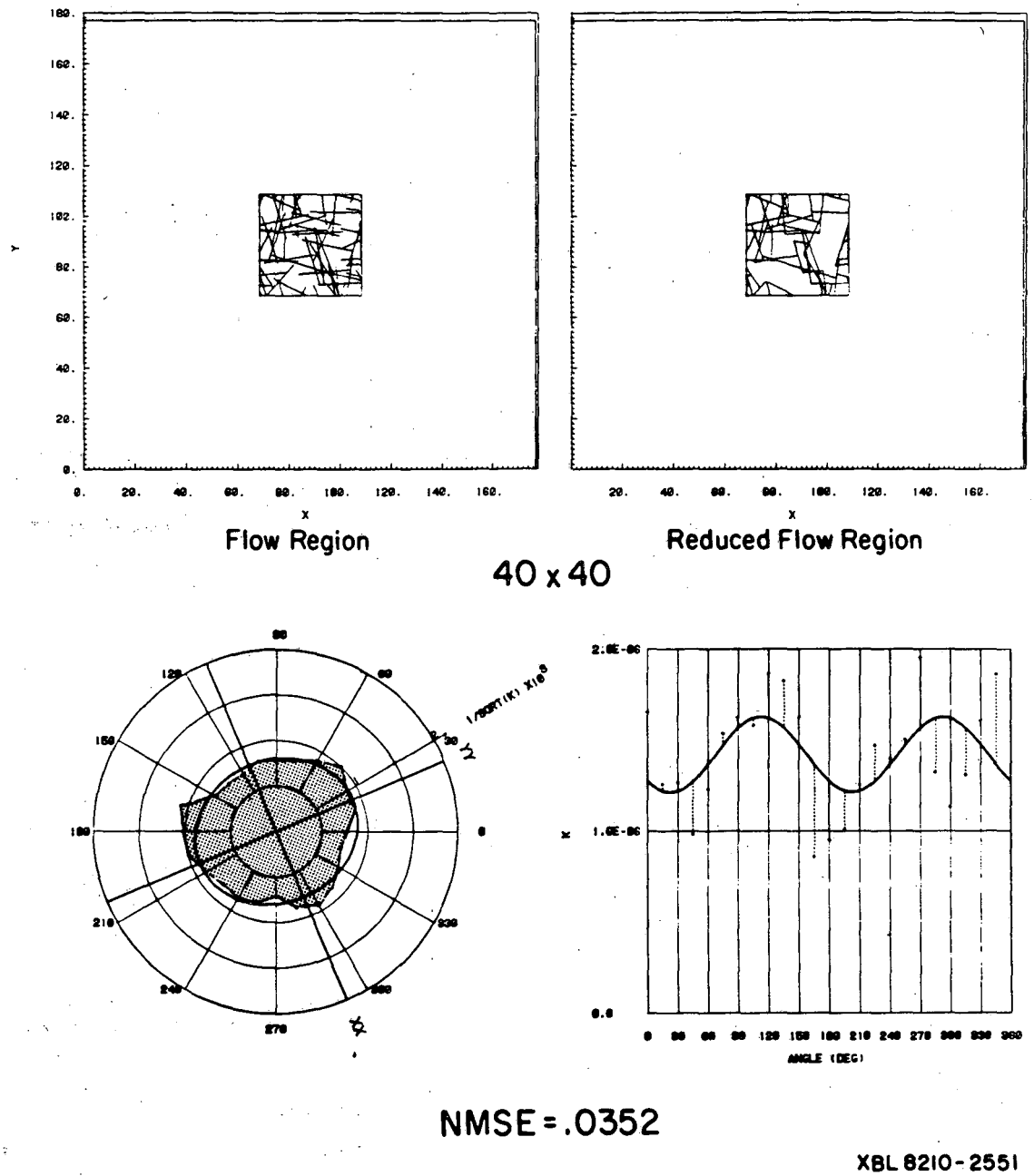

Figure 6-32. Results of REV Study with ℓ = 20 for Flow Region of 40 x 40 cm

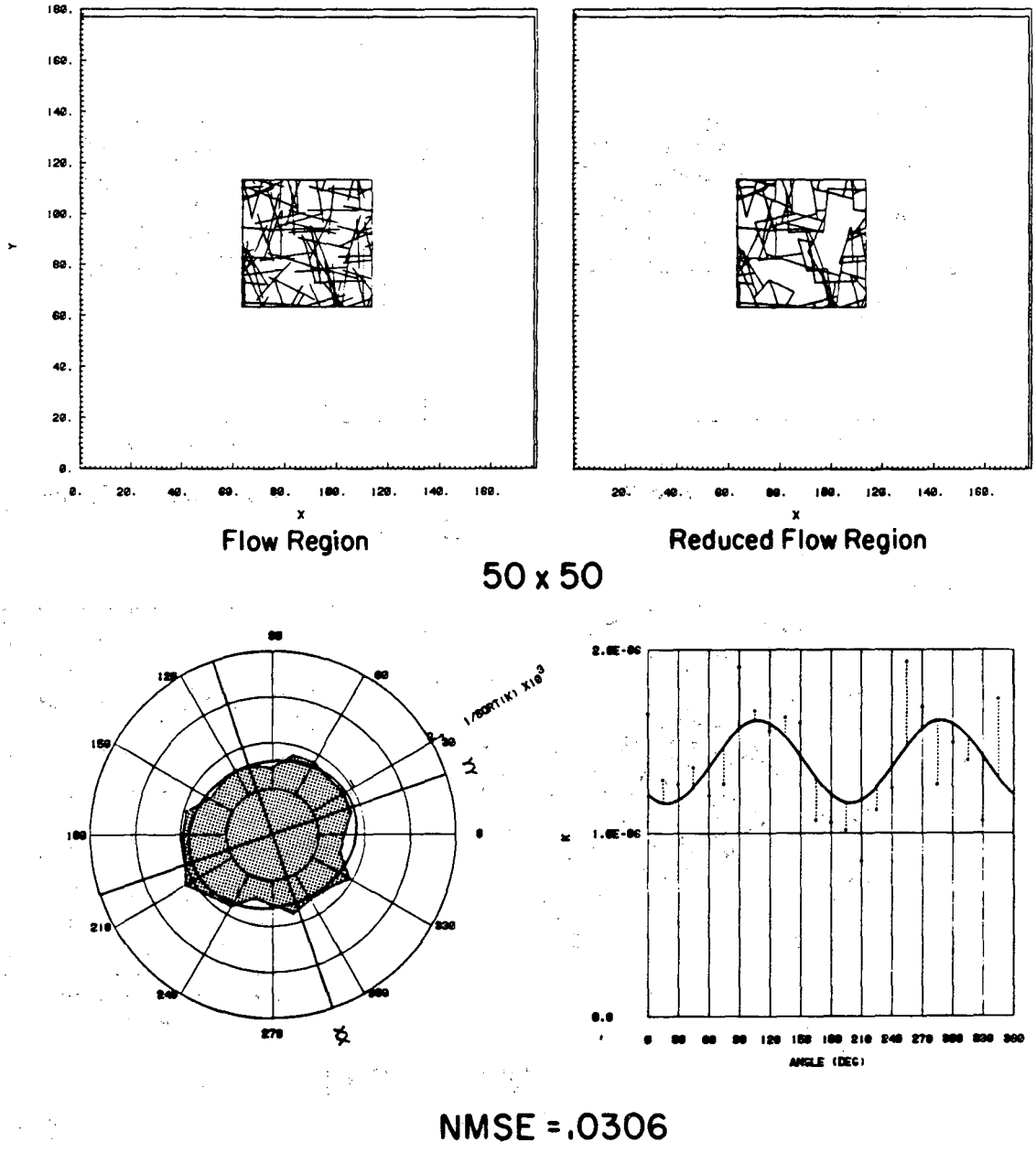

Figure 6-33. Results of REV Study with ℓ = 20 for Flow Region of 50 x 50 cm

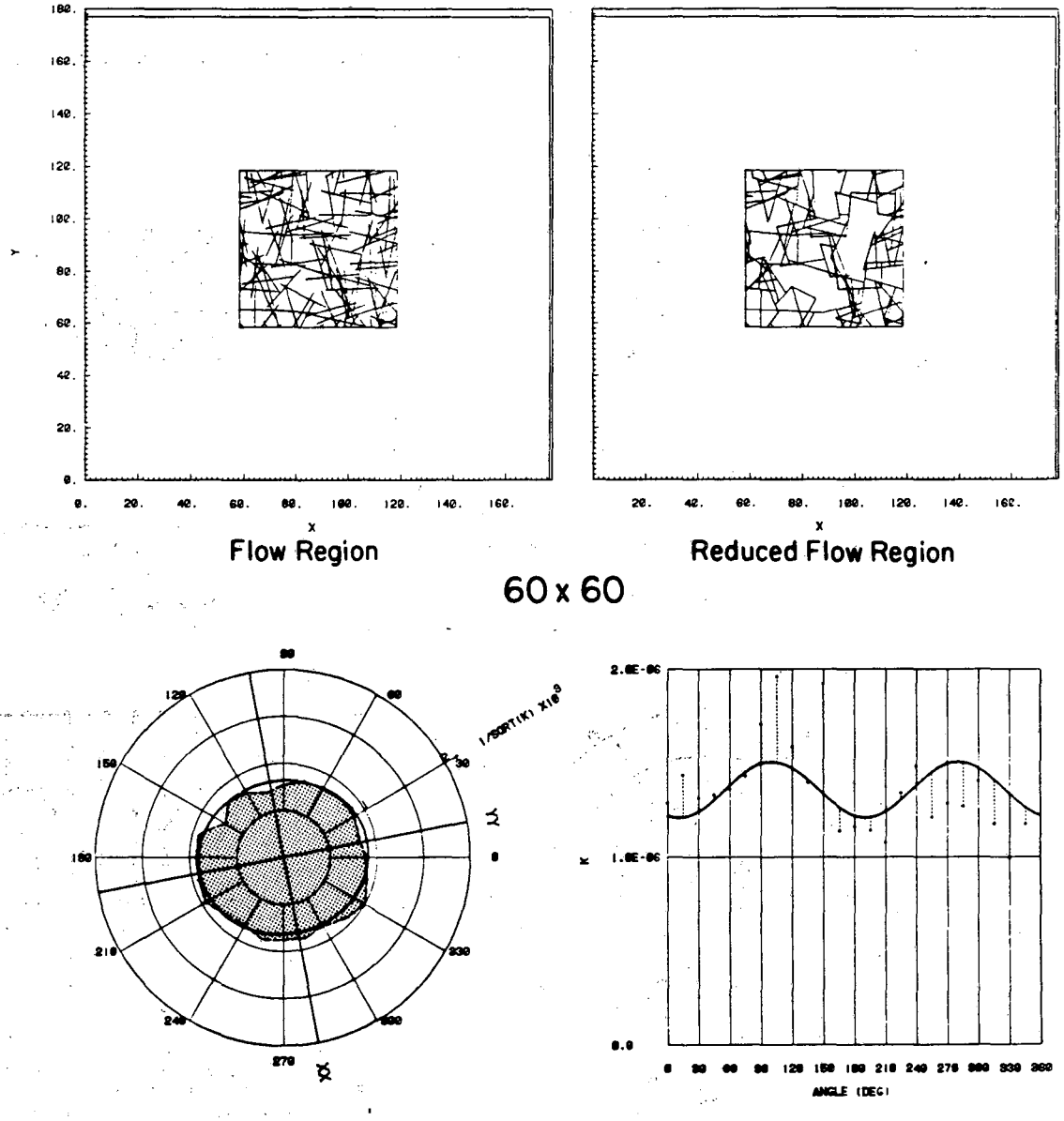

Figure 6-34. Results of REV Study with ℓ = 20 for Flow Region of 60 x 60 cm

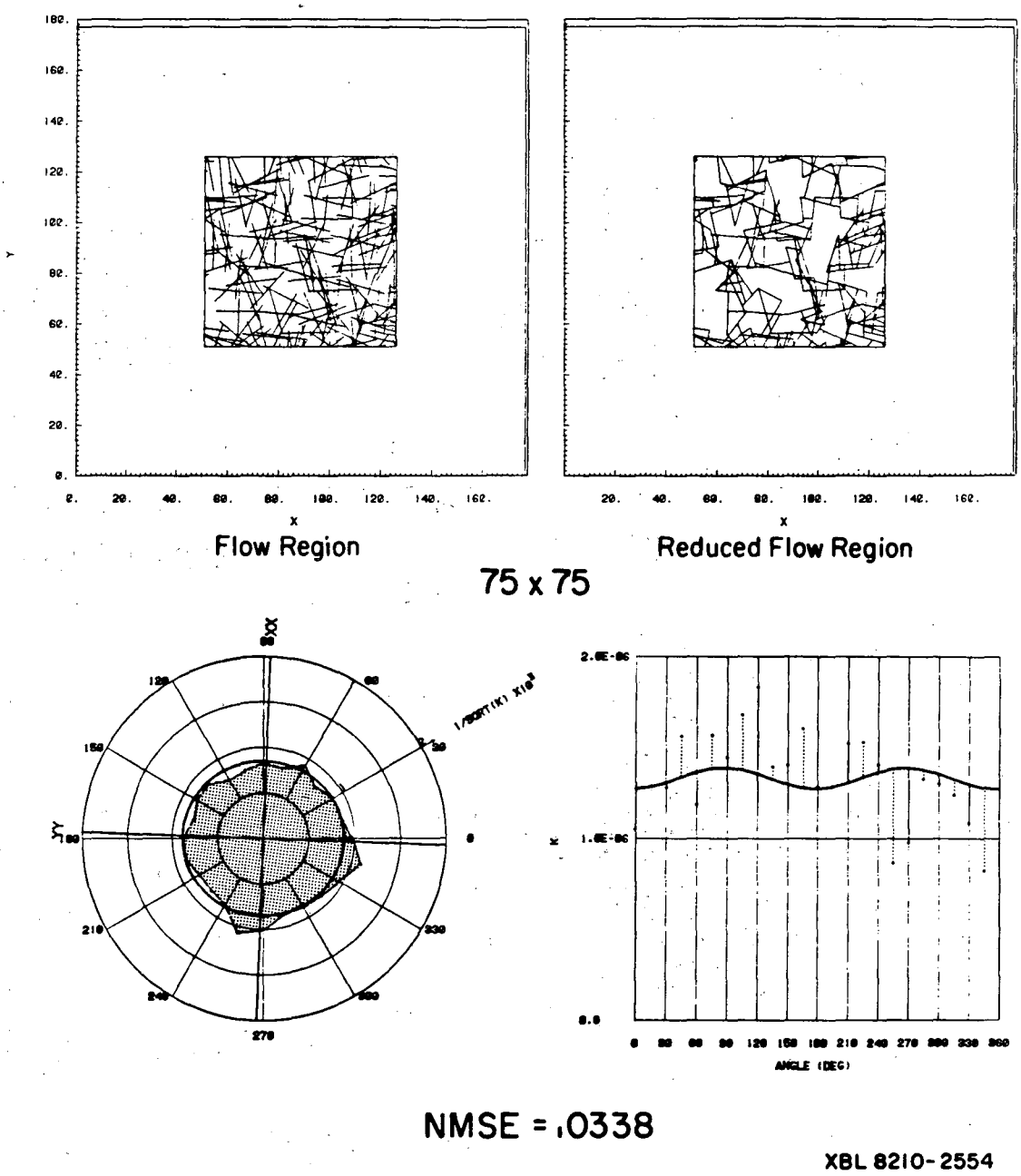

Figure 6-35. Results of REV Study with ℓ = 20 for Flow Region of 75 x 75 cm

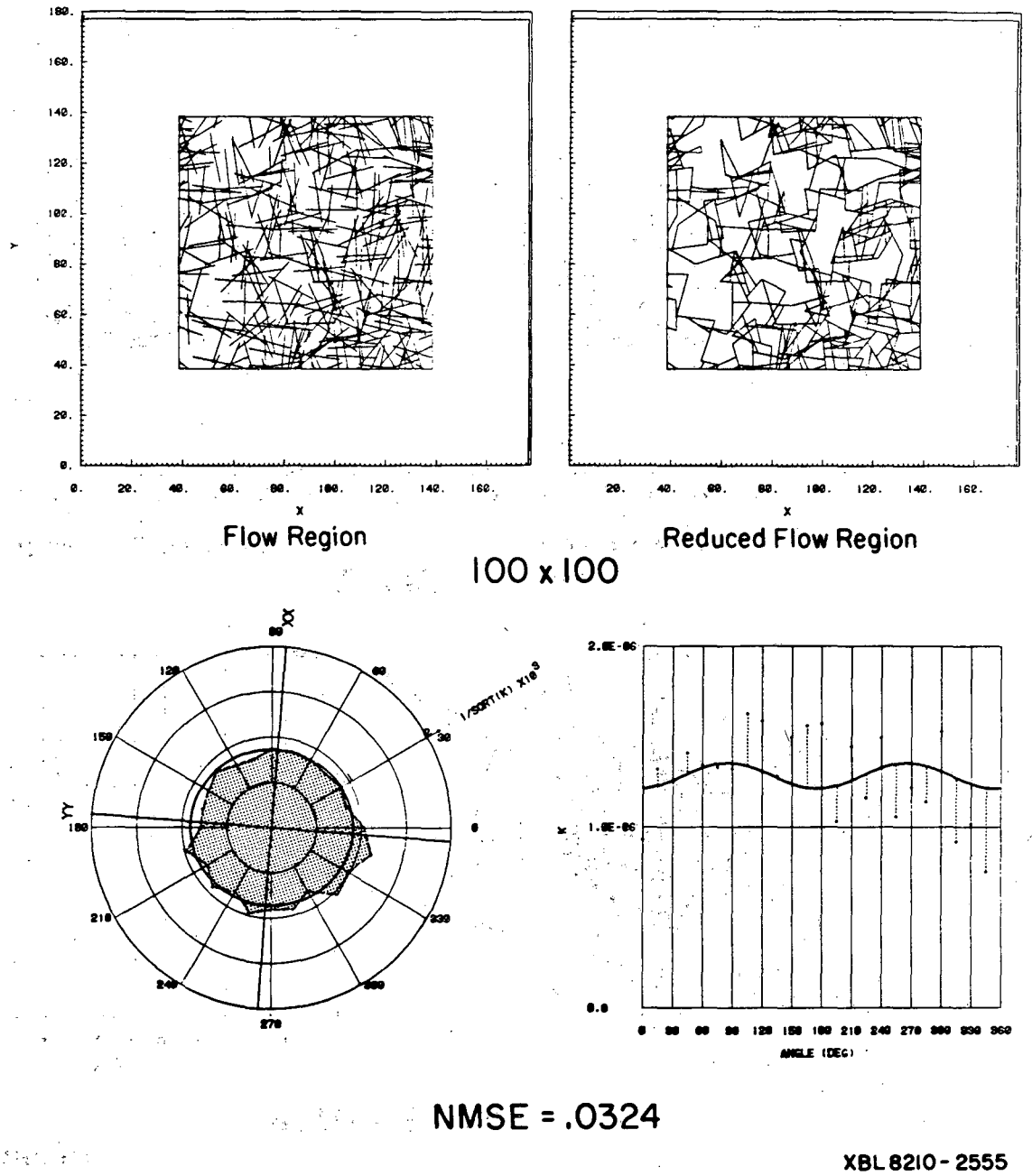

Figure 6-36. Results of REV Study with ℓ = 20 for Flow Region of 100 x 100 cm

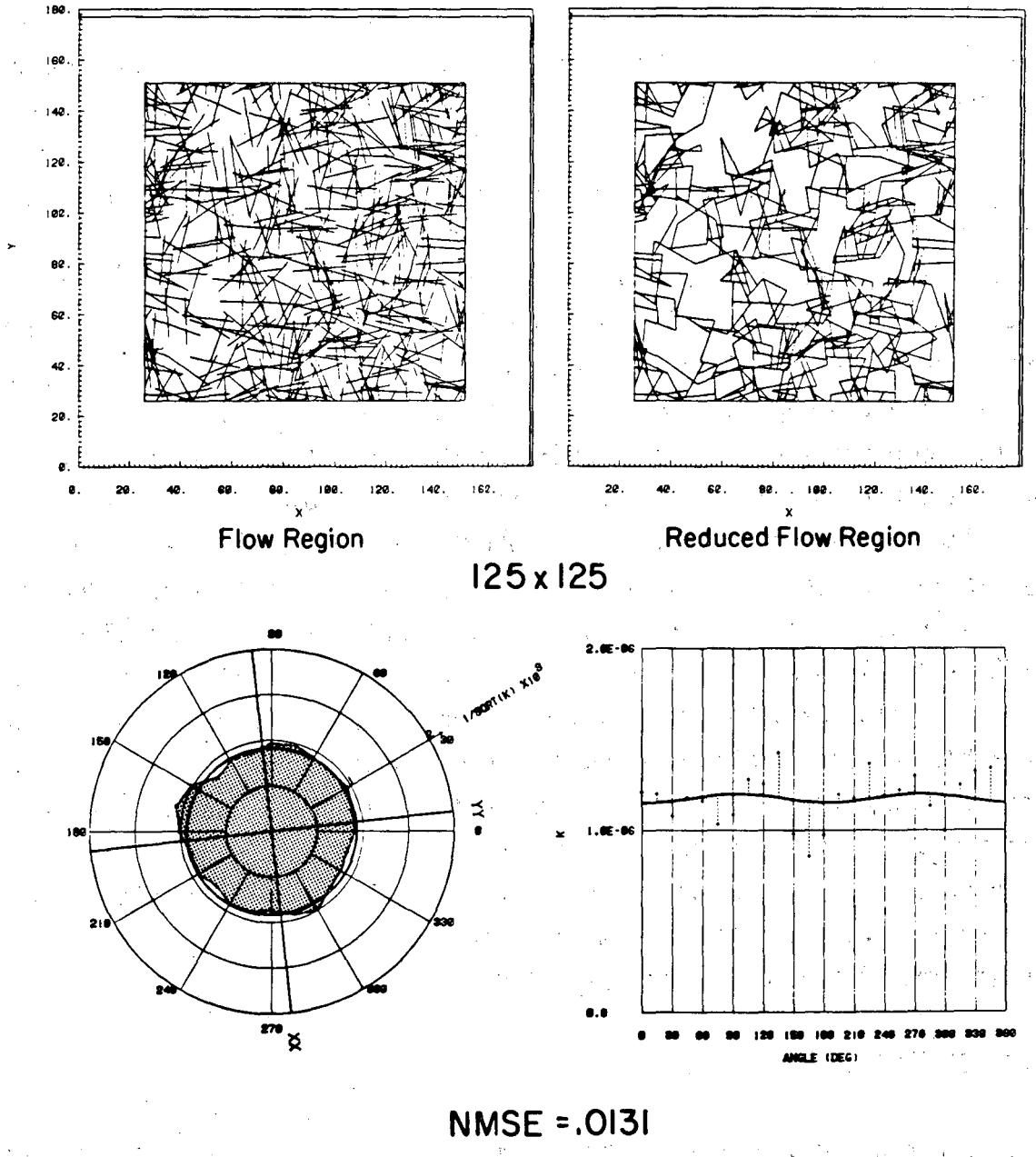

Figure 6-37. Results of REV Study with ℓ = 20 for Flow Region of 125 x 125 cm

Figure 6-38 shows plots of normalized mean fracture length in the flow region, NMSE, and K_1 and K_2 versus flow mesh area. The NMSE values are less than 0.05 for all flow regions greater than 400 cm^2. Thus large samples are not necessary for symmetric permeability tensors. At this scale of observation, however, permeability is still oscillating. Mesh sizes greater than about 1,000 cm^2 are needed to avoid rapid oscillation of K with mesh size. Beyond mesh sizes of about 1,000 cm^2, the value of K_1 and K_2 slowly decline. K_1 and K_2 converge to the same value when the area is 15,625 cm^2. Normalized mean fracture length, $\bar{\ell}/20$, has achieved most of its increase by about 9,000 cm^2. The value $\bar{\ell}/20$ in an infinite sample is 1.0, but in finite samples some fractures are always truncated, so $\bar{\ell}/20$ is always less than 1.0. Thus in this case, representative values of NMSE and permeability are observed in samples which are much smaller than a good statistical sample.

The question of what size mesh should be used for this particular fracture system in a regional ground-water model can be addressed using Figure 6-38. Any block size greater than 1,000 cm^2 would probably be acceptable since the NMSE is fairly stable in this range. However, block sizes greater than 5,000 cm^2 would provide a better estimate of permeability. Block sizes as large as possible are preferable in a regional model because they are less expensive to analyze. Constraints of the problem region must also be taken into account. Gradients in the region must be linear on the scale of the block sizes in order to have an accurate numerical solution. Thus Figure 6-38 provides information on the minimum acceptable block size, but the regional problem provides the constraint of the maximum acceptable block size.

6.7 CONCLUSIONS

The study described in this chapter was designed to see if permeability could be determined from the fracture frequency in a borehole without knowing the actual length distribution and actual fracture density. For small values of fracture length, the fracture length must be known in order to predict the permeability. For fracture systems where all boreholes intersect the same number of fractures per unit length, those with shorter fracture lengths and higher density will have lower permeability than those with longer fracture lengths and lower density. Furthermore, fracture systems with shorter

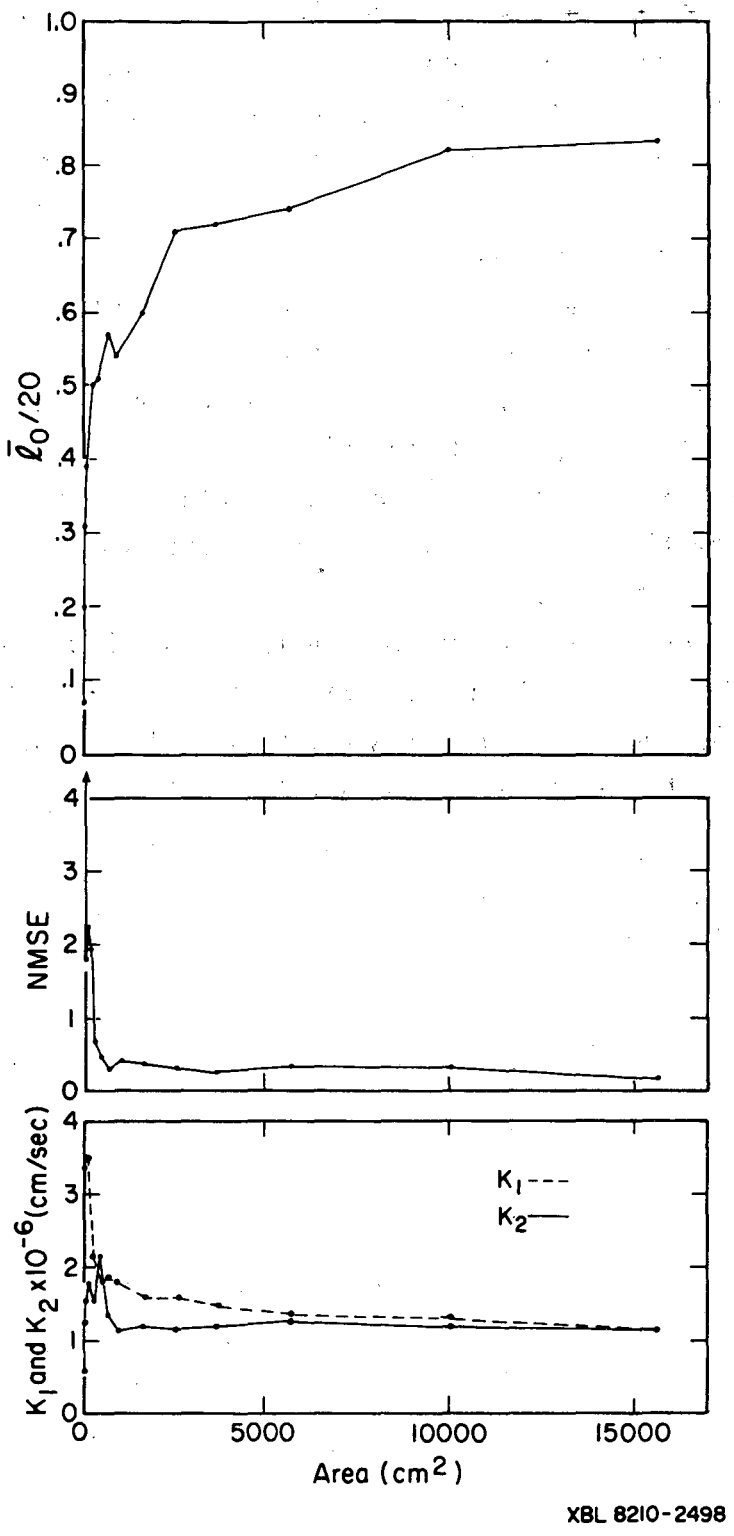

Figure 6-38. Summary of Results of REV Study with ℓ = 20

fractures behaved less like porous media than fracture systems with longer lengths. The measured values of permeability and NMSE were much more strongly linked to fracture length than to sample size. Thus if a fracture system does not behave like a porous medium on one scale, increasing the scale of observation may do little to improve the behavior. Intuitive prediction of these results would not have been easy.

For large values of fracture length, the increase in permeability with increase in fracture length may become negligible. For fractures longer than a certain minimum, it would not be necessary to exactly specify the length and fracture density. Specification of the fracture frequency as measured in a borehole along with the aperture and orientation distributions would be sufficient. However, this trend could not be confirmed because of the size limitations of the computer.

The numerical study that was performed was based on an isotropic system of fractures with constant apertures. However the general trend in behavior exhibited by these isotropic systems should also be observed in anisotropic systems and in systems with distributed apertures.

7 USE OF FIELD DATA FROM THE UNDERGROUND RESEARCH LABORATORY

7.1 INTRODUCTION

The Lac du Bonnet granitic batholith in the Canadian Province of Manitoba is the site of investigations for the Canadian Nuclear Fuel Waste Management Program. As part of this program, Atomic Energy of Canada Limited (AECL) is conducting hydrologic research at the Underground Research Laboratory (URL) site in the Lac du Bonnet batholith.

This chapter describes two studies in which hydrogeologic data from this site were used in the existing two-dimensional model of permeability. The analysis serves as an example of the application of field data to the model and what can be learned about the site from even limited amounts of data. Types of field data which could be used to further this analysis are discussed in Appendix A.

In the first study, the effect of a correlation between length and aperture was examined. Models were created in which length and aperture are both correlated and uncorrelated. When length and aperture are correlated, the longer fractures tend to have the larger apertures. The study shows that the hydraulic behavior of correlated systems is significantly different from the behavior of uncorrelated systems. This study serves to demonstrate the importance of understanding the relationship between length and aperture.

A second study evaluates the use of steady state well tests to determine the true mean aperture of the fracture system. Field data, including well test data were used to create a fracture model. Then well tests were simulated in the model. The simulated well tests are analyzed to see if the input data on fracture aperture can be retrieved. The study shows that steady state well tests are inadequate for determining the aperture distribution.

At the time of this investigation, five boreholes, URL-1 through URL-5, had been drilled and tested at the URL site (Figure 7-1). Fracture traces on the extensive surface exposures had been mapped. Data from these sources indicate that approximately the upper 200-300 m of rock are fractured. The rock below this zone, as examined by these boreholes, is relatively unfractured except for one or two small fracture zones on the order of 10 m thick. Data from the upper fractured zone and the surface are the focus of attention

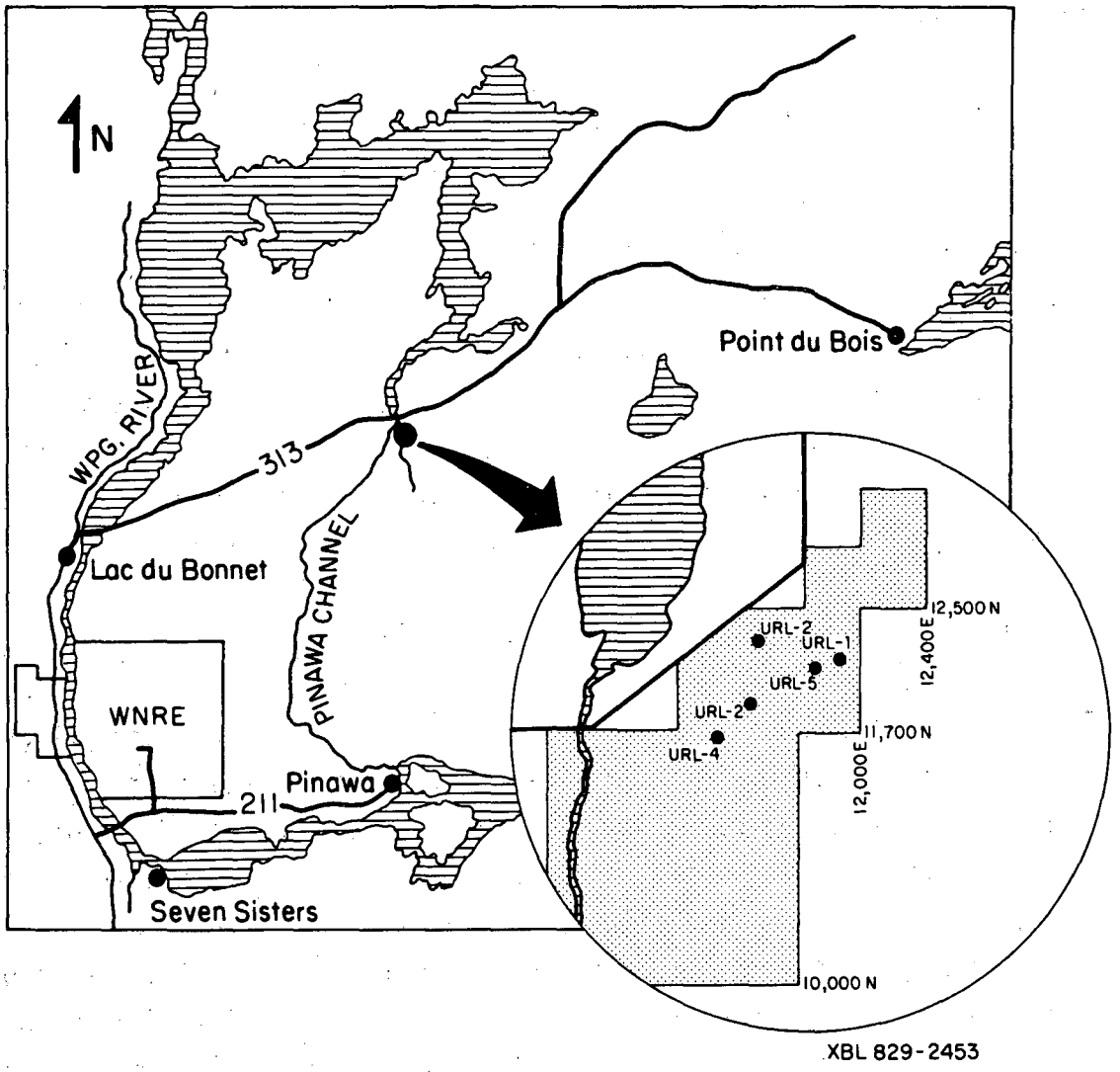

Figure 7-1. Underground Research Laboratory Site Map

for this analysis. Specifically, potential sources of data for analysis of the upper fractured zone are:

(1) URL 1 70 m - 120 m
(2) URL 2 45 m - 155 m
(3) URL 3 50 m - 155 m
(4) URL 4 0 m - 90 m
(5) URL 5 90 m - 110 m
(6) Surface Trace Data

All fracture data were assumed to be samples from the same overall population. Spatial correlation was assumed to be lacking. Where the input parameters could not be determined from maps, well tests, or logs, a range of values was used.

7.2 TWO-DIMENSIONAL ANALYSIS OF A THREE-DIMENSIONAL FRACTURE SYSTEM

Analysis of a real three-dimensional fracture system with a two-dimensional model has drawbacks. The primary drawback is that fractures which do not intersect in the plane of analysis may intersect somewhere outside the plane of analysis as shown in Figure 7-2. Also, fractures parallel or subparallel to the plane of analysis are not represented in the analysis. For both these reasons, a two-dimensional analysis tends to underestimate permeability in the plane of analysis. Furthermore, there is no good way at this time to correct for this error. In a sense a two-dimensional analysis is a bounding study. However, for the purposes of waste storage, this bounding study is not a conservative analysis.

The two-dimensional analysis is useful for examining the relationship between fracture geometry and the hydraulic behavior of the system. A fracture system which behaves like an equivalent porous medium in two dimensions will probably behave like an equivalent porous medium in three dimensions.

The permeability in a horizontal plane of the upper fractured zone at URL was analyzed because information about trace length and orientation distribution could be easily obtained from excellent trace maps of surface exposures. However, it is difficult to obtain a consistent data set for analysis of the horizontal plane. All the hydraulic data are from wells which have preferentially sampled horizontal fractures. Samples of fractures taken from traces in the horizontal plane are biased towards vertical fractures. Furthermore, most of the information on fracture patterns comes from the surface. Since

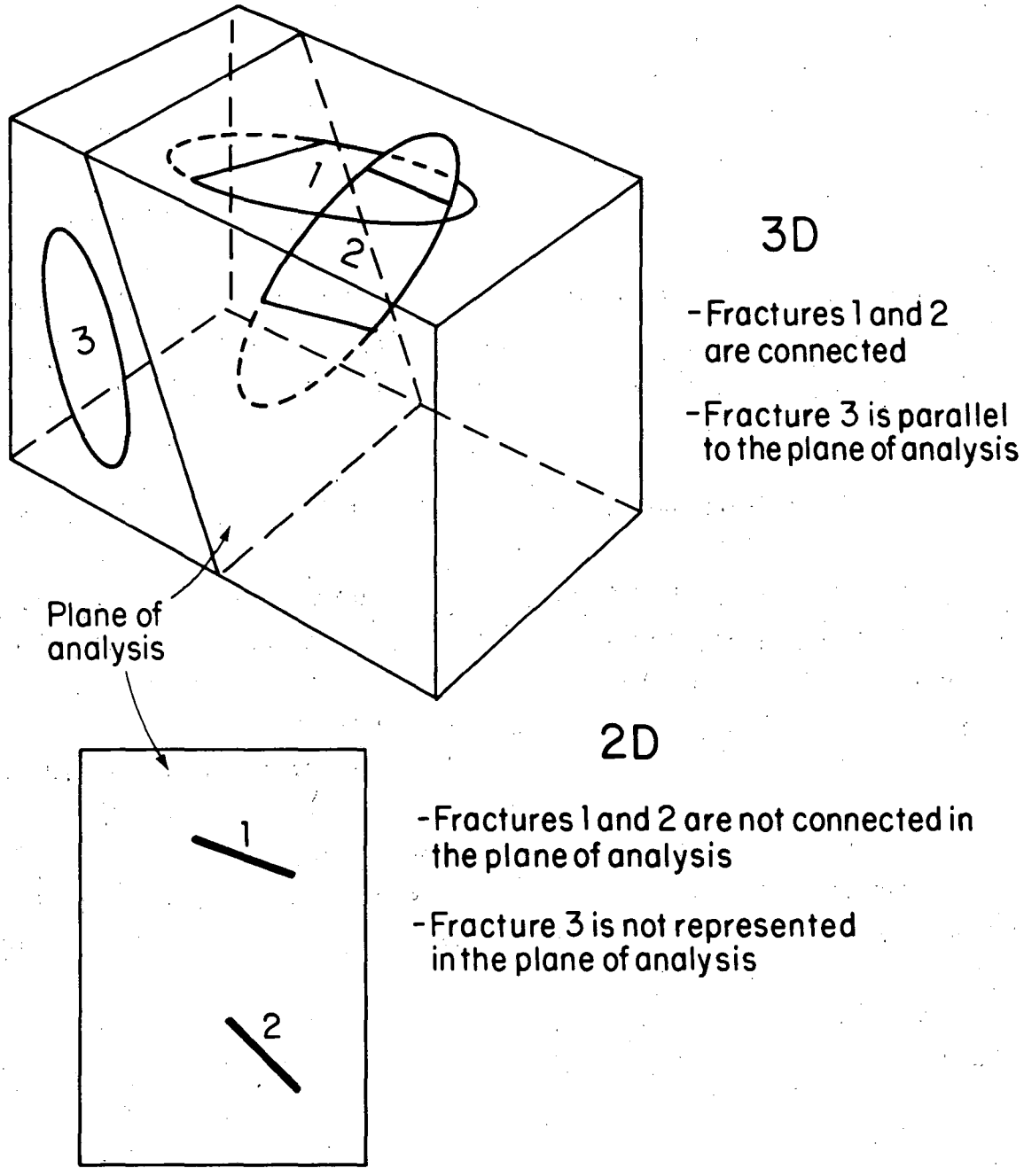

XBL 829-2443

Figure 7-2. Essential Differences Between Three-Dimensional and Two-Dimensional Analysis

stress conditions at depth are quite different from those at the surface, the fracture pattern is also likely to be different. This study proceeds initially on the assumption that the aperture distribution of near vertical fractures is the same as that at the surface. This assumption was then evaluated in examining the results.

7.3 INPUT PARAMETERS USED IN THE STUDY

Input for the model was obtained in two steps. First, density, orientation, and length input statistics were derived from the surface trace data. That is, the fracture pattern was determined completely from the surface data. Second, apertures were assigned to the fractures in the pattern.

For the first study, the same realization of this fracture pattern was used for each calculation of permeability. However, for each different calculation the fracture pattern was given a different assignment of apertures. Seven different statistical models for aperture were used. In five of these models, the correlated models, A, B1, B2, B3, and C, an aperture was assigned to each fracture such that the longer fractures tended to be assigned the larger apertures. In two other uncorrelated models, D and E, apertures were assigned randomly without regard to the fracture length. All seven, correlated and uncorrelated models, have the exact same fracture pattern. That is, each has fractures of the same length and orientation which are located in the same place. However, in each model the apertures are distributed differently.

An analysis of the effect of packer spacings was also made. For this study, many realizations of the fracture pattern were used; each with the same distribution of apertures determined by the B1 model. In each of these models the statistical distributions are the same, but each is a different random realization. The packer spacing study is a Monte Carlo type study.

7.3.1 Fracture Pattern

The fracture pattern input data was obtained from a fracture trace map provided by AECL. A 3,100 m^2 triangular area of the map was chosen for study becasue of the good exposure in this area (Figure 7-3). Two sets of fractures were identified. Set 1 strikes approximately N27°E and Set 2 strikes N115°E.

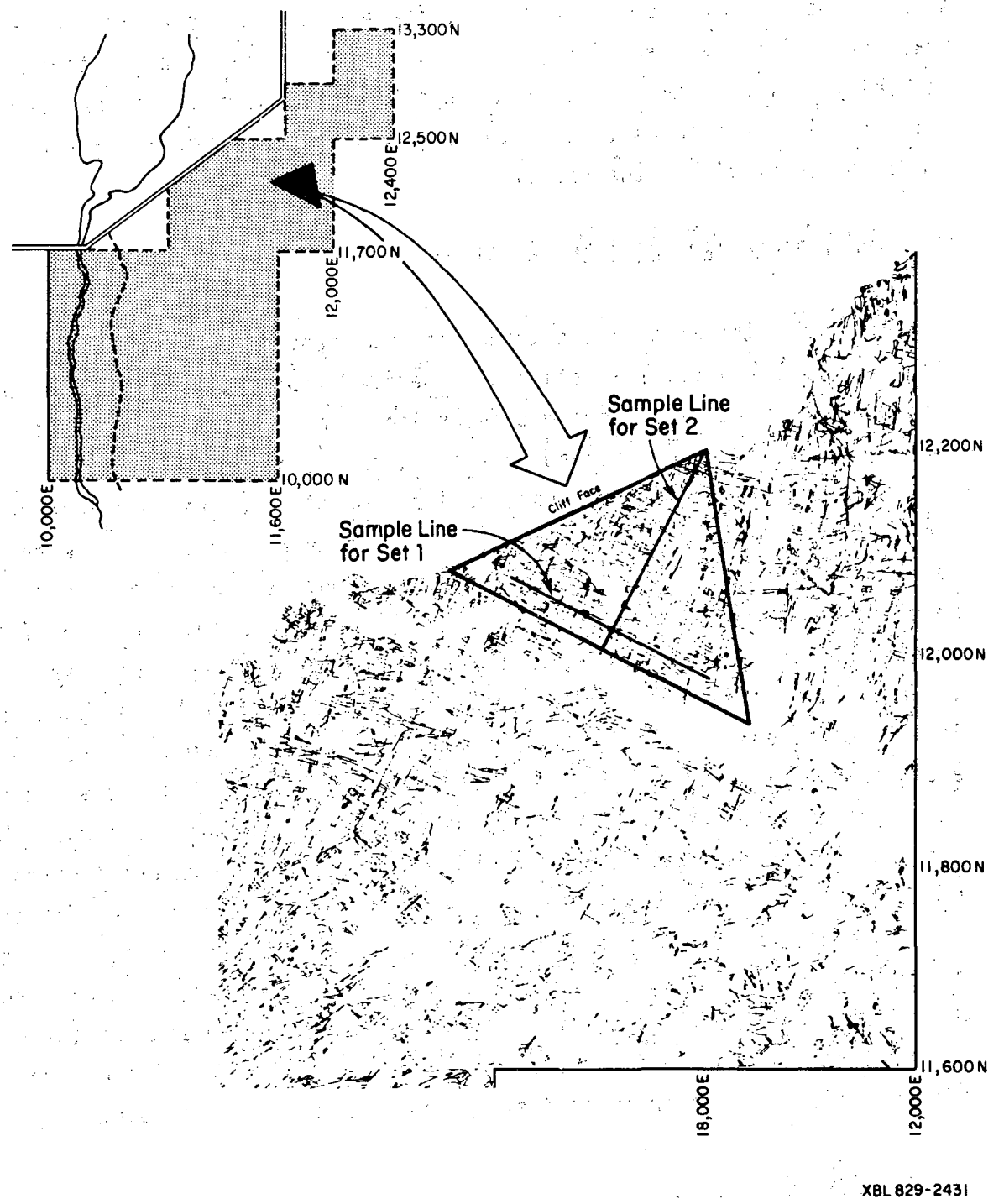

Figure 7-3. Fracture Trace Map of the Underground Research Laboratory Site.

A 200 m sample line was drawn on the map for each set. The sample lines were approximately perpendicular to the mean strikes of the fracture sets. The lengths and orientations of the fractures intersecting the sample lines were recorded. The statistics of this sample are summarized in Table 7-1.

Table 7-1. Underground Research Laboratory Fracture Statistics

	Orientation		Length			Density
Set	Mean (Strike)	Standard Deviation	Mean (m)	Standard Deviation (m)	Range (m)	Number of fractures per unit length (m-1)
1	N27°E	2.74	24.72	26.9	5.0-100.0	0.100
2	N115°E	2.34	25.0	26.9	2.0-112.0	0.135

For data input the mean and standard deviations for length were rounded off to two digits. The fracture density for each set was calculated using the length-density relationship described in Chapter 6. Recall that if the sample line is perpendicular to the strike of the fracture, the number of fractures per unit sample length equals the product of mean fracture length and number of fractures per unit area:

$$\lambda_\ell = \bar{\ell}\lambda_A \tag{7-2}$$

$$\lambda_A = \lambda_\ell/\bar{\ell}. \tag{7-3}$$

For Set 1,

$$\lambda_A = \frac{0.001\ \text{cm}^{-1}}{2500\ \text{cm}} = 4.0 \times 10^{-7}/\text{cm}^2, \tag{7-4}$$

and for Set 2,

$$\lambda_A = \frac{0.00135\ \text{cm}^{-1}}{2500\ \text{cm}} = 5.4 \times 10^{-7}/\text{cm}^2. \tag{7-5}$$

The input data for density, orientation, and length are summarized in Table 7-2. Orientation in the model is measured counterclockwise from the x-axis (East). The fracture mesh pattern generated using the data in this table is shown in Figure 7-4.

Table 7-2. Input Data

	Areal Density (cm^{-2})	Orientation, SD	Length, SC (cm)
Set 1	4×10^{-7}	63°, 2.7°	2500, 2200
Set 2	5.4×10^{-7}	155°, 2.3°	2500, 2700

7.3.2 Apertures

The available borehole well test data were analyzed in order to obtain an estimate of the aperture distribution. In the zones of interest, data from 12 packer tests in the URL boreholes were available. For these test zones, the equivalent aperture of a single fracture, b_1, which would account for the measured permeability in the test zone was calculated. Then the number of open fractures, N, intersecting the zone was counted using the T.V. log of the borehole. Assuming all N fractures were of equal aperture, the value of that aperture, b_A, which would account for the permeability was calculated. Table 7-3 gives the results of these calculations.

A simple correlation model for length and aperture was developed based on this data. In Figure 7-5, various plots of the log of fracture length, ℓ, versus aperture, b, illustrate the models used. Four points as summarized in Table 7-4 are labeled 1, 2, 3, and 4. Point 1 is the mean length and the approximate mean aperture; Point 2 is the maximum recorded length and the maximum expected aperture; Point 3 is the minimum recorded length and the minimum recorded aperture; Point 4 is the mean plus two standard deviations of length and the mean plus two standard deviations of aperture. The points do not lie on a straight line. The lines on the graph show the model relationships between ℓ and b that were chosen for the A, B, and C models.

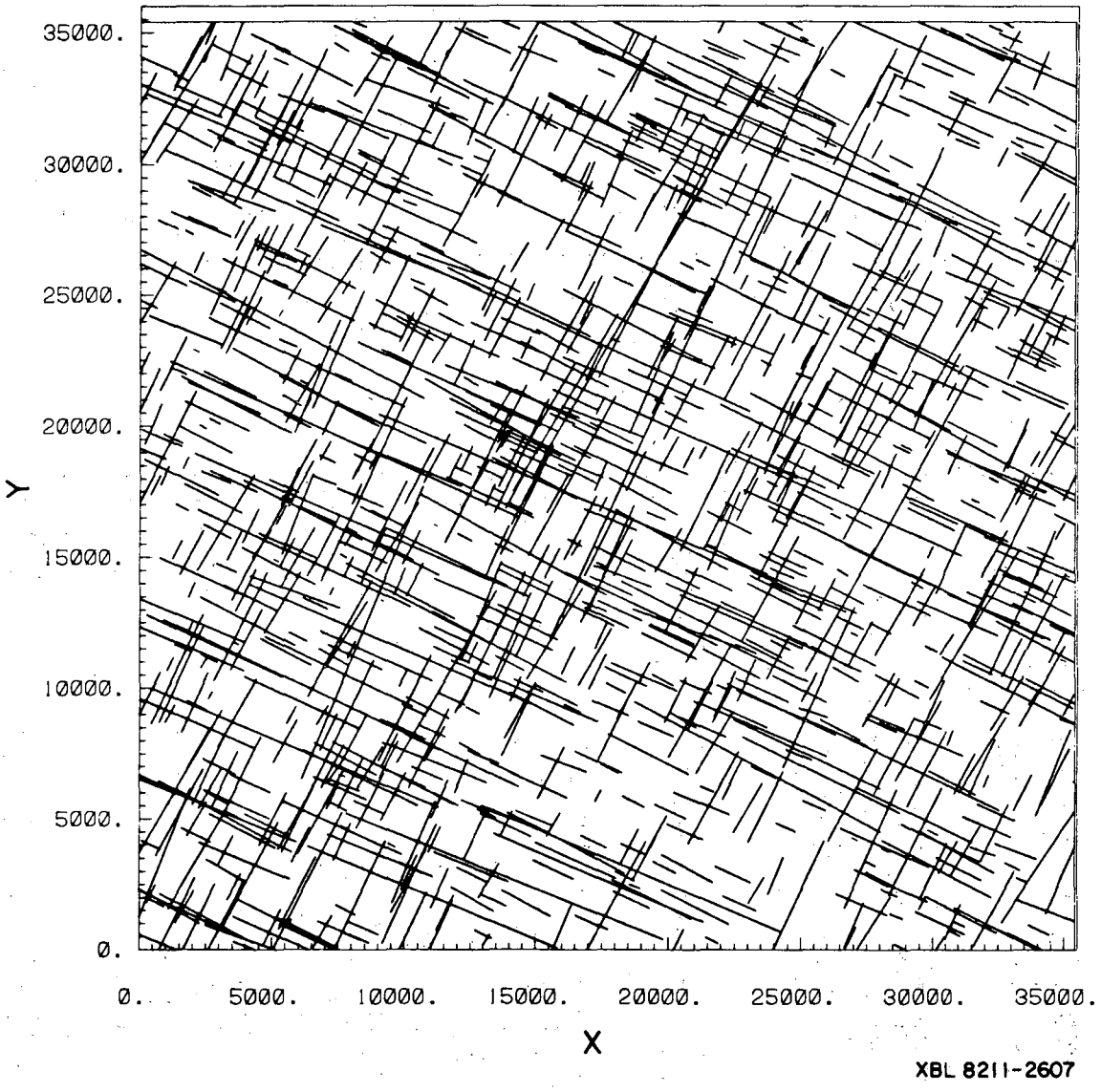

Figure 7-4. Fracture Pattern for the Underground Research Laboratory Data

All the models were chosen such that they passed through Point 3. This was done to insure that any fractures with generated lengths less than those observed in the field sample would have a minimum aperture and therefore a small effect on the flow. These trial correlation models are fairly simple; only one straight line segment on the semilog plot (Figure 7-5) is used to govern the choice of aperture for fractures with lengths greater than 100 cm. Model A was chosen as a probable maximum. Model B was chosen to give some weight to Points 1, 2, 3, and 4. Model C was chosen to give weight only to Points 1 and 3. Model C was chosen to achieve a good match with the average aperture statistics as given at the bottom of Table 7-3.

Table 7-3. Aperture Data

Hole	Zone (m)	N # of Open Fractures	K Conductivity cm/s^{-1}	Equivalent Single Fracture b_1** (cm)	Aperture N Fractures b_A** (cm)	# of Fractures per Unit Length in the Zone (m^{-1})
URL-1	73.9-91.1	3	1.5×10^{-7}	3.16×10^{-3}	2.19×10^{-3}	0.1744
URL-1	108.6-115.6	12	4.0×10^{-6}	7.00×10^{-3}	3.06×10^{-3}	1.714
URL-2	45.0-55.2	7	5.0×10^{-6}	8.55×10^{-3}	4.47×10^{-3}	1.457
URL-2	60.0-70.2	3	1.5×10^{-6}	5.72×10^{-3}	3.97×10^{-3}	2.941
URL-2	86.0-96.2	3	5.25×10^{-7}	4.0×10^{-3}	2.80×10^{-3}	2.941
URL-2	105.0-115.2	1	2.0×10^{-6}	6.29×10^{-3}	6.29×10^{-3}	0.0984
URL-2	120.0-130.2	4	2.0×10^{-6}	1.36×10^{-2}	8.55×10^{-3}	0.3921
URL-2	130.0-140.2	2	6.0×10^{-7}	4.22×10^{-3}	3.35×10^{-3}	0.1961
URL-2	148.0-158.2	0	2.0×10^{-7}	-	-	0.0
URL-3	61.0-64.5	2*	1.0×10^{-8}	7.54×10^{-4}	5.98×10^{-4}	1.75
URL-3	116.0-120.5	4*	2.0×10^{-7}	2.23×10^{-3}	1.40×10^{-3}	0.8
URL-4	2.36-62.84	9*	not avail.	-	-	0.319
URL-5	79.35-94.11	0*	2.6×10^{-8}	-	-	0.0
URL-5	94.11-108.87	31	9.0×10^{-5}	2.53×10^{-2}	8.06×10^{-3}	2.1

*Estimated from fracture frequency graphs, T.V. log not available.

** $b = \sqrt[3]{\frac{KL}{N}\frac{12\mu}{\rho g}}$

L = zone length
N = number of fractures assumed to be conducting

$\bar{b}_1 = 7.35\times10^{-3}$ cm
SD = 6.89×10^{-3} cm

$\bar{b}_A = 5.54\times10^{-3}$ cm
SD = 2.67×10^{-3} cm

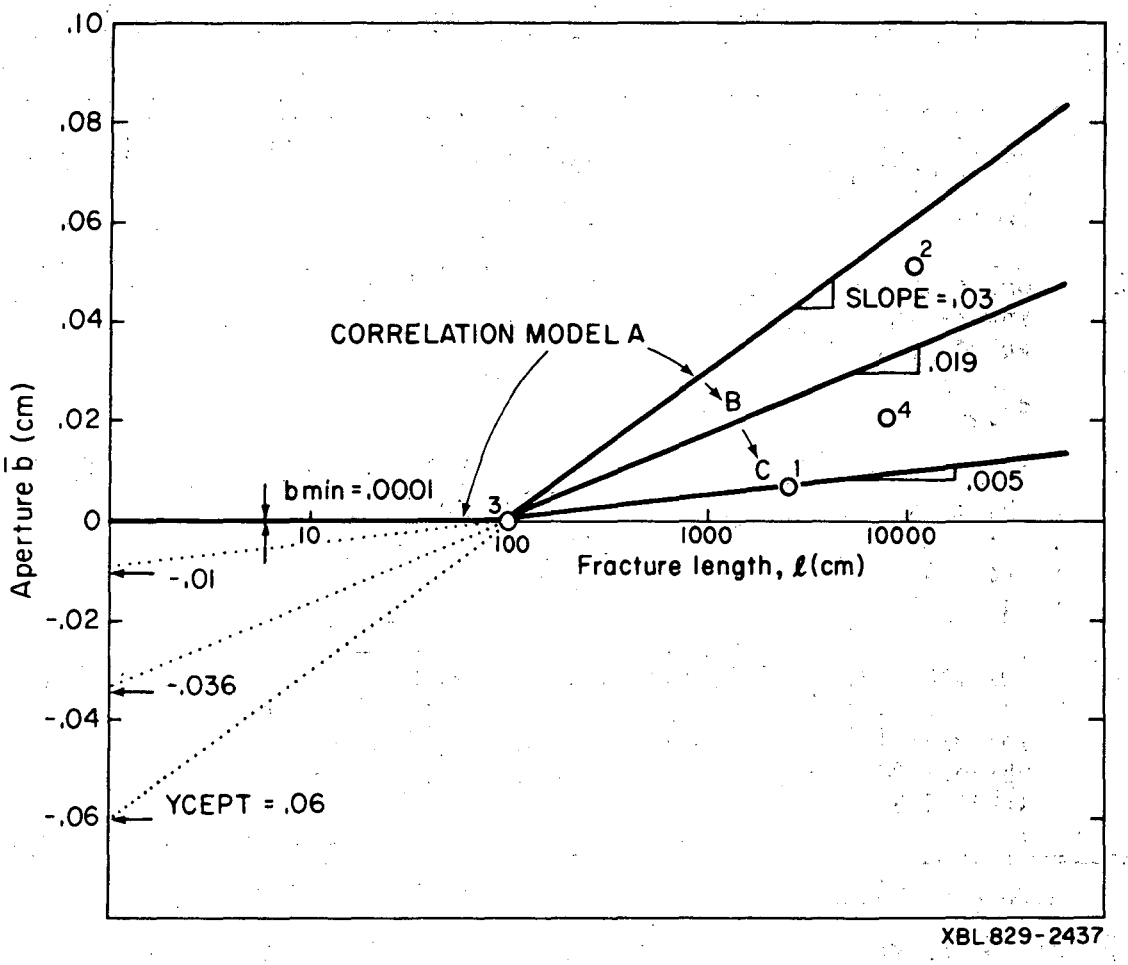

Figure 7-5. Length-Aperture Correlation Models Used in the Underground Research Laboratory Data Study

Table 7-4. Description of Length and Aperture Coordinates Used to Plot Points 1,2,3, and 4 on Figure 7-5

Point	Description of length, ℓ	Description of aperture b	Values of length and aperture (ℓ, b) (cm)
1	Approximate mean value of length from Table 7-1	Approximate average of b_1 and b_A from Table 7-3	(2,500, 0.006)
2	Order of magnitude of the maximum observed value of length in the triangle on Figure 7-3	The maximum expected aperture based on Table 7-3	(10,000, 0.65)
3	Order of magnitude of the minimum observed value of length in the triangle on Figure 7-3	Order of magnitude of the minimum observed value of aperture on Table 7-3	(100, 0.0005)
4	The mean value of length (from 1 above) plus approximately 2 standard deviations from Table 7-3	The mean value of aperture (from 1 above) plus approximately 2 standard deviations from from Table 7-3	(7,500, 0.02)

These correlation models were used to pick a value of aperture for each fracture in the existing fracture pattern. First the length, ℓ, of each fracture was used to find the value of $\bar{b}(\ell)$ on Figure 7-5. If aperture and length were perfectly correlated (i.e., a one-to-one correlation), then $\bar{b}(\ell)$ would be the aperture assigned to a fracture of length. However, in this study, $\bar{b}(\ell)$ was considered to be the mean value of aperture for all fractures of length ℓ. The value of aperture actually assigned to the fracture was assumed to be a member of a normal distribution with mean, $\bar{b}(\ell)$, and standard deviation, SDb(ℓ), specified in the input. Thus, if the values of aperture assigned to each fracture were plotted on Figure 7-5, they would be scattered around the sloped portion of the line. The amount of scatter is determined by the magnitude of SDb(ℓ). The total dispersion of the values of aperture is determined both by SDb(ℓ) and by the randomness inherent in ℓ.

Model B was run with three different standard deviations as B1, B2, and B3. In B1, SD(b(ℓ)) (the standard deviation of b(ℓ) around b(ℓ)), was 0.001; in B2, it was 0.01; in B3, it was 0.04.

Zero aperture fractures create a problem in the numerical analysis and negative aperture fractures do not make sense physically. Therefore a minimum aperture, in this case 0.0001 cm, was assigned to any fracture with a length less than 100 cm, which is the minimum length recorded in the field data. This aperture was also assigned to any fracture for which the correlation model gave a negative aperture.

In simulations D and E, length and aperture were uncorrelated. Model D used values of mean aperture and standard deviation the same as those measured in the generation region of Model B1. Model E used a slightly smaller mean aperture and a much larger standard deviation than Model D. A summary of the aperture assignments used in each model is given in Table 7-5.

For each model the permeability was calculated in 24 directions 15° apart. The superimposed flow regions for the permeability calculations are shown in Figure 7-6. The flow region size was 250 x 250 m. These dimensions are 10 times the mean fracture length, which is large enough to insure a good statistical sample. All of the models used the same fracture pattern, but apertures were assigned differently in each model. The flow regions were simplified for the purpose of economy by eliminating the isolated and deadend fractures which do not conduct. These reduced flow meshes are shown in Figure 7-7. Each of the six reduced flow regions shown represent four different directions of measurement: θ, $\theta + 90$, $\theta + 180°$, and $\theta + 270°$.

7.4 RESULTS OF THE PERMEABILITY STUDY

The results of the permeability calculations are shown in Figures 7-8 through 7-11. The left-hand side of each frame is a permeability ellipse plot. The dashed line connects the values of $1/\sqrt{K_g}$ calculated by the model. The smooth ellipse drawn with a solid line is the best fit ellipse. The right-hand side of the figure shows the values of calculated permeability plotted against rotation angle in Cartesian coordinates. The smooth solid-line curve on this plot is the best fit "ellipse." The polar plot provides a good visualization of the hydraulic behavior, but the Cartesian plot provides a

Table 7-5. Input and Output Aperture Statistics for the Underground Research Laboratory Models

Model Set	Length and Aperture Correlation	Input Correlation Parameters			Coefficient of Correlation in the Generation Region	Input Aperture Statistics		Observed Aperture Statistics in the Generation Region	
		Y-Intercept	Slope	SDb(ℓ)		b	SDb	b	SDb
A	Yes								
1		-.06	.03	.01	.5461	-	-	.0388	.0135
2		-.06	.03	.01	.6340	-	-	.0369	.0153
B1	Yes								
1		-.036	.019	.001	.8283	-	-	.0262	.00596
2		-.036	.019	.001	.8215	-	-	.0255	.00738
B2	Yes								
1		-.036	.019	.01	.3886	-	-	.0269	.0115
2		-.036	.019	.01	.5011	-	-	.0253	.0123
B3	Yes								
1		-.036	.019	.04	.084	-	-	.0343	.0337
2		-.036	.019	.04	.1656			.0312	.0318
C	Yes								
1		-.01	.005	.001	.6937	-	-	.00643	.00182
2		-.01	.005	.001	.7392			.00616	.00217
D	No								
1		-	-	-	-	.026	.0065	.027	.007
2		-	-	-	-	.026	.0065	.026	.006
E	No								
1		-	-	-	-	.02	.04	.024	.050
2		-	-	-	-	.02	.04	.019	.029

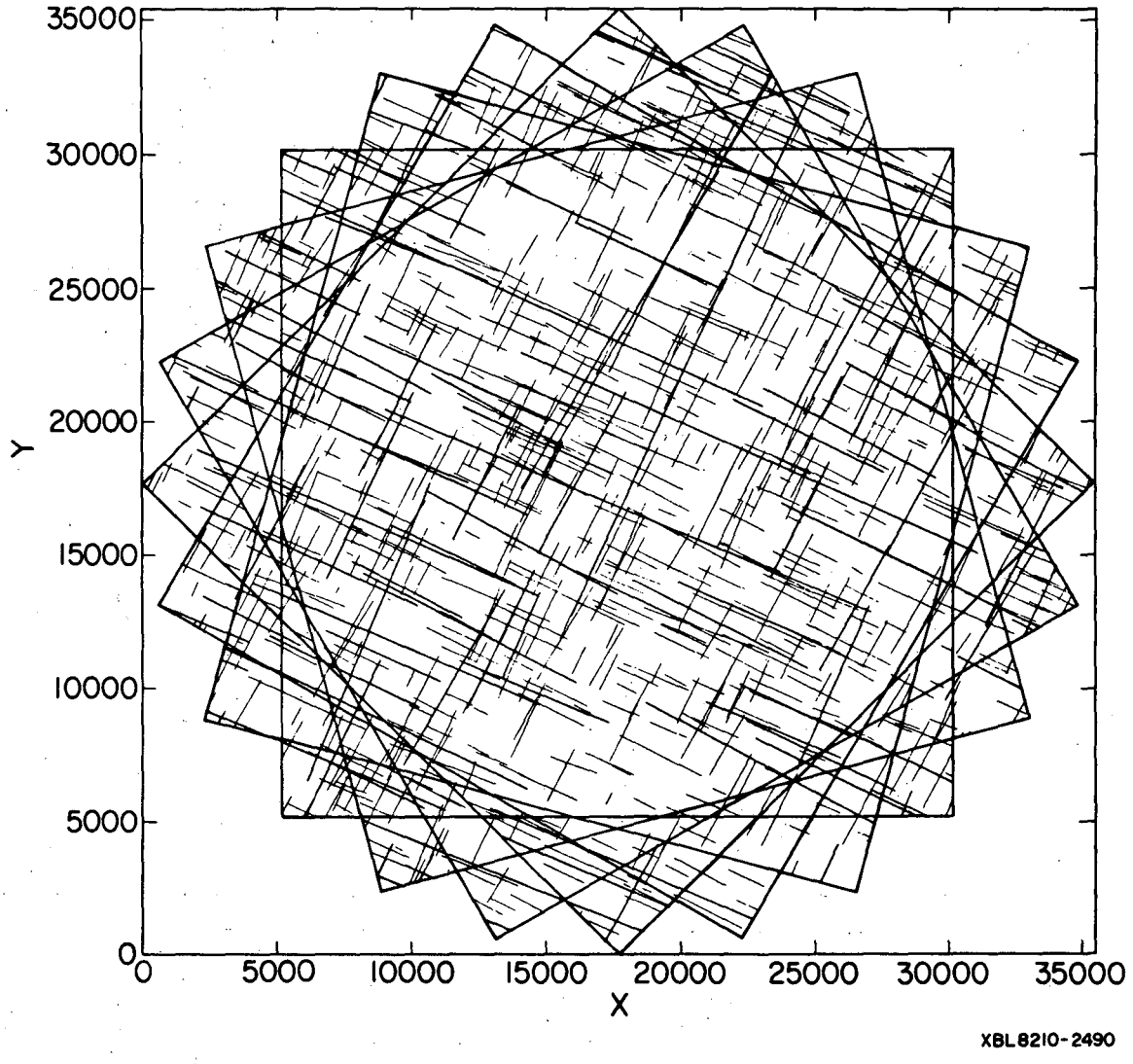

Figure 7-6. Superimposed Flow Regions for the Underground Research Laboratory Data Study

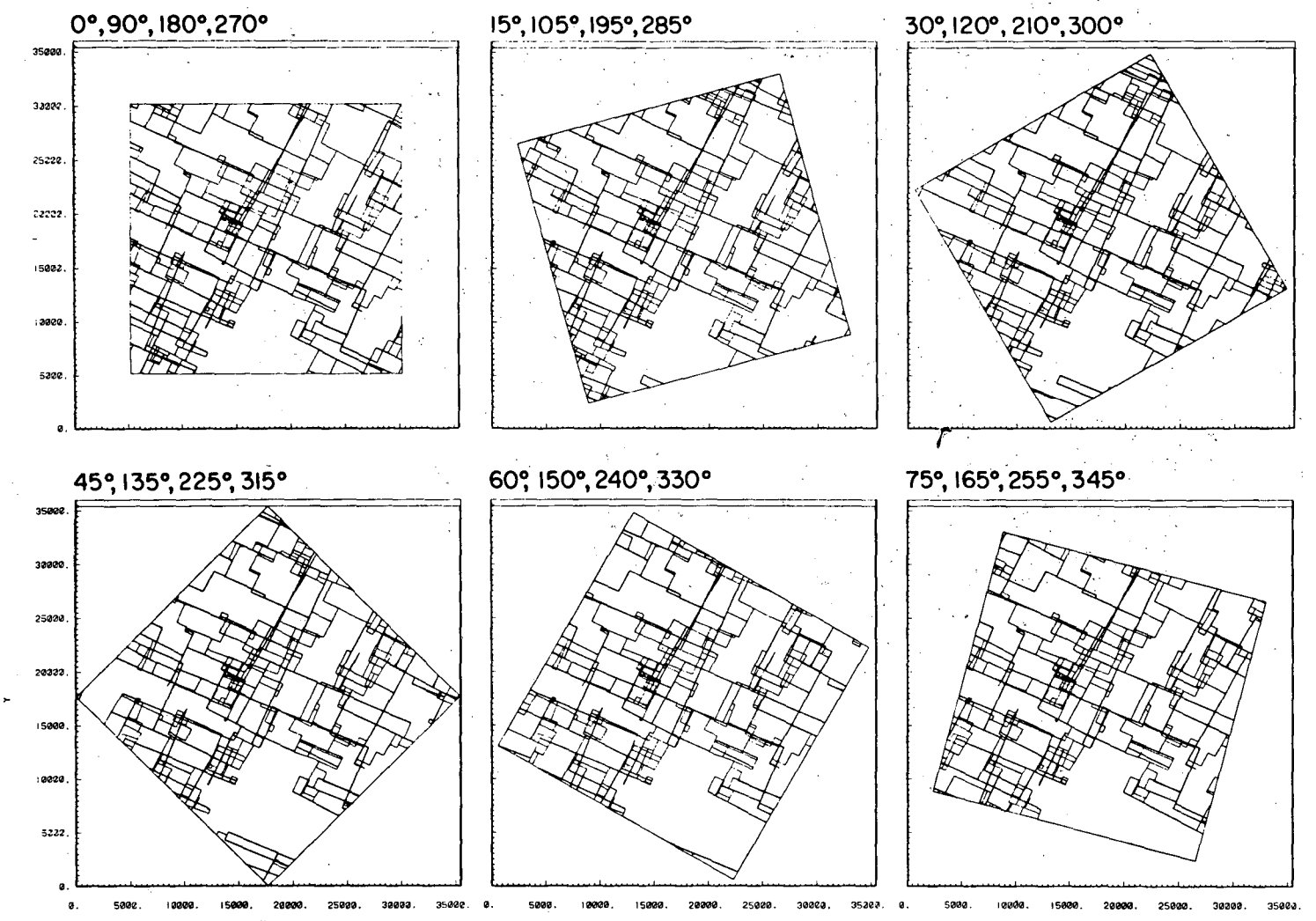

XBL 8210-2511

Figure 7-7. Reduced Flow Regions for the Underground Research Laboratory Data

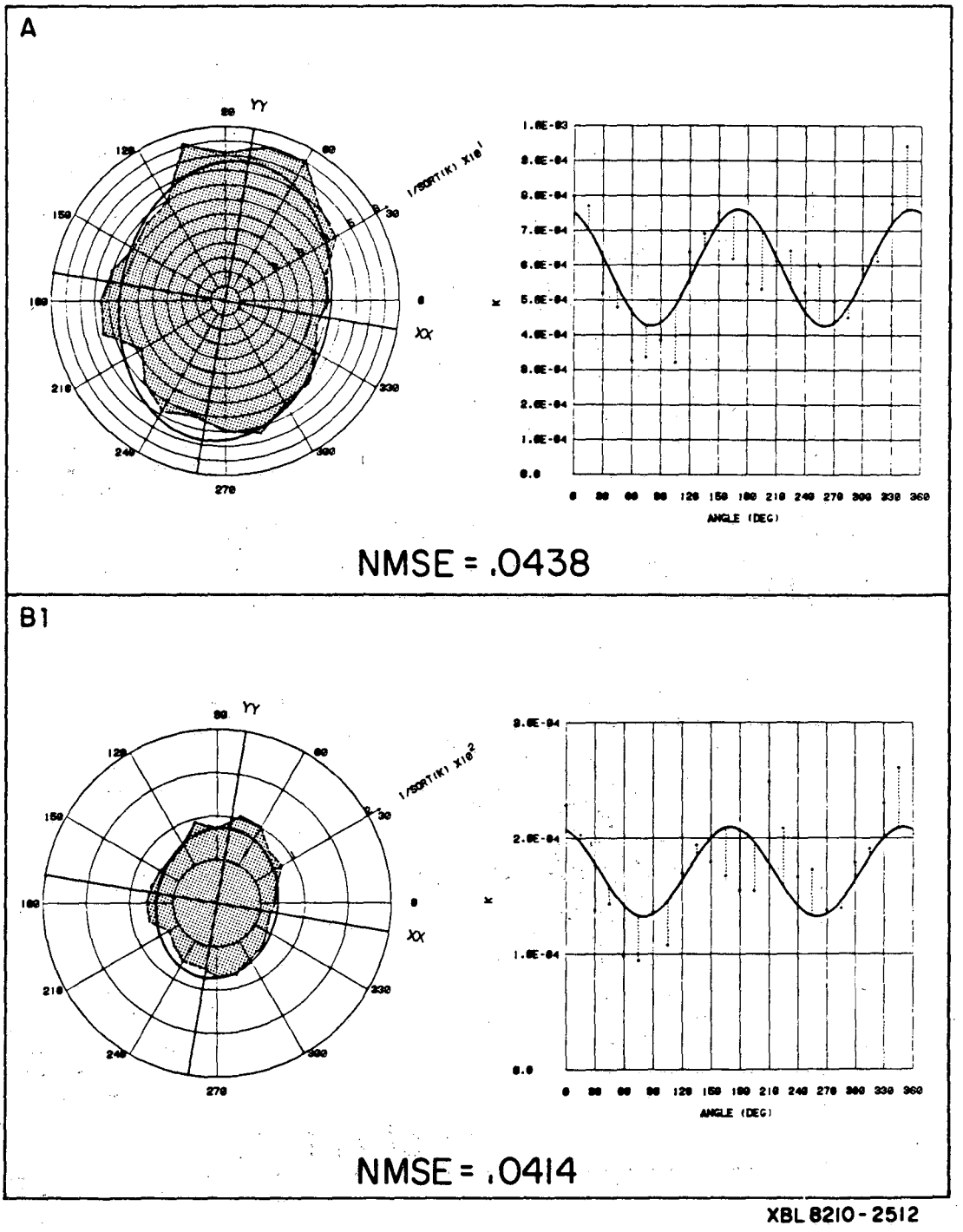

XBL 8210-2512

Figure 7-8. Permeability from Models A and B1 of the Underground Research Laboratory

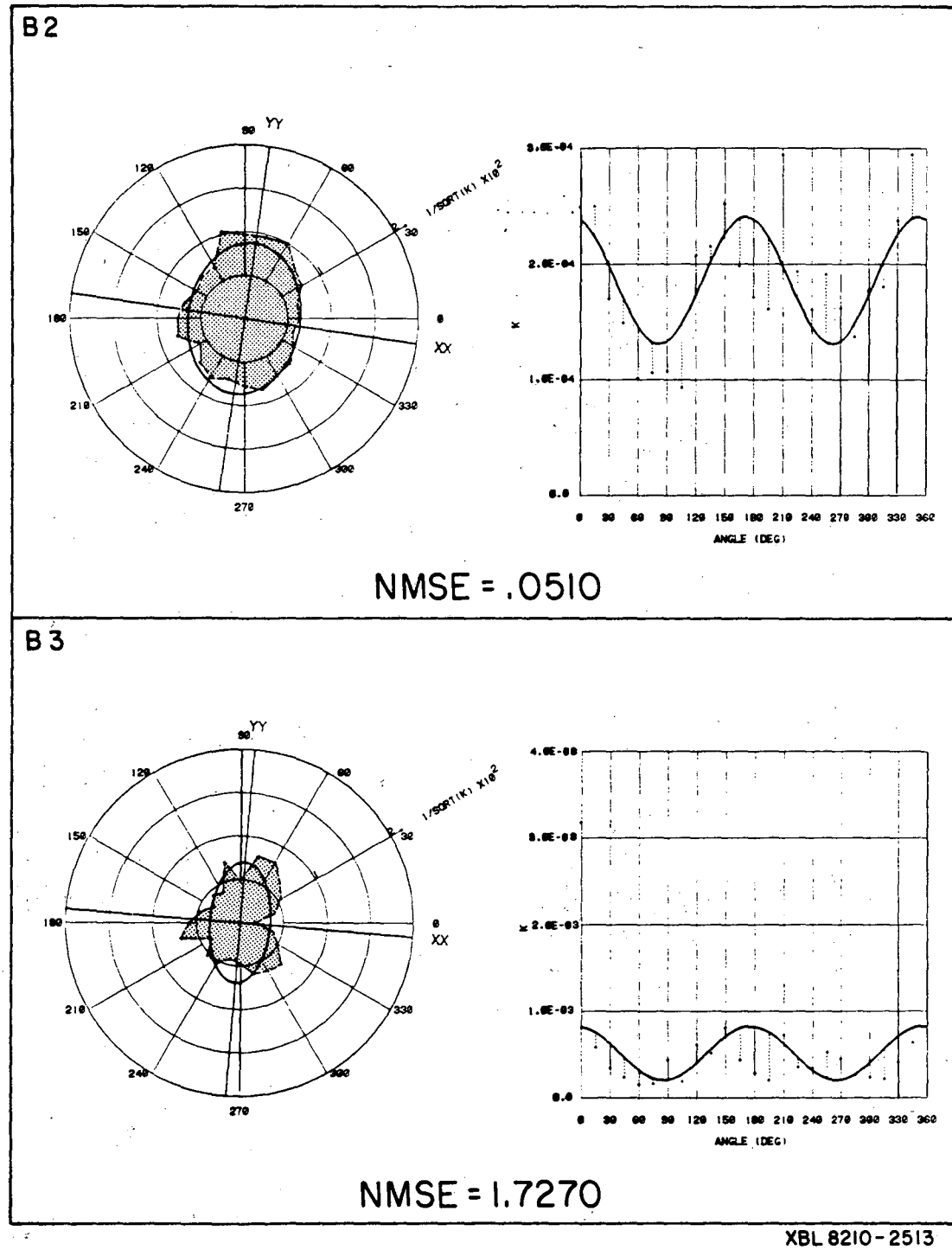

XBL 8210-2513

Figure 7-9. Permeability from Models B2 and B3 of the Underground Research Laboratory

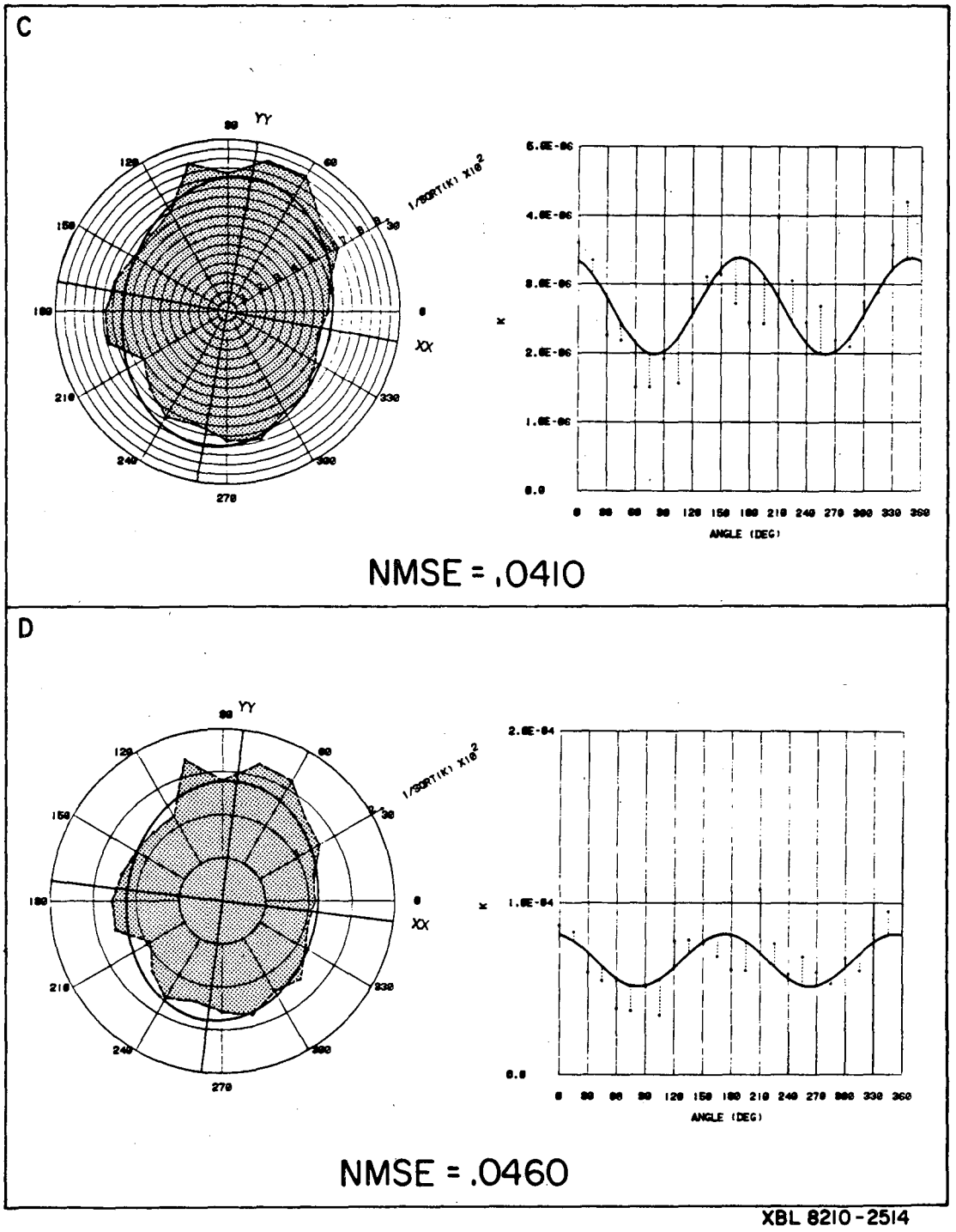

Figure 7-10. Permeability from Models C and D of the Underground Research Laboratory

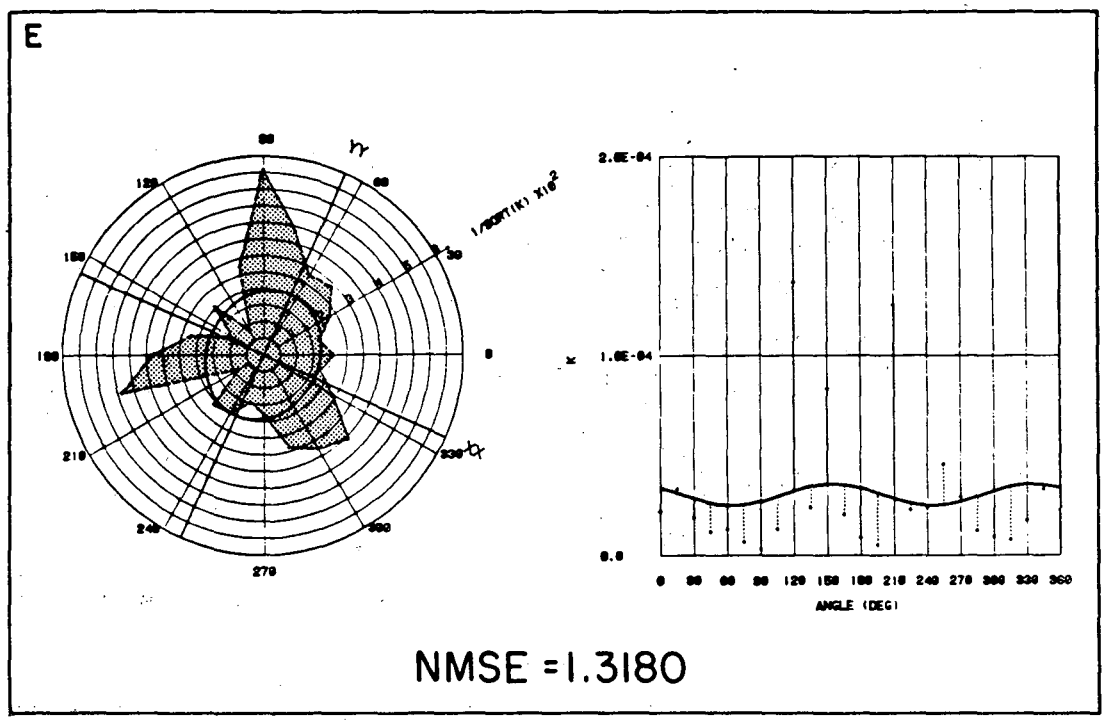

XBL8210-2515

Figure 7-11. Permeability from Model E Underground Research Laboratory

better visualization of the magnitude of permeability and the degree of scatter. The values of the principal permeabilities, the principal directions, and the normalized mean square error (NMSE) for each case are given in Table 7-6.

Table 7-6. Permeability Results for the Underground Research Laboratory Data

Model	Principal Permeabilities (cm/s) K1	K2	Principal Directions Θ_1	Θ_2	NMSE
A	7.61×10^{-4}	4.26×10^{-4}	-9.5	-80.5	0.044
B1	2.09×10^{-1}	1.32×10^{-4}	-9.5	-80.5	0.041
B2	2.40×10^{-4}	1.31×10^{-4}	-8.3	81.6	0.051
B3	8.25×10^{-4}	2.05×10^{-4}	-4.7	85.3	1.727
C	3.38×10^{-6}	1.98×10^{-6}	-10.0	80.1	0.041
D	8.17×10^{-5}	5.13×10^{-5}	-6.8	83.2	0.046
E	3.55×10^{-5}	2.51×10^{-5}	-24.6	65.4	1.317

Model A represents a probable maximum aperture model based on Figure 7-5 and thus had the largest permeability of all the models. The permeability of this model was on the order of 10^{-4} cm/s whereas the permeabilities measured in URL-1 through URL-5 are generally on the order of 10^{-6} or 10^{-7} cm/s. This difference may or may not be a discrepancy. Permeability may simply be increasing with scale of measurement. The borehole measurements were on the scale of 10 m. The permeability models were on the scale of 250 m. However, none of the individual borehole measurements were as high as 10^{-4} cm/s. The difference between the model results and the borehole measurements is strong evidence that either the aperture model is wrong or the fracture pattern from the surface does not apply at depth, or both.

The overall linear density, λ_L, of open fractures as recorded in the borehole T.V. logs for the zones of interest is about 0.65 fractures per meter. This number is larger than the values measured at the surface as given in the last column of Table 7-1. Therefore, the linear density at depth is probably larger than at the surface. All else being equal, a larger density at depth than at the surface would imply a larger permeability at

depth than predicted by the model using surface data. Yet the permeability at depth is evidently lower than predicted by Model A. This is more evidence that the apertures in Model A are too large or the fractures may be much shorter at depth than those at the surface.

The observed values of mean aperture and standard deviation of aperture in Model A are not the same as calculated from the borehole test data. The field mean aperature and standard deviation are lower than the model. Note that the overall mean aperture and standard deviation of the aperture are not assigned directly in the correlation model. These statistics can only be calculated after the model is generated. Reproducing specific aperture statistics can only be done by trial and error.

The aperture model used in A may very likely be wrong because it results in apertures which are too high. This discrepancy would also account for the permeability of the model being too high. Since the aperture statistics of Model A did not match the aperture statistics measured in the field, the B1, B2, B3 and C models were tried to see if the permeability of the models could be significantly lowered. The B models were all set to give more weight to Points 1, 2, and 4 on Figure 7-5. These models still result in a mean aperture higher than that observed in the field (Table 7-5). Some decrease in permeability from Model A to the B models was observed. However the permeability of the B models is still significantly larger than the packer test results.

From Model B1 to B3, the only significant change in the fracture mesh is an increase in the standard deviation of the overall aperture distribution. This increase has two net effects. The first is the permeability increases slightly and the second is the normalized mean square error (NMSE) increases substantially. The net increase in permeability can be explained because the flux carried by the fracture is proportional to aperture cubed. When the standard deviation is increased, a fracture of initial aperture, b, is likely to have its aperture increased or decreased by an amount, say Δ. However, in this case the resulting net increase in flux is greater than the net decrease. This can be seen by calculating $(b - \Delta)^3$ and $(b + \Delta)^3$.

$$(b - \Delta)^3 = b^3 - 3\Delta b^2 + 3\Delta^2 b - \Delta^3 \tag{7-6}$$

$$(b + \Delta)^3 = b^3 - 3\Delta b^2 + 3\Delta^2 b + \Delta^3 \tag{7-7}$$

The magnitude of increase in b^3 is

$$(b + \Delta)^3 - b^3 = 3\Delta b^2 + 3\Delta^2 b - \Delta^3 \tag{7-8}$$

The magnitude of decrease in b^3 is

$$b^3 - (b - \Delta)^3 = \Delta^3 + 3\Delta b^2 - 3\Delta^2 b. \tag{7-9}$$

The magnitude of the increase is greater than the magnitude of the decrease by $6\Delta^2 b$. Therefore the permeability of individual fractures increases systematically. However, with a higher standard deviation of aperture the connections between fractures in the pattern are more heterogeneous, and therefore the NMSE increases. This increase in heterogeneity itself also causes random decrease and increase in the permeability. When length and aperture are correlated the net result of both the systematic and random effects of increasing standard deviation seems to be an increase in permeability.

Model C was designed to find an aperture-length model which would achieve permeabilities on the order of 10^{-6} cm/s with the same fracture pattern used in the A and B models. Mean apertures in this model were decreased by a factor of about 1/4 from the B1 models. The permeability of C was decreased by a factor of about 1/62, which is approximately equal to $(1/4)^3$. Model C best represents the field statistics. The permeability of Model C was therefore on the same order of magnitude as the field test results.

Permeabilities of models with uncorrelated length and aperture are smaller than those of correlated models. Model D was designed to determine the magnitude of decrease in permeability caused by having length and aperture uncorrelated. Model D has approximately the same overall aperture statistics as Model B1.

Model D has a slightly higher NMSE and a significantly lower permeability than B1. In B1, the correlated model, large apertures are not "wasted" on short fractures which do not as often connect to other fractures. Therefore the correlated Model B1 has a higher permeability than the uncorrelated Model D. Correlation did not seem to produce a large effect on the NMSE.

A comparison can be made between B3 and E. The correlated Model B3 has a lower standard deviation of aperture than the uncorrelated Model E. In this

case, however the correlated model has a higher NMSE. This disparity is apparently due to a random long, higher aperture fracture which connects the inflow side at 0° rotation to an adjacent side rather than the opposite side. This creates the anomalously high permeability at 0° and the anomalously low value at 180°. It may be that correlation between length and aperture may be responsible for creating a "super conductor" which increases the value of NMSE. In both the correlated and uncorrelated models, an increase in the standard deviation of aperture increases the NMSE.

All else being constant, an increase in the standard deviation of aperture increases the NMSE. If length and aperture are correlated, an increase in standard deviation of aperture will probably increase the permeability. All else being constant, uncorrelated models have lower permeability than do correlated models. All else being constant, increasing the mean aperture by a factor of m increases the permeability by a factor of about m^3. Correlation between length and aperture may explain the occurrence of "super conductors."

7.5 THE MONTE CARLO PACKER SPACING STUDY

A study was conducted to observe the influence of packer spacing on the ability to predict the true mean aperture of the fracture system. First a 350 x 350 m fracture mesh generation region was created using the fracture statistics of Model B1. Then, a series of flow regions were defined in the generation region. All the flow regions were at 0° rotation and the sizes varied as follows: 1 x 1 m, 2 x 2 m, 5 x 5 m, 10 x 10 m, 20 x 20 m, 50 x 50 m, 80 x 80 m, 150 x 150 m. In the first set of runs, the sizes ranged from 1 x 1 m to 50 x 50 m. Then another set of runs was made to see the results in regions larger than 50 x 50 m. In this second set of runs flow regions ranged in size from 1 x 1 m to 250 x 250 m. In each set of runs, 20 different generation regions and the associated flow regions were created as different realizations of the same statistics. Figure 7-12 shows one of these realizations from the second set of runs. Figure 7-13 shows the flow regions of different sizes for this realization. Figure 7-14 shows the reduced flow regions.

In each of the flow regions, permeability was calculated in the x-direction. In fact, two values of permeability were calculated for each

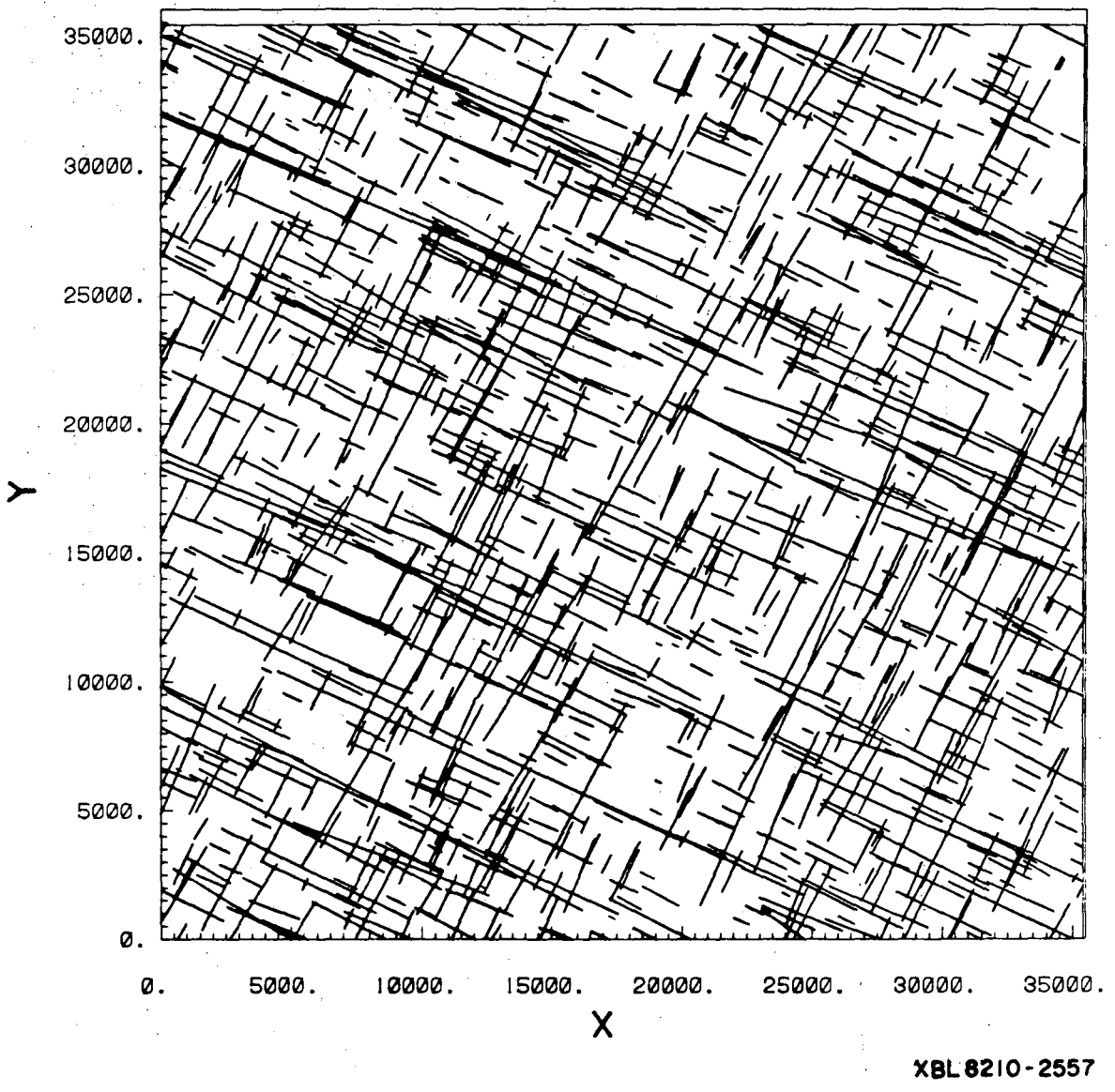

Figure 7-12. Generation Region for One Realization of the Packer Spacing Study

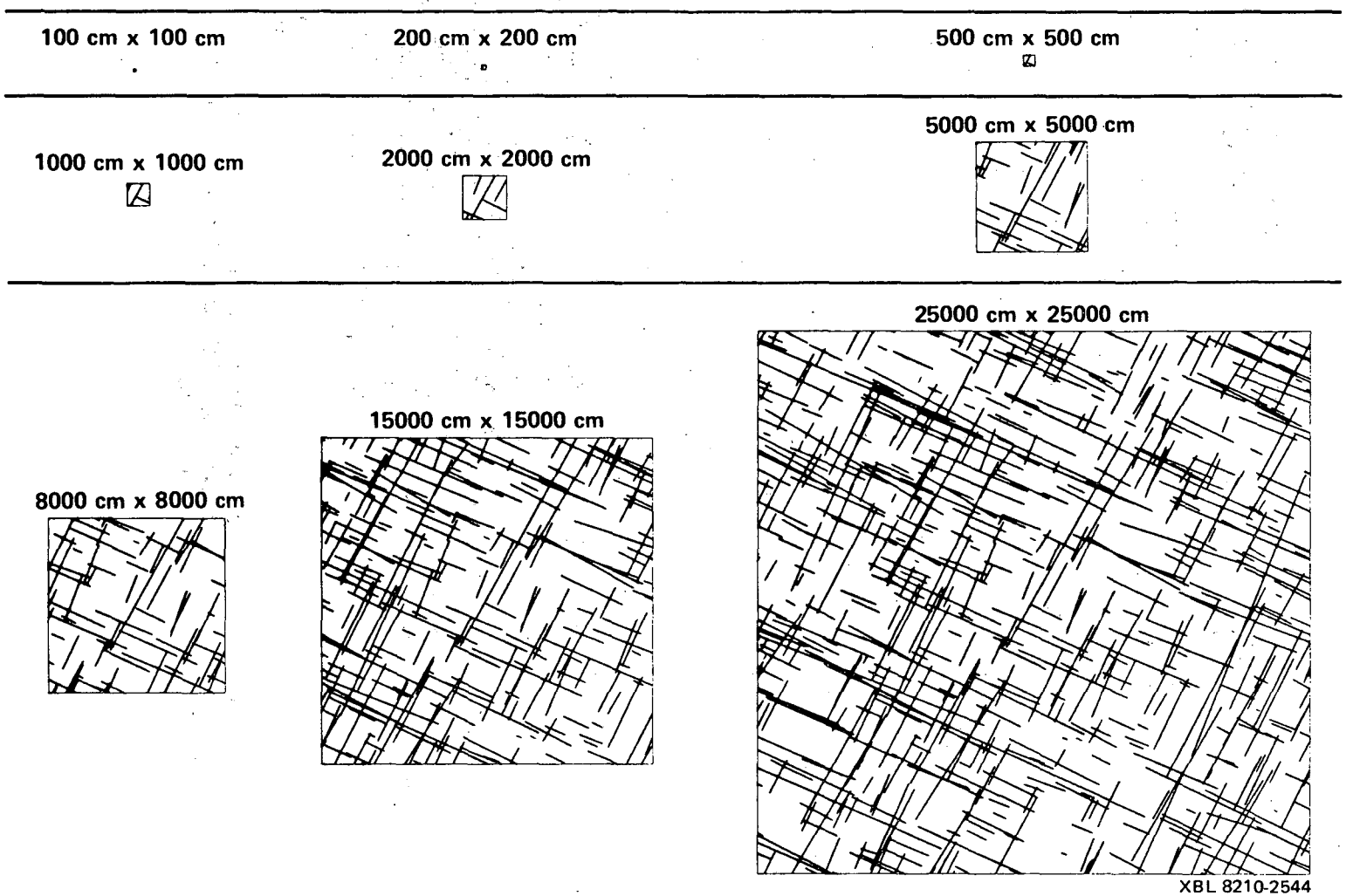

Figure 7-13. An Example of One Realization: Flow Regions from 100 x 100 cm to 25,000 x 25,000 cm

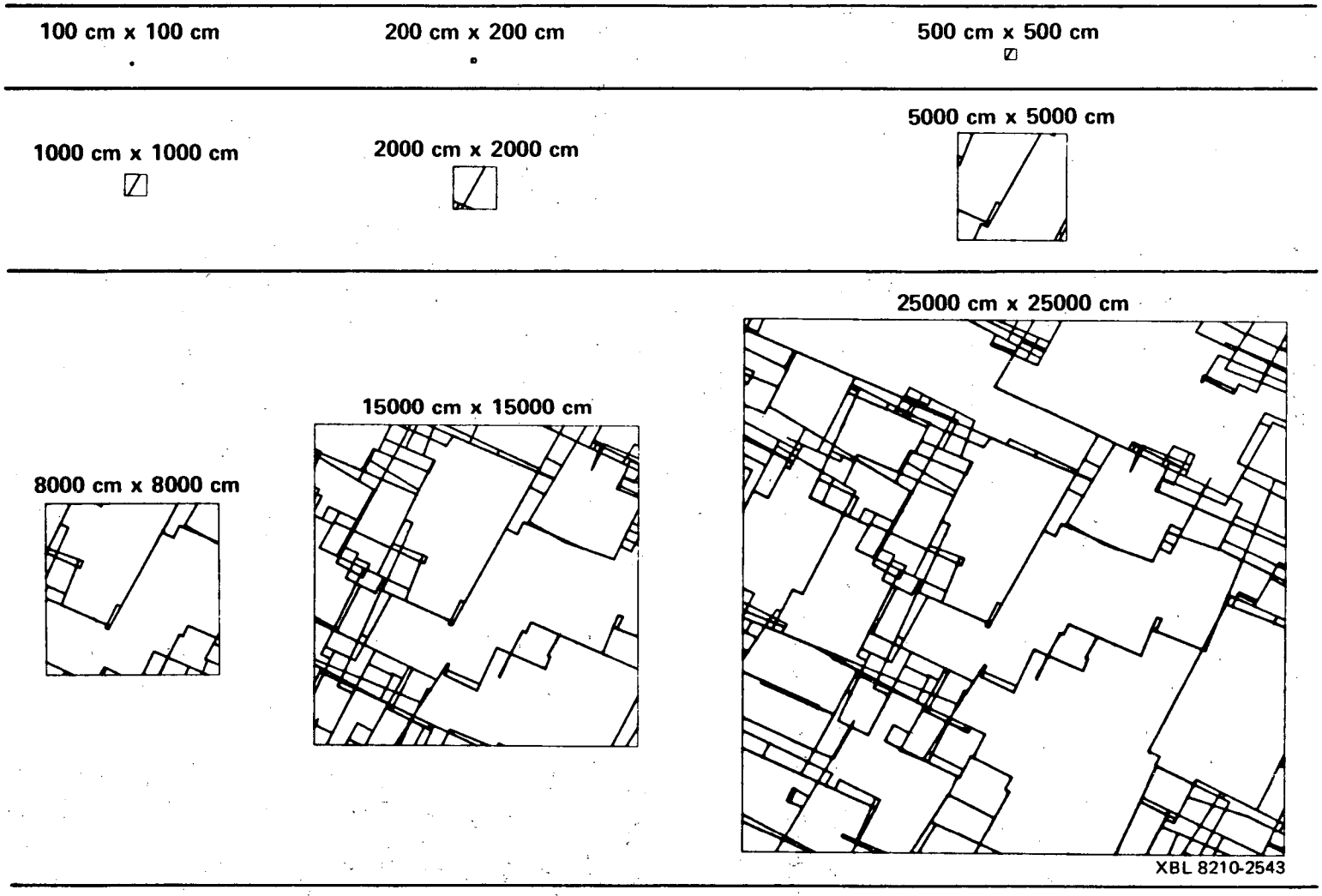

Figure 7-14. Reduced Flow Regions from Figure 7-13

flow region, one based on flow into the region in the x-direction and one based on flow out of the region in the x-direction. Therefore 40 values of K_{xx} were calculated for each set of runs and each size of flow region. These values of K_{xx} were assumed to represent the results of permeability tests in a well bore when the packer spacing is equal to the flow region dimensions. The values of K_{xx} were used to calculate fracture apertures in the same way that the field data in Section 7.5 was analyzed. That is, a single equivalent aperture, b_1, was calculated as

$$b_1 = \sqrt[3]{\frac{K_{xx}L}{\rho g/12\mu}}\,, \tag{7-10}$$

where L is the zone length or flow region dimension. Then the number of fractures, N, which actually intersected the side in question was counted. An average equivalent aperture, $\bar{b}_A$, was calculated as

$$b_A = \sqrt[3]{\frac{K_{xx}L}{N\,\rho g/12\mu}}\,. \tag{7-11}$$

The actual apertures b of the N fractures which intersected the zones as they existed in the model were also recorded. Then for each set of 20 runs, the average values of b_1, b_A, and b were calculated: $\bar{b}_1$, $\bar{b}_A$, and $\bar{b}$. The mean aperture of all the fractures in all of the 40 generation regions was approximately constant at 0.026 cm.

Figure 7-15 shows $\bar{b}$, $\bar{b}_1$, and $\bar{b}_A$ plotted versus zone length, L. The true mean aperture for all of the generation region is shown as a horizontal line. The object of doing the packer tests is to determine this value of mean aperture.

For all zone lengths the mean of the actual fracture apertures intersecting the well zone is larger than the true mean aperture of fractures in the whole region as Figure 7-15 shows. Because length and aperture are correlated, the fractures with larger aperture are also longer and thus more likely to intersect the well zone. If length and aperture were uncorrelated, the average actual aperture would be expected to converge to the average aperture for the whole region.

The values of $\bar{b}_1$ and $\bar{b}_A$ are less than the mean aperture of the generation regions for all the zone lengths tested. The value of $\bar{b}_A$ is stable for all

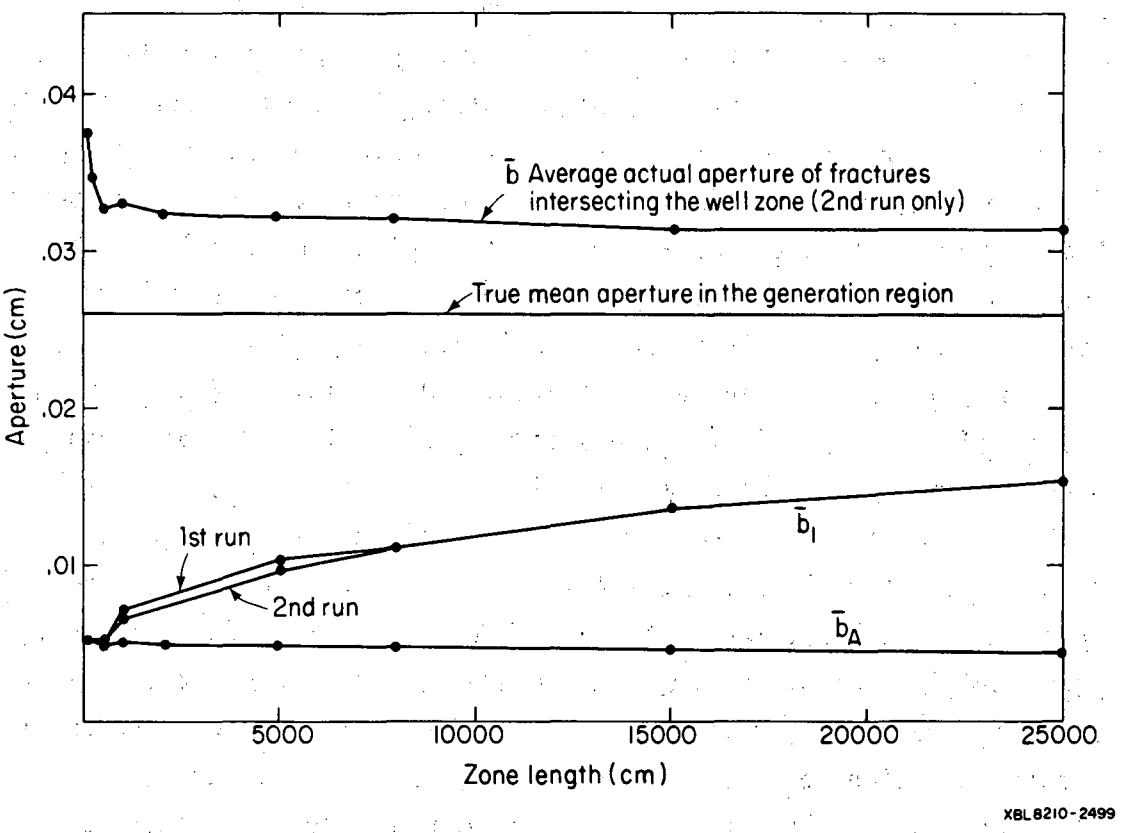

Figure 7-15. Plot of Mean Aperture, $\bar{b}_1$, and $\bar{b}_A$ Versus Zone Length

zone lengths. A slight decline in $\bar{b}_A$ with zone length can be explained by the slow decline in average permeability of all the samples with flow mesh size as shown in Figure 7-16. This effect also explains why the increase in $\bar{b}_1$ does not become a linear function of the packer spacing.

Within the limits of the size of the fractured zone at URL, neither $\bar{b}_1$ nor $\bar{b}_A$ are likely to provide good estimates of the mean aperture. The magnitudes of $\bar{b}_1$ and $\bar{b}_A$ are lower than the mean aperture because of two factors. First, the calculation of b_1 or b_A assumes the fractures are perpendicular to the well when in fact they are not necessarily perpendicular. The error involved is proportional to the cube root of cos Θ where Θ is the angle between the fracture and the plane perpendicular to the well.

The second error in calculating b_1 and b_A results from assuming that the fractures are all perfectly connected and conducting. A good example of this error can be seen in Figures 7-12, 7-13 and 7-14 for the 2,000 x 2,000 cm (20 x 20 m) flow region. Figure 7-12 is one realization from the packer spacing study, and Figure 7-13 shows the flow regions which were analyzed. As can be seen in Figure 7-13, the right-hand side (the outflow side) of this mesh intersects two fractures. But, as can be seen in the 2,000 x 2,000 cm reduced flow mesh of Figure 7-14, both of these fractures have been eliminated from the flow calculation because they do not connect with any other fractures or any other boundary. Thus in this extreme example, the well intersects two isolated fractures but zero permeability is measured. So zero apertures would be calculated for the two fractures if they were assumed to be "connected." In fact, they are not connected and have nonzero apertures.

In less extreme cases, the larger aperture fractures that intersect the well are connected, but only through smaller aperture fractures. When a large aperture fracture feeds into a smaller one, the flux carried by the larger aperture fracture is reduced. Therefore, the measured permeability is reduced and the calculated equivalent aperture is smaller than the real aperture. In the opposite case, when a small aperture fracture is connected through larger aperture fractures, the flux is not significantly increased.

This effect can be illustrated by considering the example of two fractures in series. Figure 7-17 shows two such fractures, A and B, under an overall field gradient, J_F. The equivalent overall permeability in the x-direction,

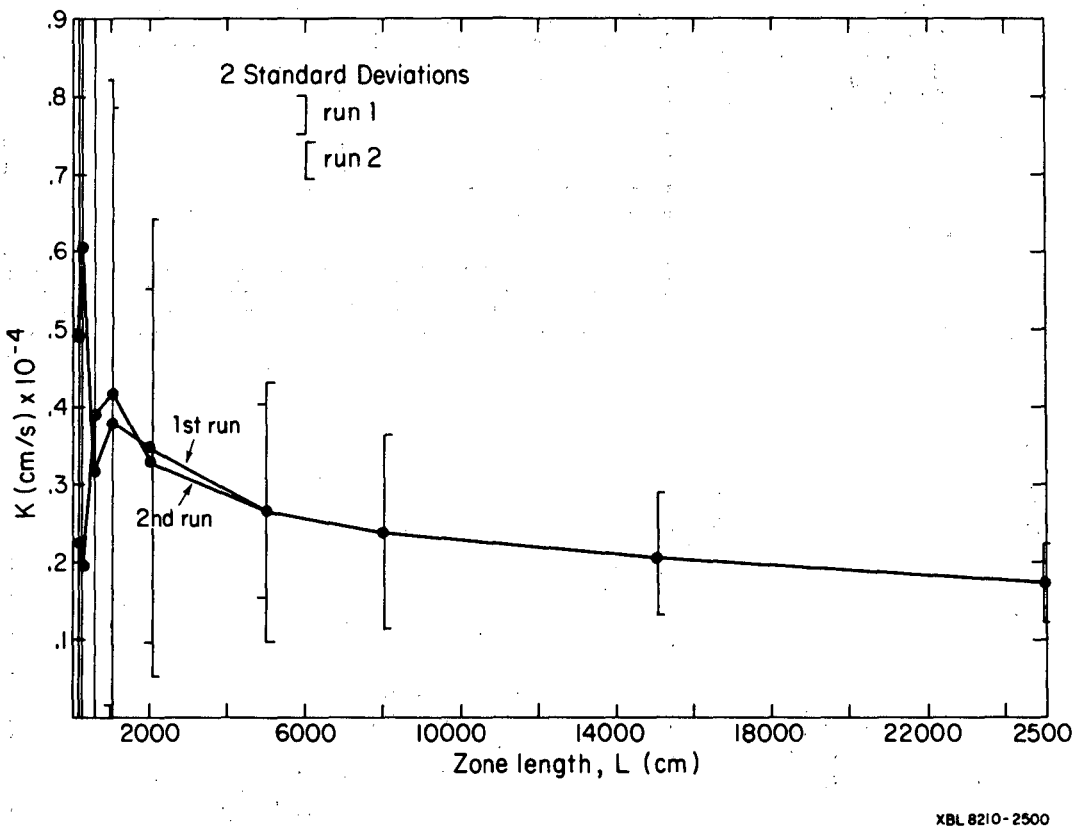

Figure 7-16. Mean Permeability in the x-Direction as a Function of Zone Length

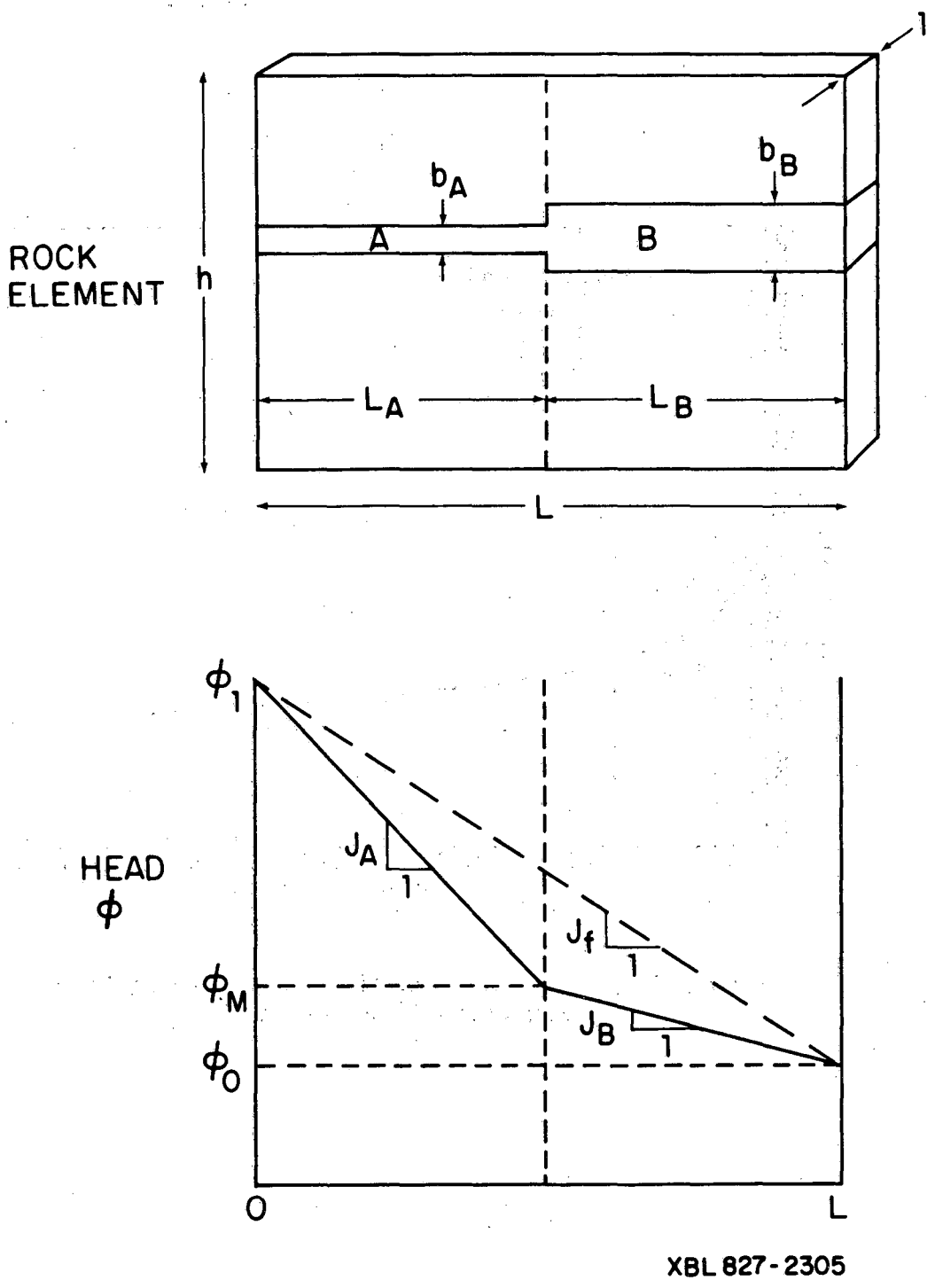

Figure 7-17. Two Fractures in Series

K, of the two fractures can be found by equating the flux through A to the flux through B. That is,

$$Q_A = Q_B = Q, \tag{7-12}$$

$$b_A^3 \frac{\rho g}{12\mu} \frac{(\phi_1 - \phi_M)}{L_A} - b_B^3 \frac{\rho g}{12\mu} \frac{(\phi_M - \phi_2)}{L_B} = 0, \tag{7-13}$$

where ϕ_1 is the head at the left-hand face of the rock element, ϕ_0 is the head at the right-hand face and ϕ_M is the head at the intersection. Solving for the head ϕ_M at the intersection,

$$\phi_M = \frac{L_B b_A^3 \phi_1 + L_A b_B^3 \phi_0}{L_A b_B^3 + L_B b_A^3}. \tag{7-14}$$

The field gradient J_f is

$$J_f = \frac{\phi_1 - \phi_0}{L_A + L_B}. \tag{7-15}$$

The equivalent K for this rock element in the direction of the field gradient is

$$K = \frac{Q}{J_f h} = \frac{b_A^3 b_B^3}{12\mu h} \frac{L_A + L_B}{L_A b_B^3 + L_B b_A^3}. \tag{7-16}$$

The single equivalent aperture, b, for this system is found by equating

$$Q = K J_f h = b^3 \frac{\rho g}{12\mu} J_f. \tag{7-17}$$

So we have:

$$b = \sqrt[3]{\frac{Kh}{\rho g/12\mu}},$$

$$b = \sqrt[3]{\frac{(L_A + L_B) b_A^3 b_B^3}{L_A b_B^3 + L_B b_A^3}}, \tag{7-18}$$

or

$$b = b_B \sqrt[3]{\frac{(L_A + L_B)/L_B}{\frac{L_A}{L_B}\left[\left(\frac{b_B}{b_A}\right)^3 + 1\right]}}. \tag{7-19}$$

If b_B is much greater than b_A, and L_A and L_B are both approximately equal to each other, then $b_B/b_A >> 1$ and

$$b \approx b_B \sqrt[3]{\frac{2}{(b_B/b_A)^3}}, \tag{7-20}$$

$$b \approx b_A \sqrt[3]{2} \approx 1.26 b_A. \tag{7-21}$$

So if b_A is smaller than b_B, the equivalent aperture, b, is approximately equal to b_A.

Heterogeneous connections between fractures usually result in the measured aperture being less than the actual aperture. In this case, although the average of the actual apertures of fractures intersected by the well zone is higher than the true mean aperture this does not compensate for the lack of perfect connection. In the case where length and aperture are not correlated, the average of the actual aperture of fractures intersected by the well will be closer to the true mean aperture of the system. However as a result, in the uncorrelated case the estimate of aperture obtained in steady-state well tests may be even worse than the correlated case.

7.6 CONCLUSIONS AND RECOMMENDATIONS

In these model studies the aperture distributions were varied in three different ways. The mean and standard deviation of aperture were varied and aperture was assigned to the fractures such that it was correlated or uncorrelated to fracture length. These three variants influence both the magnitude of the permeability and the NMSE. The magnitude of the permeability is most affected by the magnitude of the mean aperture. An m-fold increase in mean aperture results in an m^3 increase in permeability. Thus even a less than an order of magnitude change in mean aperture can result in several orders of magnitude of change in permeability. The next strongest influence on the magnitude of the permeability is correlation between length and aperture. Correlated systems may have permeabilities about an order of magnitude higher than similar uncorrelated systems. Finally the standard deviation of the aperture

distribution influences the magnitude of the permeability. An increase in the standard deviation of aperture when fracture apertures are correlated to fracture lengths results in an increase in permeability. If they are not correlated, then an increase in the standard deviation may increase or decrease the permeability. Thus, in order of importance the magnitude of the permeability is affected by the mean aperture, the correlation between length and aperture and the standard deviation of aperture.

The value of NMSE is most significantly influenced by a change in the standard deviation of the aperture distribution. An order of magnitude change in standard deviation can result in a change in NMSE of two orders of magnitude. Corelation between length and aperture has some influence on the NMSE. If length and aperture are correlated, long, high aperture fractures may be formed which serve to increase the NMSE. The value of the mean aperture effectively has no influence on the NMSE. Thus, in order of importance the magnitude of the NMSE is affected by the standard deviation of the aperture distribution, and the correlation between length and aperture.

Based on Model C of this study, the best estimate of the NMSE of URL rock is very roughly 0.04. A value of 0.04 means the permeability ellipse is probably fairly regular. This estimate would be decreased by adding a third dimension to the analysis. However, it would be increased by shortening the fracture lengths or by restricting the sample size to the width of the upper fracture zone. Since we have no estimate of the length of fractures or depth this estimate of NMSE must be treated with extreme caution.

For these statistical systems, NMSE values as high as 1.7 still produce permeability plots that are closed figures. Thus approximation of the URL rock as a porous medium may be acceptable. However, due to the combination of adding a third dimension, shortening the fractures, and decreasing the sample size, the net change in the NMSE may be an increase. If such increase in NMSE produces a permeability plot which is not closed, approximation as a porous medium will be poor.

Steady-state packer tests are likely to give estimates of the mean apertures that are lower than the true mean. In estimating the mean aperture, the packer spacing is not very important as long as b_A is used to estimate the mean aperture instead of b_1 and enough tests are run. The relationship between the true mean aperture and b_A has not been established, but it will clearly be

a complex function of fracture densities, orientations, lengths, and the correlation between length and aperture.

Research and data collection in several areas would be very useful at URL. The correlation between length and aperture should be examined. Field data collected at depth using transient methods (Doe et al, 1982) that provide data on local hydraulic aperture and fracture extent would help to determine whether and how length and aperture are correlated. Complementary theoretical work from a rock mechanics standpoint on the relationship between length and aperture would help to guide these field efforts. More numerical analyses aimed at uncovering the relationship between $\bar{b}_A$, $\bar{b}$, and the true mean aperture under various correlation conditions would greatly help to interpret steady-state packer tests at URL. Research on the relationship of radial flow permeability test results to the behavior of fractured rock under quasi-linear regional flow would also allow for better interpretation of well tests. The development of a three-dimensional fracture model as described in Chapter 8 would greatly reduce uncertainty in understanding the hydraulic behavior of the fractured rock at URL. Finally, some error will likely be associated with application of classical tensorial analysis to flux in the upper fracture zone. Work should be done to quantify this error, possibly by using the methods presented in Chapter 10.

8 EXTENSION OF THE MODEL TO THREE DIMENSIONS

8.1 INTRODUCTION

A two-dimensional model of a system of finite fractures is useful for examining qualitative relationships between fracture geometry and permeability. However, two-dimensional models will never be able to completely describe three-dimensional behavior. The reason for this is that fractures which are not connected in the plane of a two-dimensional analysis may be connected in some other part of the rock mass. Permeability will always be underestimated and hydraulic behavior will always appear to be less like porous media in a two dimensional analysis than in a three-dimensional analysis. Thus, a three-dimensional model would greatly increase the reliability of the results when field data are analyzed using a fracture model.

In reality fractures are irregular, finite discontinuities in the rock. In two dimensions we made the idealization that the fractures could be modeled by straight line segments. Likewise, we will assume fractures are planar segments in three dimensions. We now have to make a further assumption about the shape of the planar segments.

As described in Chapter 2, there is support in the literature for elliptically shaped fractures. However, the simplest and most pragmatic approach is to assume fractures are circular. Circles of course are a subset of ellipses. The identification of intersections between circular fractures is much more straightforward than that for elliptical fractures. The calculation of flow in a fracture between intersections is simplified. Also if circular fractures are assumed, the lateral dimensions of the fracture can be specified with only one parameter, the radius. For ellipses, three parameters are needed: the dimensions of the major and minor axes and the orientation of the axes. The assumption of a circle is pragmatic because the availability of statistically significant field data on the length versus width of fractures and the orientation of the major axes of the ellipse in the fracture plane is unlikely. Therefore fractures will be represented as circles.

The radii of these discs can be considered to vary lognormally, just as the length of fractures in the two-dimensional model varied. Baecher and Larney (1978) have shown that lognormally distributed radii give rise to lognormally

distributed trace lengths. Since lognormally distributed trace lengths are observed in the field the assumption of lognormally distributed radii is reasonable. Fracture centers are located randomly. Fracture orientations and apertures are distributed by sets in a manner similar to the construction of the two-dimensional model except that orientations can vary in two directions. Distributions such as Arnolds' spherical normal distribution (Mahtab et al, 1972) or Bingham's distribution (Mahtab, 1982) can be used to generate the orientations. Also, discrete field data could be used to specify the orientations directly.

The complete three-dimensional model consists of randomly located discs with distributed orientations, apertures, and radii (Figure 8-1) These discs intersect to form the flow system. The form of the intersections is a line segment, whereas in the two-dimensional model the intersections are points. Thus the line segments will become the "nodes" of the three-dimensional model. Steady flow takes place in any given disc-shaped fracture from one node to another.

The fracture system can be generated in a spherical generation region and the flow region will be a cube that lies entirely within the generation region (Figure 8-2). Boundary conditions for the overall model will be similar to those of the two-dimensional model. Boundaries will be the faces of the cubic flow region rather than the edges of the square flow region in the two-dimensional model. As an example consider Figure 8-1. Suppose Side 1 is the inflow face and Side III is the outflow face. Then Side I will be assigned a head of unity. Any fracture intersecting Side I will have a node with prescribed unit head. Thus the intersection of fracture 3 with Side I will have a prescribed head of one. Likewise, Side III will be assigned a head of zero, and the intersection of fracture 5 with Side III will be a node with prescribed head of zero. On Sides II, IV, V, and VI the head will have a fixed, linear distribution. A plot of the head distribution over these boundaries would look like a wedge: the head would be unity along the edge where each of these sides intersects Side I and zero along the edge where each of these sides intersects Side III. The head in between these two lines can be found by linear interpolation. Fractures such as 2 and 4 intersect the distributed head boundaries. The treatment of these nodes will be discussed below.

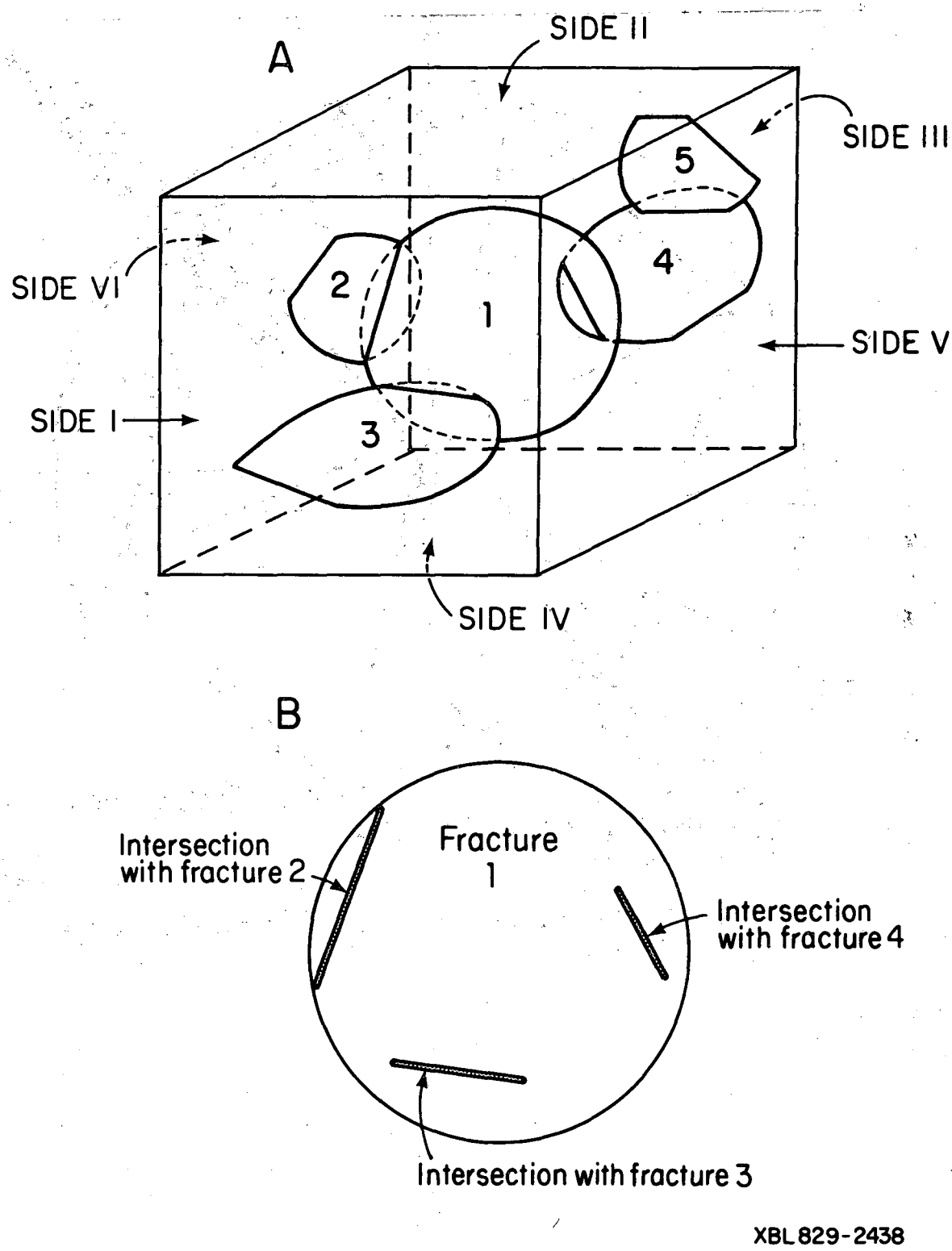

Figure 8-1. Three-Dimensional Fracture Model

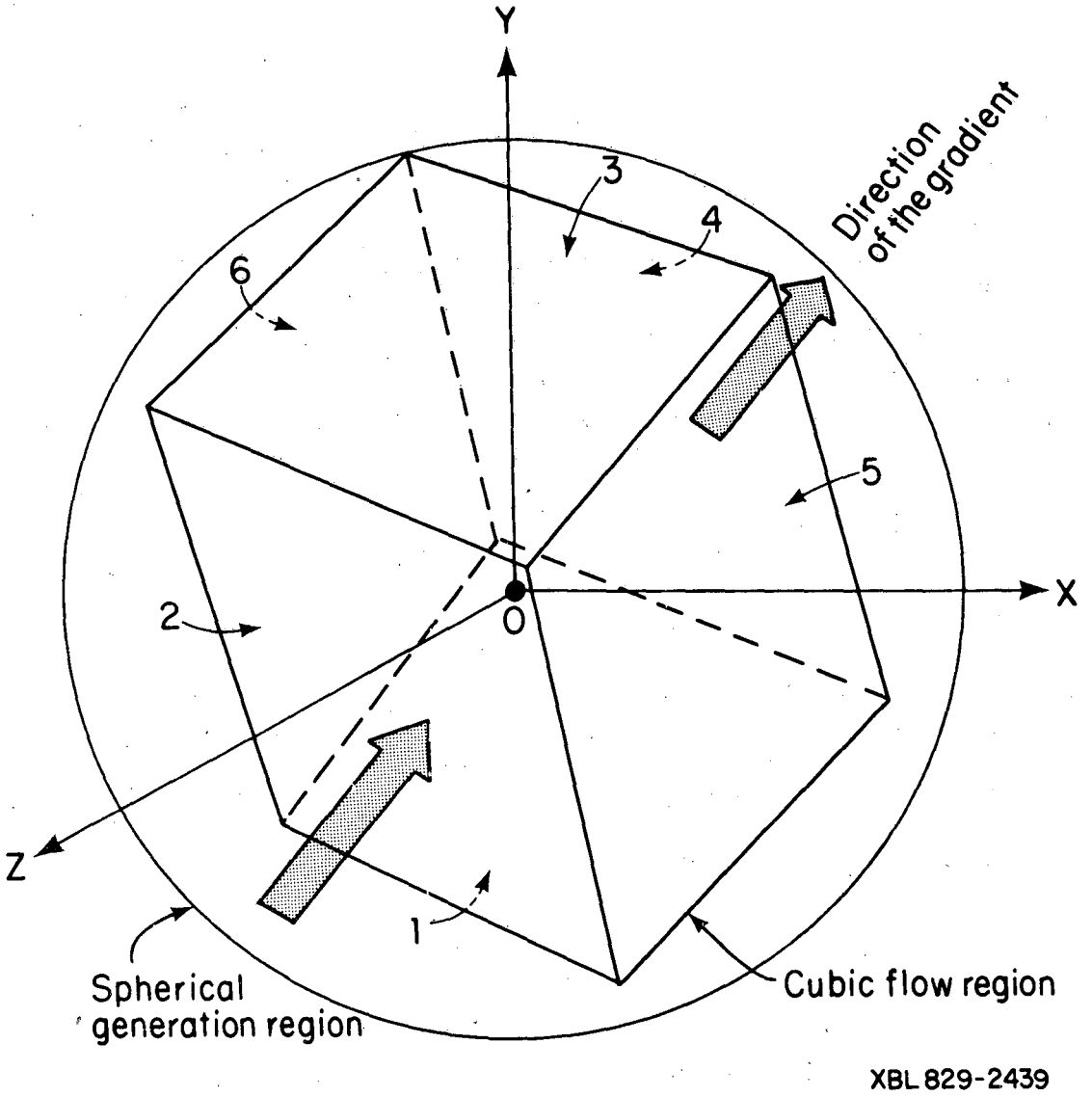

Figure 8-2. Three-Dimensional Generation and Flow Region

As in the two-dimensional model, permeability in the direction of gradient can be measured. The direction of gradient can be changed by mathematically defining different cubic regions of simulated rock oriented in different directions but centered at the same point. In the two-dimensional model the flow region was rotated in equal intervals from 0° to 180° to obtain the entire permeability ellipse. In three dimensions, the rotations must be over a half-sphere in order to define the permeability ellipsoid.

8.2 SOLUTION OF THE FLOW EQUATION

As in the two-dimensional model, a general analytical solution cannot be found for flow in large, random, three-dimensional fracture systems. On the other hand, in three dimensions, a purely numerical solution scheme such as used in the two-dimensional problem would require discretization of each fracture plane. While this is theoretically possible, this approach has two practical problems. The first is that the total number of unknowns would be equal to the number of fractures times the average number of elements in each fracture. Thus there would be severe limitations on the size of problem which could be analyzed. Secondly, the intersections between fractures are randomly located in the fracture disc. Thus the development of a numerical mesh generator which could successfully discretize every fracture would be difficult. The solution technique proposed here is an approximate mixed numerical and analytical method. Flow in each fracture plane is handled analytically. The flux through the system is then calculated using a numerical solution based on mass balance in the system.

The analytical solution in each fracture plane is based on the assumption that each fracture intersection acts like a source or sink with constant strength per unit line length (Figure 8-3). The fracture itself acts like a permeable disc with impermeable boundaries. Solution of the Laplace equation for this case allows calculation of the head distribution along each fracture intersection (node) in terms of the total flux entering or leaving each of the nodes in the fracture disc (Figure 8-3C). When this is done in each fracture disc, two different head distributions will have been found for each node, one for each fracture which forms the intersection.

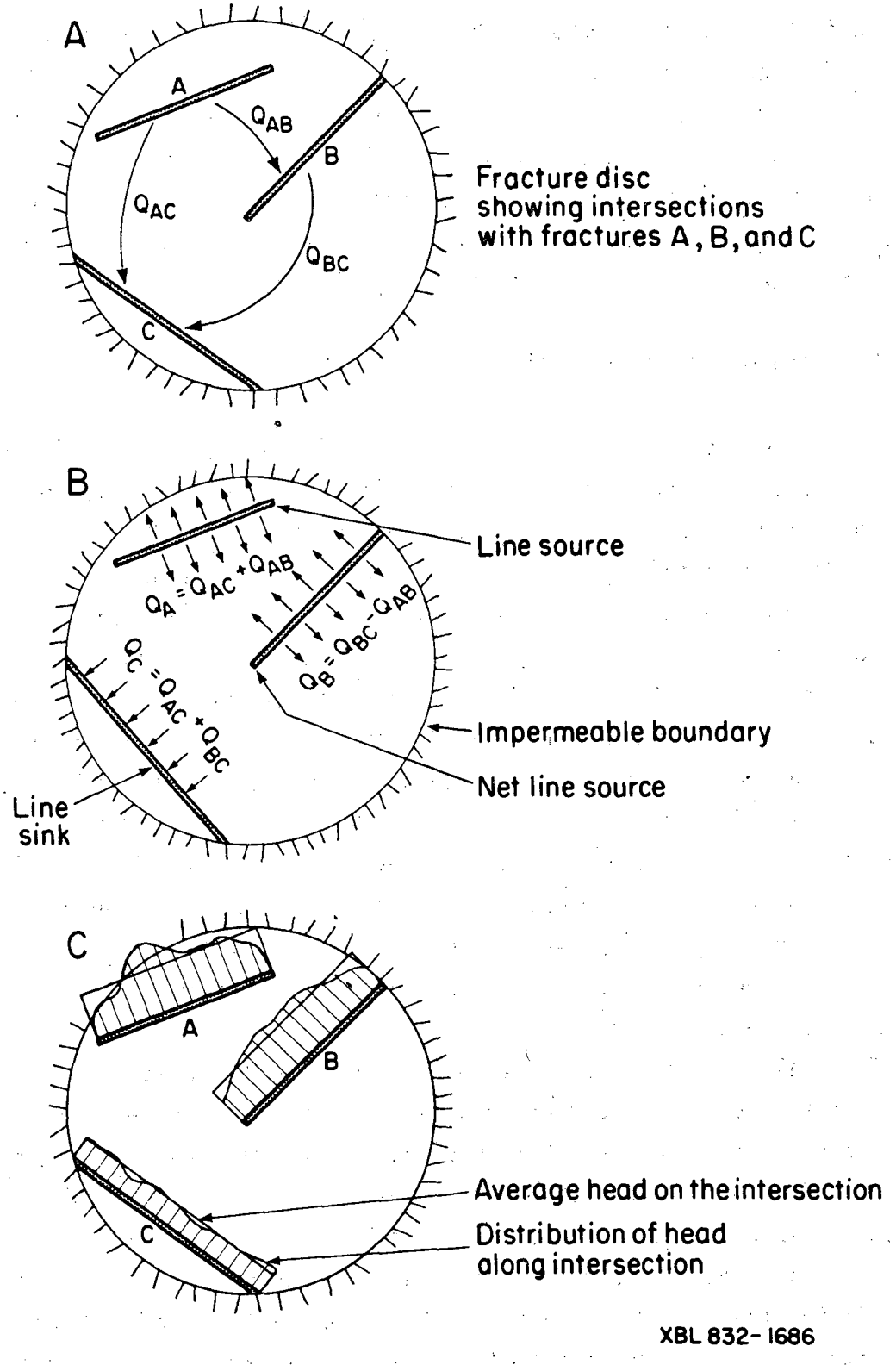

Figure 8-3. Flow Conditions in a Fracture

It is impossible to force these two head distributions to be identical under the assumption that the intersections are of constant strength per unit line length. In reality, the nodes will not have constant strength per unit line length and the head distribution along the node must be the same as measured in either fracture. The actual distribution of strength along the intersections can only be found by using the completely numerical scheme described above, but such a procedure is impractical. In this mixed numerical/analytical scheme, the total flux into or out of an intersection is assumed to be approximately equal to the flux predicted with a source of constant strength per unit length. Furthermore, we require only the average head along the fracture intersection to be the same in each of the fractures which form the intersection. Therefore, for each intersection, the two unknowns are the value of average head and the total flux through the intersection.

Solution of the Laplace equation in each fracture disc allows us to write a set of equations for the average head at each of the intersections in terms of the total flux into or out of each of the intersections. The particular form of these expressions will be determined by the particular geometry of intersections present in that fracture. When inverted this set of equations produces an equation for the total flux into or out of each intersection in terms of the average head at each of the nodes. A global mass balance equation can then be written by equating the flux into a node from one of its associated fractures to the flux out of the intersection into the other fracture. Just as in the two-dimensional case, there will be one equation for each node. Solution of these equations gives the average head at each intersection. Knowing the average heads, the flux through each intersection can be calculated using the analytical solutions for each fracture. The flux through the boundary nodes of each boundary can then be cumulated to find the total flux through the boundary.

8.2.1 Flow in a Fracture Disc

Flow can only take place in a fracture if it is intersected by at least two other fractures. If a fracture is intersected by only one other fracture, then it is a dead end which does not conduct fluid. If a fracture is intersected by two other fractures, then one of the intersections acts as a line

source and the other acts as a line sink. If the fracture is interested by more than two other fractures then at least one of the intersections acts like a source and at least one acts like a sink.

The solution of the problem of flow in the fracture discs uses image sources and sinks to account for the impermeable boundaries. In fact, the simplicity of the image system for a souce or sink within a circle is a major advantage of assuming fractures are circular. The solution for an arbitrary number of line sources and sinks within a disc with impermeable boundaries is derived from the solution for a point source within a circular flow region. Consider a circular disc which contains a point source of strength +m at B as shown in Figure 8-4. For steady state conditions, Milne-Thomson (1968, p. 222) gives an image system which accounts for the impermeable boundary at $r = a$. If the source is located in the circle at $r = g$, then there is an image source of strength +m at $r = a^2/g$ and an image sink of strength -m at $r = 0$. Since the source and the images all lie on the same radial line, the head at any point in the fracture can be found by cumulating the head contributions of the source and the two images.

Recall at least two fracture intersections in a fracture disc are necessary to have flow in the disc, and at least one of the intersections must act like a source and at least one must act like a sink. Furthermore, in order that the total flow into the fracture equals the total flow out of the fracture, the total strength of all sources must be equal and opposite to the total strength of all sinks. Therefore, the total strength of all required images at $r = 0$ will always be zero.

Now we allow point sources to be distributed along an arbitrary line segment in the circle such that the strength per unit line length is constant. First we must find the locus of the distributed images. Then we must find the expression for the total head at any point in the circle due to the sources along the intersection and along the image.

A nonradial line segment source will have an arc-shaped image constructed as shown in Figure 8-5. A radial source will have a radial segment image. The equations for the locus of the arc and radial images can be derived as follows. The equation of the line on which the segment lies can be given as $Ax = By = C$. Changing to radial coordinates, let $x = r\cos\theta$ and $y = r\sin\theta$. Then the equation is $Ar\cos\theta + Br\sin\theta = C$, or

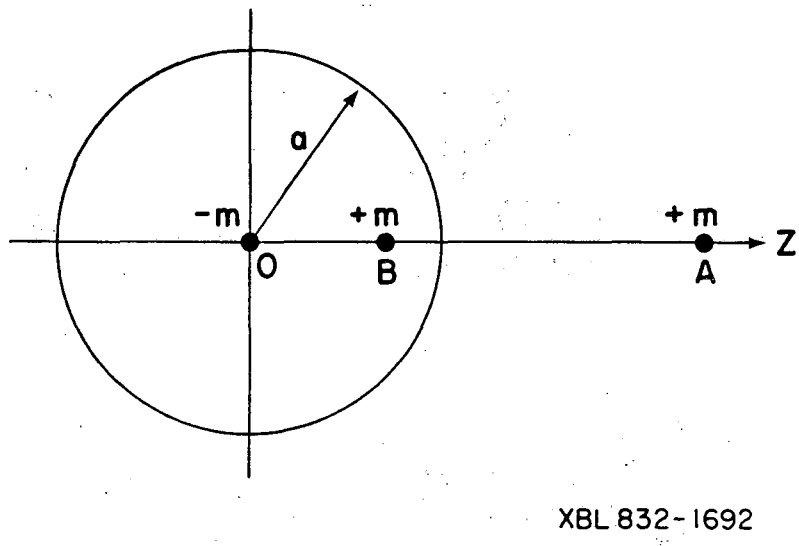

Figure 8-4. Image System for a Point Source in a Circle

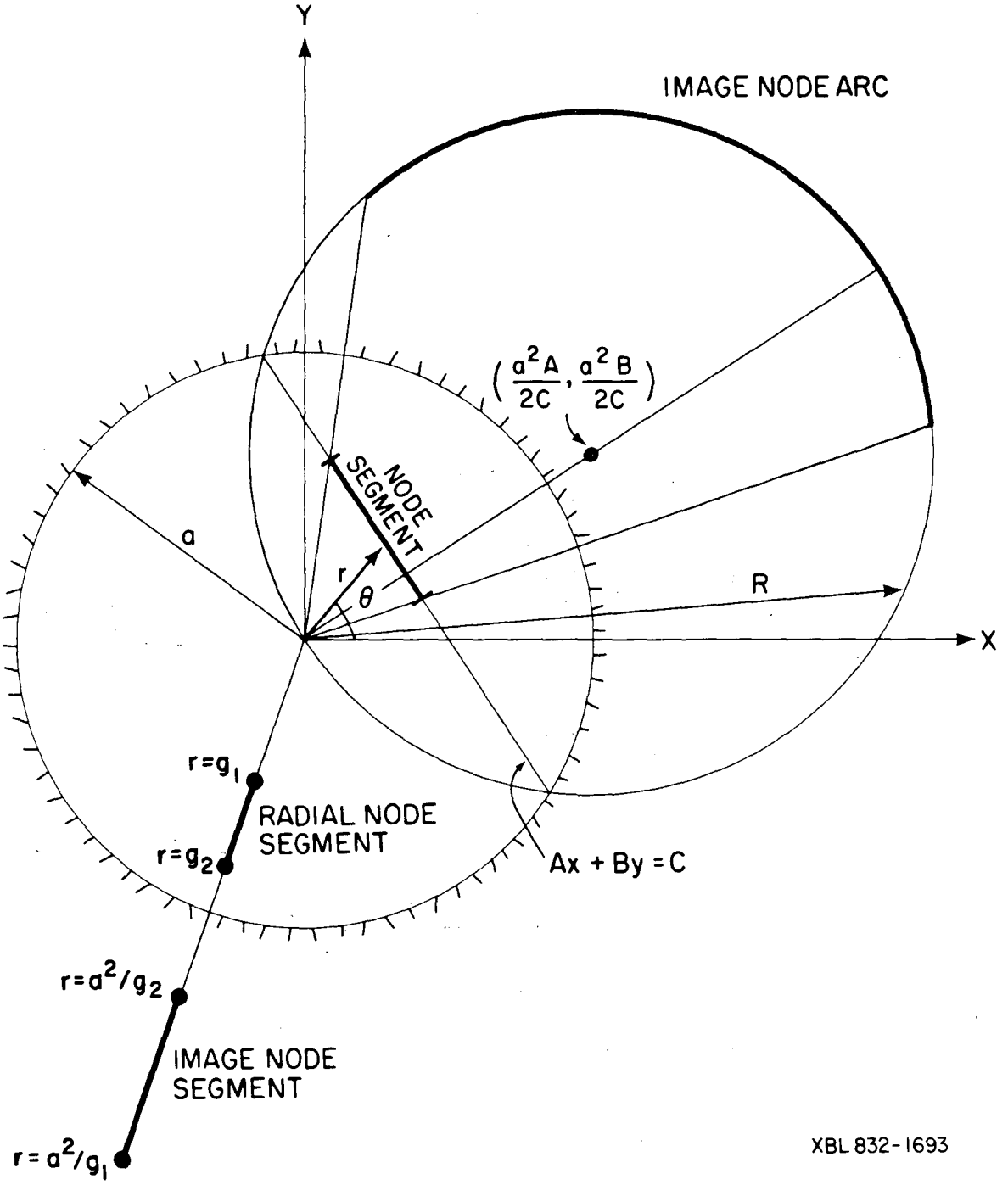

Figure 8-5. Construction of the Nodal Images

$Ar\cos\theta + Br\sin\theta = C$, or

$$r = \frac{C}{A\cos\theta + B\sin\theta} . \tag{8-1}$$

If the line segment is radial, $C = 0$, so

$$\theta = \tan^{-1}(-A/B), \tag{8-2}$$

is the equation of the image segment. The endpoints of the image segment are given by $r = a^2/g_1$ and $r = a^2/g_2$, where a is the radius of the fracture and g_1 and g_2 are the distances from the endpoints of the intersection to the center of the fracture.

If $C \neq 0$, the equation of the image arc, R, is

$$R = \frac{a^2}{r} = \frac{a^2}{C}(A\cos\theta + B\sin\theta). \tag{8-3}$$

Returning to Cartesian coordinates, let

$$\cos\theta = \frac{x}{R} = \frac{x}{\sqrt{x^2 + y^2}} ,$$

and

$$\sin\theta = \frac{y}{R} = \frac{y}{\sqrt{x^2 \quad y^2}} .$$

So we have

$$\left(x - \frac{a^2A}{2C}\right)^2 + \left(y - \frac{a^2B}{2C}\right)^2 = \frac{a^4}{4C^2}(A^2 + B^2). \tag{8-4}$$

Equation 8-4 is the equation of a circle centered at

$$\left(\frac{a^2A}{2C}, \frac{a^2B}{2C}\right) , \quad C \neq 0,$$

with radius

$$\frac{a^2}{2}\frac{\sqrt{A^2 + B^2}}{C}$$

and which always passes through the origin.

Now it remains to evaluate the potential distribution in the circle due to both the sources distributed on the intersection itself and the sources distributed on the image arc or radial segment. In the following, ϕ_{iN}^k will be the potential due to the sources distributed along the intersection i on fracture k; $\bar{\phi}_{iI}^k$ will be the potential due to the sources distributed along the image. The potential due to the presence of intersection i is $\phi_i^k = \phi_{iN}^k + \phi_{iI}^k$. The total potential due to all the intersections in the circle will be given by Φ^k, and the average potential on the intersection will be $\bar{\Phi}_i^k$.

First, consider a nonradial intersection (Figure 8-6). A local arbitrary X, Y coordinate system is established for each fracture disc. All the equations for potential distribution must be referred to X, Y coordinates before they are added. Coordinates convenient for calculation are the x', y' coordinates shown on Figure 8-6. These coordinates are centered at one endpoint of the intersection. The y'-axis lies on the intersection. Point O is the center of the fracture. Point P is an arbitrary point in the plane.

The fundamental solution of the Laplace equation for a point source in an infinite plane is

$$\phi = Kh = \frac{-Q}{2\pi} \ln r, \tag{8-5}$$

where m = Q is the strength of the source, r is the distance from the source, K is the permeability ($K = b^2\rho g/12\mu$), and h is the hydraulic head. Milne-Thomson (1968) shows that the potential due to sources distributed over a line segment of length ℓ on the y'-axis is given by

$$\phi_{iN}^k = K^k h_{iN} = \frac{Q_i}{2\pi\ell} \int_0^\ell \frac{1}{2} \ln[x'^2 + (y' - \xi)^2]\, d\xi, \tag{8-6}$$

where $m_\xi = Q_i/\ell$ is the strength per unit line length and Q_i is the total strength of the line source. The subscript i refers to intersection i. This integral has been evaluated in Selby (1965, p. 334, No. 380):

$$\phi_{iN}^k = -\frac{Q_i}{4\pi\ell} \left\{ (\xi - y') \ln[x'^2 + (y' - \xi)^2] - 2\xi + 2|x'| \tan^{-1}\left(\frac{\xi - y'}{|x'|}\right) \right\}_0^\ell . \tag{8-7}$$

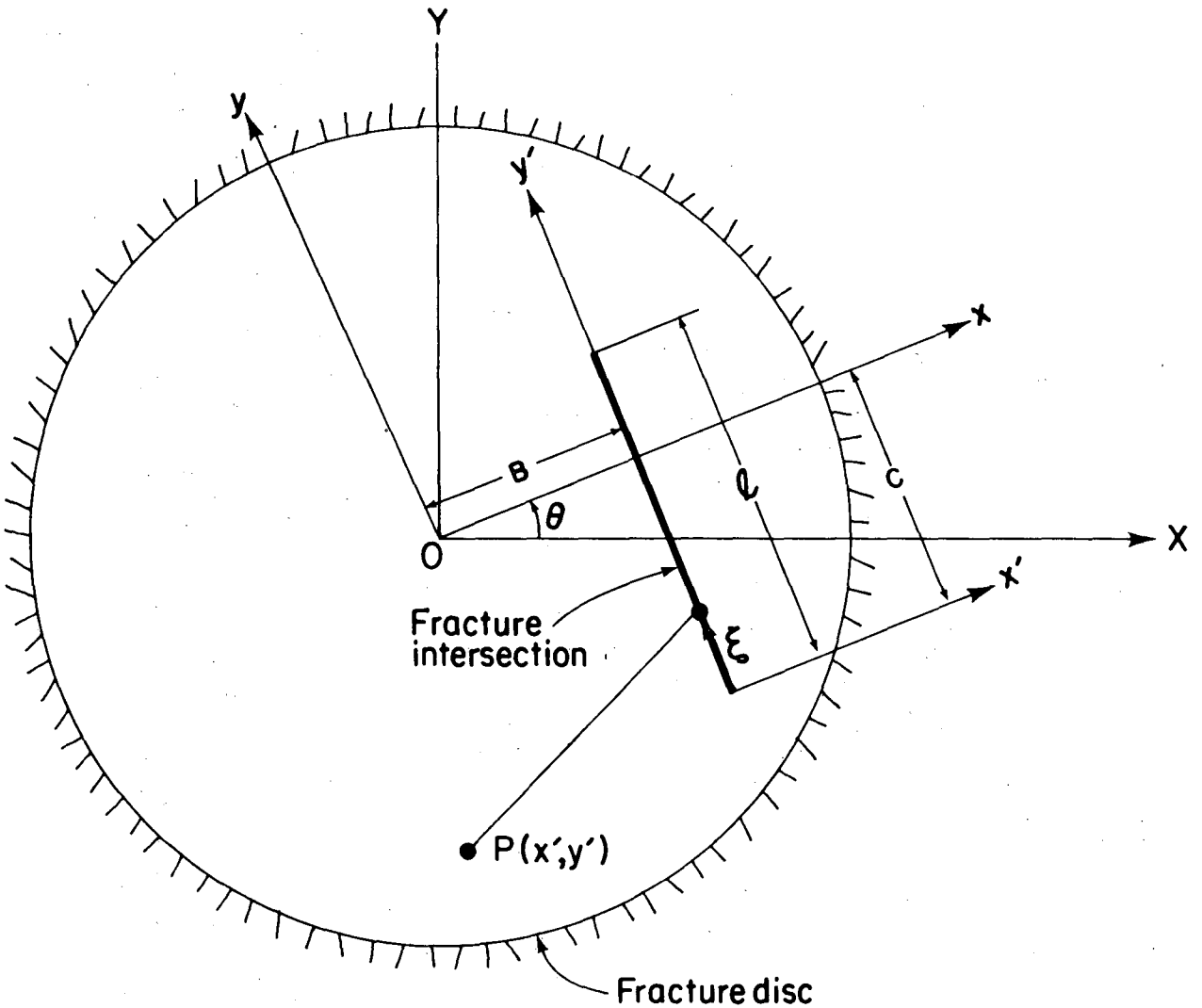

XBL 832-1699

Figure 8-6. A Fracture Intersection in a Fracture Disc

Changing to x, y-coordinates (see Figure 8-6)

$$x = x' + B; \qquad y = y' - C. \tag{8-8}$$

So Equation 8-7 becomes

$$\phi_{iN}^{k} = -\frac{Q_i}{4\pi\ell}\left\{\left[(\ell - y + C)\ln\left((x - B)^2 + (y - C - \ell)^2\right) - 2\ell + 2|x - B|\tan^{-1}\left(\frac{\ell - y + C}{|x - B|}\right) - \left[(-y + C)\ln\left((x - B)^2 + (y - C)^2\right) + 2|x - B|\tan^{-1}\frac{C - y}{|x - B|}\right]\right\}, \tag{8-9}$$

where B and C are defined on Figure 8-6. This expression must now be written in X, Y coordinates which involves the rotation:

$$x = X\cos\theta - Y\sin\theta; \qquad y = X\sin\theta + Y\cos\theta. \tag{8-10}$$

After this substitution we have an expression of the form

$$\phi_{iN}^{k} = Q_i f_{iN}^{k}(X,Y). \tag{8-11}$$

Now consider the image arc as shown in Figure 8-7. The total strength of the sources on the image arc is Q_i because the total strength of the sources on the intersection is Q_i. However, the strength per unit arc length on the image is not constant as it is on the intersection. For any infinitesimal piece of the intersection, $d\xi$, the total strength is

$$m_\xi\, d\xi = \frac{Q_i}{\ell}\, d\xi. \tag{8-12}$$

The total strength on the corresponding infinitesimal piece of image arc, ds, is also $(Q_i/\ell)d\xi$. However along the arc this strength is distributed over the length ds. Thus, the strength per unit line length along the image arc, m_I is

$$m_I = \frac{Q_i}{\ell}\frac{d\xi}{ds}. \tag{8-13}$$

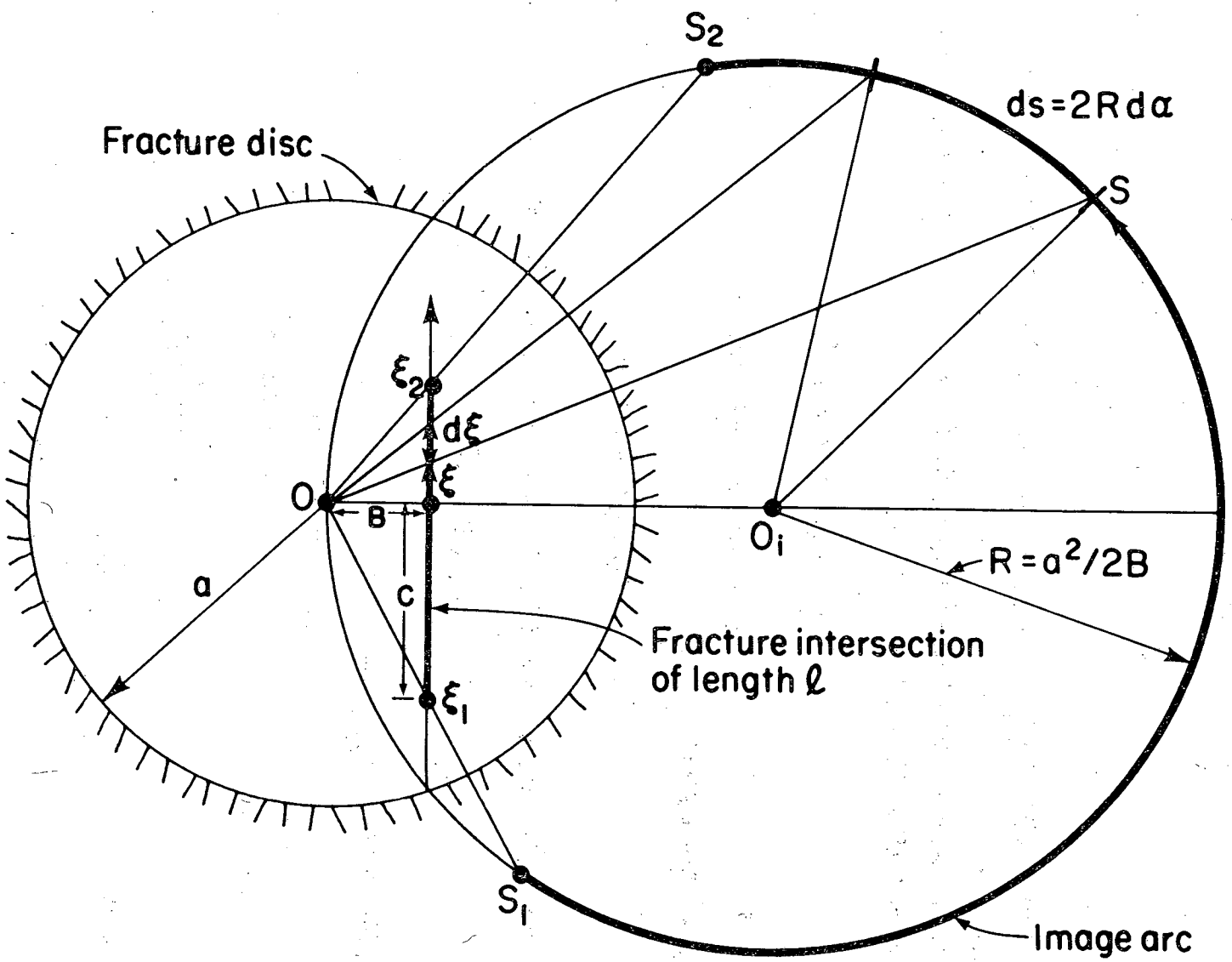

XBL 832-1698

Figure 8-7. Construction for Calculating the Distribution of Strength Along an Image Arc

The integral for the head distribution at any point in the plane due to sources on S distributed according to m_I can be written. Figure 8 shows the coordinate systems used to evaluate this integral:

$$\phi_{iI}^{k} = K^{k} h_{iI} = \frac{-Q_i}{2\pi\ell} \int_{S_1}^{S_2} \frac{d\xi}{ds} \ln r_p \, ds, \tag{8-14}$$

where r_p is the distance from a point S on the arc to any point P in the plane.

In order to avoid evaluating $d\xi/dS$, we wish to find r_p in terms of ξ and integrate from ξ_1 to ξ_2. On S we have

$$x_s' = R \cos\theta' = \frac{a^2}{2B} \cos\theta' , \tag{8-15}$$

$$y_s' = R \sin\theta' = \frac{a^2}{2B} \sin\theta' .$$

So r_p is given by

$$r_p^2 = (x' - R \cos\theta')^2 + (y' - R \sin\theta')^2, \tag{8-16}$$

where (x', y') is any point in the plane. Expanding and collecting terms:

$$r_p^2 = x'^2 + y'^2 + R^2 - 2R(x'\cos\theta' + y'\sin\theta'). \tag{8-17}$$

Now referring to Figure 8-8:

$$\begin{aligned} \cos\theta' &= \cos 2\alpha \\ &= 1 - 2\sin^2\alpha \\ &= 1 - 2\left(\frac{\xi^2}{\xi^2 + B^2}\right), \end{aligned} \tag{8-18}$$

and

$$\begin{aligned} \sin\theta' &= \sin 2\alpha \\ &= 2\sin\alpha \cos\alpha \\ &= \frac{2\xi B}{\xi^2 + B^2} . \end{aligned} \tag{8-19}$$

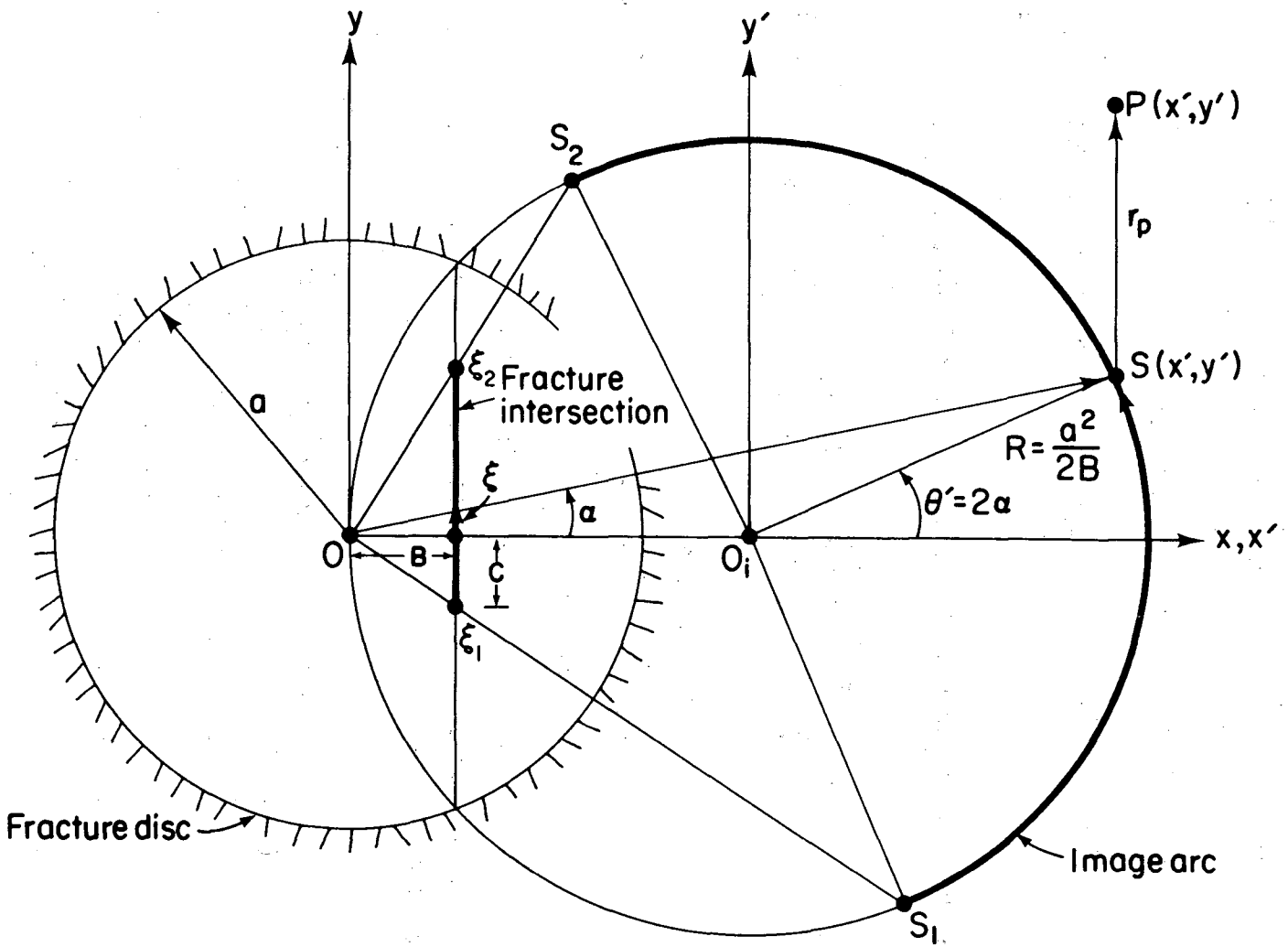

XBL 832-1695

Figure 8-8. Construction for Calculation of Potential due to Sources on the Image Arc

So

$$r_p^2 = x'^2 + y'^2 + R^2 + 2R\left[-x' + \frac{2x'\xi^2 - 2y'\xi B}{(\xi^2 + B^2)}\right]. \tag{8-20}$$

Expanding and collecting terms in the numerator gives:

$$r_p^2 = \frac{(x'^2 + y'^2 + R^2 + 2Rx')\xi^2 - (4Ry'B)\xi + (x'^2 + y'^2 + R^2 - 2Rx')B^2}{\xi^2 + B^2}. \tag{8-21}$$

Now ϕ_{iI}^k can be written in terms of ξ. Substituting 8-21 into 8-14 gives

$$\phi_{iI}^k = K^k h_{iI} = \frac{Q_i}{4\pi\ell}\left\{\int_{\xi_1}^{\xi_2} \ln[\Omega]\, d\xi - \int_{\xi_1}^{\xi_2} \ln(\xi^2 + B^2)\, d\xi\right\}; \tag{8-22}$$

where

$$\begin{aligned} \Omega &= \gamma\xi^2 + \beta\xi + \alpha; \\ \gamma &= (x'^2 + y'^2 + R^2 + 2Rx'); \\ \beta &= -(4Ry'B); \\ \alpha &= (x'^2 + y'^2 + R^2 - 2Rx')\, B^2. \end{aligned} \tag{8-23}$$

These integrals can be evaluated using the same formula used to evaluate 8-6, Selby (1965, p. 334, No. 380):

$$\phi_{iI}^k = K^k h_{iI} = \begin{cases} \dfrac{-Q_i}{4\pi\ell}\left[\left(\xi + \dfrac{\beta}{2\gamma}\right)\ln\Omega - 2\xi + \dfrac{\sqrt{4\alpha\gamma - \beta^2}}{\gamma}\tan^{-1}\left(\dfrac{2\gamma\xi + \beta}{\sqrt{4\alpha\gamma - \beta^2}}\right)\right. \\ \qquad \left. - \left(\xi\ln(\xi^2 + B^2) - 2\xi + 2|B|\tan^{-1}\dfrac{\xi}{|B|}\right)\right]_{\xi_1}^{\xi_2}, \\ \qquad \text{if } (\beta^2 - 4\alpha\gamma) < 0, \\ \text{or} \\ \dfrac{-Q_i}{4\pi\ell}\left[\left(\xi + \dfrac{\beta}{2\gamma}\right)\ln\Omega - 2\xi + \dfrac{\sqrt{\beta^2 - 4\alpha\gamma}}{\gamma}\tanh^{-1}\dfrac{2\gamma\xi + \beta}{\sqrt{\beta^2 - 4\alpha\gamma}}\right. \\ \qquad \left. - \left(\xi\ln(\xi^2 + B^2) - 2\xi + 2|B|\tan^{-1}\dfrac{\xi}{|B|}\right)\right]_{\xi_1}^{\xi_2}, \\ \qquad \text{if } (\beta^2 - 4\alpha\gamma) > 0. \end{cases} \tag{8-24}$$

To move to x, y coordinates allow

$$x' = x - R = x - (a^2/2B) \qquad (8\text{-}25)$$
$$y' = y.$$

The value of $4\alpha\gamma - \beta^2$ can be positive or negative depending on the k values of x and y for point P where ϕ^k_{iI} is to be evaluated. Finally Equation 8-24 must be written in X, Y coordinates by using the transformation given in Equation 8-10. After this substitution we have

$$\phi^k_{iI} = K^k h^k_{iI} = Q_i f_{iI}(X, Y). \qquad (8\text{-}26)$$

If the intersection is radial, a different form must be used for Φ^k_{iN} and Φ^k_{iI}. Figure 8-9 shows the geometry for this case. For Φ^k_{iN} we have

$$\phi^k_{iN} = K^k h_{iN} = \frac{-Q_i}{2\pi\ell} \int_B^C \frac{1}{2} \ \ell n[(x' - \xi)^2 + y'^2] \, d\xi. \qquad (8\text{-}27)$$

This integral is evaluated by the same formula as 8-6 and 8-24.

$$\Phi^k_{iN} = \frac{-Q_i}{4\pi\ell} \left\{(\xi - x')[\ell n \ (x' - \xi)^2 + y'^2] - 2\xi + 2|y'|\tan\left(\frac{\xi - x'}{y'}\right)\right\}_0^{C-B}. \qquad (8\text{-}28)$$

Changing to x, y coordinates

$$x' = x - B$$
$$y' = y. \qquad (8\text{-}29)$$

The equation becomes

$$\phi^k_{iN} = \frac{-Q_i}{4\pi(C - B)} \left\{\left[(C - x + B) \ \ell n[y^2 + (x - B)^2 - 2(x + B)C + C^2] - 2C + 2|y|\tan^{-1}\left(\frac{C - B - X}{|y|}\right)\right] - \left[(-x + 2B) \ \ell n[y^2 + (x - 2B)^2] - 2B + 2|y|\tan^{-1}\left(\frac{2B - x}{|y|}\right)\right]\right\}. \qquad (8\text{-}30)$$

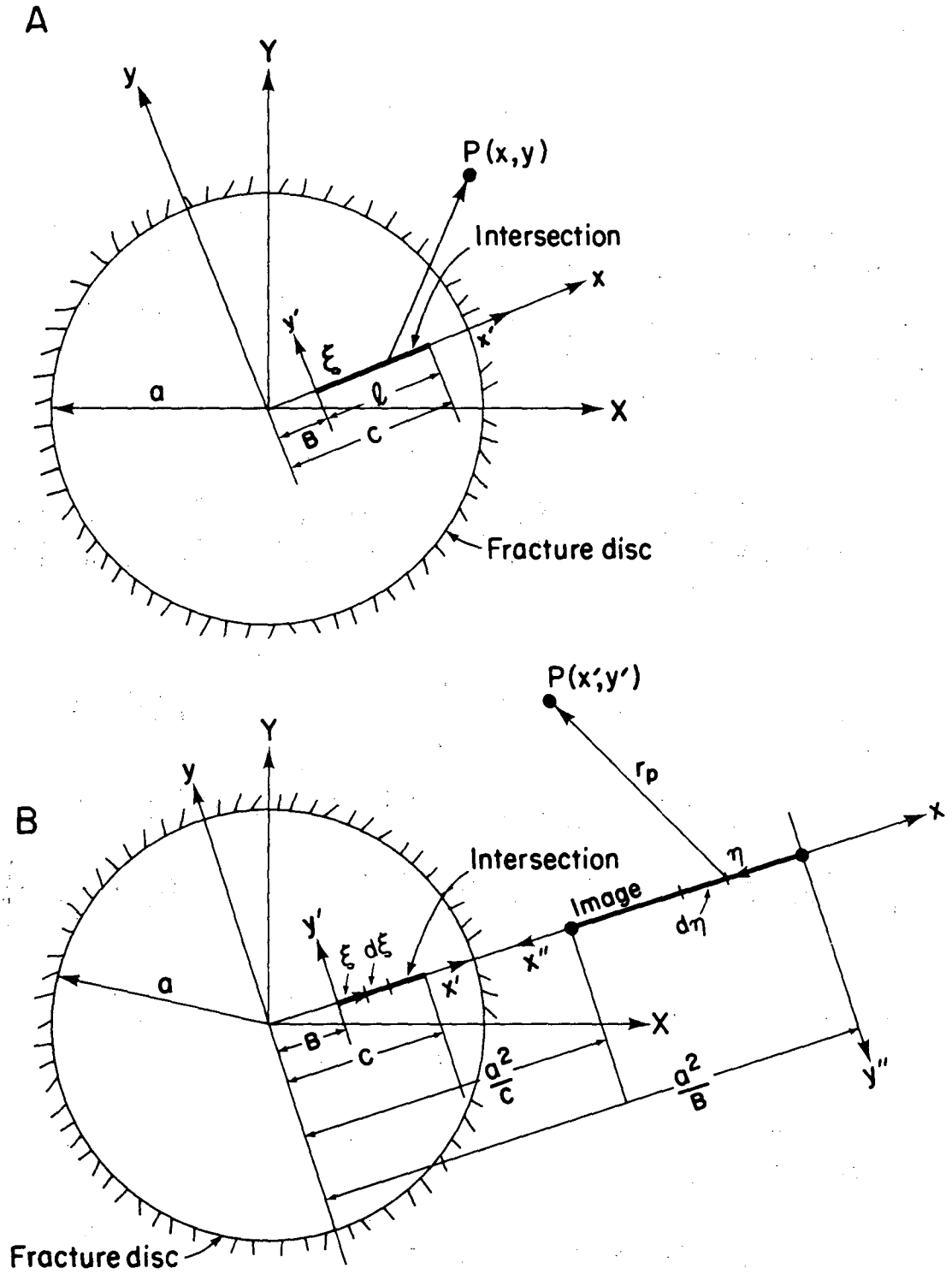

XBL 832-1694

Figure 8-9. A. Radial Intersection. B. Radial Image

The image for this case is also a radial line segment. First the strength per unit length, m_I must be evaluated. Referring to Figure 8-9B:

$$m_I = m_\xi \frac{d\xi}{d\eta} \tag{8-31}$$

$$m_I = \frac{Q_i}{\ell} \frac{d\xi}{d\eta} = \frac{Q_i}{C - B} \frac{d\xi}{d\eta}$$

The distance from a point on the image to any point P(x', y') is

$$r_p^2 = [(\eta - x'')^2 + y''^2] \quad . \tag{8-32}$$

Now we have

$$\phi_{iI}^k = K^k h_{iI} = \frac{Q_i}{4\pi(C - B)} \int_0^{\left(\frac{a^2}{B} - \frac{a^2}{C}\right)} \frac{d\xi}{d\eta} \ln[(\eta - x'')^2 + y''^2] \, d\eta, \tag{8-33}$$

but

$$\eta = \frac{a^2}{B} - \frac{a^2}{\xi + B}, \tag{8-34}$$

and to change x, y-coordinates:

$$x'' = \frac{a^2}{B} - x$$
$$y'' = - y. \tag{8-35}$$

So 8-33 becomes

$$\phi_{iI}^k = K^k h_{iI} = \frac{-Q_i}{4\pi(C-B)} \int_B^C \ln\left[\left(x - \frac{a^2}{\xi + B}\right)^2 + y^2\right] d\xi. \tag{8-36}$$

Expanding the term in square brackets we have

$$\left[\left(x - \frac{a^2}{\xi + B}\right)^2 + y^2\right]$$
$$= x^2 - \frac{2a^2x}{\xi + B} + \frac{a^4}{(\xi + B)^2} + y^2$$
$$= \frac{(x^2 + y^2)\xi^2 + 2((x^2 + y^2)B - a^2x)\xi + (x^2 + y^2)B^2 - 2a^2xB + a^4}{\xi^2 + 2\xi B + B^2}. \tag{8-37}$$

Equation 8-36 can now be written:

$$\phi_{iI}^{k} = \frac{-Q_i}{4\pi(C - B)} \left\{ \int_B^C \ln \Omega \, d\xi - \int_B^C \ln(\xi^2 + 2\xi B + B^2) \, d\xi \right\}, \qquad (8\text{-}38)$$

where

$$\Omega = \alpha + \beta\xi + \gamma\xi^2,$$

$$\alpha = (x^2 + y^2) B^2 - 2a^2 x B + a^4,$$

$$\beta = 2((x^2 + y^2) B - a^2 x),$$

$$\gamma = x^2 + y^2.$$

Since $\beta^2 - 4\alpha\beta$ can be positive or negative depending on the values of x and y, two forms of the solution are needed as in Equation 8-24. The two forms are given in Equation 8-39. Furthermore, if the radial intersection passes through the center of the fracture there will be two image segments, one on each side of the fracture. In this case B is zero and two values of C, C_1 and C_2, are defined, one positive and one negative. ϕ_{iI} then becomes the sum of the two versions of Equation 8-39, one using C_1 and the other using C_2.

$$\phi_{iI}^{k} = K^k h_{iI} = \begin{cases} \dfrac{-Q_i}{4\pi(C - B)} \left\{ \left[\left(\xi + \dfrac{\beta}{2\gamma}\right) \ln \Omega - 2\xi + \dfrac{\sqrt{4\gamma\alpha - \beta^2}}{\gamma} \tan^{-1} \dfrac{2\gamma\xi + \beta}{\sqrt{4\gamma\alpha - \beta^2}} \right] - \left[(\xi + B) \ln(\xi^2 + 2B\xi + B^2) - 2\xi \right] \right\}_B^C, \\ \qquad \text{if } (\beta^2 - 4\alpha\gamma) < 0, \\ \text{or} \\ \dfrac{-Q_i}{4\pi(C - B)} \left\{ \left[\left(\xi + \dfrac{\beta}{2\gamma}\right) \ln \Omega - 2\xi + \dfrac{\sqrt{\beta^2 - 4\alpha\gamma}}{\gamma} \tanh^{-1} \dfrac{2\gamma\xi + \beta}{\sqrt{\beta^2 - 4\alpha\gamma}} \right] - \left[(\xi + B) \ln(\xi^2 + 2B\xi + B^2) - 2\xi \right] \right\}_B^C, \\ \qquad \text{if } (\beta^2 - 4\alpha\gamma) > 0. \end{cases} \qquad (8\text{-}39)$$

Finally the rotation of coordinates expressed by Equation 8-10 is applied to Figure 8-39 and the result is of the form

$$\phi_{iN}^{k} = Q_i \, f_{iN}^{k} \, (X,Y),$$
$$\phi_{iI}^{k} = Q_i \, f_{iI}^{k} \, (X,Y). \tag{8-40}$$

8.2.1 <u>The Global Mass Balance Equations</u>

The potential in fracture k due to any intersection and its images is

$$\phi_i^k \, (X,Y) = \phi_{iN}^k + \phi_{iI}^k \, . \tag{8-41}$$

Note that a third potential term, ϕ_{i0}, associated with intersection i could also have been defined. This term would be the potential due to an image of strength $-Q_i$ at the center of the fracture. However, as previously explained, the total strength of all such images at the center is zero, so no head is contributed from the sum of the images at the center.

Now the total potential in fracture k is

$$\Phi^k(X,Y) = \sum_{i=1}^{I} \phi_i^k = \sum_{i=1}^{I} (\phi_{iN}^k + \phi_{iI}^k). \tag{8-42}$$

where I are the numbers of the intersections in the fracture disc, k. Equation 8-42 becomes

$$\Phi^k(X,Y) = \sum_{i=1}^{I} Q_i F_i^k(X,Y), \tag{8-43}$$

where

$$F_i^k = f_{iN}^k + f_{iI}^k.$$

The F_i^k represent shape functions for the total head distribution over i the entire fracture due to the presence of the ith intersection. Now the average potential at each intersection, i, of fracture k is

$$\bar{\Phi}_i^k = \frac{1}{\ell_i} \int_{\ell_i} \Phi^k(X,Y)d\ell_i = \frac{1}{\ell_i} \int_{\ell_i} \sum_{j=1}^{I} Q_j F_j^k(X,Y)d\ell_i \ , \tag{8-44}$$

$$\bar{\Phi}_i^k(X,Y) = \sum_{j=1}^{I} \left(Q_j \frac{1}{\ell_i} \int_{\ell_i} F_j^k(X,Y)d\ell_i \right) = \sum_{j=1}^{I} Q_j \mathscr{F}_{ji}^k \ ,$$

where $\mathscr{F}_{ji}^k$ is the shape function for the average head on intersection i in fracture k due to the intersection j also on fracture k. That is,

$$\mathscr{F}_{ji}^k = \frac{1}{\ell_i} \int_{\ell_i} F_j^k \, d\ell_i \ . \tag{8-45}$$

The value of $\mathscr{F}_{ji}^k$ may be difficult to obtain analytically, but it can be easily approximated by evaluating F_j at a discrete number of points on each intersection.

Changing to indicial notation, where summation over repeated subscript indices is implied, we have

$$\Phi_i^k = Q_j \mathscr{F}_{ji}^k \ , \tag{8-46}$$

where i, j take on I values and the I are the numbers of the intersections on fracture k. By inverting Equation 8-42 we have

$$Q_j = [\mathscr{F}_{ji}^k]^{-1} \Phi_i^k = G_{ji}^k \Phi_i^k \ , \tag{8-47}$$

where $[\mathscr{F}_{ji}^k]^{-1} = G_{ji}^k$. Equation 8-43 is the analytical solution for the average head on the ith intersection of fracture k.

Now assume all the fracture intersections in the whole system have been numbered sequentially, 1 to N. In Equation 8-43, i and j assume the intersection numbers which lie on fracture k. Thus for instance if intersection 3,7, and 9 lie on fracture k = 4, we have

$$\begin{aligned} Q_3 &= G_{33}^4 \bar{\Phi}_3^4 + G_{37}^4 \bar{\Phi}_7^4 + G_{39}^4 \bar{\Phi}_9^4 \ ; \\ Q_7 &= G_{73}^4 \bar{\Phi}_3^4 + G_{77}^4 \bar{\Phi}_7^4 + G_{79}^4 \bar{\Phi}_9^4 \ ; \\ Q_9 &= G_{93}^4 \bar{\Phi}_3^4 + G_{97}^4 \bar{\Phi}_7^4 + G_{99}^4 \bar{\Phi}_9^4 \ . \end{aligned} \tag{8-48}$$

Note that the order of the indices on G_{ij} is important. G_{ij} may not be symmetric.

Equation 8-47 can be written twice for each intersection, once for each fracture k associated with intersection i. If fractures k_1 and k_2 make up intersection j, then Q_j for k_1 equals $-Q_j$ for k_2:

$$G^{k_1}_{ji_1}\bar{\Phi}^{k_1}_{i_1} + G^{k_2}_{ji_2}\bar{\Phi}^{k_2}_{i_2} = 0, \tag{8-49}$$

where the i_1 are the numbers of the intersections on fracture k_1 and the i_2 are the numbers of the intersections on fracture k_2.

8.2.2 Construction of the Matrix Equations

To explain the formation of the matrix equations, an example fracture system has been chosen (Figure 8-10). In this fracture system both the fractures and the intersections have been numbered. The intersection numbers are circled. Table 8-1 describes each intersection. Remember that any intersection between two fractures or a fracture and a side is referred to as a node.

Assume that the shape factors, G^k_{ij}, have been calculated for each intersection i, with reference to every other intersection j, in fracture k. The matrix equations will then be formed by writing Equation 8-49 for each intersection. Equation 8-49 is written in terms of the average potential, $\bar{\Phi}^k_i$. In order to solve for the average head, h_i at each intersection, i, we write:

$$\bar{\Phi}^k_i = K^k h_i \tag{8-50}$$

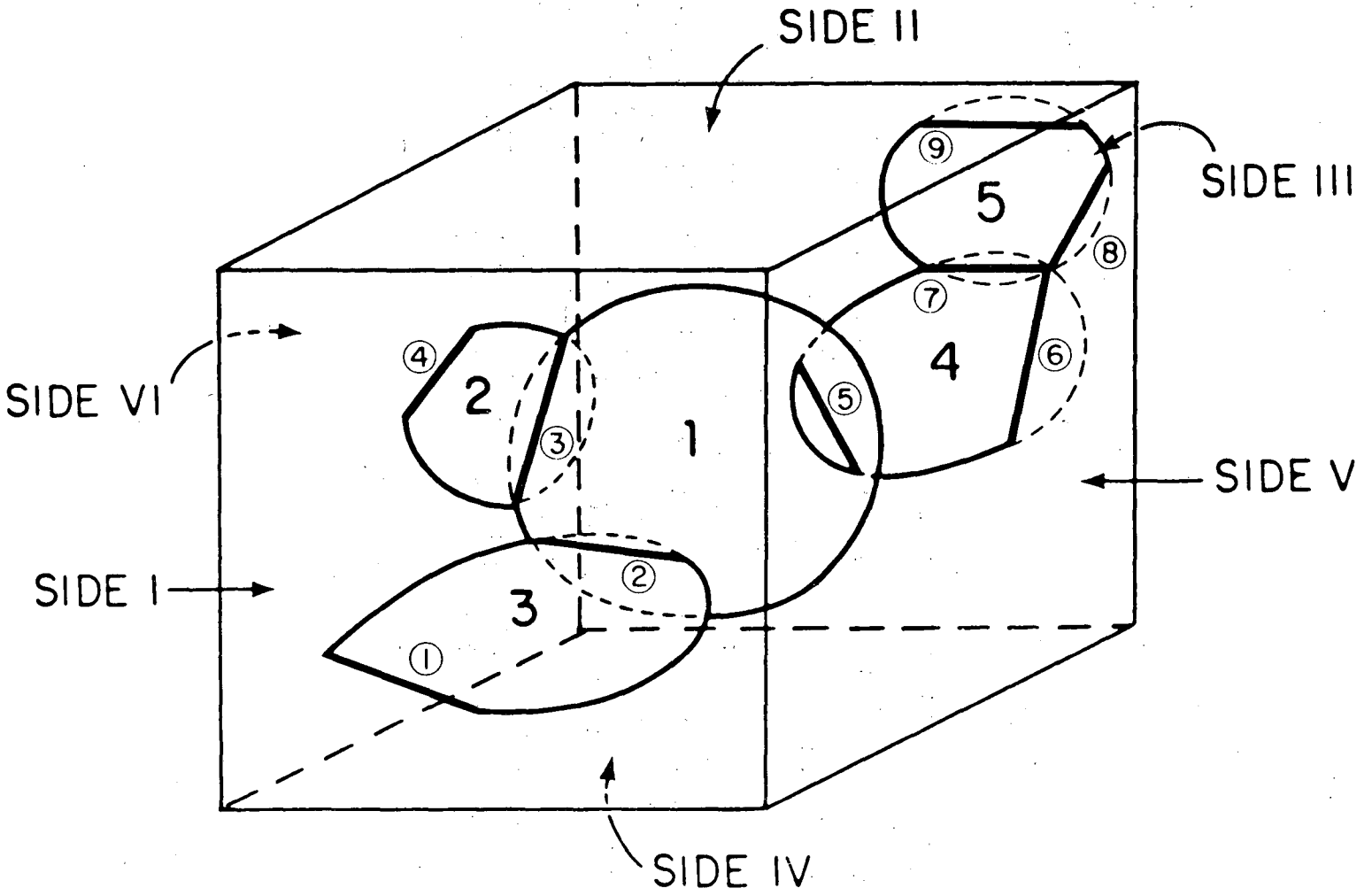

XBL832-1719

Figure 8-10. Example Three-Dimensional Fracture System

Table 8-1. Description of Intersections for Figure 8-10.

Node No.	Node Description	This node is an intersection between: Fracture Numbers		Side Number
1	Boundary	3	-	I
2	Internal	3	1	-
3	Internal	1	2	-
4	Boundary	2	-	VI
5	Internal	1	4	-
6	Boundary	4	-	V
7	Internal/Boundary*	4	5	V
8	Boundary	5	-	V
9	Boundary	5	-	III

*Node 7 is an internal node which intersects Side V at one point.

Note that if permeability, K^k, is different in the two fractures forming the intersection then the potential $\bar{\Phi}_i^k$ will have a different value in each of the two fractures. However, the head, h_i is the same as measured in either fracture.

Now the following equations can be written for flux through each intersection:

$$Q_1 = G_{11}^3 K^3 h_1 + G_{12}^3 K^3 h_2;$$

$$Q_2 = G_{21}^3 K^3 h_1 + G_{22}^3 K^3 h_2;$$

$$Q_2 = G_{22}^1 K^1 h_2 + G_{23}^1 K^1 h_3 + G_{25}^1 K^1 h_5;$$

$$Q_3 = G_{33}^2 K^2 h_3 + G_{34}^2 K^2 h_4;$$

$$Q_3 = G_{32}^1 K^1 h_2 + G_{33}^1 K^1 h_3 + G_{35}^1 K^1 h_5;$$

$$Q_4 = G_{44}^2 K^2 h_4 + G_{43}^2 K^2 h_3;$$

$$Q_5 = G_{52}^1 K^1 h_2 + G_{53}^1 K_1 h_3 + G_{55}^1 K^1 h_5;$$

$$
\begin{aligned}
Q_5 &= G^4_{55}K^4h_5 + G^4_{56}K^4h_6 + G^4_{57}K^4h_7; \\
Q_6 &= G^4_{65}K^4h_5 + G^4_{66}K^4h_6 + G^4_{67}K^4h_7; \\
Q^4_7 &= G^4_{75}K^4h_5 + G^4_{76}K^4h_6 + G^4_{77}K^4h_7; \\
Q_7 &= G^5_{78}K^5h_8 + G^5_{79}K^5h_9 + G^5_{77}K^5h_7; \\
Q_8 &= G^5_{87}K^5h_7 + G^5_{88}K^5h_8 + G^5_{89}K^5h_9; \\
Q_9 &= G^5_{97}K^5h_7 + G^5_{98}K^5h_8 + G^5_{99}K^5h_9.
\end{aligned}
\tag{8-51}
$$

By equating the flux into and out of each intersection and identifying the known values of head on the boundary nodes with H we have

Intersection	Equation
1	$h_1 = H_1$
2	$0 = G^3_{21}K^3H_1 + G^3_{22}K^3h_2 + G^1_{22}K^1h_2 + G^1_{23}K^1h_3 + G^1_{25}K^1h_5$
3	$0 = G^2_{33}K^2h_3 + G^2_{34}K^2H_4 + G^1_{32}K^1h_2 + G^1_{33}K^1h_3 + G^1_{35}K^1h_5$
4	$h_4 = H_4$
5	$0 = G^1_{52}K^1h_2 + G^1_{53}K^1h_3 + G^1_{55}K^1h_5 + G^4_{55}K^4h_5 + G^4_{56}K^4H_6 + G^4_{57}K^4(h^i_7 + H^e_7)/2$
6	$h_6 = H_6$
7	$0 = G^4_{75}K^4h_5 + G^4_{76}K^4H_6 + G^5_{78}K^5H_8 + G^5_{79}K^5H_9 + G^4_{77}K^4(h^i_7 + H^e_7)/2 + G^5_{77}K^5(h^i_7 + H^e_7)/2$
8	$h_8 = H_8$
9	$h_9 = H_9$

(8-52)

Note that the special case of node 7 has been treated by allowing the average head, h_7, to be equal to the average of the head at the point on the boundary, H_7^e, and the head at the opposite endpoint of the intersection, h_7^i. In this case we solve for h_7^i and then calculate h_7.

Now rearranging these equations and putting them in matrix form we have:

$$
\begin{bmatrix}
1 & & & & & & & & \\
 & \begin{pmatrix} G_{22}^3K^3 \\ +G_{22}^1K^1 \end{pmatrix} & G_{23}^1K^1 & G_{25}^1K^1 & & & & & \\
 & G_{32}^1K^1 & \begin{pmatrix} G_{33}^2K^2 \\ +G_{33}^1K^1 \end{pmatrix} & G_{35}^1K^1 & & & & & \\
 & & & 1 & & & & & \\
 & G_{52}^1K^1 & G_{53}^1K_1 & \begin{pmatrix} G_{55}^1K^1 \\ +G_{55}^4K^4 \end{pmatrix} & \frac{1}{2}G_{57}^4K^4 & & & & \\
 & & & & 1 & & & & \\
 & & & G_{75}^4K^4 & \begin{pmatrix} \frac{1}{2}G_{77}^4K^4 \\ +\frac{1}{2}G_{77}^5K^5 \end{pmatrix} & & & & \\
 & & & & & & 1 & & \\
 & & & & & & & 1 &
\end{bmatrix}
\begin{bmatrix} h_1 \\ h_2 \\ h_3 \\ h_4 \\ h_5 \\ h_6 \\ h_7^i \\ h_8 \\ h_9 \end{bmatrix}
=
\begin{bmatrix}
H_1 \\
-G_{21}^3K^3H_1 \\
-G_{34}^2K^2H_4 \\
H_4 \\
-G_{56}^4K^4H_6 - \frac{1}{2}G_{57}^4K^4H_7^e \\
H_6 \\
G_{76}^4K^4H_6 - \frac{1}{2}G_{77}^4K^4H_7^e \\
-G_{78}^5K^5H_8 - G_{79}^5K^5H_9 - \frac{1}{2}G_{77}^5K^5H_7^e \\
H_8 \\
H_9
\end{bmatrix}
$$

XBL 834-1774

that is, $A_{ij}h_i = b_j$.

In general most of the elements of the b_j vector will be zero. However, in this simple example each fracture is either connected to a boundary directly or connected to another fracture which is directly connected to a boundary. As a result all the elements in b_j are non-zero. For each fracture that does not intersect a boundary or another fracture which intersects the boundary, the value of b_j will be zero.

The matrix is sparse, banded and nonsymmetric. When the matrix equation is solved, the values of h_i can be substituted into Equation 8-47 to determine the fluxes through each node. The fluxes through the nodes on each boundary can then be added to find the total flux through each boundary.

8.3 REQUIRED OUTPUT FROM THE FRACTURE MESH GENERATOR

In order to fill the A_{ij} matrix and modify the b_j vector for the connections to the boundary, the fracture mesh generator must provide the following tables: a fracture list, a node list, and a fracture plane geometry list. These are given below in Tables 8-2, 8-3, and 8-4.

Table 8-2. Fracture List

Fracture Number	Aperture	Radius	Number of Intersecting Fractures
o	o	o	o
o	o	o	o
o	o	o	o
.	.	.	.
.	.	.	.
.	.	.	.

Table 8-3. Node or Intersection List

Intersection or	Boundary Code 0-Internal 1-Const. ϕ (-1-const.q)	Side Code	Number of Fractures Forming the Intersection		Global Coordinates of the End Points of Intersection	
Node Number	2-Int'l/bdry	1 → 6	I	J	$(x,y,x)_K$	$(x,y,z)_L$
1	o	o	o	o	o	o
2	o	o	o	o	o	o
3	o	o	o	o	o	o
.	.	.	.	.	.	.
.	.	.	.	.	.	.
.	.	.	.	.	.	.

Table 8-4. Fracture Geometry List

Fracture Number	Intersecting Fractures	Definition of Local Coordinates in the Fracture in Column 1	End Points of IJ Intersection in Local Coordinates	
			(x_1, y_1)	(x_2, y_2)
I	J	4		
I	K	∘	∘	∘
I	L	∘	∘	∘
I	M	∘	∘	∘
J	I	∘	∘	∘
J	Q	∘	∘	∘
.	.	.	.	.
.	.	.	.	.
.	.	.	.	.

9 SUMMARY

This investigation defined criteria for determining when the permeability of a two-dimensional discontinuous fracture system can be represented by a symmetric permeability tensor. Tests to establish these criteria compare the average hydraulic behavior of the fractured medium to that of an ideal homogeneous anistropic porous medium. That is, when the directional permeability, K_g, of the fracture systems is measured, $1/\sqrt{K_g}$ should plot as an ellipse in a polar plot for those systems where flux through the system can be predicted with a symmetric permeability tensor. This ellipse provides a means to calculate the values of the permeability tensor.

The literature on fracture statistics was reviewed to develop a stochastic model of fracture geometry. The size, orientation, and location of fractures in an impermeable matrix were selected as the controlling random variables. These variables served as the basis for random generation of discontinuous fracture systems. Selected portions of these fracture systems called flow regions were then analyzed by finite-element methods to calculate flux through the fracture system. Using Darcy's law, directional permeability was then calculated by dividing the flux through the flow region by the gradient and the cross-sectional area.

To determine directional permeability without ambiguity, it was necessary to impose boundary conditions that would produce a constant gradient in the flow region of systems that were ideally homogeneous and anisotropic (see Figure 3-2). The behavior predicted by using these boundary conditions will be the actual behavior of the rock volume in the field only if the rock volume does in fact behave as an ideal, homogeneous and anisotropic medium. The boundary conditions were rotated for selected regions of the fracture networks to obtain directional permeabilities in different directions. Flow is induced across the flow region, but flux may also occur into or out of the sides of the region since none of the boundaries are impermeable. Thus the inflow on a given side may not equal outflow on the opposite side. The convention adopted in this investigation was that the inflow into the region of interest in the direction of interest would be used in the calculation of permeability. Thus, permeability for the θ-direction may be different than for the 180 + θ-direction. In an ideal anisotropic porous medium, inflow equals outflow on

opposite sides. Thus, permeability in the Θ-direction equals permeability in the $\Theta + 180°$-direction.

Use of this model demonstrated that fracture systems behave more like porous media when (1) the fracture density is increased, (2) apertures are constant rather than distributed, (3) orientations are distributed rather constant, and (4) larger sample sizes are tested.

A regression technique was developed to quantitatively interpret the directional permeability data by determining a best-fit permeability tensor. The differences between the values of directional permeability calculated using the tensor and the measured values is considered the "error." The mean square error can then be calculated and normalized by dividing by the product of the principle permeabilities. This normalized mean square error (NMSE) approaches zero as the behavior of the fracture system approaches that of an anisotropic, homogeneous porous medium.

A series of parameter studies were performed to examine the effect of fracture length and density on fracture system permeability. For a given set of fractures in a given rock matrix, the number of fractures intersected by a unit length of borehole perpendicular to the set provides a characteristic parameter, λ_L. In two dimensions, λ_L is the product of areal density of the fractures, λ_A, and mean fracture length, $\bar{\ell}$. In three dimensions, λ_L is the product of the volumetric density, λ_V, and the mean fracture area.

The linear density, λ_L, can be measured in a borehole but $\bar{\ell}$ and λ_A are very difficult to measure. To investigate the importance of these parameters, fracture systems were analyzed where λ_L was held constant and $\bar{\ell}$ and λ_A varied such that $\lambda_A\bar{\ell} = \lambda_L$. The ratio of mesh size to fracture length was also kept constant to ensure the statistical samples were similar. For very short fracture lengths and high areal densities, the permeability values were relatively low and the value of NMSE was very high because there were very few connections between fractures. As $\bar{\ell}$ increased and λ_A decreased, the permeability increased. For higher values of $\bar{\ell}$ the rate of increase in permeability appeared to decline. This trend was expected but could not be confirmed due to the inability to analyze larger problems with the computer.

The value of NMSE could be used to categorize fracture systems based on the criteria of an acceptable error level. For instance, the fracture systems used in this study with values of NMSE below 0.05 could be considered to be

well represented by a porous medium. For a system with values of NMSE above about 0.3, representation as a porous medium could be considered marginal. With values above 1.0, representation could be considered poor. The same categorization system will not apply to all fracture systems.

Because this length-density analysis was based on a single realization for each statistically different case, a Monte Carlo-type analysis seemed necessary to provide substantiation for the results. The Monte Carlo study was limited due to the costs of computer time required. However the results tended to confirm the general observations based on the single realizations. Furthermore they showed that for a series of realizations of a given fracture system, when the NMSE is higher, the standard deviation of permeability will also be higher. Thus the reliability of regional ground-water models based on the equivalent porous medium concept will be subject to more uncertainty when their NMSE values are higher.

Another series of fracture systems was studied to determine if an increase in the mesh size would reduce the NMSE. In general, the NMSE slightly decreased with increase in mesh size. However, for a particular instance where the NMSE was high to begin with, increasing the mesh size produced an apparently random decrease and then increase in NMSE. This case suggests that certain fracture systems with values of $\bar{\ell}$ below a critical level will not behave like a porous medium on any scale.

An REV study was performed to observe the development of equivalent porous medium behavior as the scale of measurement increases. In this study, the oscillation and gradual leveling off of permeability and NMSE was plotted as a function of the area of the flow region. These plots can be used to determine a lower limit for the scale of the REV for use in a continuum ground-water model.

The modeling techniques were applied to data from the Underground Research Laboratory (URL) facility of Atomic Energy of Canada Ltd. in Manitoba, Canada. Good surface exposures were used to develop a model of the fracture pattern. This fracture pattern was assumed to persist at depth. Well test data were used to estimate aperture distribution models for the model. Seven different aperture models were used to assign apertures to the same fracture pattern model. In the first five models, aperture was correlated with fracture length such that long fractures tended to be assigned larger apertures and shorter

fractures were assigned smaller apertures. In the last two models length and aperture were independent.

The permeabilities of models with uncorrelated length and aperture were smaller than those for correlated models with the same overall fracture statistics. The NMSE of certain correlated models may become high due to the production of very long, high-aperture "superconductors." Increasing the standard deviation of the apertures increases the value of NMSE. For correlated models increasing the standard deviation of the apertures increases the permeability. Increasing the mean aperture in the model by a factor of m increases the permeability by about m^3 as expected.

For all the models tested, the permeability plots were closed figures, even when the NMSE was as high as 1.7. However the permeability of the model which best reproduced the field data for apertures well represented the permeability measured in the well tests. However, the fracture pattern at depth may not be as well connected as that at the surface. A less well-connected fracture pattern implies a lower permeability and also a higher NMSE. However, the NMSE would probably be decreased by adding a third dimension to the analysis. The permeability plot may or may not produce a closed figure if the change in NMSE is a net increase.

Another Monte Carlo study was performed using the URL data to investigate the effect of well test packer spacing on the ability to predict the true aperture distribution. A total of 40 different realizations of the URL fracture system were produced using a correlated aperture-length model. In each of these, flow regions with sizes, L x L from 1 x 1 m to 250 x 250 m were isolated. Flow through all of these regions was calculated. These fluxes were used to determine the mean aperture, $\bar{b}_1$ of the single equivalent fracture which would account for the flux, and the mean aperture, $\bar{b}_A$, of N equivalent fractures where N was the number of fractures which intersected the "test zone." For each flow region the apertures of the fractures which actually intersected the test zone were recorded and the mean $\bar{b}$ was calculated.

The results showed that the fractures which actually intersected the test zone had a mean aperture, $\bar{b}$, that is higher than the true mean aperture. Since length and aperture were correlated, longer fractures with higher apertures were more likely to intersected by the test zone. The value of $\bar{b}_1$ and $\bar{b}_A$ are both less than b and also less than the true mean aperture. This is because the fractures are not perfectly connected and not perpendicular to

the borehole as was assumed in the calculation of $\bar{b}_1$ and $\bar{b}_A$. The value of $\bar{b}_1$ increased with L as expected, but $\bar{b}_A$ very quickly became stable. The value of $\bar{b}_A$ was approximately 1/5 the true mean for all the packer spacings tested. This factor would have been even smaller if length and aperture were uncorrelated.

Finally, the extension of the fracture model to three dimensions was discussed. A model was described where fractures are discs randomly located in space. The intersections between the fracture discs are line segments. Flow in each fracture occurs between the line segment intersections. These line segments are assumed to be at constant head. An approach to an analytical solution for the flow in a fracture disc between all the line segment intersections was described using the method of images and the principle of superposition. An approximate solution was given which analytically calculates the flux between line segments as a function of the geometry of the fracture disc and the average head at each intersection line segment. Then global mass balance equations were developed to solve for the head at each intersection. Fluxes through each intersection can then be back-calculated. This development provides a basis for extending the two-dimensional method of analyzing networks of discontinuous fractures to three dimensions.

10 CONCLUSIONS AND RECOMMENDATIONS

10.1 USE OF THIS TECHNIQUE

It is obvious that an analytical expression cannot be written for the overall permeability of a network of randomly located, discontinuous fractures. Therefore, in this work a numerical approach has been adopted. In this approach a statistical description of fracture network geometry is used to produce random realizations of fracture systems. By measuring the permeability of these network realizations one can investigate the important parameters of fracture flow in a systematic manner. There are, however, certain trade-offs: (1) many realizations must be made in order to obtain the mean and standard deviation of the permeability of the statistically described fracture system, and (2) there is no quantitative way to predict the permeability of fracture systems which have not been measured. Prediction of hydraulic behavior with these techniques is cumbersome.

Use of this model, however, does provide insight into the behavior of fracture systems that was heretofore unavailable. The techniques can be used to study the conditions under which an equivalent porous media permeability can be used to represent the behavior of a fractured rock. The effect on the hydraulic behavior of each of the geometric fracture system parameters can be examined. Field data on fracture geometry can be used in the model. The model can then be used to determine the most important needs for further data collection. In all applications to field situations, the limitations inherent in a two-dimensional model of three-dimensional reality must be remembered. A two-dimensional analysis does not include all the connections between fractures that exist in a three-dimensional fracture system.

A three-dimensional model is necessary for prediction of in-situ behavior but it is not sufficient. In order to have a predictive tool, means must be found to provide the geometric data for the model and to verify the results. Well tests used to determine these parameters are difficult to interpret. It may be that one of the best uses of this model will be an interactive process of (1) using well tests to obtain model parameters, (2) creating a fracture network model, (3) numerically reproducing the well tests in the model, (4) adjusting the interpretation of the well test data and collecting more data,

and (5) adjusting the fracture model, etc. If the basic assumptions are correct, this iterative process should converge to a prediction of hydraulic behavior of the rock mass.

10.2 MODELING TECHNIQUES

The major limitation in the numerical analysis of systems of random fractures is problem size. Over the period in which this research was conducted two major steps were taken to increase the maximum size of the problem which could be solved. The first was to recode the programs to run on the Vax-11 computer which has virtual memory and thus increase the allowable number of unknowns. The second was to eliminate the dead-ends and isolated fractures from the flow analysis and thus decrease the number of unknowns that had to be solved. This streamlining could be augmented in several other ways. The numbering system of the nodes could be changed to decrease the band width. More efficient solvers could be incorporated. Finally, the fracture system could be further reduced to a hydraulic equivalent for flux calculations through an algorithm combining fractures in series or fractures in parallel into hydraulic equivalent fractures.

Such an algorithm would first identify nodes which connect only two fracture elements. For such nodes, the two fracture elements could be combined into one equivalent. Then each fracture element could be compared to every other element to see if it is connected to the same two nodes. If so, these two fracture elements would be combined. The process could be repeated until no further changes could be made. Once the mesh was simplified, it would no longer be easy to determine the average isopotentials, as explained in Chapter 3. Also the details of the velocity distribution would be lost. However, the advantage would be that much more could be learned about permeability.

The boundary conditions used in this work are only useful for determining the best-fit permeability tensor and the NMSE when the system does behave as a porous medium, i.e., if NMSE is small. If the system does not behave as a porous medium on the scale of interest, then the boundary conditions are unrealistic. This is because the actual head distribution on the boundaries will be more variable with a higher value of NMSE.

A technique for predicting the behavior of fracture systems which do not have porous medium equivalents could be developed based on the current methods

that have been discussed. The primary change in the analysis would be the addition of a study region within the flow region. The boundary conditions would be applied to the flow region and the flow region would be rotated as before. However, the flux into and out of the smaller study region within the flow region would be used to develop the permeability analysis.

The relative difference in size between the flow region and the study region may depend on how far the fracture system deviates from porous medium behavior. For higher values of the NMSE, the distance between the study region and the flow region may have to be larger. For a system with NMSE close to zero, the flow region and study region can be the same size. The appropriate ratio between the dimensions of the flow region and the study region might also be determined by steadily increasing the ratio from unity until there is no change in the resulting permeability. Alternatively, the appropriate ratio might be determined by a field situation where the real boundaries would be known. At the least, the ratio should probably be large enough such that no fracture in the study region intersects the boundaries of the flow region.

The implications of using a study region in the computer analysis may be difficult to surmount in some cases. Flow through the entire flow region must still be calculated. Therefore it may be difficult to analyze large study regions, especially for high values of NMSE. Furthermore, the mesh simplification techniques discussed above could not be applied in a straightforward manner. Care would have to be taken to ensure that flux through the boundaries of the study region remains unchanged for the simplified mesh. This could probably be accomplished by tagging each fracture which intersects the study region boundaries and exempting these from the simplification procedure.

The permeability plot from a study region analysis could be used to predict the hydraulic behavior in situ of fractured rocks which do not behave as porous media. Two approaches could be used. One is to assume a mean and deviation of behavior that can be expressed by a permeability ellipse and a function of the NMSE. The second method would be appropriate if some pattern of nonsymmetry persistently recurred in most or all realizations of the fracture system. It might then be possible to quantify this pattern in a probabilistic manner such that the response of the rock volume to a specified gradient could be calculated. In both methods, Darcy's law would be used as it is in other stochastic modeling methods. However, in the first method the

permeability would be a symmetric tensor with associated error. In the second, the quantification of the permeability plot pattern would replace the tensor.

The use of NMSE, especially when measured with a study region as described above, is probably valid as a quantification of error. The derivation of the term should be kept in mind during application to a stochastic ground-water model. The NMSE is the sum of the squared difference between the measured and best-fit values of K_g, all divided by the product of the principal permeabilities. The lowest value the measured K_g can have is zero but there is no maximum value. Thus, there is a limit to the contribution to NMSE made by values of measured K_g less than the best-fit values. There is no limit to the contribution made by values of measured K_g greater than the best-fit values.

10.3 PARAMETER STUDIES

The parameter studies examined the effect on permeability of aspects of fracture geometry that are poorly understood. The motivation behind the length-density study was to determine the extent permeability could be quantified by measuring fracture frequency in a borehole, given the orientation and aperture distribution. Such a relationship would be very useful since fracture length and density are difficult to measure and fracture frequency in a borehole is easy to measure.

Fracture frequency is proportional to both the density and the mean length of fractures. If the length or the density of the fractures increases, the permeability should increase. Therefore, for some range in values when the product of length and density is constant, the net effect on permeability might be small. Unfortunately, such a range of values could not be identified in the study. Access to a larger computer is needed to extend this part of the investigation.

The results do indicate that, at least for shorter fractures, the mean value of permeability is roughly proportional to fracture length. Also the shorter the fracture length is the higher the NMSE tends to be. In fact, for the range of fracture lengths studied, although a porous medium equivalent is a good approximation for the systems with longer fracture lengths, it is not a good approximation for the systems with shorter fracture lengths. Given a measurement of the fracture frequency in a borehole, some knowledge of fracture

length is critical to determining the permeability and in deciding whether to use an equivalent porous-medium approach in ground-water analysis.

If the programs used in this analysis were streamlined as described in Section 10.2, fracture systems with longer lengths could be analyzed. For given values of borehole fracture frequency, aperture distribution and orientation distribution, it may then be possible to determine whether or not there is a critical value of fracture length. For mean values of fracture length less than the critical length, permeability and NMSE are strongly dependent on fracture length. For mean values of fracture length greater than the critical value, permeability and NMSE are only weakly dependent on fracture length. This information would be useful to site exploration programs where efforts could be concentrated on determining whether the mean fracture length was larger or smaller than the critical value.

In the REV study, the model was used to show how representative behavior develops as scale increases. Such an analysis of field data would be useful in selecting an appropriate scale for elements in a regional ground-water flow model. This analysis also gives a very good indication of how large large-scale permeability tests should be in such situations.

The URL data study has shown the importance of possible correlations between length and aperture. If length and aperture are correlated, permeability is higher than if they are not. Also the correlation between length and aperture can possibly provide a method for predicting the existence of "super conductors" or "big cracks" so commonly encountered in wells and underground excavations. The actual relationship between length and aperture should be pursued. A study of the mechanics of crack formation might provide a useful model for the relationship between length and aperture. Field data using transient techniques which indicate both the size of the aperture and extent of an isolated fracture are largely unavailable but would be of great use.

The packer spacing study of the URL data demonstrated that steady-state analyses of well tests underestimate the true mean aperture of the fractures. New research should be done to determine the relationship between the true mean aperture and well test results. These results also point out the need for transient well test analysis. Such transient analysis will give a good estimate of the apertures of the fractures which intersect the wells. If length and aperture are correlated however both the mean aperture and the mean

lengths will be overestimated since the longer fractures with larger apertures are more likely to intersect the well. With a known correlation between length and aperture, the model studies can be used to determine the mean length and aperture of fractures intersecting a line sample. These values can be compared to the mean length and aperture of the fracture sample as a whole. In this manner model studies can be used to develop correction factors for steady state well test analyses.

In all the parameter studies, values of NMSE below about 0.05 appeared to have very regular, symmetric permeability plots. However, there is no distinct upper value of NMSE above which the permeability plots are irregular open figures where $1/\sqrt{K}$ is infinite in some directions. In the length density study, values of NMSE greater than 0.2 produced permeability plots that were not closed. In the URL study, values of NMSE as high as 1.7 were observed, but for all cases the permeability was never zero in any direction. This disparity is due in part to three factors. First, the boundary conditions are not realistic for high values of NMSE, so NMSE is only a valid measurement when it has a low value (e.g., below 0.05). Secondly, whether or not the permeability is zero in a given direction depends only on the fracture pattern, not on the aperture distribution. The NMSE, however, depends on both pattern and aperture distribution. Thus, the values of NMSE based on the URL fracture data are higher because the apertures are distributed rather than constant as they were in the length density study. Finally, NMSE is based on the difference between the best fit and measured values of K_g, not $1/\sqrt{K_g}$. Therefore, anomalously large measured values of K_g can contribute to a large value of NMSE. However, in the polar plot, the value of $1/\sqrt{K_g}$ for these directions can, at most, plot near the origin and do not cause the ellipse to become an open figure. Care must be taken in comparing the values of NMSE from different statistical systems when the values of NMSE are high. Even when evaluating with a study region as discussed above, a higher value of NMSE does not give a quantitative measure of the shape of the permeability plot. The NMSE is only a measure of relative error and as such is really more important than the shape of the polar plot.

10.4 THE THREE-DIMENSIONAL MODEL

The three-dimensional model shows great promise for understanding the permeability of real fracture systems. A major problem with this model will be verification. Because of the nature of the circular fractures, there is no limiting case which reduces to a two-dimensional problem. It may be that verification can only be accomplished with a laboratory study. As an alternative, it may be possible to partially validate this approximate model with numerical techniques. One good technique may be to divide each intersection into n parts which are then treated as n independent intersections. Dividing each intersection into increments allows a more accurate representation of the head distribution along the intersection. An optimal value of n may be identified in this process. Another possibility is to write a completely numerical solution that discretizes each fracture. This model could then be compared to the mixed analytical/numerical model in a limited number of small cases.

The two-dimensional parameter studies that have been presented here should be repeated with the three-dimensional model in order to observe the behavior of three-dimensional systems and also evaluate the error associated with using a two-dimensional analysis as opposed to a three-dimensional analysis. Also the possibility of including mechanical transport in the three-dimensional model should be pursued. Once the solution for flow is known, the head distribution throughout the fractures is known. Thus, it may be possible to identify and trace flow tubes through the system.

Three- or two-dimensional models to predict permeability should be used with caution. Determining the hydraulic aperture distribution from borehole investigations is very difficult. Yet this parameter is extremely important in the calculation of permeability since the bulk permeability is proportional to the aperture cubed. In some cases, the model may be better used to determine the relative error associated with using a porous medium model for the fracture system. In these cases the skewedness of the aperture distribution is more important than its magnitude. In fact, this use of the model is quite important because the NMSE or its equivalent is not easily measured in the field whereas the magnitude of the permeability can be measured. If one desires to use this model to predict the magnitude of permeability throughout

a site, then the techniques used in collecting small-scale data must be validated. Large-scale permeability measurements performed at the same location where small-scale data is collected for use in the model can serve to validate the technique. Such large-scale measurements and their relation to the synthesis of data on small-scale fracture geometry data have been discussed by Long et al (1980).

11 REFERENCES

Baecher, G. B., N. A. Lanney, and H. H. Einstein, 1977. "Statistical Description of Rock Properties and Sampling", Proceedings of the 18th U.S. Symposium on Rock Mechanics, American Institute of Mining Engineers.

Baecher, G. B. and N. A. Lanney, 1978. "Trace Length Biases in Joint Surveys", Proceedings of the 19th U.S. Symposium on Rock Mechanics, American Institute of Mining Engineers, pp. 56-65.

Barton, C. M., 1978. "Analysis of Joint Traces", Proceedings of the 19th U.S. Symposium on Rock Mechanics, American Institute of Mining Engineers, pp. 38-40.

Bear, J., 1972. Dynamics of Fluids in Porous Media, Elsevier, New York.

Benjamin, J. and C. A. Cornell, 1970. Probability Statistics and Decisions for Civil Engineers, McGraw-Hill, New York, NY.

Bianchi, L. and D. T. Snow, 1968. "Permeability of Crystalline Rock Interpreted from Measured Orientations and Apertures of Fractures", Annals of the Arid Zone, Vol 8(2), pp. 231-245.

Caldwell, J. A., 1971. The Theoretical Determination of the Fluid Potential Distribution in Jointed Rocks, M.Sc. Thesis, Univ. of Witwatersrand, Johannesburg, South Africa.

Caldwell, J. A., 1972. "The Theoretical Determination of the Permeability Tensor for Jointed Rock", Proceedings, Symposium on Percolation Through Fissured Rock, Stuttgart, International Society for Rock Mechanics and International Association of Engineering Geology.

Carman, R. C., 1937. "Fluid Flow Through a Granular Bed", Transactions, Institute of Chemical Engineering, Vol. 15, pp. 150-156.

Childs, E. C., 1957. "The Anisotropic Hydraulic Conductivity of Soil", Journal of Soil Science, Vol. 8(1), pp. 42-47.

Collins, R. E., 1961. Flow of Fluids Through Porous Materials, Reinhold Publishing Corporation, New York, NY.

Conrad, F. and C. Jacquin, 1973. Representation of a Two-Dimensional Fracture Network by a Probabilistic Model: Application to Calculation of the Geometric Magnitude of Matrix Blocks, UCRL-Trans-10814 (1975), University of California, Lawrence Livermore Laboratory, Berkeley, CA.

Crawford, P. B. and R. E. Collins, 1954. "Estimating Effect of Vertical Fractures on Secondary Recovery", Transactions, American Institute of Mining Engineers, Vol. 201, p. 192.

Crawford, P. B., and B. L. Landrum, 1955. "Effect of Unsymmetrical Vertical Fractures on Production Capacity", Transactions, American Institute of Mining Engineers, Vol. 204, p. 251.

Davis, S. N., 1969. "Porosity and Permeability of Natural Materials", Flow Through Porous Media, ed. R.J.M. DeWeist, Academic Press, New York, NY, pp. 54-89.

Day, P. R., 1974. "Soil Water Dynamics: A Syllabus for Soil Science 220", University of California, Berkeley, CA.

Doe, T. R., J.C.S. Long, H. E. Endo, and C. R. Wilson, 1982. "Approaches to Evaluating the Permeability and Porosity of Fractured Rock", Proceedings, 23rd Symposium on Rock Mechanics, University of California, Berkeley, CA.

Edelin, D. and A. Kydoniefs, 1972. An Introduction to Linear Algebra, American Elsevier, Inc., New York, NY.

Fara, H. D. and A. E. Scheidegger, 1961. "Statistical Geometry of Porous Media", Journal of Geophysical Research, Vol. 66, pp. 3279-3284.

Fatt, I., 1956. "The Network Model of Porous Media, I, II, and III", Transactions, American Institute of Mining Engineers, Vol. 207, pp. 144-181.

Ferrandon, J., 1948. "Les Lois de l'Ecoulment de Filtration", Genie Civil, Vol. 125, pp. 24-28.

Fisher, R. A., 1953. "Dispersion on a Sphere", Proceedings in the Royal Society of London, Series A, Vol. 217, pp. 295-306.

Freeze, R. A., 1975. "A Stochastic-Conceptual Analysis of One-Dimensional Groundwater Flow in Nonuniform Homogeneous Media", Water Resources Research, Vol. 11(5), pp. 725-741.

Gale, J. E., 1975. A Numerical Field and Laboratory Study of Flow in Rocks with Deformable Fractures, Ph.D. Dissertation, University of California, Berkeley, CA.

Gray, W. G. and K. O'Neill, 1976. "On the General Equations for Flow in Porous Media and Their Reduction to Darcy's Law", Water Resources Research, Vol. 12(2), p. 148.

Greenkorn, R. A., C. R. Johnson, and L. K. Schallenbarger, 1964. "Directional Permeability of Heterogeneous Anisotropic Porous Media", Transactions, American Institute of Mining Engineers, Vol. 231, pp. 124-132.

Hall, W. A., 1956. "An Analytical Derivation of the Darcy Equation", Transactions, American Geophysical Union, Vol. 37, pp. 185-188.

Hammersly, J. M. and D. C. Hanscomb, 1964. Monte Carlo Methods, Methuen and Co., London.

Hoel, P. G., S. C. Port, and C. J. Stone, 1971. Introduction to Probability Theory, Houghton Mifflin Co., Boston, MA.

Hubbert, M. K., 1940. "The Theory of Groundwater Motion, Part I", Journal of Geology, Vol. 48(8), pp. 785-944.

Hubbert, M. K., 1956. "Darcy's Law and the Field Equations of the Flow of Underground Fluids", Petroleum Transactions, American Institute of Mining Engineers, Vol. 207, pp. 222-239.

Hudson, J. A. and S. D. Priest, 1979. "Discontinuities and Rock Mass Geometry", International Journal of Rock Mechanics, Mineral Science and Geomechanics, Abstracts, Vol. 16, pp. 339-362.

Huitt, J. L., 1956. "Fluid Flow in Simulated Fractures", American Institute of Chemical Engineers Journal, Vol. 2, pp. 259-264.

Irmay, S., 1955. "Flow of Liquids Through Cracked Media", Bulletin of the Resources Council, Israel, Vol. 5A(1), p. 84.

Irmay, S., 1968. "On the Theoretical Derivation of Darcy and Forschheimer Formulas", Transactions, American Geophysical Union, Vol. 39, pp. 702-707.

Iwai, K., 1976. Fundamental Studies of Fluid Flow Through a Single Fracture, Ph.D. Dissertation, University of California, Berkeley, CA.

Johnson, W. E. and R. V. Hughes, 1948. "Directional Permeability Measurements and Their Significance", Producers Monthly, Vol. 13(1), pp. 17-25.

Kozeny, J., 1927. "Uber Kajillare Leitung des Wassers im Boden", Sitzungsber Akad. Wiss. Wien, Vol. 136, pp. 271-306.

Lippmann, M. J., 1973. Two-Dimensional Stochastic Model of a Heterogeneous Geologic System, Ph.D. Dissertation, University of California, Berkeley, CA.

Long, J.C.S., J. S. Remer, C. R. Wilson, and P. A. Witherspoon, 1982. "Porous Media Equivalents for Networks of Discontinuous Fractures", Water Resources Research, Vol. 18(3), pp. 645-658.

Long, J.C.S., P. A. Witherspoon, C. R. Wilson, and A. O. DuBois, 1980. "Large Scale Permeability Testing at Stripa", Proceedings 3rd Invitational Well-Testing Symposium, Lawrence Berkeley Laboratory, University of California, Berkeley, CA.

Louis, C., 1969. A Study of the Groundwater Flow in Jointed Rock and Its Influence on the Stability of Rock Masses, Imperial College Rock Mechanics Research Report No. 10, Imperial College, London.

Maasland, M., 1957. "Soil Anisotropy and Land Drainage", Drainage of Agricultural Lands, ed. J.N. Luthin, American Society of Agronomy, Madison, WI, pp. 216-246.

Mahtab, M. A. and F. M. Yegulalp, 1982. "A Rejection Criterion for Definition of Clusters in Orientation Data", Proceedings, 23rd Symposium on Rock Mechanics, University of California, Berkeley, CA.

Mahtab, M. A., D. B. Bolstad, J. R. Alldredge, and R. J. Shanley, 1972. Analysis of Fractured Orientations for Input to Structural Models of Discontinuous Rock, Investigation No. 7669, U.S. Department of the Interior, Bureau of Mines Report.

Maini, Y.N.T., 1971. In Situ Hydraulic Parameters in Jointed Rock-Fluid Measurement and Interpretation, Ph.D. Dissertation, Imperial College, London.

Marcus, H. and D. E. Evanson, 1961. "Directional Permeability in Anisotropic Porous Media", Water Resources Center Contribution No. 31, University of California, Berkeley, CA.

Marcus, H., 1962. "The Permeability of a Sample of an Anisotropic Porous Medium", Journal of Geophysical Research, Vol. 67, pp. 5215-5225.

Marine, I. W., 1980. "Determination of the Location and Conductivity of Fractures in Metamorphic Rock with in Hole Tracers", Groundwater, Vol. 18(3), pp. 252-261.

Milne-Thomson, R. M., 1968. Theoretical Hydrodynamics, MacMillan Co., New York, NY.

Moran, J. H., 1962. "Discussion of Paper by Fara and Scheidegger, 'Statistical Geometry of Porous Media'", Journal of Geophysical Research, Vol. 67, p. 2085.

Morita, N. and K. E. Gray, 1980. "Three-Dimensional Permeability Measurements", 55th Annual Fall Technical Conference and Exhibition of the Society of Petroleum Engineers of the American Institute of Mining Engineering, (September 21-24, 1980), SPE 9377.

Narasimhan, T. N., 1980. "A Note on Volume Averaging", Advances in Water Research, Vol. 3, pp. 135-139.

Ollos, G., 1963. "Examen Hydraulique de L'écoulement dans des Roches Crevassées sur des Modèles Réduits", Bulletin of International Association of Scientific Hydrology, Vol. 8(2), p. 9.

Parsons, R. W., 1966. "Permeability of Idealized Fractured Rock", Society of Petroleum Engineering Journal, Vol. 10, pp. 126-136.

Philip, J. R., 1957. "Transient Fluid Motions in Saturated Porous Media", Australian Journal of Physics, Vol. 10(1), pp. 43-53.

Pincus, H. J., 1953. "The Analysis of Aggregates of Orientation Data in the Earth Sciences", Journal of Geology, Vol. 61(6), pp. 482-509.

Pollard, D. D., 1978. "Forms of Hydraulic Fractures as Deduced from Field Studies of Sheet Intrusions", Proceedings 19th U.S. Symposium on Rock Mechanics, pp. 1-9.

Pollard, D. D., and O. H. Muller, 1976. "The Effects of Gradient in Regional Stress and Magma Pressure in the Form of Sheet Intrusions in Connection", Journal of Geophysical Research, Vol. 81(5), pp. 975-984.

Pollard, D. D., 1976. "On the Form and Stability of Open Hydraulic Fractures in the Earth's Crust", Geophysical Research Letters, Vol. 3(9), pp. 513-516.

Priest, S. D., and J. Hudson, 1976. "Discontinuity Spacings in Rock", International Journal of Rock Mechanics and Mining Science, Vol. 13, pp. 135-148.

Rats, M. V., and S. N. Chernyashov, 1965. "Statistical Aspect of the Problem on the Permeability of Jointed Rocks", Paper No. 73, Symposium on the Hydrology of Fractured Rocks, Dubrovnik, Yugoslavia, AISH-UNESCO, p. 227-236.

Rissler, P., 1978. Determination of the Water Permeability of Jointed Rock, English Edition of Volume 5, Publication of the Institute for Foundation Engineering Mechanics, Rock Mechanics and Waterways Construction, RWTH University, Aachen, Federal Republic of Germany.

Robertson, A., 1970. "The Interpretation of Geological Factors for Use in Slope Stability", Proceedings, Symposium on the Theoretical Background to the Planning of Open Pit Mines with Special Reference to Slope Stability, pp. 55-71.

Rocha, M. and F. Franciss, 1977. "Determination of Permeability in Anisotropic Rock Masses from Integral Samples", Structural and Geotechnical Mechanics, ed. W. J. Hall, Prentice-Hall, New York, NY, pp. 178-202.

Roegiers, J. C., J. H. Curran, and W. F. Bawden, 1978. Numerical Modeling of Flow in Fractured Rock Masses, prepared for Energy, Mines and Resources, Canada, Earth Physics Branch, Ottawa, Ontario.

Sagar, B., and A. Runchal, 1982. "Permeability of Fractured Rock: Effect of Fracture Size and Data Uncertainties", Water Resources Research, Vol. 18(2), pp. 266-274.

Sayles, R. S., and T. R. Thomas, 1978. "Surface Topography as a Non-Stationary Random Process", Nature, Vol. 271, February, pp. 431-434.

Scheidegger, A. E., 1954. "Directional Permeability of Porous Media to Homogeneous Fluids", Geofisica pura Applicata, Vol. 28, pp. 75-90.

Scheidegger, A. E., 1960. The Physics of Flow Through Porous Media (Revised Edition), University of Toronto Press.

Secor, D. T. and D. D. Pollard, 1975. "On the Stability of Open Hydraulic Fractures in the Earth's Crust", Geophysical Research Letters, Vol. 2(11), pp. 510-513.

Selby, S. M., ed., 1965. Standard Mathematical Tables, 14th Edition, The Chemical Rubber Co., Cleveland, OH.

Serafim, J. L. and A. del Campo, 1965. "Interstitial Pressure on Rock Foundations of Dams", Journal Soil Mechanics and Foundations Division, ASCE, Vol. 91(5), p. 65.

Sharp, J. C., 1970. Fluid Flow Through Fissured Media, Ph.D. Dissertation, Imperial College, London.

Simonson, E. R., A. S. Abou-Sayed, and R. J. Clifton, 1978. "Containment of Massive Hydraulic Fractures", Journal of the Society of Petroleum Engineering, February, pp. 27-32.

Smith, L., 1978. Stochastic Analysis of Steady State Groundwater Flow in a Bounded Domain, Ph.D. Dissertation, University of British Columbia, Vancouver, Canada.

Smith, L. and R. A. Freeze, 1979a. "Stochastic Analysis of Steady State Groundwater in a Bounded Domain, 1: One-Dimensional Simulations", Water Resources Research, Vol. 15(3), pp. 521-528.

Smith, L. and R. A. Freeze, 1979b. "Stochastic Analysis of Steady Groundwater Flow in a Bounded Domain, 2: Two-Dimensional Simulations", Water Resources Research, Vol. 15(6), pp. 1543-1559.

Snow, D. T., 1965. A Parallel Plate Model of Fractured Permeable Media, Ph.D. Dissertation, University of California, Berkeley, CA.

Snow, D. T., 1969. "Anisotropic Permeability of Fractured Media", Water Resources Research, Vol. 5(6), pp. 1273-1289.

Strack, O.D.L., 1980. Assessment of Effectiveness of Geologic Isolation Systems Analytic Modeling for Flow in a Permeable Fissured Medium, 1: Isolated Cracks, PNL-3547, Pacific Northwest Laboratory, Richland, WA.

Sun, R. J., 1969. "Theoretical Size of Hydraulic Induced Horizontal Fractures and Corresponding Surface Uplift in an Idealized Medium", Journal of Geophysical Research, Vol. 74(25), pp. 5995-6011.

Terzaghi, R., 1965. "Sources of Error in Joint Surveys", Geotechnique, Vol. 15, pp. 287-303.

Toth, J., 1967. "Groundwater in Sedimentary (Clastic Rocks)", Proceedings, National Symposium on Groundwater Hydrology (San Francisco, CA, November 6-8), pp. 91-100.

Veneziano, D., 1979. "Probabilistic Model of Joints in Rock", Civil Engineering Department, Massachusetts Institute of Technology, Boston, MA.

Warren, J. E. and H. S. Price, 1961. "Flow in Heterogeneous Porous Media", Society of Petroleum Engineering Journal, Vol. 1, pp. 153-169.

Wilson, C. R., 1970. An Investigation of Laminar Flow in Fractured Porous Rocks, Ph.D. Dissertation, University of California, Berkeley, CA.

Wilson, C. R., J.C.S. Long, R. M. Galbraith, K. Karasaki, H. K. Endo, A. O. DuBois, M. J. McPherson, and G. Ramqvist, 1982. Geohydrological Data from the Macropermeability Experiment at Stripa, LBL-12520, SAC-37, Lawrence Berkeley Laboratory, Berkeley, CA.

Witherspoon, P. A., J.S.Y. Wang, K. Iwai, and J. E. Gale, 1979. "Validity of Cubic Law for Fluid Flow in a Deformable Rock Fracture", Water Resources Research, Vol. 16(6), pp. 1016-1024.

APPENDIX A

FIELD DATA WHICH CAN BE USED TO DETERMINE THE INPUT PARAMETERS FOR THE MODEL

A.1 FRACTURE LENGTH

Some information about fracture length can be obtained from measurements made in the borehole. Such information may be extracted from well test results on fractures isolated by packers if transient methods are used (Doe, et al, 1982). At URL and other sites, trace length data are available at the surface and in excavations. This is currently the primary source of data on fracture length. For each fracture set, measuring the mean and standard deviation of the observable trace lengths is useful. The data can be collected as shown in Table A-1. The minimum trace length included in the sample indicates where the length distribution is effectively truncated. A plot such as shown in Figure A-1 is useful for determining the distribution parameters.

If apparent apertures (i.e., apertures as measured with a caliper) can be measured at the same time as trace length, it may be possible to gain information on the relationship between length and aperture. This possibility is explained below under the section on aperture.

A.2 AREAL DENSITY

If the horizontal plane is chosen for analysis, areal density can be estimated from the trace observations at the surface. Areal density is defined as the number of open fractures per unit area per set and should be fairly easy to obtain. Fractures too small to be included in the trace length data should also be excluded from the density data. The data may also be recorded as shown on Table A-1. The sample area should be as large as feasible. Also, the surface data provides direct information on both length and orientation.

For any plane a length-density analysis can be performed as described in Chapter 6. Data can be obtained from boreholes in or near the plane of analysis. In this case, the number of open or partly open fractures of each set intersecting the borehole zones under consideration and the angle between

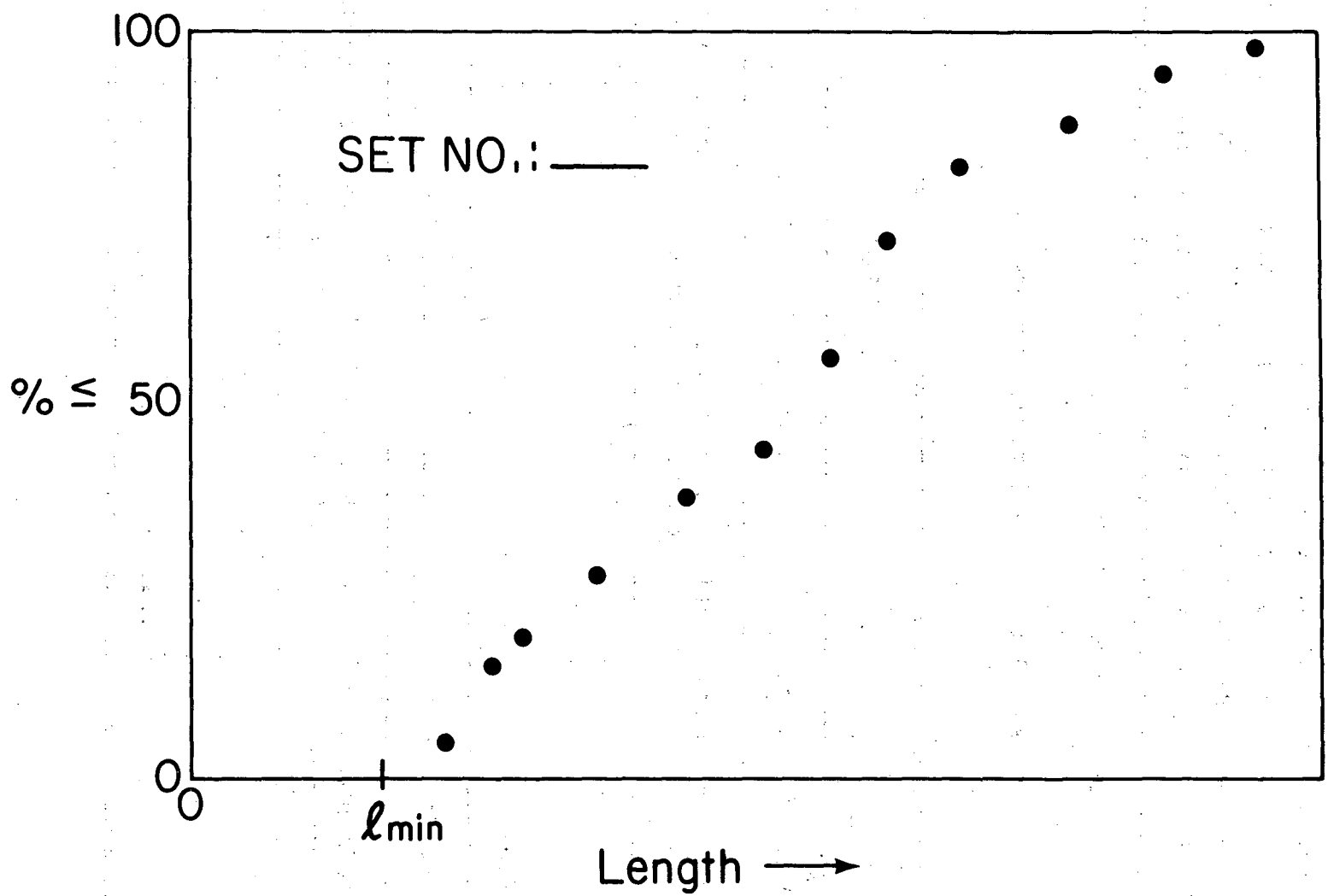

Figure A-1. Example Trace Length Data Plot

the mean pole for each set and the borehole must be known. These values can be obtained from a borehole television survey.

If borehole surveys are used to determine the number of fractures per unit length, the boreholes should preferably be drilled perpendicular to each set. But if only one survey can be run, a direction halfway between the strike of the two most prominant sets would be best. The data needed are shown in Table A-2. Data can be recorded as in Table A-1.

Table A-1. Sample Data Form for Area Surveys

SAMPLE No._____ AREA OF SAMPLE:_____

Set 1 Mean Orientation:_____ Std. Dev. of Orientation:_____

Fracture Number	Trace Length	Number of Visible end points (0, 1 or 2)	Apparent Aperture
o	o	o	o
o	o	o	o
o	o	o	o
o	o	o	o

Set 2 Mean Orientation:_____ Std. Dev. of Orientation:_____

Fracture Number	Trace Length	Number of Visible end points (0, 1 or 2)	Apparent Aperture
o	o	o	o
o	o	o	o
o	o	o	o
o	o	o	o

Table A-2. Sample Data Form for Line Survey

SURVEY NO.: _____ LENGTH OF SURVEY LINE: _____ ORIENTATION OF SURVEY LINE: _____

Set	No. of Fractures From Set Intersecting the Line Sample	Mean Strike of Set	Standard Deviation Strike	Mean Trace Length for Fractures of Set 1 Intersecting the Sample	Standard Deviation of Trace Length
1					
	⋮	⋮	⋮	⋮	⋮
2					
	⋮	⋮	⋮	⋮	⋮

A.3 ORIENTATION

The orientation distribution obtained from the surface trace data will be of primary interest to the study of the horizontal plane. The open fractures should be divided into sets. The mean and standard deviation of orientation (i.e., strike) for each set should be calculated. A plot for each set such as shown in Figure A-2 would be useful to determine the form of the orientation distribution. Dip angle is ignored for the analysis of the horizontal plane.

For application to another plane of analysis similar data could be obtained from a borehole T.V. survey. But, in this case the mean and dispersion of the fracture pole directions for each set should be calculated. Stereographic projections of these data would be useful.

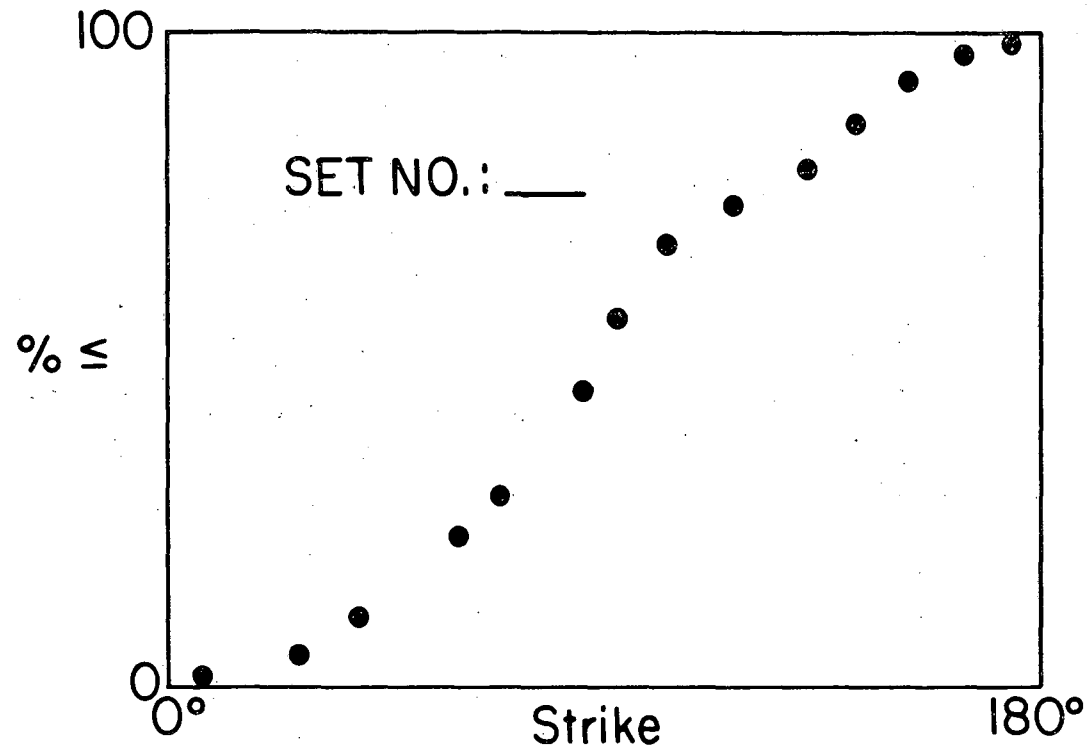

or

for strikes ≃ 0°

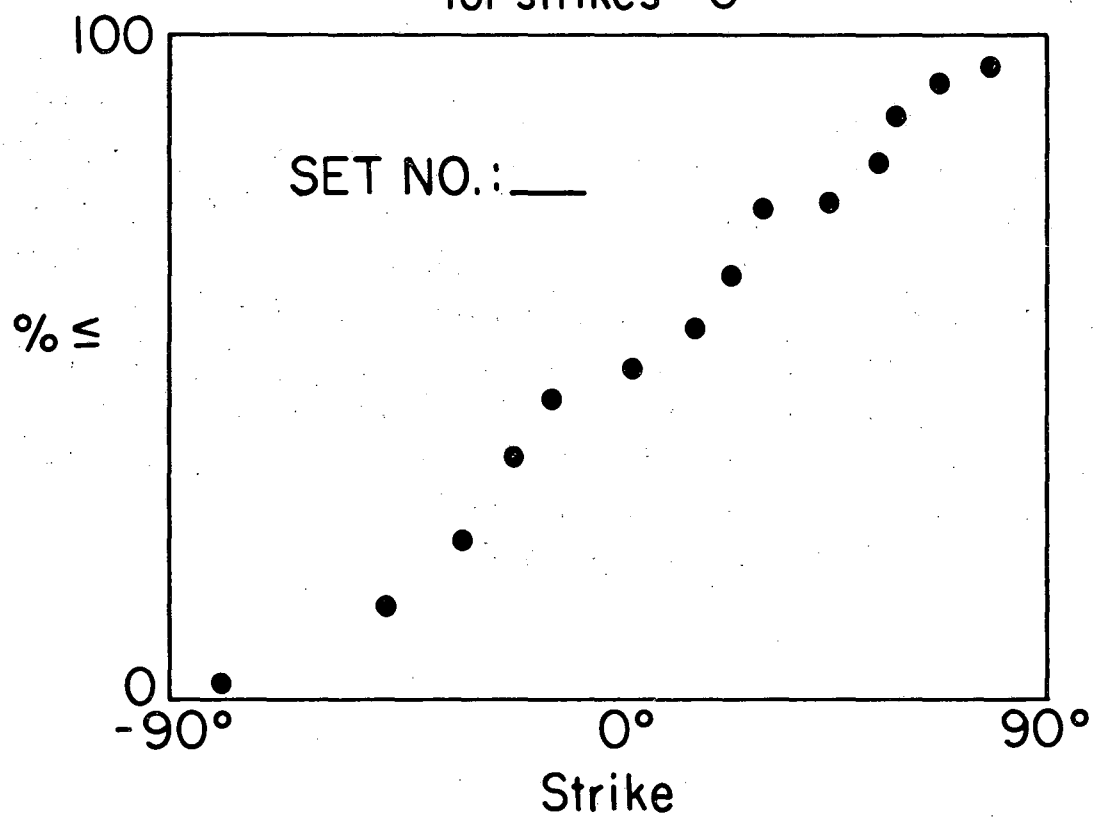

XBL 8210-2495

Figure A-2. Example Orientation Data Plots

A.4 APERTURE

Aperture is a very difficult parameter to estimate. The only way to obtain effective hydraulic apertures may be to measure them in a well in which each fracture is packed off separately. Very little, if any, of this type of data is available on any site. Well tests performed on short zones containing several fractures may be available. From these data one can make an educated guess about the aperture distribution by assuming the largest fracture in each zone was responsible for all or most of the permeability, or by assuming all the fractures conducted equally. The usefulness of these assumptions are examined in Section 7.4.

Furthermore, fracture length, ℓ, can initially be assumed to be related to hydraulic aperture, $\bar{b}$, for example by:

$$1/n\ b = \log C\underline{P} \qquad \text{(A-1)}$$

where C is a constant and $n \geq 1$. The physics of fracture formation and measurements of fracture roughness as described in Chapter 2 suggest a correlation between length and aperture. The hydrologic importance of this relationship is that the permeability should be higher if length and aperture are correlated than if they are not. If length and aperture are correlated, the long conductors which tend to be connected will also tend to be the strong conductors. The short fractures which tend to be unconnected will also tend to be weak conductors.

The best way to determine a correlation model for length and aperture might be to perform transient constant head tests on isolated fractures in the borehole. The early time data (i.e., the first minute) from such tests give an estimate of the hydraulic aperture of the fracture intersecting the well. Later time data can give information about the size of the fracture (Doe et al, 1982).

As an alternative, a correlation model might be obtained using surface trace data. The mean apparent aperture can be estimated by a caliper measurement. If fracture trace lengths and mean apparent apertures are recorded as suggested in Table A-1, it may be possible to deduce a correlation model from a regression analysis of the data, perhaps as shown in Figure A-3. Linear and

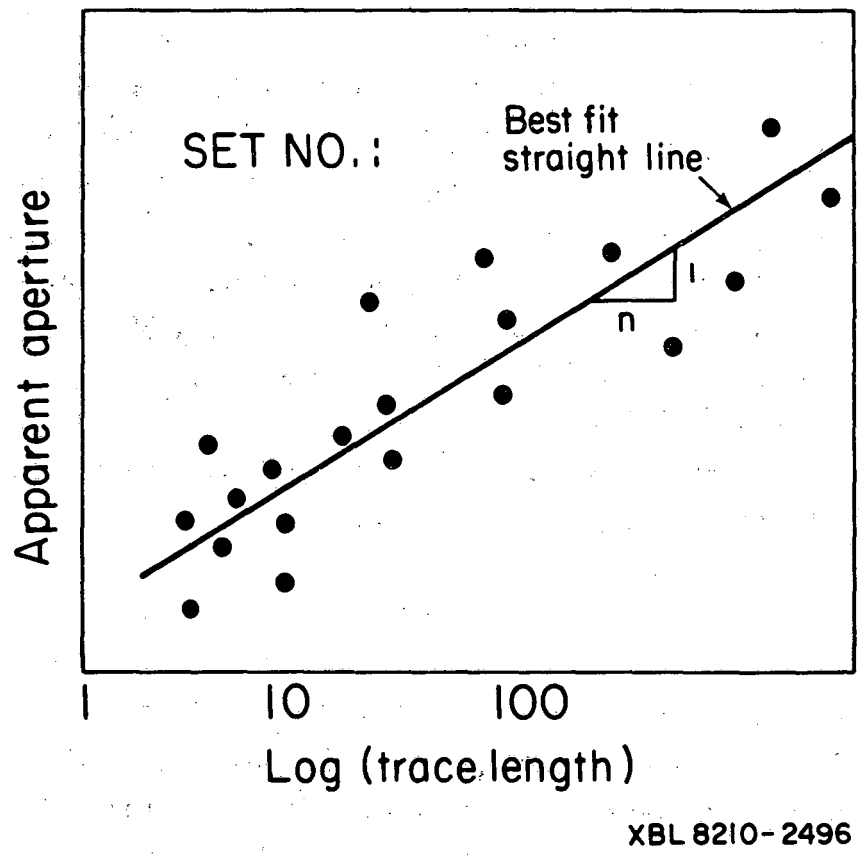

Figure A-3. Example Length-Apparent Aperture Data Plot

exponential models could also be tried. Data should be plotted by sets for open fractures only. The model might then be adjusted using the results of permeability tests on isolated single fractures in the boreholes. From the measured permeability, the values of effective apperture, b, can be calculated. The mean value of effective aperture should then be compared to the mean aperture as measured by T.V. log. The ratio of mean hydraulic aperture to mean observed aperture can then be used to move the regression line up or down.

The aperture-length correlation model proposed in Equation A-1 is only a guess. However, so far no work has been done on the relationship between length and aperture which would help to derive a model. Since a correlation between length and aperture is very important to the hydraulics of fracture networks, this simple model was tried in Chapter 7.

OCRD

Office of Crystalline Repository Development

BATTELLE Project Management Division
505 King Avenue
Columbus, Ohio 43201-2693